ISSN
2712-8172

Magazine of Civil Engineering

112(4), 2022

Magazine of Civil Engineering

ISSN 2712-8172

Online peer-reviewed open-access scientific journal in the field of Civil and Construction Engineering

Founder and Publisher: Peter the Great St. Petersburg Polytechnic University

This journal is registered by the Federal Service for Supervision of Communications, Information Technology, and Mass Media (ROSKOMNADZOR) in 2020. Certificate El No. FS77-77906 issued February 19, 2020.

Periodicity: 8 issues per year

Publication in the journal is open and free for all authors and readers.

Indexing: Scopus, Web of Sceince (ESCI, RSCI), DOAJ, Compendex, EBSCO, Google Academia, Index Copernicus, ProQuest, Ulrich's Serials Analysis System, CNKI

Corresponding address: 29 Polytechnicheskaya st., Saint Petersburg, 195251, Russia

Chief science editor: associate member of RAS, Sc.D. in Engineering, Vitaly V. Sergeev

Deputy chief science editor:
Sc.D. in Engineering, Galina L. Kozinetc

Executive editor: Ekaterina A. Linnik

Translator, editor: Darya Yu. Alekseeva

DT publishing specialist:
Anastasiya A. Kononova

Contacts:
E-mail: mce@spbstu.ru
Web: http://www.engstroy.spbstu.ru

Date of issue: 04.07.2022

Contents

Magazine of Civil Engineering

ISSN 2712-8172

journal homepage: http://engstroy.spbstu.ru/

Research article

UDC 624.046

DOI: 10.34910/MCE.112.1

Phase composition of belite cements of increased hydraulic activity

O.A. Miryuk

Rudny Industrial Institute, Rudny, Kazakhstan

✉ *mirola_1107@mail.ru*

Keywords: cements, clinker, belite, alite, aluminates' phase, binders, hydration, hardening

Abstract. The work is devoted to resource-saving technology development of belite cements. To solve the problem of slow hardening of belite cements, the influence of clinker phases on hydration and structure formation of binders has been studied. Composition and structure of substances were analyzed using X-ray, differential thermal methods and microscopy. Dependence of belite cements' design strength with a saturation rate of SR = 0.73–0.80 on the content and properties of C_3S alite was determined. Increase in C_3S activating ability during formation of alite, based on natural silicates structures was revealed. It was found that the combination of C_2S belite and calcium silicoaluminate C6A4MS in cement stimulates hydration and hardening processes. Intensive formation of stable hexagonal hydroaluminates and hydrogelenite provides a high rate of structure formation. Advantages of co-hydration of C_2S with C_3S and C_6A_4MS were realized in the mixed cement obtained from belite and aluminate clinkers. Studies of clinkers based on skarn-magnetite ore dressing waste indicate the preference of technogenic raw materials for improving belite cements technology.

Funding: This research is funded by the Science Committee of the Ministry of Education and Science of the Republic of Kazakhstan (Grant No. AP08856219).

Citation: Miryuk, O.A. Phase composition of belite cements of increased hydraulic activity. Magazine of Civil Engineering. 2022. 112(4). Article No. 11201. DOI: 10.34910/MCE.112.1

1. Introduction

Cement production status determines the level of industrial potential of the state and the rate of construction. Cement industry is a large consumer of raw materials, fuel and energy. Efficient use of resources is an important condition for effective development of production and cement usage. A fundamental resource saving direction is belite cements technology development, characterized by low content of alite phase C_3S [1, 2]. Belite cements are characterized by low saturation rate (SR), the value of which does not exceed 0.80. When belite cements producing, the consumption of calcium carbonate in the raw material mixture is reduced, the cost of thermal energy for clinker burning is reduced and carbon dioxide emissions are reduced as well [3–7]. Belite cements favourably differ in low liberation of heat during hydration; and ensure concrete durability when used in aggressive environment. However, difficulties in obtaining and using cements with low alite content arise due to low grind ability and slow hardening thanks to C_2S increased belite proportion [1, 6].

To intensify belite cements hardening, it was proposed to stabilize active modifications of C_2S by introducing additives into the raw material mixture [8–10], shifting the process of C_2S formation to a high temperature region [2, 11, 12] and high clinker cooling rate [2, 13]. Attempts to increase clinker activity specifically due to the belite phase require complex technical solutions and therefore have not been implemented yet.

A promising direction of intensification of belite cements curing involves C_2S combination with phases of high hydration activity. This can be achieved by changing a raw material mixture composition to obtain a clinker or by belite cement combining with other cements [14–17]. Most of the developments are devoted to cement containing belite and calcium sulfoaluminate [18, 19]. Information on the effect of other clinker phases on intensification of belite cements hardening is scarce. The relevance of the problem increases with technogenic raw materials involvement in cement production, accompanied by a change in clinker phases' composition [8, 12, 18, 20–26].

The purpose of the work is studying the possibility of intensifying belite cements hardening by adjusting the phase composition.

To achieve the objective, the following areas were identified:

- synthesis and study of belite cements using polymineral technogenic material;
- study of belite cements with different alite contents;
- development of a mixed cement composition based on studies' results of hydration and hardening of belite and aluminate phases.

This work is aimed at creating low-energy-intensive cements characterized by intense hardening, high strength and durability.

2. Methods

2.1. Raw materials

The object of the study was belite cements, obtained by co-grinding of 95 % of belite clinker and 5 % of calcium sulfate dehydrate. Belite clinker was synthesized by raw material mixture burning, consisting of limestone, skarn-magnetite ore dressing waste and silica clay rock (Table 1). Waste contains modifying elements, wt.%: TiO_2 0.50 – 0.53; P_2O_5 0.25 – 0.30; MnO 0.35 – 0.40; V_2O_5 0.04 – 0.06; Cu 0.04 – 0.05. Mineral base of waste is composed of silicates of various genesis, composition and structure, wt.%: pyroxenes 20 – 25; epidote 10 – 13; feldspars 8 – 12; chlorites 7 – 10; scapolite 8 – 11; grenades 7 – 12; amphiboles 7 – 14. The following waste is also present, wt.%: pyrite 4 – 8; calcite 4 – 7; quartz 2 – 4; magnetite 3 – 4.

Table 1. Chemical composition of raw materials.

Material	Containing of the oxide, %								
	SiO_2	Al_2O_3	Fe_2O_3	CaO	MgO	SO_3	R_2O	other	loss during sintering
Limestone	0.6	0.1	0.3	50.9	4.9	0.2	0.1	0.1	42.8
Skarn-magnetite ores tails	37.5	9.1	16.8	10.4	5.1	1.2	14.3	1.5	4.1
Silica clay	77.2	5.7	2.5	0.7	1.3	1.2	1.8	0.2	9.4
Lignite-bauxite	13.4	50.2	3.2	0.9	0.4	0.2	5.1	0.1	26.5

To obtain aluminate clinker, raw material mixtures of limestone and lignite-bauxite were prepared (Table 1). Lignite-bauxite includes the remains of carbonized wood. Sulfoaluminate clinker was synthesized from a raw material mixture containing limestone, lignite-bauxite and skarn-magnetite ore dressing waste. FeS_2 pyrite presence in waste determined the possibility of their use as a sulfate-containing component.

2.2. Experimental details

Raw materials were preliminarily crushed to a complete screening through № 008 screen. Composition of raw mixtures for clinkers was calculated by well known methods. Raw mixtures were prepared by thoroughly mixing all the components. Samples of raw mixtures were fired at temperatures of 1300 – 1350 °C until clinkers' formation. Clinker phase composition was determined by the X-ray method.

Cements were obtained by grinding belite clinker with additives (calcium sulfate dehydrate, aluminate clinker). Strength properties of cements were determined on samples of 20×20×20 mm in size, made of cement dough. Cement samples hardened in water. Samples of materials hardened were analyzed using X-ray, differential thermal methods and electron microscopy. Differential thermal analysis method was carried out on a derivatograph of the Q –1500 D of system F. Paulik, J. Paulik, L. Erdey. The phase composition of the cements was determined using general purpose X – ray diffractometer, type DRON – 3M. The diffractometer is equipped with an BSV – 24 type X – ray tube with CuK α – radiation. The diffractograms were processed using difWin program.

3. Results and Discussion

3.1. Features of belite cements based on skarn-magnetite ore dressing waste

The results of chemical and mineral composition analysis of skarn-magnetite ore dressing waste indicate the possibility of using technogenic material in Portland cement technology. Experimental studies have confirmed feasibility of introducing waste into the composition of raw material mixture to obtain clinker cement [7]. Clinker phases of alite C_3S and belite C_2S inherit crystalline structures of natural silicates, characterized by close contact of main elements and impurities. This increases deformation of the crystal lattice and doping of clinker phases. Differences in structures of natural silicates determine the multistage formation of C_2S with the advantage of high-temperature synthesis of belite. It is known [2, 4, 11] that significant amount of C_2S formation in a narrow range of high temperatures increases the degree of thermal effect on the material and activates alite's formation. Convergence of synthesis processes of C_2S and C_3S enhances phase disequilibrium and increases their hydration activity. Modification of β-C_2S belite is stabilized due to increased sulfur concentration in the feed mixture. Belite crystallizes in the form of rounded grains, the size of which increases with increasing firing temperature (Fig. 1).

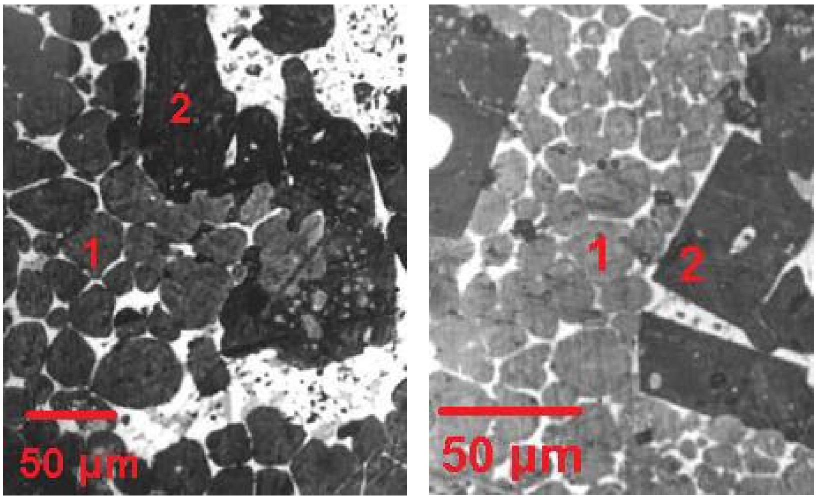

Figure 1. Belite clinkers microstructure (1 – C_2S; 2 – C_3S).

Clinkers synthesized using skarn-magnetite ore dressing waste are characterized by high grinding ability. This is due to increased defectiveness of macrostructure; deformation of crystal lattices of phases during sulfur, manganese, titanium and phosphorus impurities introduction; coarse-grained microstructure of clinker.

Features of clinker formation with the participation of skarn-magnetite ore dressing waste led to an increase in hydraulic activity of belite clinker at the age of 28 days (Table 2).

Table 2. Characteristics of clinkers based on skarn-magnetite ore-dressing waste.

SR	Burning temperature, ^0C	Phases composition, %		Compressive strength, MPa, in age, days				
		C_3S	C_2S	3	7	28	60	360
0.80	1350	35	43	54	70	83	102	100
0.75	1330	25	52	32	53	82	98	101
0.73	1310	20	58	28	51	81	98	97
0.70	1300	13	67	11	21	60	77	95
0.67	1250	0	75	n/a	9	18	57	57
0.90	1450	60	20	71	80	95	92	90

Analysis of the results of clinker cement studies with different SR values revealed the dependence of cement strength on C_3S content (Table 2). This determined interest in studying alite effect on belite cements hardening.

3.2. The effect of alite on belite cements hardening

Hydration processes of belite cements, differing in alite content, were studied (Table 2 and 3). For comparison, cement with SR = 0.90 from traditional raw materials was used.

Table 3. Hydration activity of belite clinker phases.

Phase	Duration of hardening, days	Hydration degree of phases,%, in clinkers with SR					
		0.67	0.70	0.73	0.75	0.80	0.90
Alite	1	no	22	24	25	31	18
	3	no	58	58	60	65	45
	7	no	68	71	73	76	61
	28	no	95	92	85	80	70
Belite	1	0	2	3	4	5	7
	3	1	5	6	8	10	12
	7	4	12	17	20	27	18
	28	8	28	31	35	37	25

C_3S modification in clinkers of various compositions (Table 4) was determined by configuration of the maximum in the angle range of 2θ = 51 – 53°. The firing temperature and impurity elements modifying the liquid phase have decisive influence on polymorphic state of alite. The monolithic reflex d = 0.176 nm characterizes rhombohedral alite form for clinkers with SR = 0.80, fired at a temperature of 1350 °C. In clinkers with small values of saturation rate, synthesized at temperatures of 1300 – 1330 °C, a monoclinic modification was recorded.

Table 4. Diffraction characteristics of alite in clinkers of various compositions.

SR	Intensity of alite's reflection d = 0.176 nm in the X-ray diffraction pattern of clinker, rel. units	Configuration of diffraction maxima in the range of angles 2θ = 51 – 53°	Alit's modification
0.70	11	Forked peak reflex	Monoclinic
0.75	25	Forked peak reflex	Monoclinic
0.80	56	Monolithic reflex	Rhombohedral

Morphology of alite crystals is diverse. Along with small prismatic grains of a clear cut, there are accumulations of large crystals of irregular shape (Fig. 1).

The degree of clinker phases' hydration is determined by changing the height of analytical diffraction maxima. The amount of belite not participating in hydration was approximately calculated from the difference in intensity of joint reflections of alite and belite d = 0.278; 0.219 nm and self reflection of alite d = 0.176 nm.

Results' analysis (Table 2) indicates that cements with a low C_3S content are characterized by higher hydration activity of alite. This is due to two factors. First, the gel-like products of belite hydration adsorb calcium ions from a supersaturated solution and thereby contribute to maintaining interaction activity of alite with water [27, 28]. Secondly, these are conditions of C_3S formation in the studied clinker. Hydration ability of alite depends on modification and nature of C_3S crystallization. In the initial period of hydration (1 – 7 days), increased activity of rhombohedral alite (cement with SR = 0.80) is observed. For clinkers with a monoclinic modification of alite, characterized by polygranularity, the dependence of hydration degree on saturation rate in early stages is small, but by 28 days hardening increases.

Hydration of C_3S is accompanied by abundant secretion of $Ca(OH)_2$ portlandite, which activates belite hardening. With an increase in SR, the rate of hydration of belite in early stages almost doubles (Table 3). Stable hardening of belite cements (Table 2) is facilitated by $Ca(OH)_2$ involvement in composition of calcium hydrosilicates. The content of portlandite, which is almost the same by 28 days of hydration for various cements, decreases in the stone of belite cement with prolonged hardening (Table 5). This will provide hardened cement with increased corrosion resistance.

Table 5. Portlandite content in hydrated cements (according to differential thermal analysis data).

SR	Weight loss of hydrated cements at a temperature of 550 ^{0}C,%	
	28 days	60 days
0.75	10.8	12.5
0.80	11.6	20.8
0.90	12.3	24.2

Active hydration of alite ensures the release of the bulk of $Ca(OH)_2$ in early stages of hardening. This determines predominant participation of portlandite in primary crystalline framework formation. Such a hydrate formation mechanism is favorable for hardening of the setting mass. Since in a later period, when secondary hydrates are released, smooth crystallization of portlandite is required to achieve high strength. This contributes to even distribution of neoplasm in the structure of the stone.

Studies of composition and structure of long-hardening cement stone revealed that portlandite is the basis of crystalline hydrates. Conservation of readily soluble portlandite during prolonged exposure to water was facilitated by the dense stone structure (Fig. 2).

Calcium hydrosilicates have a cryptocrystalline state. Cement stone is characterized by structural and morphological heterogeneity due to differences in the stages of growth and intergrowth of hydrate particles.

Consequently, characteristics of chemical and mineral composition of skarn-magnetite ore dressing wastes affect the rate of clinker formation, structure and activity of phases, especially alite. As a result, belite cements acquire high hydraulic activity at the age of 28 days, stable hardening and resistance of cement stone with prolonged hardening.

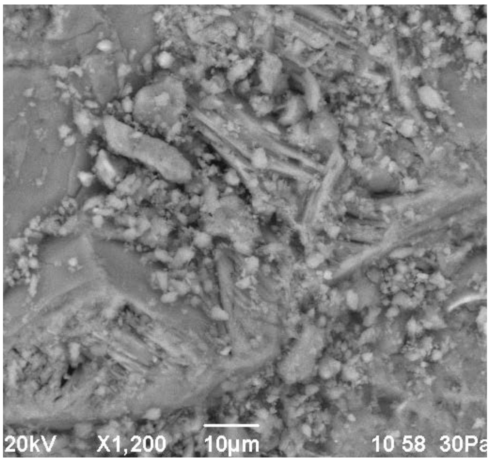

Figure 2. The micrograph of cement stone after 360 days of hardening.

At the same time, the problem of slow hardening of cements during early stages remains unsolved. This is a serious obstacle to the development of low-energy belite cement technology.

3.3. Effect of magnesium calcium silicoaluminate on hydration and hardening of belite cement

Advantages of cements with a high content of belite are realized in synthesis of clinkers containing modified aluminate phases [16, 17, 19]. Firing of modified clinkers is characterized by reduced energy costs. The high hardening rate of aluminate cements allows us to abandon the heat treatment of concrete [29, 30]. Clinkers containing calcium sulfoaluminate were most widely used [18, 19, 31, 32].

The modern raw material base of cement production is expanding due to industrial waste [20–26, 33–35]. To obtain aluminate and sulfoaluminate clinkers, raw materials are used, they contain minerals based on silicon, magnesium, and iron [6, 10, 17, 31, 32, 34, 35]. In clinkers produced from raw calcium mixtures of complex composition, C_6A_4MS magnesium calcium silicoaluminate is formed, which is also called magnesia pleochroite or phase Q [29, 36, 37]. It was established [38] that C_6A_4MS formation is accompanied by minimization or exclusion of inert phases of C_2AS and MgO. The joint presence of C_6A_4MS and $3(CA)CaSO_4$ clinkers was revealed during the initial and predominant formation of calcium sulfoaluminate. C_6A_4MS formation is promoted by increased concentration of Fe_2O_3 in the raw mixes. High hydraulic activity of cements containing magnesium calcium silicoaluminate indicates advisability of C_6A_4MS phase presence in aluminate clinker. A method for calculating the composition of raw mixes for clinkers containing C_6A_4MS was proposed [39].

Sulfoaluminate clinkers containing various amounts of C_6A_4MS phase were synthesized (Fig. 3). C_6A_4MS phase identified by the following x-ray indices: 0.372; 0.309; 0.289; 0.276; 0.271; 0.244; 0.240; 0.218 nm.

Presence of a little-studied phase in clinkers necessitates a study of the effect of C_6A_4MS on belite hydration. Model binders were prepared by mixing monophasic cements from C_6A_4MS and C_2S, which were previously synthesized from chemical reagents. Results of physical and mechanical tests of model binders are presented in Fig. 6. Composition of binders after hydration was investigated using X-ray.

In C_6A_4MS presence, the early hardening of belite cement is intensified. The increased strength of mixed binders is disproportionate to the content of C_6A_4MS (Fig. 4). An increase in the content of calcium hydroaluminates during hardening of mixed binders indicates accelerated hydration of C_6A_4MS in the presence of C_2S. A strong crystalline framework of cement stone is formed from hexagonal calcium hydroaluminates. A feature of hardening mixture composition is C_2ASH_8 hydrogelite, which provides increase in binder's strength.

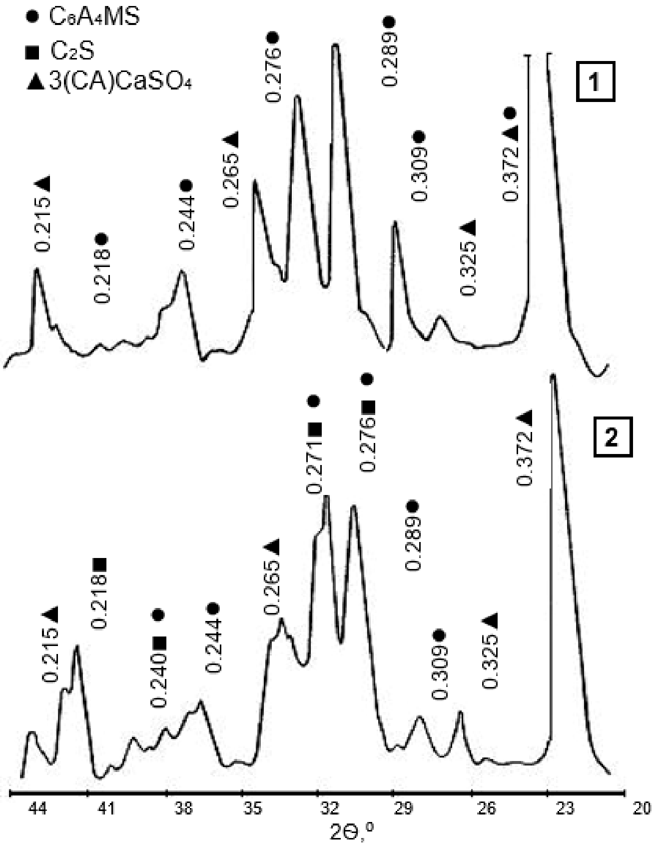

Figure 3. Diffraction patterns of sulfoaluminate clinkers (1 – 60 % C6A4MS; 2 – 20 % C6A4MS).

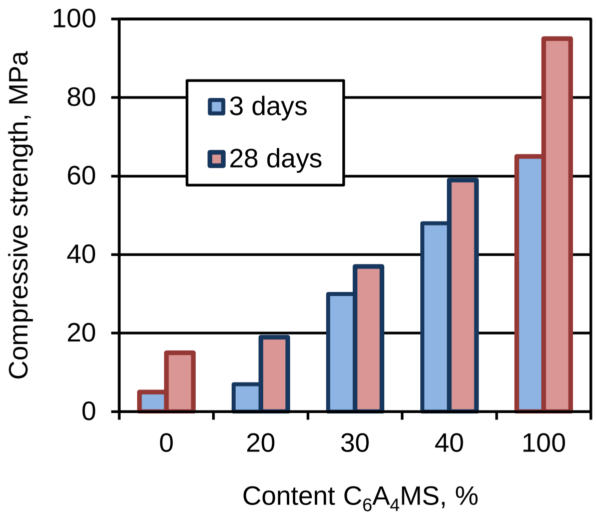

Figure 4. The effect of C_6A_4MS phase on hardening of a model binder.

Hydrogelenite formation is the result of diffusion of calcium hydrosilicates into the matrix structure from metastable calcium hydroaluminates. The nature of hydrate formation in mixed binders (Tables 6 and 7) indicates that C_2ASH_8 hydrogelite is formed with the participation of C_2AH_8.

Intensity of C_2ASH_8 formation is determined by saturation of the liquid phase with calcium ions and depends on the content of C_2S in the binder. The amount of C_2ASH_8 is limited by C_2AH_8 concentration. This is confirmed by a slight difference in the content of hydrogelite for binders that differ in phase composition.

It is known [40], that calcium hydroaluminates stability decreases with increasing hardening temperature. Influence of heat treatment on hydrate formation in binders with different content of belite is investigated. Cement samples containing 20 % and 60 % of C_2S, after 1 day of hardening at a temperature of 20 °C, were subjected to heat treatment at a temperature of 80 °C (Table 7).

Table 6. The effect of C_6A_4MS phase on hydrates composition of the model binder.

Content C_6A_4MS,%	Intensity of hydrate reflections on the roentgenogram of cement stone, rel. units					
	CAH_{10} (1.41 nm)		C_2AH_8 (1.07 nm)		C_2ASH_8 (1.26 nm)	
	Duration of hardening, days					
	3	28	3	28	3	28
20	9	traces	7	traces	16	17
40	21	12	10	no	13	19
100	18	19	16	17	no	no

With increasing temperature, hydration of C_2S and formation of calcium hydrosilicates are accelerated. This contributes to C_2ASH_8 formation. However, at C_2S content of 20 %, recrystallization of hexagonal calcium hydroaluminates is observed.

Table 7. The effect of temperature on hydrates composition of model binders.

Content C_2S, %	Intensity of hydrate reflections on the roentgenogram of cement stone, rel. units									
	CAH_{10} (1.41 nm)		C_2AH_8 (1.07 nm)		C_2ASH_8 (1.26 nm)		C_3AH_6 (0.51 nm)		AH_3 (0.48 nm)	
	Temperature of hardening, ºC									
	25	80	25	80	25	80	25	80	25	80
20	28	no	15	no	no	13	no	18	no	9
60	28	22	no	no	14	16	no	no	no	traces

Therefore, cubic hydrates C_3AH_6 and AH_3 are formed and predominate in the cement stone. With an increase in C_2S content to 60 %, the bulk of C_2ASH_8 is formed at normal hardening temperature. Heat treatment of the binder does not violate hexagonal calcium hydroaluminates stability.

Consequently, the combined hydration of C_6A_4MS and C_2S is favorable for intensive hardening and formation of strong cement stone.

3.4. Mixed cements from belite and aluminate clinkers

The activating effect of C_6A_4MS on C_2S hydration justifies intensification of belite cements hardening by adding aluminate clinker. Obtaining double-clinker cements is an effective technological technique that allows you to adjust composition and properties of binders.

Mixed cements of various compositions were obtained from belite clinkers and aluminate clinker containing 80 % of C_6A_4MS (Table 8, Fig. 5).

Table 8. Characteristics of mixed cements.

Composition of mixed cement, %		SR (belite clinkers)	Content phases, %			Water / Cement, %
aluminate clinker	belite clinker		C_3S	C_2S	C_6A_4MS	
0	100	0.67	0	75	0	26.0
		0.74	22	56		25.8
		0.80	35	43		25.4
		0.84	42	33		25.6
10	90	0.67	0	68	8	26.1
		0.74	20	50		26.0
		0.80	31	39		25.5
		0.84	38	30		25.8
20	80	0.67	0	60	16	26.7
		0.74	18	45		26.2
		0.80	28	34		25.6
		0.84	34	26		26.0

Composition of mixed cement, %: aluminate clinker	belite clinker	SR (belite clinkers)	Content phases, %: C_3S	C_2S	C_6A_4MS	Water / Cement, %
30	70	0.67	0	52	24	27.1
		0.74	15	39		26.6
		0.80	24	30		25.9
		0.84	29	23		26.3
40	60	0.67	0	45	32	27.4
		0.74	13	34		27.0
		0.80	21	26		26.2
		0.84	25	20		26.8
50	50	0.67	0	37	40	27.7
		0.74	11	28		27.3
		0.80	17	21		26.8
		0.84	21	16		27.1

Intensive hardening of mixed cement is provided by mutual activation of the following phases: C_6A_4MS and C_2S. The nature of C_6A_4MS effect on cement hardening depends on clinkers' SR. The greatest increase in strength was achieved for cement made of belite clinkers with reduced SR values. For all the binders studied, the maximum hardening effect in the early stages of hardening is manifested at 30 – 50 % aluminate additives.

The strength of mixed cement at the initial stages of hardening is 1.3 times higher than belite cement's strength. Introduction of aluminate clinker also makes it possible to increase belite cement's strength by 30 % at the age of 28 days.

Presence of aluminate component practically did not affect the activity of cement containing clinker with SR = 0.84. Ambiguous nature of the change in cements strength is due to influence of portlandite released during alite hydration. As the clinker saturation rate in a mixed binder increases, the proportion of highly basic calcium hydroaluminates C_2AH_8 and C_4AH_{13} increases. In this case, the highest content of hydrogelite is characteristic of hardening cement from clinker with SR = 0.74, and in the cement stone with SR = 0.84, the proportion of C_2ASH_8 is minimal.

Obviously, with an excess of calcium ions, the stability of hydrogelite decreases. A significant increase in CaO : Al_2O_3 ratio in hardening cements contributes to formation of cubic calcium hydroaluminate C_3AH_6. The process is accompanied by cement stone destruction. For this reason, aluminate additive practically does not accelerate the rate of hardening of cement with SR = 0.84.

As a result of the studies, the preferred phase composition of the mixed cement was established, wt.%: 35 – 45 C_2S; 25 – 35 C_6A_4MS; 15 – 20 C_3S.

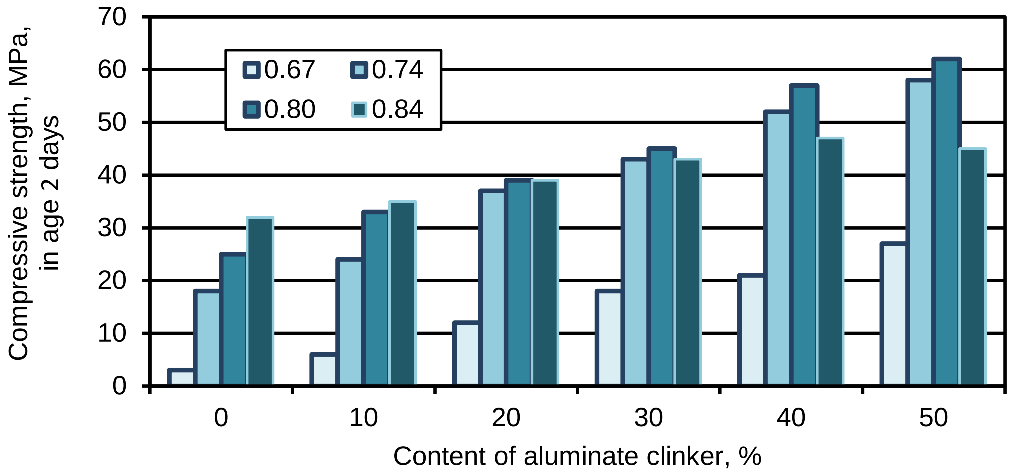

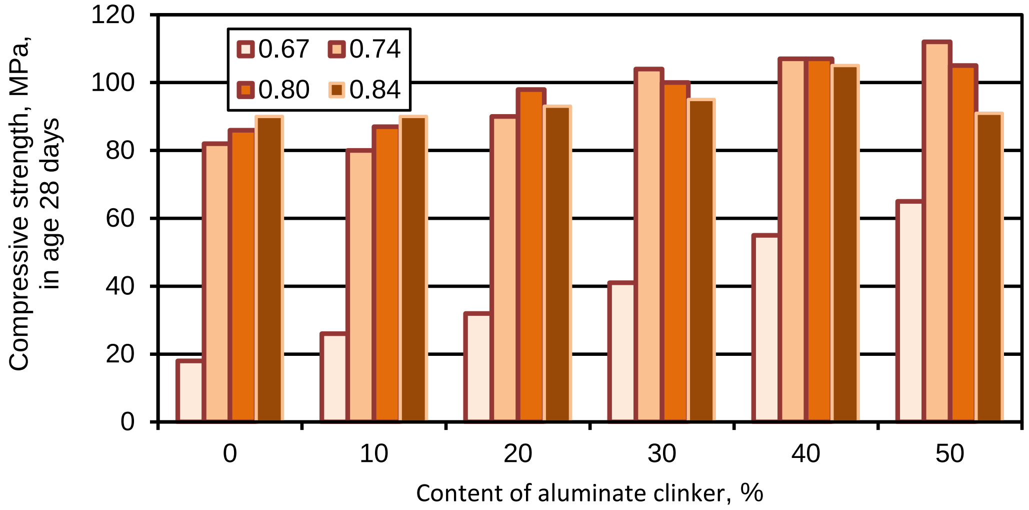

Figure 5. The effect of aluminate clinker additives on mixed cement hardening.

Effectiveness of the combination of clinkers of different phase composition is determined by two factors: intensification of hardening of belite cement with SR = 0.74 – 0.80; stabilization of strength properties of aluminate cement stone due to formation of stable hydrates and crystalline structure formation.

4. Conclusions

The results of hydration activity studies of clinkers synthesized with the use of skarn-magnetite ore dressing waste indicate that the rates of hydration and structure formation of belite cements with SR = 0.74 – 0.80 significantly depend on accompanying phases composition.

1. It was revealed that the setting rate of belite cements is very sensitive to the content of alite phase. The design strengths of cements with 20 – 35 % C_3S are comparable with characteristics of traditional Portland cement.

2. It has been established that high reactivity of C_3S in belite cement is due to formation of clinker phases based on the structures of natural silicates, influence of modifying impurities contained in technogenic raw materials.

3. The effect of C_6A_4MS phase on hydration and hardening of belite cement has been studied for the first time. It has been proven that C_6A_4MS and C_2S combination promotes intensive hardening and ensures high binder strength. It is substantiated that in the presence of C_2S hydration of C_6A_4MS is accelerated, stability of hexagonal calcium hydroaluminates increases, and hydrogenite is formed. Change in composition of hydrated phases ensures formation of a solid structure of the cement stone.

4. A method for intensifying belite cements' hardening has been proposed, which provides for introduction of an additive with high hydration activity. The developed cement is distinguished by addition of aluminate clinker, which consists mainly of C_6A_4MS, to belite cement.

5. Phase composition of mixed cement, including 35 – 45 % C_2S; 25 – 35 % C_6A_4MS; 15 – 20 % C_3S, provides high rates of hardening at all stages of hardening, durability of the cement stone.

References

1. Chatterdzhi, A.K. Perekhod k stroitelstvu na osnove tsementa s nizkim «uglerodnym sledom»: trebovaniya i prepyatstviya [Transition to low carbon cement-based construction – imperatives and obstacles]. Tsement i yego primeneniye. 2018. (2). Pp. 54–59. (rus)
2. Sudakas, L.G., Kraplya, A.F., Fedik, A.A. Nauchnyye printsipy proizvodstva aktivnykh nizkoosnovnykh klinkerov [Scientific principles for the production of active low-base clinkers].Tsement. 1989. (3). Pp. 16–17. (rus)
3. Ávalos-Rendóna, T.L., Pastén Chelala, E.A., Mendoza Escobedo, C.J., Figueroa, I.A., Lara, H.V., Palacios-Romerod, L.M. Synthesis of belite cements at low temperature from silica fume and natural commercial zeolite. Materials Science and Engineering: B. 2018. 229. Pp. 79–85. DOI: 10.1016/j.mseb.2017.12.020
4. Bouzidi, M.A., Tahakourt, A., Bouzidi, N., Merabet, D. Synthesis and characterization of belite cement with high hydraulic reactivity and low environmental impact. Arabian Journal for Science and Engineering. 2014. 39(12). Pp. 8659–8668. DOI: 10.1007/s13369-014-1471-2
5. Park, S.-J., Jeon, S.-H., Kim, K.-N., Song, M.-S. Hydration characteristics and synthesis of hauyne-belite cement as low temperature sintering cementitious materials. Journal of the Korean Ceramic Society. 2018. 55(3). Pp. 224–229. DOI: 10.4191/kcers.2018.55.3.04

6. Pawluk, J. The importance of marls with high silica modulus as raw materials for belite cements production. Cement Wapno Beton. 2018. 23(1). Pp. 40–47.
7. Miryuk, O.A. The effect of waste on the formation of cement clinker. IOP Conference Series: Materials Science and Engineering. 2019. 510. DOI: 10.1088/1757-899X/510/1/012012
8. Koumpouri, D., Angelopoulos, G.N. Effect of boron waste and boric acid addition on the production of low energy belite cement. Cement and Concrete Composites. 2016. 68. Pp. 1–8. DOI: 10.1016/j.cemconcomp.2015.12.009
9. Zhao, Y., Lu, L., Wang, S., Gong, C., Lu, L. Dicalcium silicates doped with strontia, sodium oxide and potassia. Advances in Cement Research. 2015. 27(6). Pp. 311–320. DOI: 10.1680/adcr.14.00011
10. Ohno, M., Niijima, S., Kurokawa, D., Hirao, H. A study on the control of hydration reactivity of belite – strength improvement of high belite cement containing abundant MgO. Cement Science and Concrete Technology. 2016. 70(1). Pp. 61–68. DOI: 10.14250/cement.70.61
11. Barbanyagre, V.D., Goloviznina, T.Ye. Polucheniye bystrotverdeyushchego nizkoosnovnogo klinkera kratkovremennym vysokotemperaturnym legirovaniyem [Obtaining quick-hardening low-base clinker with short-term high-temperature alloying]. Tsement i yego primeneniye. 1999. (5). Pp. 23–26. (rus)
12. Gong, Y., Fang, Y. Preparation of belite cement from stockpiled high-carbon fly ash using granule-hydrothermal synthesis method. Construction and Building Materials. 2016. 111. Pp. 175–181. DOI: 10.1016/j.conbuildmat.2016.02.043
13. Kacimi, L., Simon-Masseron, A., Salem, S., Ghomari, A., Derriche, Z. Synthesis of belite cement clinker of high hydraulic reactivity.Cement and Concrete Research. 2009. 39(7). Pp. 559–565. DOI: 10.1016/j.cemconres.2009.02.004
14. Koga, G.Y., Comperat, P., Albert, B., Roche, V., Nogueira, R.P. Effect of endogenous chloride contamination on the electrochemical and hydration responses of reinforced belite-ye'elimite-ferrite (BYF) cement mortars. Cement and Concrete Research. 2019. 122. Pp. 212–226. DOI: 10.1016/j.cemconres.2019.04.022
15. Morin, V., Termkhajornkit, P., Huet, B., Pham, G. Impact of quantity of anhydrite, water to binder ratio, fineness on kinetics and phase assemblage of belite-ye'elimite-ferrite cement. Cement and Concrete Research. 2017. 99. Pp. 8–17. DOI: 10.1016/j.cemconres.2017.04.014
16. Kang, E.H., Yoo, J.S., Kim, B.H., Choi, S.W., Hong, S.H. Synthesis and hydration behavior of calcium zirconium aluminate (Ca7ZrAl6O18) cement. Cement and Concrete Research. 2014. 56. Pp. 106–111. DOI: 10.1016/j.cemconres.2013.11.007
17. Iacobescu, R.I., Pontikes, Y., Koumpouri, D., Angelopoulos, G.N. Synthesis, characterization and properties of calcium ferroaluminate belite cements produced with electric arc furnace steel slag as raw material. Cement and Concrete Composites. 2013. 44. Pp. 1–8. DOI: 10.1016/j.cemconcomp.2013.08.002
18. Rungchet, A., Chindaprasirt, P., Wansom, S., Pimraksa, K. Hydrothermal synthesis of calcium sulfoaluminateebelite cement from industrial waste materials. Journal of Cleaner Production. 2016. 115. Pp. 273–283. DOI: 10.1016/j.jclepro.2015.12.068
19. Wang, S., Liu, B., Zhao, P. Effect of early-strength-enhancing agents on setting time and early mechanical strength of belite-barium calcium sulfoaluminate cement. Journal of Thermal Analysis and Calorimetry. 2018. 131(3). Pp. 2337–2343. DOI: 10.1007/s10973-017-6837-8
20. Junwei, S., Jielu, Z. Hydration heat evolution of high-belite cement–phosphate slag binder. Journal of Thermal Analysis and Calorimetry. 2019. 138(1). Pp. 135–143. DOI: 10.1007/s10973-019-08241-5
21. Kavas, T., Angelopoulos, G.N., Iacobescu, R.I. Production of belite cement using boron and red mud wastes. Cement Wapno Beton. 2015. 20(5). Pp. 328–334.
22. Mazouzi, W., Kacimi, L., Cyr, M., Clastres, P. Properties of low temperature belite cements made from aluminosilicate wastes by hydrothermal method. Cement and Concrete Composites. 2014. 53. Pp. 170–177. DOI: 10.1016/j.cemcon-comp.2014.07.001
23. Suthatip, S., Kittipong, K., Suwimol, A. Synthesis of belite cement from nano-silica extracted from two rice husk ashes. Journal of Environmental Management. 2017. 190(1). Pp. 53–60. DOI: 10.1016/j.jenvman.2016.12.016
24. Farag, L.M., Radwan, M.M., Abd El-Hamid, H.K. Effect of oil shale additions on the raw mix and clinker for high belite cement. ZKG International. 2016. 69(12). Pp. 48–55.
25. Rungchet, A., Poon, C.S., Chindaprasirt, P., Pimraksa, K. Synthesis of low-temperature calcium sulfoaluminate-belite cements from industrial wastes and their hydration: Comparative studies between lignite fly ash and bottom ash. Cement and Concrete Composites. 2017. 83. Pp. 10–19. DOI: 10.1016/j.cemconcomp.2017.06.013
26. Dahhou, M., Barbach, R., Moussaouiti, M.E. Synthesis and characterization of belite-rich cement by exploiting alumina sludge. KSCE Journal of Civil Engineering. 2019. 23. Pp. 1150–1158. DOI: 10.1007/s12205-019-0178-z
27. Sychev, M.M., Sychev, V.M. Priroda aktivnykh tsentrov i upravleniye aktami gidratatsii [The nature of active centers and the management of hydration events].Tsement. 1990. (5). Pp. 6–10. (rus)
28. Maheswaran, S., Kalaiselvam, S., Palani, G.S., Sasmal, S. Investigations on the early hydration properties of synthesized β-belites blended cement pastes. Journal of Thermal Analysis and Calorimetry. 2016. 125(1). Pp. 53–64. DOI: 10.1007/s10-973-016-5386-x
29. Kuznetsova, T.V. Glinozemistyy tsement [Alumina cement]. Alitinform: Tsement. Beton. Sukhiye smesi. 2008. (2). Pp. 8–24. (rus)
30. Galkin, Yu.Yu., Udodov, S.A., Vasil'eva, L.V. The phase composition and properties of aluminate cements after early loading // Magazine of Civil Engineering. 2017. (7). Pp. 114–122. DOI: 10.18720/MCE.75.11
31. Kharchenko, I.Ya., Pustovgar, A.P., Pashkevich, S.A., Yeremin, A.V., Ivanova, I.S., Bazhenov, Yu.M., Kharchenko, A.I. Gidratatsiya i strukturoobrazovaniye pri tverdenii rasshiryayushchikhsya tsementov v usloviyakh ogranichennykh deformatsiy. Inzhenerno-stroitelnyy zhurnal. 2017. 75(7). Pp. 161–170. DOI: 10.18720/MCE.75.16
32. Bullerjahn, F., Schmitt, D., Haha, M.B. Effect of raw mix design and of clinkering process on the formation and mineralogical composition of (ternesite) belite calcium sulphoaluminate ferrite clinker. Cement and Concrete Research. 2014. 59. Pp. 87–95. DOI: 10.1016/j.cemconres.2014.02.004
33. Bastos da Costa, E., Rodríguez, E.D., Bernal, S.A., Provis, J.L., Gobbo, L.A., Kirchheim, A.P. Production and hydration of calcium sulfoaluminate-belite cements derived from aluminium anodising sludge. Construction and Building Materials. 2016. 122. Pp. 373–383. DOI: 10.1016/j.conbuildmat.2016.06.022
34. Slavcheva, G.S., Baidzhanov, D.O., Khan, M.A., Shvedova, M.A., Imanov, Y.K. S linkerless slag-silica binder: hydration process and hardening kinetics // Magazine of Civil Engineering. 2019. (92). C. 96–105. DOI: 10.18720/MCE.92.8

35. Xue, P., Xu, A., He, D., Yang, Q., Liu, G., Engström, F., Björkman, B. Research on the sintering process and characteristics of belite sulphoaluminate cement produced by BOF slag. Construction and Building Materials. 2016. 122. Pp. 567–576. DOI: 10.1016/j.conbuildmat.2016.06.098
36. Bobel, A., Kim, K., Wolverton, C., Walker, M., Olson, G.B. Equilibrium composition variation of Q-phase precipitates in aluminum alloys. Acta Materialia. 2017. 138(1). Pp. 150–160. DOI: 10.1016/j.actamat.2017.07.048
37. Kim, K., Bobel, A., Baik, S., Walker, M., Voorhees, P.W., Olson, G.B. Enhanced coarsening resistance of Q-phase in aluminum alloys by the addition of slow diffusing solutes. Materials Science and Engineering. 2018. 735. Pp. 318–323. DOI: 10.1016/j.msea.2018.08.059
38. Miryuk, O. Synthesis of special clinkers with the use of technogenic raw materials. Key Engineering Materials. 2018. 769. Pp. 9–16. DOI: 10.4028/www.scientific.net/KEM.769.9
39. Miryuk, O.A. Synthesis and properties of aluminates clinker of complex composition. ARPN Journal of Engineering and Applied Sciences. 2019. 14(14). Pp. 2605–2613.
40. Liu, K., Chen, A., Shang, X., Chen, L., Zheng, L., Gao, S., Zhou, Y., Wang, Q., Ye, G. The impact of mechanical grinding on calcium aluminate cement hydration at 30 °C. Ceramics International. 2019. 45(11). Pp. 14121–14125. DOI: 10.1016/j.ceramint.2019.04.112

Information about authors:

Olga Miryuk*,*
Doctor in Technical Sciences,
ORCID: https://orcid.org/0000-0001-6892-2763
E-mail: mirola_1107@mail.ru

Received 01.02.2020. Approved after reviewing 07.09.2021. Accepted 08.09.2021.

Magazine of Civil Engineering

ISSN 2712-8172

journal homepage: http://engstroy.spbstu.ru/

Research article

UDC 691.88

DOI: 10.34910/MCE.112.2

Bearing capacity of riveted connections of mineral wool sandwich panels

A. Galyamichev [a], ***E. Gerasimova*** [b] ✉, ***D. Egorov*** [a], ***D. Serdjuks*** [c], ***A.M. Grossman*** [a], ***D.A. Lysenko*** [a]

[a] *Peter the Great St. Petersburg Polytechnic University, St. Petersburg, Russia*

[b] *NIUPC, Mezhregional'nyj institut okonnyh i fasadnyh konstrukcij, St. Petersburg, Russia*

[c] *Riga Technical University, Riga, Latvia*

✉ *katyageras17@gmail.com*

Keywords: bearing capacity, sandwich structures, facades, dynamic loads, pull-out strength, connectors

Abstract. The article presents a study on the pulling-out bearing capacity of the connection between a curtain wall system and an outer sheet of a wall sandwich panel with a mineral wool core realized through blind rivets. An experimental study was carried out on samples of sandwich panels with various parameters of fastening in order to assess the influence of the considered factors on the value of bearing capacity. Results obtained for the studied type of sandwich panel allowed us to determine the minimum permissible edge distance for a blind rivet in order to prevent delamination of the outer sheet as well as the influence of the end profile installation and cyclic load action on the bearing capacity of the joint. Experimental results showed that the edge distance of 75 mm or more does not affect the bearing capacity of the joint. The pulling-out bearing capacity of a blind rivet with a diameter of 4.8 mm was determined for both single and cyclic load actions. The presence of an additional stiffening element such as end face profile contributed to an increase of this value. Recommended scheme for the installation of the fastening elements was proposed based on dependencies obtained during the experimental investigation.

Acknowledgement: The research group would like to thank Prof. Dr.-Ing. Jörg Lange, TU Darmstadt, Germany, for his assistance and contributions. Furthermore, we would like to thank company ISOPAN for providing the samples of sandwich panels, and companies Alternativa and U-kon for supplying with the samples of curtain wall systems.

Citation: Galyamichev, A., Gerasimova, E., Egorov, D., Serdjuks, D., Grossman, A.M., Lysenko, D.A. Bearing capacity of riveted connections of mineral wool sandwich panels. Magazine of Civil Engineering. 2022. 112(4). Article No. 11202. DOI: 10.34910/MCE.112.2

1. Introduction

Nowadays in construction practice three-layer sandwich panels are often used as enclosing structures in buildings and facilities for various purposes because of their weight, cost, and structural characteristics. Different cladding types such as aluminum composite panels, fiber cement boards, or high-pressure laminate (HPL) panels can be applied for covering the external walls made of three-layer sandwich panels on new construction sites (Figures 1 and 2) as well as for existing buildings under reconstruction (Figure 3).

Figure 1. Platov Airport, Rostov-on-Don (Russia).

Figure 2. Historical park "Russia – my history", Volgograd (Russia).

Figure 3. Shopping mall «MEGA Khimki», Moscow (Russia).

Several fastening options exist depending on the structural scheme of a cladding system attachment to the external sandwich panel:

- Fastening to bearing structures situated behind a sandwich panel (through);
- Fastening to an external framework;
- Fastening to an outer metal sheet.

This paper presents a study on the fastening to the outer steel sheet of the sandwich panel with mineral wool insulation core. One of the main reasons of failure when the system no longer fulfills the Ultimate Limit State conditions is the delamination of the sandwich panel (Figure 4) [1]. Delamination occurs under a variety of dynamic and quasi-static load conditions [2], therefore it should be carefully revised when designing an enclosing structure.

Within the framework of this study, the delamination of sandwich panels with the mineral wool core is analyzed. Such a phenomenon was already observed among other failure modes for sandwich panels with other types of core, such as multi-layered aluminum foam core and multi-layered hybrid aluminum foam / ultra-high-molecular-weight polyethylene (UHMWPE) laminate core in [3]. Article [4] presents an overview and failure maps on the dependencies of the critical failure modes including the delamination on the structural parameters and load/support combinations for sandwich panels with polyurethane (PUR) core. The flexural properties, collapse modes, and crush characteristics of different types of composite panels are described in [5] on the basis of series of flexural tests. The panels were subjected to both mechanical and thermal actions. Polyurethane (PUR) and polyvinylchloride (PVC) core sandwich panels subjected to tension, compression, and shear loading were tested and modeled using the Finite Element Method in [6] taking into account non-linear behavior of the foam core and skin-core cohesive interaction. Foam-core sandwich composites subjected to low-velocity impact are studied in [7]. The study [8] is dedicated to the detection of delamination in composite structures including the ones with PUR core under free vibration. The peculiarity of low-velocity impact response of synthetic foam core panels is defined in [9], and high-velocity impact is simulated in [10].

Dynamic interfacial debonding in sandwich panels was studied in [11], where the authors applied a nonlinear dynamic analytical approach in order to investigate the structural behavior of panels and their failure mechanism. As the character of loading significantly influences the structural response, it is necessary to take into account load characteristics at both the experimental and numerical modeling stages. Article [12] demonstrates experimental and numerical results of the research on damage sequence including debonding and delamination of honeycomb sandwich panels subjected to bending. The effect of shear loading on the mechanical response of a Y-frame core sandwich panel was investigated in [13]. According to [13], delamination failure was the dominant failure mode for the considered type of panels.

The low-velocity impact on the sandwich panel with honeycomb core is studied in [14]. The article contains a comparison of the results obtained for various damage modes. The mechanical behavior of foam-filled corrugated core panels in lateral compression is discussed in the study [15]. Experiments identified localized delamination as well as debonding between layers.

Recent researches in the field of innovative materials and technologies offer a vision for the development of products with enhanced characteristics. For panel strengthening and improvement of its structural performance by means of increased stiffness, the panels can be reinforced with special glass fiber reinforced polymer ribs [16]. Another potential solution for obtaining better properties such as resistance to delamination of sandwich panels is the use of 3D fabrics made of glass fiber [17].

High-quality bonding of core and skins is one of the key factors for providing overall stiffness and structural strength [18]. Different methodologies can be applied for modeling the cohesive zone in sandwich panels [19], [20]. Paper [21] proposes a calculation methodology for determining the critical energy release rate for interfacial delamination.

Experimental investigations of the load-bearing capacity taking into account face sheet and foam core interaction within a sandwich panel are presented in [22]. The analysis provided in the research leads to the development of a consistent model, which proposes modifications to the current design and calculation methodologies.

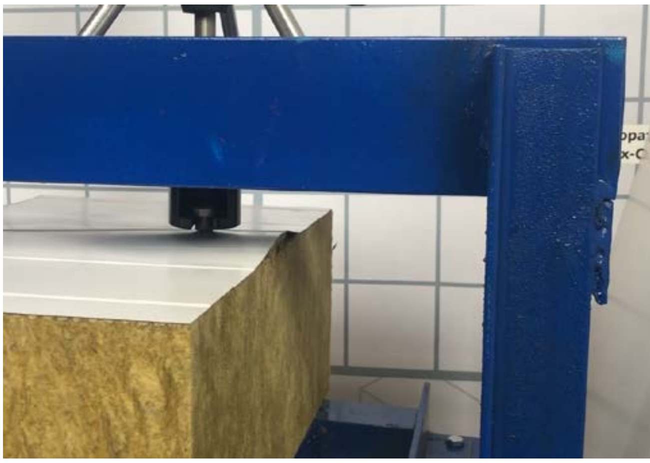

Figure 4. Delamination of the outer sheet of wall sandwich panel.

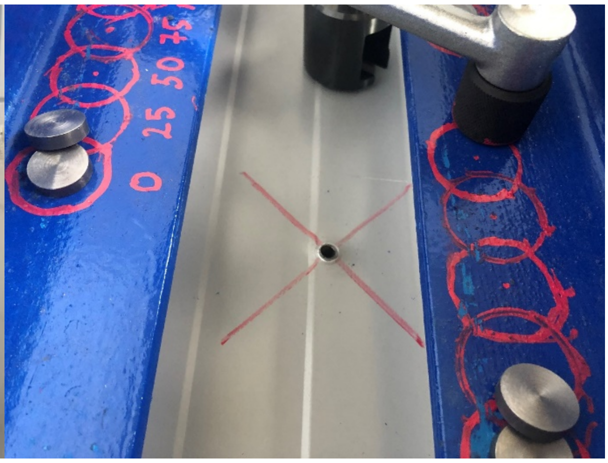

Figure 5. Pulling of a rivet from steel sheet.

The aim of the study was to determine the value of the bearing capacity of the connection between the rivet and an outer sheet of the sandwich panel, the influence of the installation of an end face profile and the cyclic load on this value, and the critical edge distance in order to prevent delamination. The research aimed at the characterization of the principal limiting factors and test approach for the structural solution where fastening was made to an outer metal sheet of a sandwich panel. The study addressed the following tasks:

- Performing an experimental study to determine the minimum allowable distance from the edge of a sandwich panel for installing a blind rivet;
- Determining the bearing capacity of the fastening by a group of blind rivets under the action of pulling force;
- Determining the bearing capacity of the fastening by a group of blind rivets under the combined action of pulling and shear forces;
- Determining the effect of shear forces on joint performance.

2. Methods

The characteristic feature of the study is the usage of the special equipment, which does not directly affect the tested panel sheet (Figure 6). Panel’s fastening to the test bench is performed on the lower side of the panel while pulling force is applied to the rivet installed on the upper metal sheet. The experimental setup shown in Figures 6 and 7 was used for the tests described in sections 2.1 to 2.3. The experimental setup for the tests described in section 2.4 is shown in Figure 21.

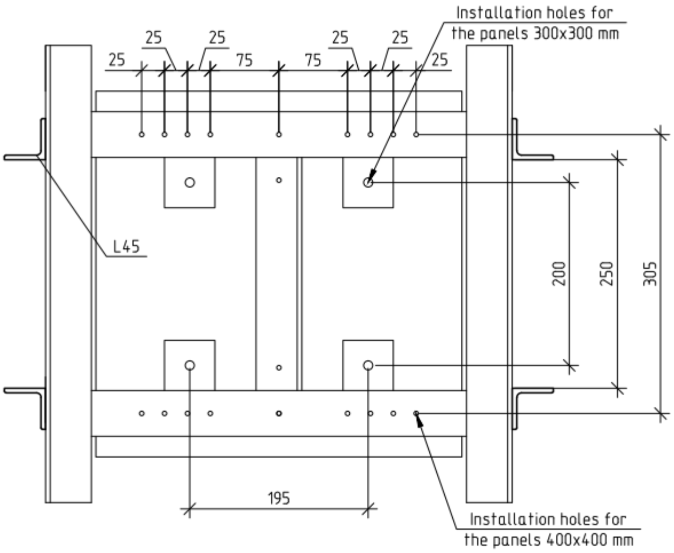

Figure 6. Location of sandwich panel fastening points on the test setup, top view.

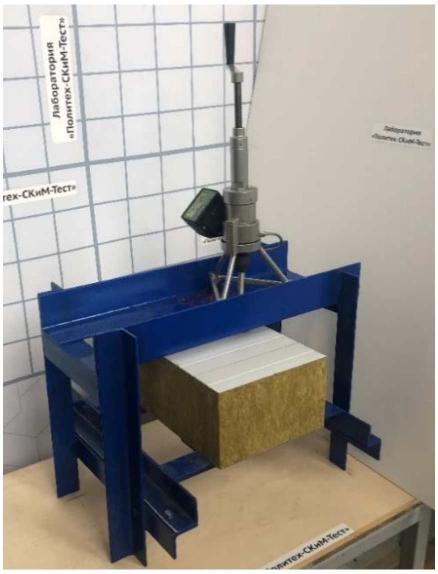

Figure 7. Test setup.

In this study, tests were carried out on a blind rivet of the structure shown in Figures 8 and 9. The designations shown in Figure 8 have the following meaning: D is a rivet body diameter; L is a rivet length; D_k is rivet head diameter; K is a rivet body height; G is a grip range; F is work hole diameter. The designations shown in Figure 9 refer to the parts of the rivet body: 1 is a rivet body end; 2 is a rivet head; 3 is a cylindrical part of the rivet; 4 is an inner space of the rivet body.

In this study, the rivets had the rivet body diameter D of 4.8 mm, the rivet head diameter D_k of 14 mm, and the rivet length L of 21 mm.

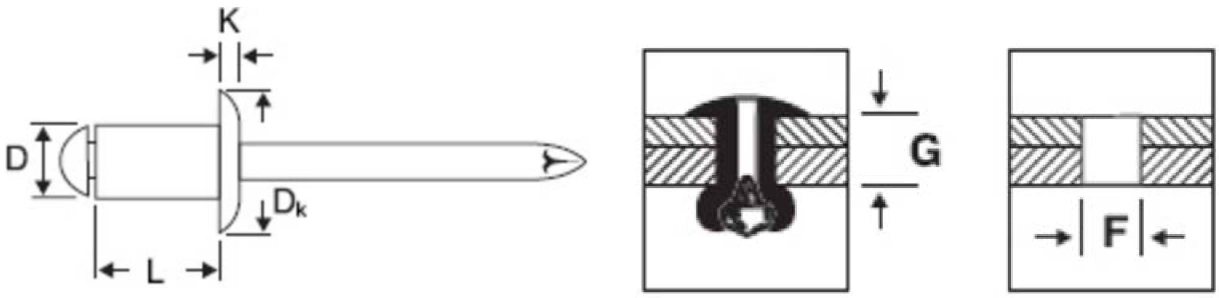

Figure 8. Blind rivet.

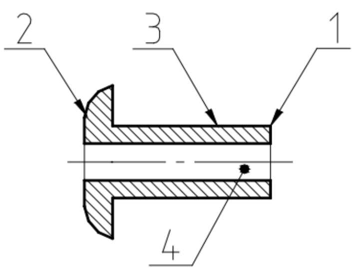

Figure 9. Rivet body.

The rivets were made of steel type 08X18H10 in Russian classification, analogous to AISI 304 (USA), 1.4301 (European Union). The mechanical properties of steel are shown in Table 1.

Table 1. Strength of steel of rivets.

Characteristic value		Design value	
Yield strength f_y, MPa	Ultimate strength f_u, MPa	Yield strength f_y, MPa	Shear strength v_c, MPa
185	510	175	100

The sandwich panels consisted of two metal sheets with a nominal thickness of 0.5 mm bonded to each side of a mineral wool core with a thickness of 150 mm. The material of metal sheets is galvanized steel 08ps in Russian classification with a nominal yield strength of 230 MPa. The nominal weight of the zinc layer declared by the manufacturer was 140 g/m^2.

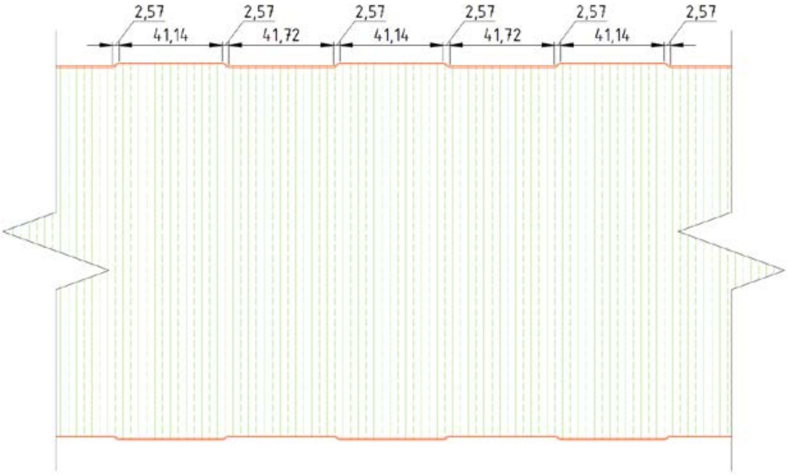

Figure 10. Profile of the sandwich panel.

The mineral wool core had the following nominal characteristics according to the technical manual provided by the manufacturer:

- Average density: 100 kg/m^3;
- Compression strength: 0.06 MPa (at 10% deformation);
- Tensile strength: 0.04 MPa according to EN 826:2013;
- Shear strength: 0.05 MPa according to EN 826:2013.

The values of strength were measured transverse the fibers.

The core was glued to the metal sheets by two-component polyurethane adhesive on the basis of isocyanate and polyol.

In sections 2.1 to 2.3 sandwich panels were attached to the lower level of the test bench with the creation of a fastening, which significantly exceeds the bearing capacity of the considered joint connection. The location of sandwich panel fastening points on the test bench is shown in Figure 6.

A test sleeve (Figure 11) was riveted to the outer sheet of the panel at a predetermined edge distance. The rivet was pulled out by means of an equipped tensile force measurer (PSO-20MG4A AD, Figure 12) using the test sleeve. Tensile force measurer was mounted on the upper level of the test bench (without contact with the surface of the sandwich panel). The speed of pulling out varied from 7 to 13 mm/min. The tensile force measurer had a speed indicator. Pulling out lasted until the loss of the bearing capacity of the joint (between a rivet and a sandwich panel) or directly a sandwich panel. The failure was determined by analysis of the displacement-load graphs, as well as visually and considering the appearance of characteristic sounds.

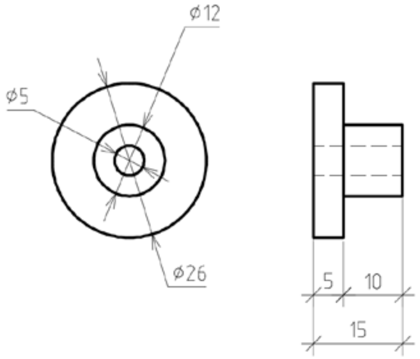

Figure 11. Test sleeve

Figure 12. Tensile force measurer PSO-20MG4A AD

2.1. Test procedure for the panels with various values of the edge distance

Edge distance was defined as the distance from the center of the rivet to the edge of the sandwich panel. Five configurations of sandwich panels with different edge distances were subjected to testing (Table 2).

Table 2. Configurations of sandwich panel samples.

Size of the panel	Edge distance, mm
400×400 mm (Figure 13, left)	200
400×250 mm (Figure 13, right)	50
400×400 mm	75
400×300 mm	100
400×350 mm	150

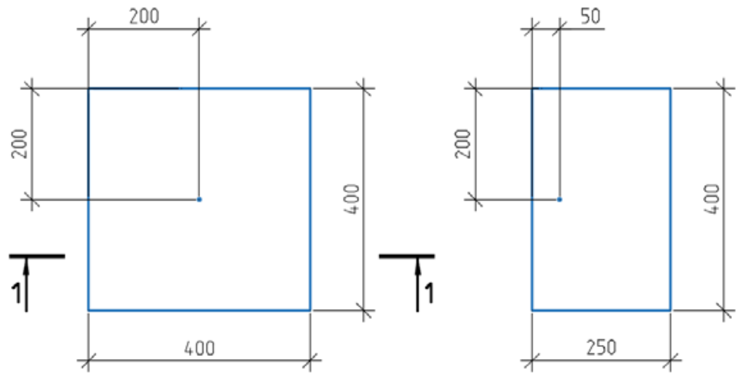

Figure 13. Test samples of sandwich panels

2.2. Test procedure for the panels with installed end face profile

Sandwich panels with dimensions of 400×400 mm and an edge distance of 50 mm in two different variations were subjected to testing (Figures 14 and 15).

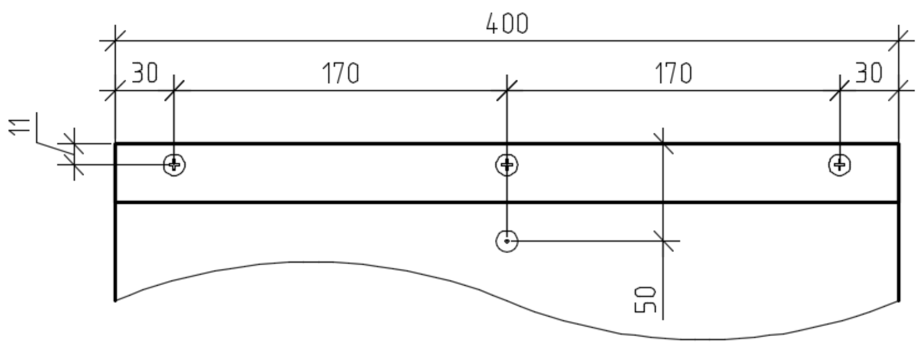

Figure 14. Coaxial scheme of placement of self-tapping screws.

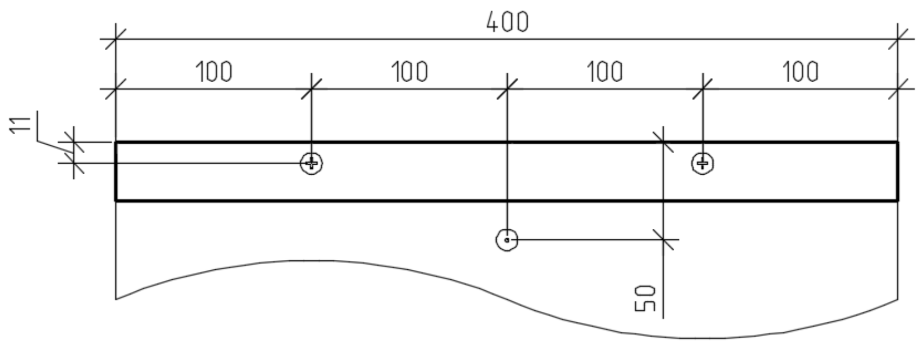

Figure 15. Span scheme of placement of self-tapping screws.

A cold-formed profile made of galvanized steel sheet was attached by self-tapping screws. In this study, the profile shown in Figure 16 had the following dimensions: a = 150 mm, b = 30 mm, t = 0.5 mm.

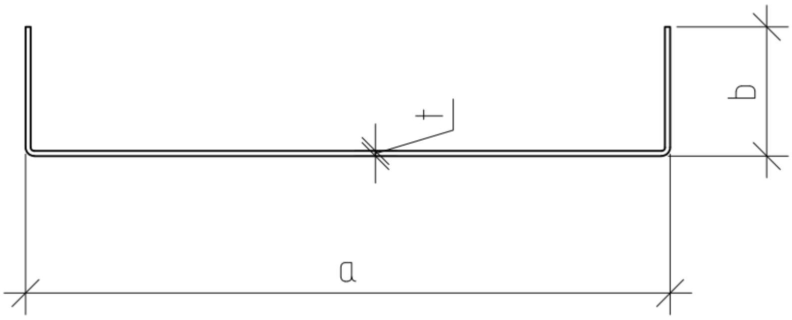

Figure 16. Drawing of the profile.

Steel self-tapping screws had a diameter of 4.2 mm and length of 19 mm in accordance with DIN 968.

Figure 17. Coaxial and span fastening schemes.

Figure 18. Edge distance of 50 mm in the coaxial scheme.

2.3. Test procedure for the panels under cyclic load action

Cyclic loading imitated peak wind load applied to the sandwich panel. The duration of single load application was set to 3 seconds in accordance with ASCE 7-05 regulations. Two types of cycles were considered: non-uniform and uniform (Table 3).

Samples with dimensions of 400×400 mm (20 units) and an edge distance of 200 mm were subjected to testing. On one side of the panel, test sleeves were fixed to the test specimen by blind rivets, and, on the other side, a T-shaped embedded plate with a width of 80 mm was attached by self-tapping screws with the creation of a fastening, significantly exceeding the bearing capacity of the studied joint connection.

Obtained samples were installed in a universal machine for tensile and compression tests (Zwick/Roell Z100). A concentrated, successively alternating load was applied to the test sleeve. The test speed ranged from 7 to 13 mm/min.

During the test, both uniform and non-uniform cycles were applied.

The value of the load was chosen in order to maintain the bearing capacity for at least 365 non-uniform and 485 uniform cycles.

According to the Russian Set of Rules 20.13330.2016 “Loads and actions”, as a result of peak wind exposure, a non-uniform cycle is characteristic for corner zones of buildings while a uniform cycle is characteristic for ordinary zones.

Table 3. Characteristics of uniform and non-uniform cycles

Non-uniform cycle	Uniform cycle
Concentrated pulling force	
P_-	
Concentrated pressing force	
$P_+ = \frac{P_- \cdot 1.2}{2.2} = 0.55 \cdot P_-$	$P_+ = P_-$
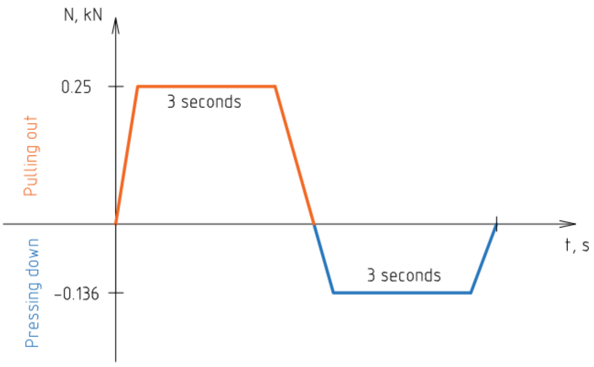	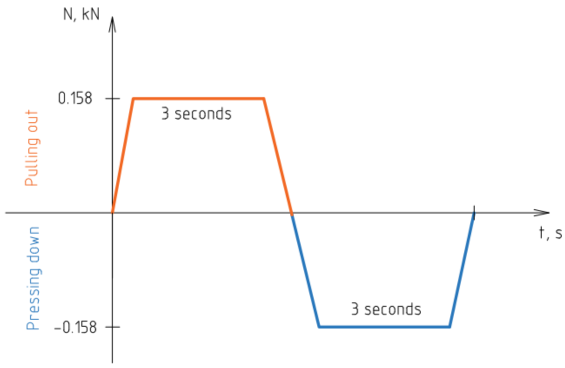
Example of a non-uniform cycle (+0.25 kN / -0.136 kN)	Example of a uniform cycle (+0.158 kN / -0.158 kN)

$$c_{p\ corner} = -2.2; c_{p\ ordinary} = 1.2; \frac{c_{p\ corner}}{c_{p\ ordinary}} = -1.83$$

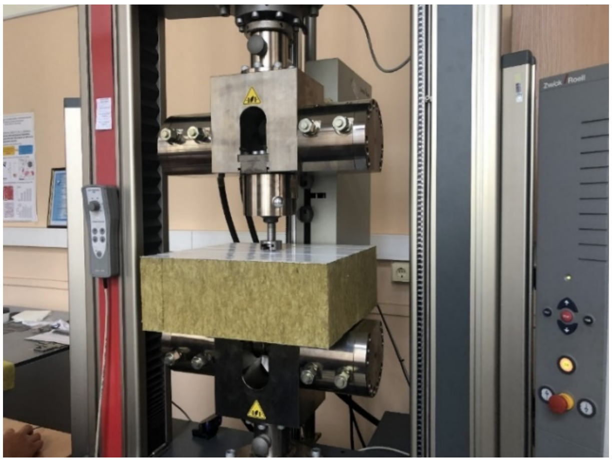

Figure 19. Test sample installed in Zwick/Roell Z100

2.4. Test procedure for a group of rivets subjected to pulling

The tests were performed on a full-sized sample of a sandwich panel under conditions of a complex stress state, which correspond to the actual operation of the system. The sandwich panel was clamped to the bearing base at four points. Steel clamps retained the panel through distribution pads. The profile shown in Figure 20 was riveted to the outer sheet of the sandwich panel in accordance with the schemes shown in Figures 24 to 28.

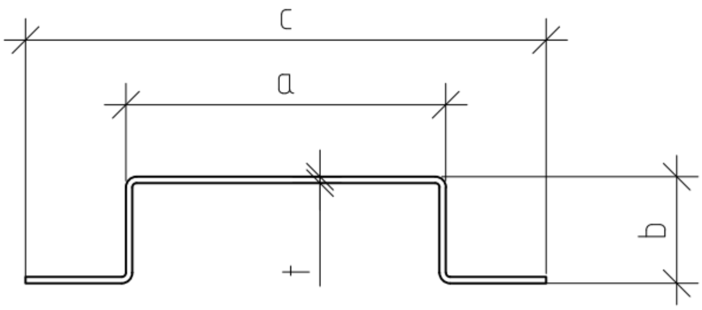

Figure 20. Cross-section of the profile used in the test

Figure 21. Test setup for the study of a cyclic load

The test consisted of two variations:

1. A constant load of 0.3 kN was applied to the sample in the plane of the facade structure while a load applied out of the plane (simulating the wind effect) was sequentially increased by means of contracting jack in order to determine the critical value of the above-indicated force.

2. The test procedure was set similarly to clause 1, but without applying a constant load in the plane of the facade structure.

The magnitude of the load and the type of failure at which the loss of the bearing capacity occurred were recorded.

The test sample was a fragment of a wall sandwich panel with an installation width of 1190 mm and length of 1000 mm. The sandwich panel was fixed to the base at four points by steel clamps with distribution pads.

Test schemes are shown in Figure 22 and Figure 23:

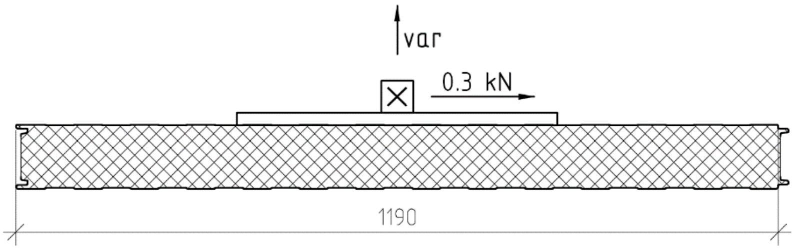

Figure 22. Scheme with the combined action of shear force and pulling force (modification 1).

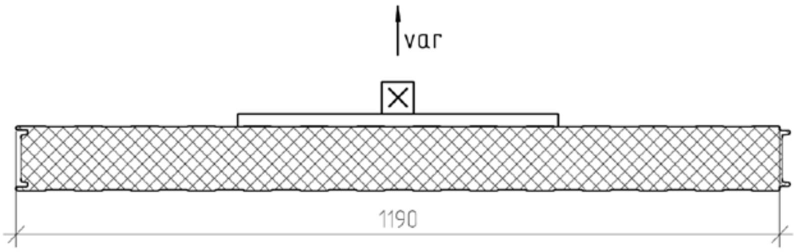

Figure 23. Scheme with the action of pulling force (modification 2).

Several test schemes (Figures 24 – 28) were tested in order to evaluate the influence of fastening parameters on the occurrence of delamination.

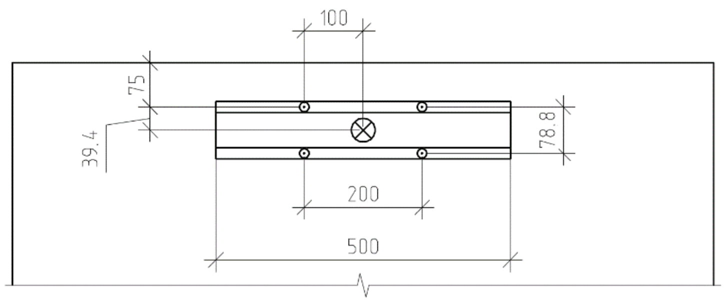

Figure 24. First scheme option.

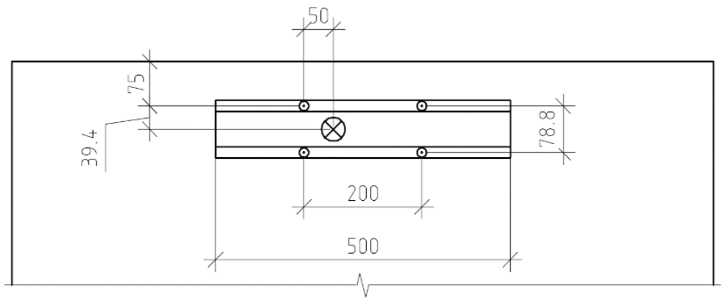

Figure 25. Second scheme option.

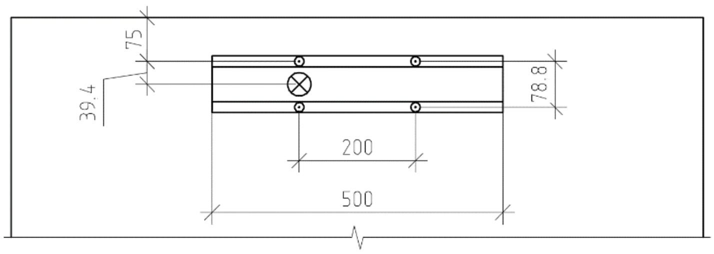

Figure 26. Third scheme option.

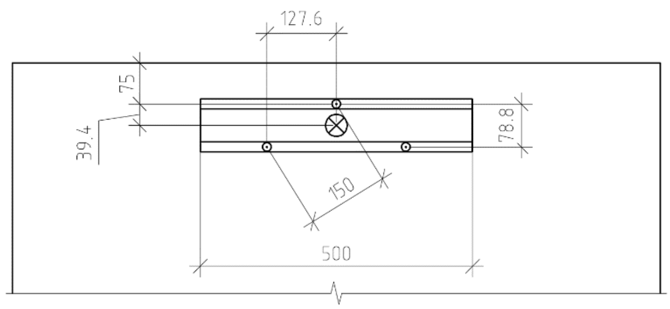

Figure 27. Forth scheme option (coaxial).

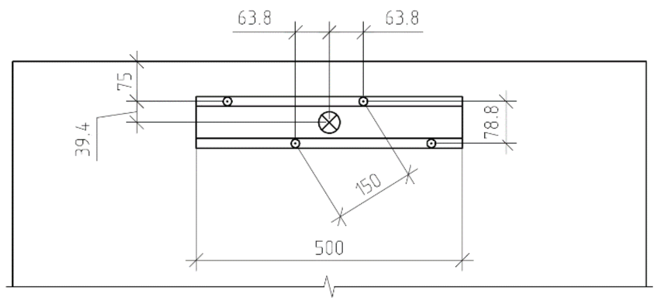

Figure 28. Fifth scheme option (span).

3. Results and Discussion

Depending on the method of load application, characteristics of the bearing capacity of the joint were determined either based on unit values of the destructive load or based on load values corresponding to the end of the elastic deformation zone.

One or two extreme values were excluded from the series of unit results if their absolute value and (or) the nature of failure sharply differed from the series of values.

The average load value, the standard deviation of the unit load values, and the coefficient of variation were calculated using formulas (1), (2), and (3) for the series of unit test results N_i.

Average load value:

$$N_{average} = \frac{\sum_{i=1}^{n} N_i}{n} \tag{1}$$

Standard deviation of the unit load values:

$$S = \sqrt{\frac{\sum_{i=1}^{n} (N_i - N)^2}{n-1}} \tag{2}$$

Coefficient of variation:

$$v = \frac{S}{N} \tag{3}$$

Allowable load (without safety factor):

$$F_n = \frac{N(1-tv)}{\gamma_n} \tag{4}$$

where t is the Student's coefficient of the confidence interval of 0.95. For performed 59 tests (n = 59):

$$t = 2.00099$$

γ_n is coefficient of working conditions, taken equal to 1.1, since the fastenings are installed in the laboratory;

N_i is unit load value in series of test results, kN;

n is the number of results within the series.

If the excluded from series results N_i went beyond the limits equal to $N \pm 3S$, they were finally discarded. If the excluded results N_i did not go beyond the specified limits, then the values of N, $\underline{S}$ and v were recalculated according to the results of the entire series of unit tests.

3.1. Pulling test

The test according to chapter 2.1 was carried out on 15 samples for each considered value of the edge distance.

Table 4. Summarized test results.

Edge distance, mm	Average value of pulling force, kN	Character of a fracture
50	0.570	delamination (87% of the total amount of samples)
75	0.625	pulling (100% of the total amount of samples)
100	0.615	pulling (100% of the total amount of samples)
150	0.613	pulling (100% of the total amount of samples)
200	0.591	pulling (100% of the total amount of samples)

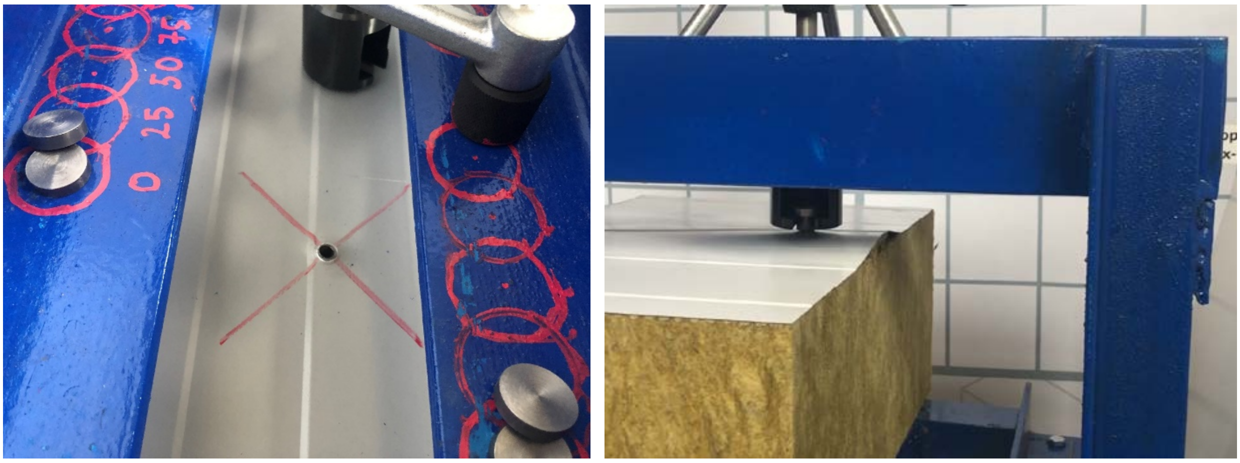

Figure 29. Left – fracture by pulling out of the outer sheet of the sandwich panel; right – fracture by delamination of the outer sheet of the sandwich panel.

Due to the uniform nature of the fracture of the samples (except delaminated panels) and the absence of a relationship between edge distance and the magnitude of the pulling force, obtained values were combined in order to evaluate the bearing capacity of rivet fastening of curtain facade system to wall sandwich panel.

Average load value:

$$N_{average} = \frac{36.13}{59} = 0.612 kN$$

Standard deviation of the unit load values:

$$S = \sqrt{\frac{0.11687}{59-1}} = 0.045 kN$$

Coefficient of variation:

$$v = \frac{0.045}{0.612} = 0.073$$

Bearing capacity (without safety factor) of the connection between a blind rivet with a diameter of 4.8 mm and the outer sheet of a sandwich panel with a thickness of 0.5 mm under a single loading of the sample:

$$F_n = \frac{0.612 \cdot (1 - 2.00099 \cdot 0.073)}{1.1} = 0.475 kN$$

When the distance from the edge of the sandwich panel to the axis of the installed blind rivet (edge distance) was equal to 50 mm, destruction due to delamination occurred in 87% of the samples.

When the edge distance was equal to 75 mm and more from the range of considered values, pull-out failure occurred in 100% of the samples.

3.2. Pulling test for the panels with installed end face profile

Calculation of the average load value, the standard deviation of the unit load values, and the coefficient of variation were carried out similarly to chapter 3.1.

Delamination did not occur in both schemes of installation of the end face profile with an edge distance of 50 mm. The loss of bearing capacity was a result of the pull-out of a rivet.

Table 5. Results of pulling test for the samples with installed end face profile.

Installation scheme	$N_{average}$, kN	S, kN	v	F_n, kN
Coaxial	0.67	0.049	0.073	0.508
Span	0.639	0.072	0.112	0.433

3.3. Cyclic load action

The cyclic tests described in chapter 2.3 led to the results given in Table 6.

Table 6. Results of cyclic loading.

Sample number	Duration, s	Number of cycles	Loading speed, mm/min	Type of cycle	$F_{(-)}$, kN	$F_{(+)}$, kN	Δ, mm	$F_{destructive}$, kN
1	340	4	10	Non-uniform	-0.400	0.218	-	0
2	134	2	10	Non-uniform	-0.450	0.245	-	0.305
3	199	21	10	Non-uniform	-0.450	0.245	-	0.345
4	130	2	10	Non-uniform	-0.450	0.245	-	0.328
5	225	3	10	Non-uniform	-0.400	0.218	-	0.26
6	472	6	10	Non-uniform	-0.400	0.218	-	0.261
7	1747	21	11	Non-uniform	-0.350	0.191	-	0.264
8	4243	52	11	Non-uniform	-0.350	0.191	-	0.276
9	9708	131	11	Non-uniform	-0.300	0.164	-	0.06
10	**23993**	**550**	**11**	**Non-uniform**	**-0.158**	**0.086**	**0.44**	**no destruction**
11	**22293**	**365**	**11**	**Non-uniform**	**-0.250**	**0.136**	**0.92**	**no destruction**
12	9420	125	11	Uniform	-0.250	0.250	-	0.25
13	**28228**	**558**	**11**	**Uniform**	**-0.158**	**0.158**	**0.90**	**no destruction**
14	16090	229	11	Uniform	-0.250	0.250	-	0.25
15	**27179**	**462**	**11**	**Non-uniform**	**-0.250**	**0.136**	**0.73**	**no destruction**
16	**29264**	**542**	**11**	**Uniform**	**-0.158**	**0.158**	**0.55**	**no destruction**
17	**28178**	**485**	**11**	**Uniform**	**-0.158**	**0.158**	**0.85**	**no destruction**
18	**27640**	**520**	**11**	**Uniform**	**-0.158**	**0.158**	**0.83**	**no destruction**
19	**29647**	**550**	**11**	**Uniform**	**-0.158**	**0.158**	**0.77**	**no destruction**
20	**28331**	**581**	**11**	**Uniform**	**-0.158**	**0.158**	**0.72**	**no destruction**

Samples withstood more than 485 uniform cycles without visible fracture under the action of an alternating load equal to:

$$F_{\pm} = \pm 0.158\text{kN}$$

Samples withstood more than 365 non-uniform cycles without visible fracture under the action of an alternating load equal to:

$$F_{+} = 0.136\text{kN}; F_{-} = -0.25\text{kN}$$

Subsequent pulling tests showed a presence of residual load bearing capacity.

Table 7. Results of pulling test for the samples after cyclic loading.

Sample number	$N_{critical}$, kN	$N_{average}$, kN	$(N_{critical} - N_{average})^2$, kN	S, kN	$N-3S$, kN	$N+3S$, kN	v	R_{n95}, kN
13	0.61		0.0023592					
15	0.48		0.0066306					
16	0.58		0.0003449					
17	0.56	0.561	2.041E-06	0.065	0.757	0.366	0.116	0.365
18	0.51		0.0026449					
19	0.52		0.0017163					
20	0.67		0.0117878					

Therefore, for calculation purposes F_+ and F_- can be assumed as values of pulling force in the connection between a blind rivet with a diameter of 4.8 mm and the outer sheet of the sandwich panel with the thickness of 0.5 mm for the angular zone of application of the peak wind load, when aerodynamic coefficients of such zone correspond to the values below:

$$F_+ = 0.136\text{kN}; F_- = -0.25\text{kN}; \frac{F_-}{F_+} = -1.83$$

if at least 10 samples were subjected to an experimental study with a similar test load.

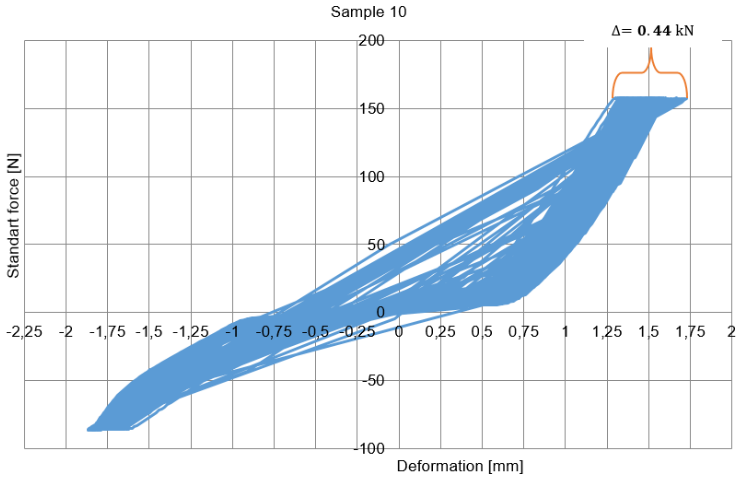

Figure 30. Cyclic load action on sample 10.

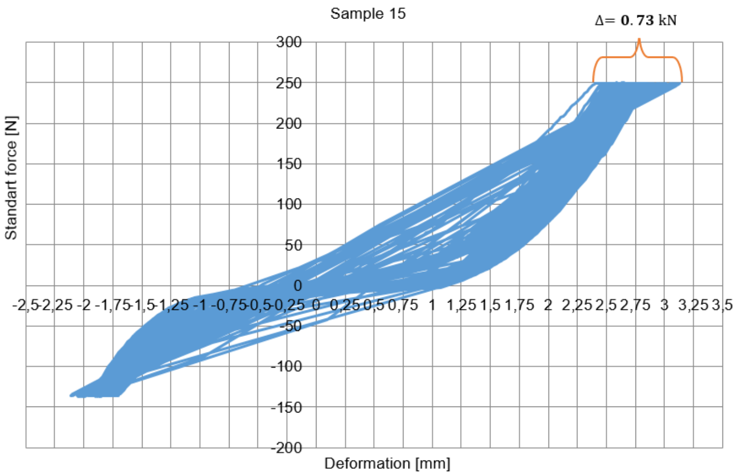

Figure 31. Cyclic load action on sample 15.

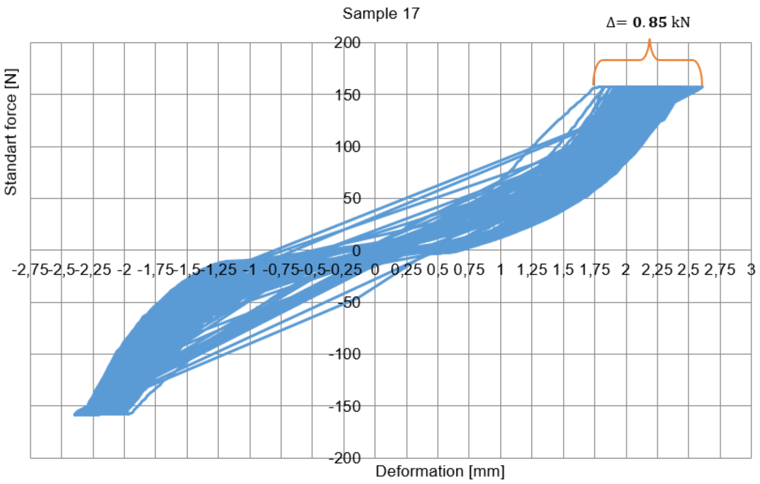

Figure 32. Cyclic load action on sample 17.

The values of bearing capacity of the connection obtained under cyclic loading, which imitates peak wind loads, are significantly lower than the values for a single pulling load. Therefore, existing practical methods of determination of the bearing capacity based solely on single loading should be improved and extended.

3.4. Pulling test for a group of rivets

Tests were performed in order to determine the bearing capacity of the fastening of the subframe to the sheathing of the sandwich panel by means of a group of blind rivets (chapter 2.4).

Test schemes were verified with the aim of preventing sandwich panel delamination.

- Schemes of the tests which ended by delamination of the samples:

First scheme option (Figure 24)

Maximum loads under the combined action of shear force and pulling force:

$$P_{hor} = const = 0.3\text{kN}; F_{\max} = 2.1\text{kN}$$

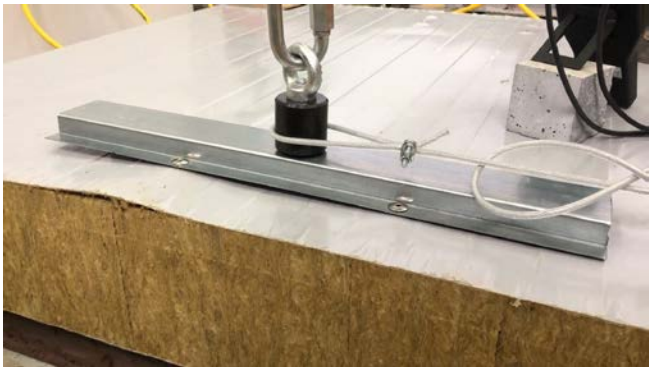

Figure 33. Delamination at $F_{\max} = 2.1\text{kN}$.

Maximum loads action of pulling force (without shear force):

$$P_{hor} = const = 0; F_{\max} = 1.7\text{kN}$$

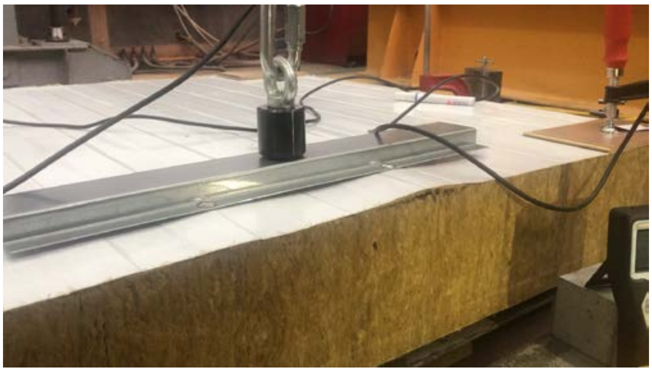

Figure 34. Delamination at $F_{\max} = 1.7\text{kN}$.

Second scheme option (Figure 25)

Maximum loads under the combined action of shear force and pulling force:

$$P_{hor} = const = 0.3\text{kN}; F_{\max} = 1.6\text{kN}$$

Third scheme option (Figure 26)

Maximum loads under the combined action of shear force and pulling force:

$$P_{hor} = const = 0.3\text{kN}; F_{\max} = 1.1\text{kN}$$

- Schemes of the tests which ended by pulling of the blind rivets:

Forth scheme option (coaxial) (Figure 27)

$$F_{\max} = 1.3\text{kN}$$

Fifth scheme option (span) (Figure 28)

$$F_{\max} = 1.9\text{kN}$$

Existing researches [3]–[5], [8], [11]–[13], [15] present studies on the phenomena of delamination and associated issues for sandwich panels with the type of a core other than mineral wool. Therefore, final results could not be comprehensively compared, however, the main approaches, methods, and general principles of calculation in accordance with Limit State design remain analogous.

4. Conclusions

The study was devoted to the investigation of the fastening to an outer steel sheet of a sandwich panel with mineral wool insulation core. The proposed test bench for the experimental investigation of the considered structural solution was described. For the studied type of panel following conclusions regarding the connection between the rivet and the outer sheet of the sandwich panel were made:

1. Edge distance equal to 75 mm or more does not affect the bearing capacity of the joint in considered structural solution.

2. Cyclic load action, which imitated peak wind loads on the panel, significantly reduced the bearing capacity of the connection in comparison with single pulling loading. It is recommended to assume the value of the bearing capacity of the connection based on the calculation made for the cyclic exposure corresponding to peak wind loads.

3. In systems where the fastening is made to an outer metal sheet when an end face profile is installed, the fastening element can be attached to the outer sheet of the sandwich panel with an edge distance of 50 mm if the step of placement of self-tapping fastening screws does not exceed 200 mm. Since the location of self-tapping screws from the position of the fastening elements affects the bearing capacity of the connection, it is recommended to install self-tapping screws at a distance of at least 75 mm from the connection.

4. Rivets used for fastening the subframe of the curtain wall system should be placed taking into account the position of the fastening element of cladding, from which concentrated load will be transferred to the system.

5. Recommended scheme of the attachment of the curtain wall subframe to the outer sheet of sandwich panels with a thickness of 0.5 mm is showed below:

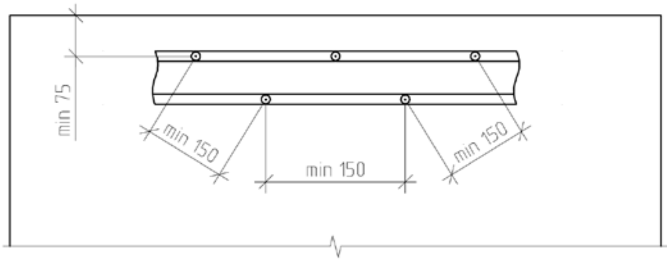

Figure 35. Recommended scheme of the attachment of the curtain wall subframe

References

1. Shazly, M., Bahei-El-Din, Y., Salem, S. Characterization of sandwich panels for indentation and impact. Journal of Physics: Conference Series. 2013. 451(1). DOI:10.1088/1742-6596/451/1/012001.
2. Paulson, S., Kedir, N., Sun, T., Fezzaa, K., Chen, W. Observation of Dynamic Adhesive Behavior Using High-Speed Phase Contrast Imaging. Proceedings of the Annual Conference on Experimental and Applied Mechanics. Reno, 2019. No. 1. Pp. 197–199. DOI: 10.1007/978-3-030-30021-0_34.
3. Cai, S., Liu, J., Zhang, P., Li, C., Cheng, Y. Dynamic response of sandwich panels with multi-layered aluminum foam/UHMWPE laminate cores under air blast loading. International Journal of Impact Engineering. 2020. No. 138. DOI: 10.1016/j.ijimpeng.2019.103475.
4. Studzinski, R., Pozorski, Z., Garstecki, A. Failure maps of sandwich panels with soft core. Proceedings of the 10th International Conference Modern Building Materials, Structures and Techniques. Vilnius, 2010. Pp. 1060–1065.
5. Mamalis, A.G., Spentzas, K.N., Manolakos, D.E., Ioannidis, M.B., Papapostolou, D.P. Experimental investigation of the collapse modes and the main crushing characteristics of composite sandwich panels subjected to flexural loading. International Journal of Crashworthiness. 2008. 13(4). Pp. 349–362. DOI: 10.1080/13588260801933691.
6. Mostafa, A., Shankar, K. In-plane shear damage prediction of composite sandwich panel with foam core. Applied Mechanics and Materials. 2013. No. 376. Pp. 69–73. DOI:10.4028/www.scientific.net/AMM.376.69.

7. Ma, J., Yan, Y. Multi-scale simulation of stitched foam-core sandwich composites subjected to low-velocity impact. Acta Metallurgica Sinica. 2013. 30(1). Pp. 230–235.
8. Rabeih, E.-A.M., Elghandour, E.I. Delamination detection inside composite structures plates under free vibration. Proceedings of the International SAMPE Technical Conference. Long Beach, California, 2013. Pp. 956–972.
9. Wang, J., Li, J., Gangarao, H., Liang, R., Chen, J. Low-velocity impact responses and CAI properties of synthetic foam sandwiches. Composite Structures. 2019. No. 220. Pp. 412–422. DOI:10.1016/j.compstruct.2019.04.045.
10. Ahmadi, H., Liaghat, G. Analytical and experimental investigation of high velocity impact on foam core sandwich panel. Polymer Composites. 2019. 40(6). Pp. 2258–2272. DOI:10.1002/pc.25034.
11. Odessa, I., Frostig, Y., Rabinovitch, O. Dynamic interfacial debonding in sandwich panels. Composites Part B: Engineering. 2020. No. 185. DOI:10.1016/j.compositesb.2019.107733.
12. Medina, S.A., Meza, J.M., Kawashita, L.F. Damage sequence of honeycomb sandwich panels under bending loading: Experimental and numerical investigation. Journal of Reinforced Plastics and Composites. 2020. 39(5–6). Pp. 175–192. DOI: 10.1177/0731684419880970.
13. Liu, J., Zhang, T., Jiang, W., Liu, J. Mechanical response of a novel composite Y-frame core sandwich panel under shear loading. Composite Structures. 2019. No. 224. DOI:10.1016/j.compstruct.2019.111064.
14. Aryal, B., Morozov, E. V, Wang, H., Shankar, K., Hazell, P.J., Escobedo-Diaz, J.P. Effects of impact energy, velocity, and impactor mass on the damage induced in composite laminates and sandwich panels. Composite Structures. 2019. No. 226. DOI:10.1016/j.compstruct.2019.111284.
15. Rejab, M.R.M., Bachtiar, D., Siregar, J.P., Paruka, P., Fadzullah, S.H.S.M., Zhang, B., Cantwell, W.J. The mechanical behavior of foam-filled corrugated core sandwich panels in lateral compression. Proceedings of the American Society for Composites 31st Technical Conference. Williamsburg, Virginia 2016.
16. Correia, J.R., Garrido, M., Gonilha, J.A., Branco, F.A., Reis, L.G. GFRP sandwich panels with PU foam and PP honeycomb cores for civil engineering structural applications: Effects of introducing strengthening ribs. International Journal of Structural Integrity. 2012. 3(2). Pp. 127–147. DOI:10.1108/17579861211235165.
17. Judawisastra, H., Ivens, J., Verpoest, I. The fatigue behaviour and damage development of 3D woven sandwich composites. Composite Structures. 1998. 43(1). Pp. 35–45. DOI: 10.1016/S0263-8223(98)00093-2.
18. Anoshkin, A.N., Zuiko, V.Y., Alikin, M.A., Tchugaynova, A. V. Influence of delamination on the mechanical properties of composite sandwich-panels. Proceeding of the 17th European Conference on Composite Materials. Munich, 2016.
19. Höwer, D., Jois, K.C., Lerch, B.A., Bednarcyk, B.A., Pineda, E.J., Reese, S., Simon, J.-W. Relevance of 3D simulations and sandwich core topology for the modeling of honeycomb core sandwich panels undergoing interfacial crack propagation. Composite Structures. 2018. No. 202. Pp. 660–674. DOI:10.1016/j.compstruct.2018.03.067.
20. Höwer, D., Jois, K.C., Bednarcyk, B.A., Pineda, E.J., Reese, S., Simon, J.-W. A novel mixed-mode cohesive zone model for delamination with severe fiber bridging applied to sandwich panels and monolithic laminates. Proceeding of the 18th European Conference on Composite Materials. Athens, 2018.
21. Ma, M., Yao, W., Chen, Y. Critical energy release rate for facesheet/core delamination of sandwich panels. Engineering Fracture Mechanics. 2018. No. 204. Pp. 361–368. DOI:10.1016/j.engfracmech.2018.10.029.
22. Ungermann, D., Lübke, S., Urbanek, D. Combined load bearing behaviour of face sheet and foam core of sandwich panels subjected to localised loads. Bauingenieur. 2013. No. 88. Pp. 261–268.

Information about authors

Alexander Galyamichev
ORCID: https://orcid.org/0000-0003-4992-2084
E-mail: gav@spbstu.ru

Ekaterina Gerasimova
ORCID: https://orcid.org/0000-0002-6056-5498
E-mail: katyageras17@gmail.com

Denis Egorov
ORCID: https://orcid.org/0000-0001-9282-3255
E-mail: egorov.dv@edu.spbstu.ru

Dmitrijs Serdjuks
Doctor of Technical Science
ORCID: https://orcid.org/0000-0002-1843-3061
E-mail: Dmitrijs.Serdjuks@rtu.lv

Anna Grossman
ORCID: https://orcid.org/0000-0003-4851-4687
E-mail: grosswoman96@gmail.com

Dmitry Lysenko
ORCID: https://orcid.org/0000-0001-5535-4701
E-mail: dmitry_0798@mail.ru

Received 08.10.2020. Approved after reviewing 19.12.2021. Accepted 19.01.2022.

Magazine of Civil Engineering. 2022. 112(4). Article No. 11203

Magazine of Civil Engineering

ISSN 2712-8172

journal homepage: http://engstroy.spbstu.ru/

Research article

UDC 691.322

DOI: 10.34910/MCE.112.3

Fine-grained cement-ash concrete for 3D-printing

L.I. Dvorkin ✉**, *V.V. Marchuk*, *V.V. Zhitkovsky***

National University of Water and Environmental Engineering, Rivne city, Ukraine

✉ *dvorkin.leonid@gmail.com*

Keywords: 3D-printing, building mixtures, polynomial models, optimization cement-ash concrete compositions

Abstract. An analysis of the main types of basic building mixtures for 3D printing and the requirements for their basic properties is presented. Using the mathematical planning of experiments, a complex of polynomial models of the properties of cement-ash fine-grained concrete mixtures for 3D printing was obtained. These properties included their "open time" extrusion suitability, the structural strength required for layering the mixture after a certain time after mixing, tensile strength during splitting characterizing the adhesion of layers and the compressive strength of extruded concrete. As mineral admixtures, the concrete included fly ash and the hardening accelerator: building gypsum. A laboratory printer was designed and used for the research. On the basis of the obtained models, an analysis of the factors of the composition of cement-ash concrete mixtures for the investigated properties is carried out. The article shows a solution to the optimization problem according to the criterion of the minimum cost of the composition of a fine-grained concrete mixture for 3D printing using computer software.

Citation: Dvorkin, L.I., Marchuk, V.V., Zhitkovsky, V.V. Fine-grained cement-ash concrete for 3D-printing. Magazine of Civil Engineering. 2022. 113(5). Article No. 11312. DOI: 10.34910/MCE.113.12

1. Introduction

A promising technology in construction production is 3D printing, which allows three-dimensional objects to be created by sequential application of layers of building mixture. 3D-printing allows to minimize the duration of the technological process of erection of structures, the cost of materials and labor, to ensure the creation of various volumetric shapes [1–12].

One of the difficult tasks arising in the implementation of 3D printing is the development of concretes and mortars that take into account the peculiarities of the 3D printer used, the technological requirements for the building mixture and the necessary physical and mechanical properties of the material at various stages of its hardening.

The most common materials used in 3D printing in the construction of buildings and structures are fine-grained fast-hardening mixtures that include various admixtures to improve certain characteristics, various types of fibers can also be introduced [3, 5, 9–18]. There is experience of using several types of concrete mixes [14]. The first one includes mixtures with water-binder ratio (W/B) 0.4–0.5 and superplasticizers to adjust the consistency. Their compressive strength after 28 days reaches 50–60 MPa. The second type of mixtures with W/B ≈ 0.23–0.3 contains silica fume, the required consistency is achieved by adding a superplasticizer. The compressive strength of these concretes reaches 125 MPa at 28 days of age. The use of such mixtures is restrained by the scarcity and high cost of silica fume.

An urgent problem in the design of concrete mixtures is to provide a set of necessary material properties when using available technogenic raw materials.

Table 1. The main indicators of the physical and mechanical properties of building mixtures and concretes based on them for 3D printers

№	Properties	Functional purpose	Index
1	Properties of mixtures		
1.1	Water holding capacity,%	Ensuring the homogeneity of the concrete mix during production, transportation through pipes and extrusion	No less 97
1.2	Delamination,%		No more 10
1.3	Viscosity, Pa·s	Providing the possibility of transportation through pipes and stable dosing of the mixture	10^9–10^{12}
1.4	Structural strength, Pa	Ensuring the necessary strength of the mixture, sufficient for laying the next layer	No less 800
1.5	Initial setting time, min	Providing the possibility of laying the layer	No less 20 after kneading
1.6	Mixture fluidity, by immersion of the cone, cm	Ensuring the mix's extrusion ability and stable geometry	8…12
	by Suttard viscometer, mm		150…170
2	Concretes properties		
2.1	Compressive strength, MPa	Ensuring the strength properties of structures	No less 20
2.2	Average density, kg/m^3	Providing thermal insulation and other physical and mechanical properties	600–2000
2.3	Adhesion, MPa	Provides adhesion between layers of the mixture for strength and uniformity of construction	No less 2
2.4	Thermal conductivity, W/(m·K)	Thermal insulation of building elements	No more 0.7
2.5	Frost resistance, cycles	Ensuring the durability of structures and resistance to alternating temperature changes	No less 100

Analysis of the results of the performed studies allows to establish the recommended [2] range of technical requirements for building mixtures for 3D printing (Table 1).

The properties of concrete mixture and concrete that determine the possibility of 3D printing include the necessary workability, structural strength after a certain time of hardening of the extruded layer, tensile strength at splitting, which characterizes adhesive strength of layers, as well as compressive strength.

Currently no standardized methods for determining the required properties of concrete mixtures for 3D printing. A number of studies have proposed requirements for the individual properties of the mixtures used [14, 18–24].

Workability (formability) is the rheological parameter of the consistency of the mixture over time. To determine the manufacturability of the extruded mixtures, can use some standard techniques, for example, Le [19] used the British test BS1337-9: 1990 and Kazemian [20] American standard ASTM C1437-15. For this purpose the Hagerman mini-cone is used [14].

Open time, or "window of opportunity for printing" is the period during which the mixture can be extruded. The mixture must also have certain adhesive properties for layering. In [19, 21], the open time was determined by measuring the shear stress in accordance with British standard BS1377-9: 1990 and German DIN 398. In another work [22] it was proposed to test open time using the V-funnel method, Vic's apparatus, shaking table and mini-cone immersion test.

The ability to build up, that is, to lay it in layers during the formation of mixtures, is determined by its structural strength after a certain period of time. To determine the ability of the mixture to build up, a method was proposed for determining the deformation when a load is applied to the sample [14]. This parameter correlates with the workability and extrudability of the mixture.

To ensure the necessary properties of mixtures for 3D-printing it is necessary to develop a methodology for the design of their compositions.

The purpose of the research was to develop a method for designing compositions of fine-grained concrete mixtures containing the mineral admixtures, providing a set of necessary properties for 3D printing.

2. Methods

In our studies, cement CEM I 42.5R of Cement Plant Dyckerhoff Ukraine, fly ash from Burshtynskaya thermal power plant, which belongs to type II ash of category B with a residue on a sieve with a mesh size of 45 µm no more than 25 % (class 2) (EN 450-1:2012) and quartz sand with a modulus fineness of

M_{fn} = 2.1 meeting the requirements of Russian standard GOST 8736-2014 were used. A polycarboxylate type superplasticizer was used (0.3 % by weight of the binder). As an accelerator for setting and hardening of the mixture, we used gypsum G-5 A II GOST 125-2018.

For determining the properties of cement-ash concrete mixtures was developed and used a laboratory 3D printer (Fig. 1).

The required water amount of was selected to obtain mixtures suitable for extrusion molding; the required workability of the mixture by immersion of a standard cone was within – 10 cm. The structural strength of the concrete mixture was determined using a device (Fig. 2), allowing allows measuring the specific loads in Pa (Fig. 3), which the mixture withstands after a certain period of time required to form one layer.

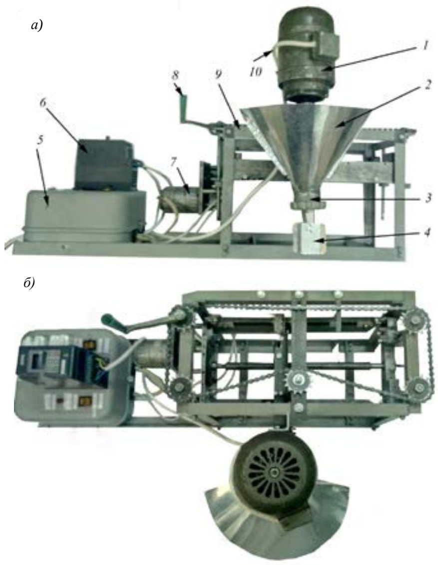

Figure 1. Laboratory printer a) front view, b) top view
1 – electric motor of the extruder; 2 – hopper of building mixture; 3 – auger; 4 – mouthpiece; 5 – control panel; 6 – frequency converter of electricity; 7 – reverse motor moving the extruder in the horizontal direction; 8 – manual drive moving the extruder in the vertical direction; 9 – frame; 10 – power cable of electric motors.

Figure 2. Device for determining the structural strength of an extruded layer of concrete mix.

a) 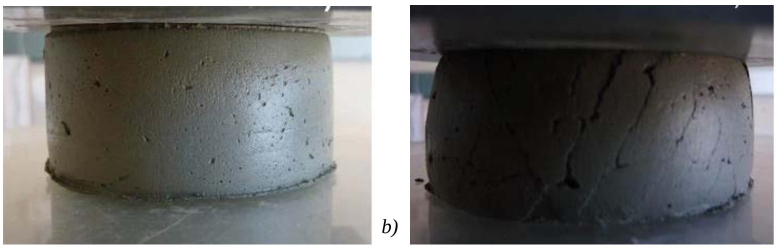

Figure 3. An example of determining the structural strength of extruded concrete, a) the sample withstands the load (structural strength is provided), b) the sample is destroyed.

3. Results and Discussion

To study the effect of the composition of building mixtures on the their main properties, algorithmic experiments were performed in accordance with the three-level three-factor plan B_3 [25]. The conditions for planning experiments are given in Table 2.

Table 2. Conditions for planning experiments

Factors: Natural	Coded	Levels of variation: –1	0	+ 1	Interval
Content of cement-ash binder, kg/m^3, (B)	x_1	400	600	800	200
Content of fly ash in the binder mixture (A),% by weight	x_2	40	30	20	10
Gypsum content (G),% by binder weight	x_3	0	5	10	5

As a result of statistical processing of experimental data, adequate polynomial models of the investigated properties were obtained with a 95 % confidence level.

General view of the models:

$$y = b_0 + \sum_{i=1}^{k} b_i x_i + \sum_{i=1}^{k} b_{ij} x_i x_j + \sum_{i=1}^{k} b_{ii} x_i^2 \tag{1}$$

where b_i, b_{ii}, b_{ij} is statistical estimates of the regression coefficients; x_i, x_j is factors taken into account; n is the number of factors.

The coefficients of the obtained mathematical models are given in Table 3.

Table 3. Cement-ash concrete properties polynomial mathematical models coefficients

Coeffi-cients	Initial setting time, min	Structural strength after mixing and hardening, Pa			Tensile splitting strength, MPa			Compressive strength, MPa		
		10 min	25 min	40 min	1 day	7 days	28 days	1 day	7 days	28 days
b_0	71.5	3083	4703	7845	3.2	7.6	11.4	20.8	41.7	56
b_1	–10.0	288	342	548	1.16	1.6	2.4	10.2	11.8	14.9
b_2	–6.0	553	888	1333	0.34	0.4	0.78	4.12	4.66	4.25
b_3	–20.0	831	885	1452	0.8	0.7	0.7	6.47	3.10	4.1
b_{11}	0.2	126	184	296	0.07	–0.5	–0.4	2.44	–1.69	–1.2
b_{22}	5.2	176	261	423	–0.01	0.1	–0.03	–0.36	-0.5	0.31
b_{33}	–10.2	149	163	260	–0.03	–0.4	–0.3	2.09	–0.25	1.41
b_{12}	–2.5	133	188	131	0.14	0.2	0.43	1.08	2.59	2.20
b_{13}	–2.5	230	117	167	–0.06	–0.6	–0.37	1.00	–2.10	–0.9
b_{23}	2.3	192	235	208	0.04	–0.1	–0.04	–0.78	–1.53	0.15

Based on the data on water demand in l/m^3 of a mixture with the required workability and tested in accordance with the accepted planning conditions, a model was obtained:

$$\begin{aligned} W &= 197 + 28.4x_1 + 3.3x_2 + 5.2x_3 + 13.9x_1^2 + \\ &+ 2.4x_2^2 - 5.1x_3^2 + 0.9x_1x_2 + 2.9x_1x_3 + 0.9x_2x_3. \end{aligned} \tag{2}$$

Analysis of the obtained coefficients of mathematical models (Table 3) and graphical dependencies (Fig. 4–9) allows to obtain important technological conclusions.

The determining factor for the beginning of setting and the structural strength of the studied mixtures is the content of gypsum and fly-ash in the binder mass (Fig. 4, 5). For the splitting tensile strength of concrete, the content of the binder and part of the ash in its have a decisive influence (Fig. 6, 7). In a joint analysis of the models of compressive strength and water demand of a concrete mixture, as expected, the most influencing factors are the binder content and part of the ash in it. For the early strength of concrete, the content of gypsum is essential (Fig. 8, 9).

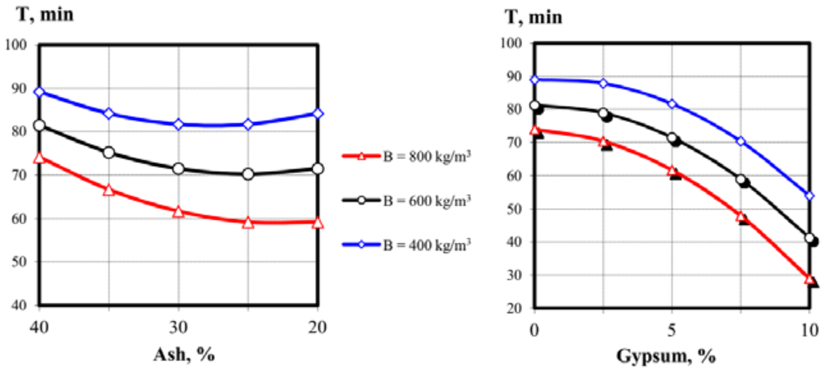

Figure 4. Graphical dependences of the mixtures initial setting for a 3D printer.

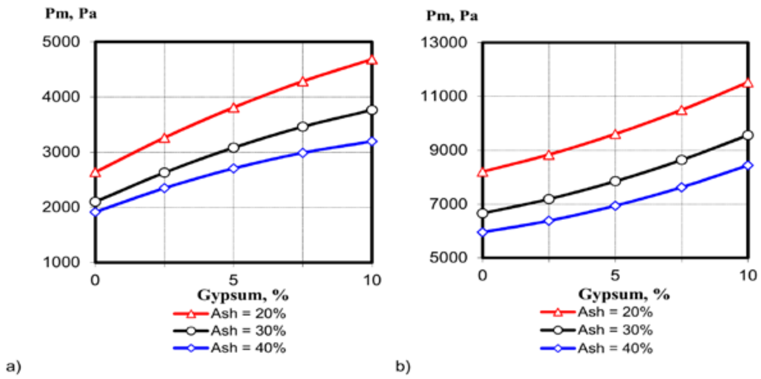

Figure 5. Graphical dependences of structural strength after 10 (a) and 40 (b) minutes of hardening of mixtures.

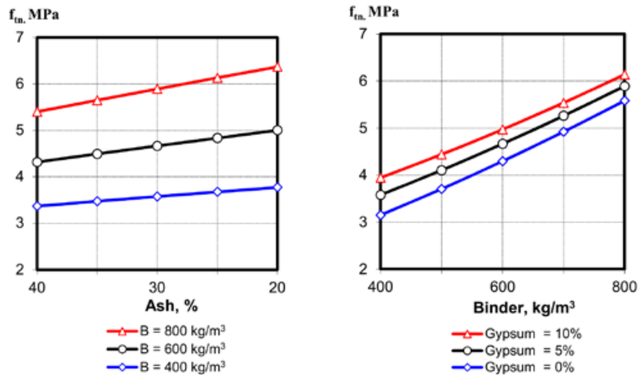

Figure 6. Graphical dependences of tensile strength at splitting at the age of 1 day.

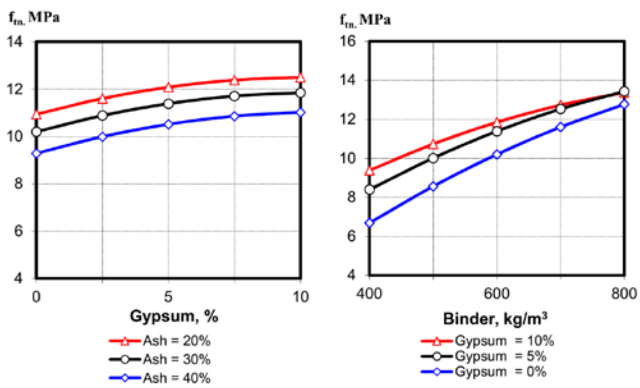

Figure 7. Graphic dependences of tensile strength at splitting at the age of 28 days.

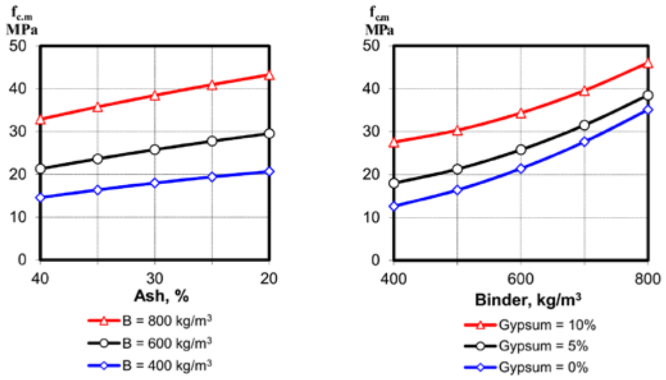

Figure 8. Graphical dependences of the compressive strength of mixtures at the age of 1 day.

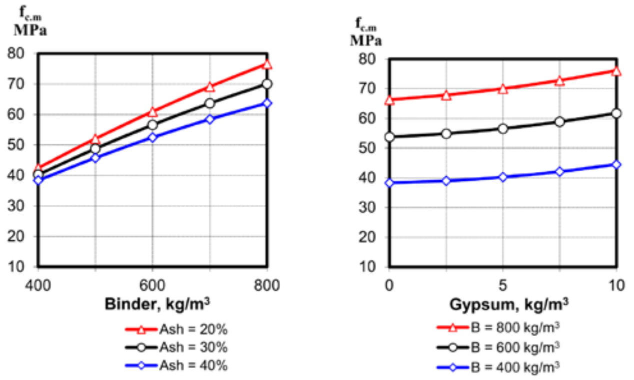

Figure 9. Graphical dependences of the compressive strength of mixtures at the age of 28 days.

The design of cement-ash concrete compositions for 3D concreting can be performed using the minimum cement consumption or minimum cost as the criteria for optimality [26].

At high cost of the admixtures, the optimal compositions of concrete mixtures by these two criteria may not coincide. In general, for a cement-ash grained concrete mixture, while minimizing its cost, the condition must be met:

$$C_c = C_{Cem} \cdot Cem + C_A \cdot A + C_G \cdot G + C_{Add} \cdot Add + C_S \cdot S \to \min \tag{3}$$

given that

$$\begin{gathered} P_1 \geq f\left(x_1, x_2, \ldots, x_n\right) \\ P_2 \geq f\left(x_1, x_2, \ldots, x_n\right) \\ P_n \geq f\left(x_1, x_2, \ldots, x_n\right) \\ x_1 \ldots x_n \in \left[a \ldots b\right], \end{gathered} \tag{4}$$

where C_c, C_{Cem}, C_A, C_G, C_{Add}, C_S is respectively the cost of concrete mixture, cement, fly ash, gypsum, admixtures and sand, for example in RUB/kg; Cem, A, G, Add, S is consumption of cement, fly-ash, gypsum, admixtures and sand, kg/m³; $P_1 \ldots P_m$ is set quality indicators of the mixture and concrete based on it; $x_1 \ldots x_n$ are the factors of the mixture composition taken into account in the models; a, b is restrictions on possible values of factors.

The conversion of the values of the parameters of the composition of the mixture, normalized in this study (Table 2) into a coded form for calculations by models was carried out according to the following dependencies:

$$x_1 = \frac{B - 600}{200}; \ x_1 = \frac{A - 30}{10}; \ x_1 = \frac{G - 5}{5}. \tag{5}$$

The consumption values of fine aggregate (sand) are found by the formula:

$$S=\left(1000-\left(\frac{Cem}{\rho_{Cem}}+\frac{A}{\rho_A}+\frac{G}{\rho_G}+\frac{W}{\rho_W}\right)\right)\cdot\rho_S. \qquad (6)$$

where ρ_{Cem}, ρ_A, ρ_G, ρ_W and ρ_S are, respectively, the densities of cement, fly ash, gypsum, water and sand.

For materials used in the study ρ_{Cem} = 3.1 g/cm^3, ρ_A = 2.9 g/cm^3, ρ_G = 2.4 g/cm^3, ρ_W = 1.0 g/cm^3, ρ_S = 2.65 g/cm^3.

The most rational way to solve this problem is to use the Microsoft Excel software, in particular, its "Search for a solution" application. At the given values of the indicators of the properties and costs of its components under certain restrictions on the values of the factors (in coded values from –1 to +1), the computer program enumerates the possible combinations of factors and parallel, determines, in order to achieve the minimum cost of the mixture, the water consumption necessary to ensure the required fluidity of the mixture according to the corresponding regression equation.

Example

Determine the composition of the cement-ash fine-grained concrete mixture for a 3D printer with compressive strength at the age of 1 and 28 days 15 MPa and 40 MPa, respectively, the tensile strength at splitting at the age of 28 days is 8 MPa, the initial setting time 55 min and structural strength after 10 min hardening 3300 Pa.

The characteristics of the used materials are given above.

We accept the cost of the main components of the mixture for a 3D printer as follows, RUB/kg: C_{Cem} = 5.2; C_A =1.5; C_G = 4.5; C_{Add} = 700; C_S = 1.

1. Using the experimental statistical models (Table 3) and substituting the values of the normalized parameters into them, we obtain the constraint functions (4):

The initial setting time, min

$$71.5-10.0x_1-5.0x_2-20x_3+0.2x_1^2+5.2x_2^2-10.2x_3^2-2.5x_1x_2-2.5x_1x_3+2.5x_2x_3=55$$

Structural strength after 10 minutes of mixture hardening, Pa

$$3083+288x_1+553x_2+831x_3+126x_1^2+176x_2^2+149x_3^2+133x_1x_2+230x_1x_3+192x_2x_3\geq 3300$$

Tensile strength at splitting at the age of 28 days, MPa

$$11.4+2.4x_1+0.78x_2+0.7x_3-0.4x_1^2-0.3x_3^2+0.43x_1x_2-0.37x_1x_3\geq 8$$

Compressive strength at the age of 1 day, MPa

$$20.8+10.2x_1+4.12x_2+6.47x_3+2.44x_1^2-0.36x_2^2+2.1x_3^2+1.08x_1x_2+1.0x_1x_3+0.78x_1x_3\geq 15$$

Compressive strength at the age of 28 days, MPa

$$56.0+14.9x_1+4.25x_2+4.0x_3-1.2x_1^2-0.31x_2^2+1.41x_3^2+2.2x_1x_2-0.9x_1x_3+0.15x_1x_3\geq 40$$

2. In equation (3) we substitute the value of the cost of the components of the mixture, and also set the constraints on the values of the factors: from –1 to 1 (in coded form).

3. Using the software application "Search for a solution", find the values of the factors that satisfy the accepted constraints, and minimize the total cost of the mixture: x_1 = –0.8; x_2 = –0.78; x_3 = 1. With such values of the factors according to coefficients regression equation (Table 3) T = 55 min and Pm_{10} = 3340 Pa, which corresponds to the required parameters. It should be noted that ensuring the required time for the initial setting time of the mixture setting required a certain increase in other normalized strength indicators, f_{cm}^{1} = 19.8 MPa, f_{cm}^{28} = 47.7 MPa and f_{tn}^{28} = 9.6 MPa.

4. The values of factors in natural form are determined by the equations (5):

$$Binder=-0.8x_1+600=-0.8\cdot 200+600=440 \text{ kg/m}^3$$

$$Fly\ ash=-0.78x_2+30=-0.78\cdot(-10)+30=37.8\,\%$$

$$Gypsum = x_3 + 5 = 1 \cdot (5) + 5 = 10\,\%$$

5. Calculated nominal composition of the cement-ash mixture without taking into account the water consumption:

$$Fly\ ash = 440 \cdot 0.378 = 166.3 \text{ kg/m}^3$$
$$Cem = 440 - 166.3 = 273.7 \text{ kg/m}^3$$
$$Gypsum = 0.1 \cdot 440 = 44 \text{ kg/m}^3$$
$$Additive\ SP = 440 \cdot 0.003 = 1.32 \text{ kg/m}^3$$

6. Find the water consumption by the equation (2):

$$W = 197 + 28.4 \cdot (-0.) + 3.3 \cdot (-0.78) + 5.2 \cdot 1 + 13.9 \cdot (-0.8)^2 + 2.4 \cdot (-0.78)^2 - 5.1 \cdot 1^2 +$$
$$+ 0.9 \cdot (-0.8) \cdot (-0.78) + 2.9 \cdot (-0.8) \cdot 1 + 0.9 \cdot (-0.78) \cdot 1 = 170.6\, l / m^3$$

7. Sand consumption from equation (6):

$$S = \left(1000 - \left(\frac{273.7}{3.1} + \frac{166.3}{2.9} + \frac{44}{2.4} + \frac{170.6}{1}\right)\right) \cdot 2.65 = 1763 \text{ kg/m}^3$$

8. The value of the minimum possible cost of 1 m3 of the mixture, excluding the cost of water (found during iterations using the software application MS Excel "Solver"):

$$C_c = 5.2 \cdot 273.7 + 2 \cdot 166.3 + 4.9 \cdot 44 + 700 \cdot 1.32 + 1 \cdot 1763 = 4658.4\, RUB$$

4. Conclusions

1. Taking into account the peculiarities of the manufacture in the construction of structures using a 3D printer, the necessary properties of extruded mixtures and concretes based on them have been determined. Methods for determining the normalized properties of the concrete mixture, the design of the laboratory printer and the device for determining the required structural strength during its layer-by-layer laying are proposed.

2. A set of mathematical models describing the influence of composition factors on the most important properties of concrete mix on cement-ash binder in the presence of hardening accelerator was obtained using mathematical planning of experiments.

3. Using mathematical programming implemented by the Microsoft Excel software environment and its application "Solver", the possibility of using a set of experimental and statistical models to solve the problem of designing optimal compositions of construction mixtures used by a 3D printer is shown.

References

1. Vatin, N., Chumadova, L., Goncharov, I., Zykova, V., Karpenya, A., Kim, A., Finashenkov, E. 3D printing in construction. Construction of Unique Buildings and Structures. 2017. 52 (1). Pp. 27–46. (rus). DOI: 10.18720/CUBS.52.3
2. Inozemtcev, A.S., Korolev, E.V., Duong Thanh, Qui. Analiz suschestvuyuschikh tekhnologicheskikh resheniy 3D-pechati v stroitel'stve [Analysis of existing technological solutions of 3D-printing in construction]. Vestnik MGSU [Proceedings of the Moscow State University of Civil Engineering]. 2018, 7 (118). Pp. 863–876. DOI: 10.22227/1997-0935.2018.7.863-876
3. Perrot, A. 3D Printing of Concrete: State of the Art and Challenges of the Digital Construction Revolution, First Edition. ISTE Ltd 2019. Published by ISTE Ltd and John Wiley & Sons, Inc. DOI: 10.1002/9781119610755
4. Ibrahim, M.I. Estimating the sustainability returns of recycling construction waste from building projects. Sustainable Cities and Society. 2016. 23. Pp. 78–93. DOI: 10.1016/j.scs.2016.03.005
5. Perrot, A., Rangeard, D., Courteille, E. 3D printing of earth-based materials: Processing aspects. Construction and Building Materials. 2018. 172. Pp. 670–676. DOI: 10.1016/j.conbuildmat.2018.04.017
6. Panda, B., Tay, Y., Paul, S.C., Jen, T.M., Leong, K., Gibson, I. Current Challenges And Future Perspectives Of 3d Concrete Printing. Materials Science and Engineering Technology. 2018/ 49 (5). Pp. 666–673. DOI.org/10.1002/mawe.201700279
7. Chen, L. et al. The research status and development trend of additive manufacturing technology. The International Journal of Advanced Manufacturing Technology. 2016. Pp. 1–10. DOI: 10.1007/s00170-016-9335-4
8. Hager, I., Golonka, A., Putanowicz, R. 3D printing of buildings and building components as the future of sustainable construction. Proceeded Engineering. 2016. 151. Pp. 292–299. DOI: 10.1016/j.proeng.2016.07.357
9. Tay, Y.W., Panda, B., Paul, S.C., Tan, M.J., Qian, S., Leong, K.F., et al. Processing and Properties of Construction Materials for 3D Printing. Materials Science Forum. 2016. Pp. 177–181. DOI: 10.4028/www.scientific.net/MSF.861.177
10. Tay, Y.W.D., Panda, B., Paul, S.C., Noor Mohamed, N.A., Tan, M.J., Leong, K.F. 3D printing trends in building and construction industry: a review. Virtual and Physical Prototyping. 2017. 12 (3). Pp. 261–276. DOI: 10.1080/17452759.2017.1326724

11. Lim, J.H., Weng, Y., Pham, Q.C. 3D printing of curved concrete surfaces using Adaptable Membrane Formwork. Construction and Building Materials. 2020. 232. Pp. 117075. DOI: 10.1016/j.conbuildmat.2019.117075
12. Vantyghem, G., De Corte, W., Shakour, E., Amir, O. 3D printing of a post-tensioned concrete girder designed by topology optimization. Automation in Construction. 2020. 112. Pp. 103084. DOI: 10.1016/j.autcon.2020.103084
13. Slavcheva, G.S., Artamonova, O.V. Rheological behavior of 3D printable cement paste: criterial evaluation. Magazine of Civil Engineering. 2018. 84 (8). Pp. 97–108. DOI: 10.18720/MCE.84.10
14. Kaszynska, M., Hoffmann, M., Skibicki, S., Zielinski, A. Evaluation of suitability for 3D printing of high performance concretes. 2018. MATEC Web of Conferences 163:01002. DOI: 10.1051/matecconf/201816301002
15. Austin, S.A., Lim, S., Buswell, R.A., Gibb, A.G.F., Thorpe, T. Mix design and fresh properties for high-performance printing concrete. Materials and Structures. 2012. 8-45. Pp. 1221–1232. DOI: 10.1617/s11527-012-9828-z
16. Youjiang Wang, Wu H.C., Victor C. Li. Concrete reinforcement with recycled fibers. Journal of Materials in Civil Engineering, 2000, 4-12. Pp. 314–319. DOI: 10.1061/(ASCE)0899-1561(2000)12:4(314)
17. Ma, G., Wang, L. & Ju, Y. State-of-the-art of 3D printing technology of cementitious material An emerging technique for construction. Sci. China Technol. 2018. Sci. 61. Pp. 475–495. DOI: 10.1007/s11431-016-9077-7
18. Kopanitsa, N., Sarkisov, Y., Sorokina, E., Demyanenko, O. Mortars for 3D printing. MATEC. Web of Conferences. 2018. 143. 02013. DOI: 10.1051/matecconf/201714302013
19. Le, T.T., et al. Hardened properties of high-performance printing concrete. Cement and Concrete Research. 2012. Vol. 42. Pp. 558–566. DOI: 10.1016/j.cemconres.2011.12.003
20. Kazemian, A., Yuan, X., Cochran, E., Khoshnevis, B. Cementitious materials for construction-scale 3D printing: Laboratory testing of fresh printing mixture. Construction and Building Materials. 2017. 145. Pp. 639–647.
21. Secrieru, E., Fataei, S., Schrofl, C., Mechtcherine, V. Formation of lubricating layer and flow type during pumping of cement-based materials. Construction and Building Materials. 2018. 178. Pp. 507–517. DOI: 10.1016/j.conbuildmat.2018.05.118
22. Ma, G., Li, Z., Wang, L. Printable properties of cementitious material containing copper tailings for extrusion based 3D printing. Construction and Building Materials. 2018. 162. Pp. 613–627. DOI: 10.1016/j.conbuildmat.2017.12.051
23. Jayathilakage, R., Rajeev, P., Sanjayan, J. Yield stress criteria to assess the buildability of 3D concrete printing. Construction and Building Materials. 2020. 240. Pp. 117989. DOI: 10.1016/j.conbuildmat.2019.117989
24. Kruger, J., Zeranka, S., van Zijl, G. 3D concrete printing: A lower bound analytical model for buildability performance quantification. Automation in Construction. 2019. 106(February). Pp. 102904. DOI: 10.1016/j.autcon.2019.102904
25. Dvorkin, L., Dvorkin, O., Ribakov, Y. Mathematical experiments planning in concrete technology. Nova Science Publishers, New York, USA, 2011, 173 p.
26. Dvorkin, L., Bordiuzhenko, O., Zhitkovsky, V., Marchuk, V. Mathematical modeling of steel fiber reinforced concrete properties and selecting its effective composition/ IOP Conference Series: Materials Science and Engineering. Reliability and Durability of Railway Transport Engineering Structures and Buildings. 2019. 708. 012085. DOI: 10.1088/1757-899X/708/1/012085

Information about authors:

Leonid Dvorkin
Doctor in Technical Science
ORCID: https://orcid.org/0000-0001-8759-6318
E-mail: dvorkin.leonid@gmail.com

Vitalii Marchuk
PhD in Technical Science
ORCID: https://orcid.org/0000-0003-0999-0402
E-mail: v.v.marchuk@nuwm.edu.ua

Vadim Zhitkovsky
PhD in Technical Science
E-mail: zhitk@ukr.net

Received 04.03.2021. Approved after reviewing 04.10.2021. Accepted 06.10.2021.

Magazine of Civil Engineering. 2022. 112(4). Article No. 11204

Magazine of Civil Engineering

ISSN
2712-8172

journal homepage: http://engstroy.spbstu.ru/

Research article
UDC 691.32
DOI: 10.34910/MCE.112.4

Combination of additives to characteristics of concrete in marine works

A.T. Nguyen[a], T.T.N. Nguyen[a], T.Q.K Lam[b]*, V.T. Ngo[b], Q.V. Vu[c]

[a] *University of Transport Technology, Hanoi, Vietnam*

[b] *Mien Tay Construction University, Vinh Long, Vietnam*

[c] *Thuy Loi University, Hanoi, Vietnam*

lamthanhquangkhai@gmail.com

Keywords: fly ash, silica fume, water-reducing admixture, Taguchi method, signal-to-noise ratio

Abstract. The deterioration of marine concrete structures due to corrosion damage is increasingly recognized as a serious worldwide challenge for researchers and managers in both technical and economic terms while also leading to other adverse factors. The cost of repairing corrupted and destroyed structures is enormous. The issue of how to improve durability in concrete has received considerable critical attention. There have been several reported longitudinal studies involving the durability of concrete. However, there has been little quantitative analysis of improving the durability of concrete in the seawater environment by incorporating additives. Thus, the aim of this study is to shine new light on using the Taguchi method, which is assisted by MINITAB 19 software to find out the appropriate mixing parameters between some main additives, including fly ash, silica fume, and additive reducing water changing with three levels. The effect of each parameter is evaluated based on the signal-to-noise (SN) ratio: compressive strength is analyzed according to the more significant criterion, while other indicators of durability such as absorption, permeability coefficient, and abrasion are less important. The study offers some important insights into the results of experiments showing the application of the Taguchi experimental method, which allows us to determine the reasonable percent of the additive components with the least number of tests.

Citation: Nguyen, A.T., Nguyen, T.T.N., Lam, T.Q.K, Ngo, V.T., Vu, Q.V. Combination of additives to characteristics of concrete in marine works. Magazine of Civil Engineering. 2022. 112(4). Article No. 11204. DOI: 10.34910/MCE.112.4

1. Introduction

Concrete structures operating in marine environment can be subject to various forms of damage: physical-mechanical, chemical, biological [1–2]. The volumetric changes, external forces, and the surrounding temperature variations, would typically result in cracking, erosion as well as abrasion of the concrete structures. Corrosive effects in a cement concrete product can result from different physical and chemical impacts, such as volumetric expansion or the component dissolution of cement rock.

The corrosion resulting from destruction of the concrete structures has been raising concerns both in research and in the practice for many years. For example, many large-scale corrosion research centers were established in various countries such as France, the USA, Russia, Norway, etc. with many high-ranking journals publishing papers on this topic [1, 3–7]. The use of additives to enhance the capabilities of marine concrete against erosion abrasion is present in many publications.

Mehta P.K. (1991) showed that under the impacts of abrasion and erosion, the transition zone between the coarse aggregate and the cement lake is often destroyed [1]. The aggregate particles tend to be pulled out of their position in the concrete. The combination of reducing W/C ratio and the use of silica fume additive helps improve the bad effects of the above problems [1].

Brember et al. (2003) showed the outstanding quality of concrete samples containing mineral additives (e.g. blast furnace slag, fly ash, silica fume) with the ones without the additives. Silica fume replacing cement at several content levels is also used as a good additive to improve compressive strength, porosity, and resistivity of concrete [7].

Dotto et al. (2004) found that with different content of silica fume replacing cement, the results show a significant improvement in the properties of the concrete, so it is recommended that silica fume be used in an environment with a potent corrosive agent [8]. The study of Bhanj et al. (2005) also gave similar results when changing the content of silica fume [9].

The other type of additive namely fly ash has also investigated in some studies. Tarun et al. used type C fly ash as a replacement of cement contents increasing from 15%-70%. The study shows that fly-ash would be used as a good additive to improve concrete strength and water permeability, diffuse ion's capacity Cl-. Also, taking advantage of the source of additives as industrial byproducts helps to significantly reduce energy costs, resulting high economic efficiency, [10–15].

The addition of silica fume components also significantly reduces water absorption, permeability of Cl ion, and concrete porosity. Furthermore, using the combination of fly ash and silica fume in concrete will dramatically improve the quality compared to concrete made of conventional cement [13–18, 32].

Nguyen T.T.H (2016) proposed the use of 20% fly ash, 10% silica fume to replace cement, and 0.4% plasticizer additive to the cement concrete for the Giao Thuy sea dyke roof in Vietnam. The modified concrete shows better properties, meeting requirements for the protective structure of the dyke and shoreline, thus being selected as the optimal aggregate to use [23].

Some conclusions can be made from literature as follows:

– Silica fume (SF) is also considered an excellent additive to improve the consistency and create uniformity for concrete, thereby increasing the waterproofing ability, creating products with high strength and long-term durability. The recommended mixing ratio of SF is 5–15% of the total binder weight in concrete.

– To limit chloride ion intrusion in the concrete with fly ash (FA), slag ash, or silica fume, has a much smaller ion diffusion coefficient than Portland cement concrete. Therefore, additive-mixed concrete has a much higher protection capacity than reinforced concrete.

According to the literature, it is possible to combine FA and SF and chemical additives in order to produce a coastal concrete. This is also the aim of this study.

In the next section, the essential parameters of concrete (e.g. compressive strength, absorption, permeability coefficient, and abrasion) are mentioned. Other concrete properties are not discussed due to practical limits.

2. Materials and Methods

2.1. Experimental planning by Taguchi method

Dr. Taguchi (Japan) laid the foundations for the Robust Design method and proposed the experimental plan named after him. The Taguchi method aims to design a process/product that is less likely to be affected by factors that cause quality deviation. The Taguchi method is one of the more practical ways of adjusting the parameters to the optimum so that the process/product is stable at the best rate. The Taguchi method uses orthogonal arrays in experimental planning. Therefore, this method allows using the minimum of necessary experiments to study the parameters' effect on a selected property of a process/product, thereby quickly adjusting and optimizing the parameters to the fastest way. Thus, it is possible to use the Taguchi method to find a combination of mineral additive parameters to ensure the necessary durability for concrete. The Taguchi method uses the signal-to-noise ratio (SN), which is converted from the loss function $L = k\,(y\text{-}m)^2$, where L is the loss due to the difference in y characteristic value obtained for the desired property value m, k is a constant. The SN ratio is built and converted to calculate for three prominent cases:

– If the characteristic value Y_i needs reaching "Larger is better" then:

$$SN_L = -10\log\left(\frac{1}{n}\sum_{i=1}^{n}\frac{1}{Y_i^2}\right); \tag{1}$$

– If the characteristic value Y_i needs reaching "Smaller is better" then:

$$SN_L = -10\log\left(\frac{1}{n}\sum_{i=1}^{n} Y_i^2\right); \quad (2)$$

– If the characteristic value Y_i needs reaching "Nominal is best" then:

$$SN_L = 10\log\left(\frac{Y^2}{S^2}\right). \quad (3)$$

In which n, S, Y is the number of experiments, standard deviation, and mean value.

In all cases, the larger the SN ratio, the better the obtaining characteristic is. Because of not using all the test combinations, Taguchi experimental method is not able to give an exact evaluation of the effect of a specific input parameter on the output, while only providing an orientation. However, evaluation of the SN ratio helps technologists to know the trend and the influence of each technology parameter on the output results. These perceptions will help researchers quickly find the technical parameters and the range of impact required to get the best output efficiency. Based on the parameters' impact assessment, the optimal combination of technical parameters can be found for the desired output performance. Many studies and applications since the 1970s have shown that the Taguchi method can be used for academic research, as well as for manufacturing applications, and is particularly suitable for people who have limited statistical knowledge [19–21].

2.2. Determining the research properties of concrete

The concrete was designed with specific requirements as follows:

- Designed concrete grade at 30 MPa;
- Required slump of a concrete mixture from 5 cm to 6 cm;
- Construction method using a manual mixer, compacted by traditional technology;
- Ensuring long service life in marine projects with compressive strength, water absorption, permeability and abrasion characteristics;
- Based on the analyzed theory and documents, three parameters were selected with three mixing levels: 0%; 20% and 30% for FA; 0%; 5% and 10% for SF; 0%; 0.3% and 0.35% for plasticizer additives. With three parameters and three levels, this software allows us to choose the Taguchi L9 plan with nine experiments (Table 4) as a standard plan.

2.3. Experimental plan

2.3.1. Materials

The materials used in the study included Portland cement, fly ash, silica fume, fine aggregates, coarse aggregates, plasticizer water-reducing admixture, and water. The physical and mechanical properties of the material were obtained according to the factory's test result certificate or determined at the LAS 381 building materials laboratory of Thuy Loi University. The results for each type of material were as follows:

The used materials used include Portland cement (PC) with a density of 3.13 g/cm^3, fine aggregate with a density of 2.68 g/cm^3 and modulus of 2.42. The density of coarse aggregate was 2.76 g/cm^3. Water-reducing Admixture or superplasticizer (SP), code HWR100 of The Castech, was used as the chemical additive.

We used the by-products of the Vung Ang I thermal power plant for fly ash (FA) [22]. This type of FA has been treated to limit the unburnt coal content to the standard of ≤ 6%. Some physical and chemical criteria are shown in Table 1.

Table 1. Results of fly ash analysis in Vung Ang I.

No	Item	Unit	Result	Method
1	Intensity activity index, percent compared to the control sample 7 days 28 days	%	 82.30 87.80	ASTM C311 ASTM C109
2	Amount of water required, percent of the control sample	%	96.70	ASTM C311
3	Expansion in Autoclave	%	0.07	ASTM C151
4	Fineness on the 45µm sieve	%	20.00	The LS particle size analyzer
5	Loss on Ignition	%	5.05	ASTM C311
	Humidity	%	0.23	
6	SiO_2	%	58.70	TCNB 03:2009
	Fe_2O_3	%	6.06	TCVN 7131:2002
	Al_2O_3	%	22.62	
7	SO_3	%	0.15	TCVN 6882:2001

Type F fly ash according to the regulations of ASTCM C618 adapted the standards for use as building materials.

Some physical and chemical properties of SF of Castech were shown in Table 2.

Table 2. Characteristics of the Castech Silica Fume.

No	Item	Unit	Result	Technical requirement TCVN 8827:2011
11	Specific Gravity	g/cm^3	2.10	-
22	Loss on Ignition	%	4.20	□ 6
33	SiO_2	%	93.45	□ 85
44	Al_2O_3	%	0.92	-
55	Fe_2O_3	%	0.52	-
66	SO	%	0.63	-
77	CaO	%	1.57	-

The criteria and testing methods for concrete were based on domestic and international standards. Compressive strength, absorption, water permeability, abrasion were determined according to TCVN

3118:1993 [24], TCVN 3113: 1993 [25], EN 12390-8: 2009 [26], ASTM C1138: 05 [27], respectively. Some illustrations of the experiments are shown in Fig.1, Fig.2.

Figure 1. Sample of concrete after splitting tensile strength and measuring penetration.

Figure 2. Machine and sample tests for concrete abrasion according to ASTM C1138 [27].

2.3.2. Concrete Mix Proportions

In the scope of the study, the authors used the method of calculating concrete components according to the guidelines of the Ministry of Construction of Vietnam presented in the book titled "Technical instructions for selecting all types of concrete components" [28], with additional consideration. Specific properties of concrete with additives ensuring the accuracy of the calculated results for the experiment are shown in Table 3.

Table 3. Proportions of concrete mixtures.

No	Mixture No	Components for 1m^3 concrete								W/B
		B	C	FA	SF	FAg	CA	SP	W	
1	$FA_0FS_0P_0$	339	339	0	0	706	1224	0.00	184	0.54
2	$FA_0FS_5P_{0.3}$	345	328	0	17	704	1222	1.04	172	0.50
3	$FA_0FS_{10}P_{0.35}$	351	316	0	35	698	1220	1.23	165	0.47
4	$FA_{20}FS_0P_{0.3}$	361	290	72	0	686	1199	1.08	172	0.48
5	$FA_{20}FS_5P_{0.35}$	368	276	74	18	680	1185	1.29	171	0.46
6	$FA_{20}FS_{10}P_0$	361	253	72	36	666	1206	0.00	166	0.46
7	$FA_{30}FS_0P_{0.35}$	374	262	11	0	661	1203	1.31	157	0.42
8	$FA_{30}FS_5P_0$	380	247	11	19	656	1160	0.00	190	0.50
9	$FA_{30}FS_{10}P_{0.3}$	386	231	11	39	652	1156	1.16	177	0.46

Note: B is Binder; FA is Fly Ash; FS is Silica Fume; FAg is Fine aggregate; CA is Coarse aggregate, W is Water, SP is Superplasticizer or Water-reducing Admixture, W/B is Water/Binder.

FAx is rate of fly ash replacement for cement is x%; FSy is rate of silica fume replacement for cement is y%; SPz is amount of superplasticizer used is z% of the amount of the binder.

3. Results and Discussion

3.1. Compressive strength at 28 days old, water absorption, permeability and abrasion at 60 days old

Testing according to the standards with nine concrete mixes corresponding to each percentage of the additives, each value was an average of 6 sample groups with the required precision. A total of 54 samples were taken, and the results are shown in Table 4. Evaluation of the parameters is shown in the next section.

Table 4. Results of concrete strength and durability.

No	Factors			Results			
	Fly Ash (%)	Silica Fume (%)	Water reducing Admixture (%)	Compressive strength (MPa)	Absorption (%)	Permeability Coefficient (cm/s)	Abrasion resistance (%)
1	0	0	0	33.8	7.10	5.30E-10	6.10
2	0	5	0.3	38.9	6.24	4.50E-11	5.70
3	0	10	0.35	41.2	5.87	3.50E-11	5.15
4	20	0	0.3	39.9	6.25	4.30E-11	5.56
5	20	5	0.35	41.6	5.75	3.00E-11	5.06
6	20	10	0	47.2	5.43	3.60E-10	5.85
7	30	0	0.35	42.0	5.92	3.90E-11	5.27
8	30	5	0	36.4	5.73	4.10E-10	5.92
9	30	10	0.3	44.6	5.56	3.90E-11	5.33

3.2. Results evaluation

3.2.1. Compressive strength

The degree of influence of factors on compressive strength by Taguchi method with SN ratio (Larger is better) were shown in Table 5 and Fig.3.

Table 5. Response Table for Signal to Noise Ratios (Larger is better)

Level	Fly Ash	Silica Fume	Water-reducing Admixture
1	31.56	31.69	31.76
2	32.63	31.80	32.27
3	32.22	32.92	32.38
Delta	1.07	1.23	0.62
Rank	2	1	3

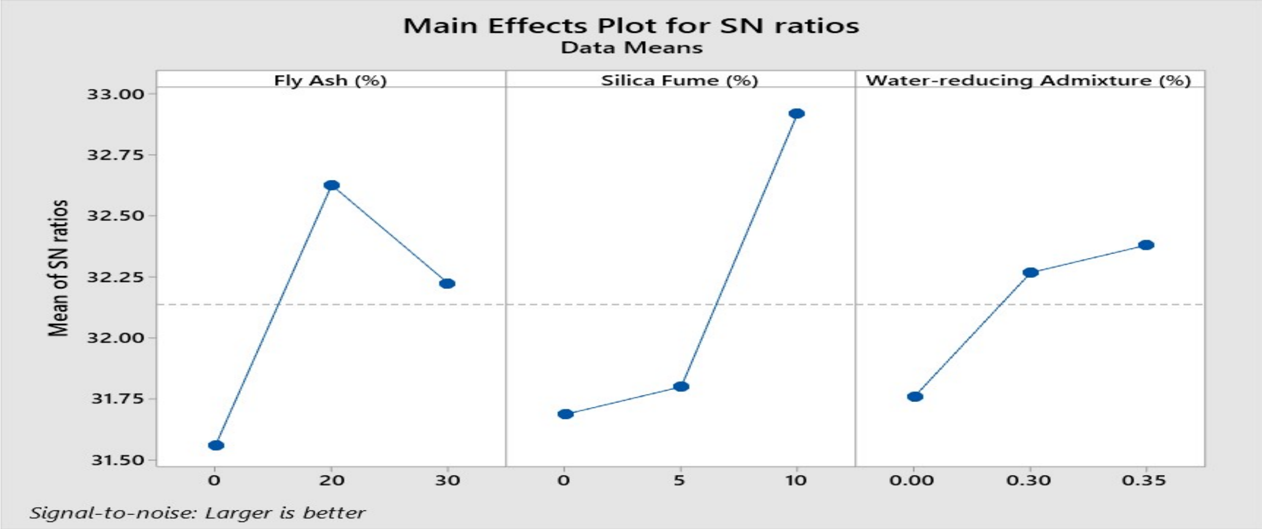

Figure 3. Graph of the effects of the additives according to 3 levels on the compressive strength of the concrete at 28 days old.

The data in Figure 3 show that silica fume was ranked the first with its powerful influence on compressive strength. Strength was affected significantly, when silica varied in the range of 5–10 %.

The fly ash mineral additive was ranked the second: the strength changed significantly when fly ash varied from 0 % to 20 %. However, this effect tended to decrease in compressive strength when increasing fly ash up to 30 %.

Compressive strength was also impacted apparent when water-reducing admixture was used from 0 % to 0.3 %. When using this additive up to 0.35 %, the compressive strength still tended to increase but not significantly. Water-reducing admixture was ranked third.

Interestingly, it can be seen from Table 4, that values of compressive strength in the range from 33.8 MPa to 47.2 MPa satisfied the original design conditions even with or without the additives. Similar to previous studies [7–10], strong evidence of significantly improved strength of the concrete was found when using admixtures.

3.2.2. Absorption

As it can be seen from Table 6, the absorption of the concrete at 60 days old is also determined by SN and the additive rating with the Smaller-is-better criterion. Meanwhile, Fig. 4 describes the effect of the additive levels according to the SN ratio.

Table 6. Response Table for Signal to Noise Ratios (Smaller is better).

Level	Fly Ash	Silica Fume	Water-reducing Admixture
1	-16.1	-16.13	-15.63
2	-15.27	-15.42	-15.57
3	-15.17	-14.99	-15.34
Delta	0.93	1.14	0.29
Rank	2	1	3

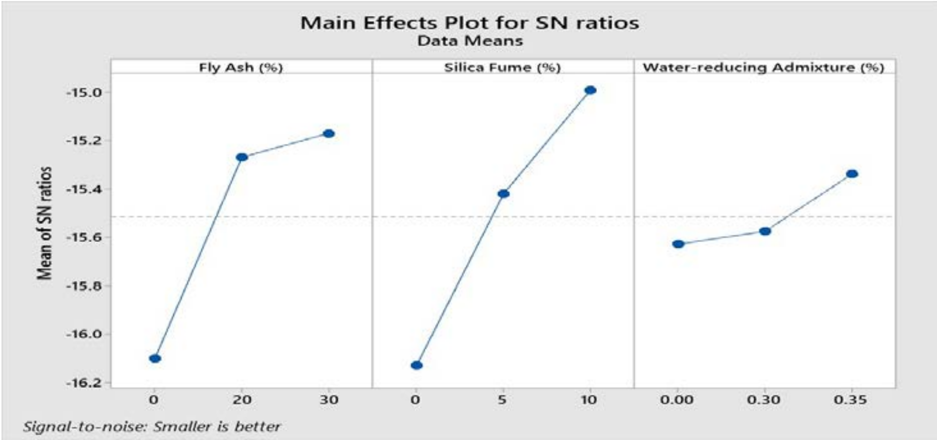

Figure 4. Graph of the effect of the additives according to 3 levels on the water absorption of the concrete at 60 days old.

Fig. 4 shows a clear downward trend for absorption in concrete when additives are used. Silica fume additive (ranked No.1) caused a substantial absorption drop when the content ranged from 0 % to 5 %; absorption continues a dramatic drop up to 10 % of content. Meanwhile, absorption also decreased with the use of fly ash. This additive (ranked No.2 in terms of influence) was used with the content changing from 0 % to 20 %, but the drop was not as significant as before when the content reached the range of 20–30 % amount of binder. Finally, the chemical additive composition (ranked No.3) was also remarkable. The absorption changed slightly with chemical additive content up to 0.3 %, and decreased more sharply with 0.35 %.

The volume of pore space in concrete is measured by absorption, and next to optimal concrete has absorption well below 10 percent by mass [33]. It can be seen from Table 4 that absorption of all main cases ranging in 5.43–7.1 % is relatively low in comparison with the 10 %. This result shows excellent concrete quality when adding some additives in components.

3.2.3. Permeability coefficient

The degree of influence of factors on the permeability coefficient by Taguchi method with SN ratio (Smaller is better) is shown in Table 7 and Fig.5.

Table 7. Response Table for Signal to Noise Ratios (Smaller is better).

Level	Fly Ash	Silica Fume	Water-reducing Admixture
1	200.5	200.3	187.4
2	202.2	201.7	207.5
3	201.4	202.1	209.3
Delta	1.7	1.7	21.9
Rank	3	2	1

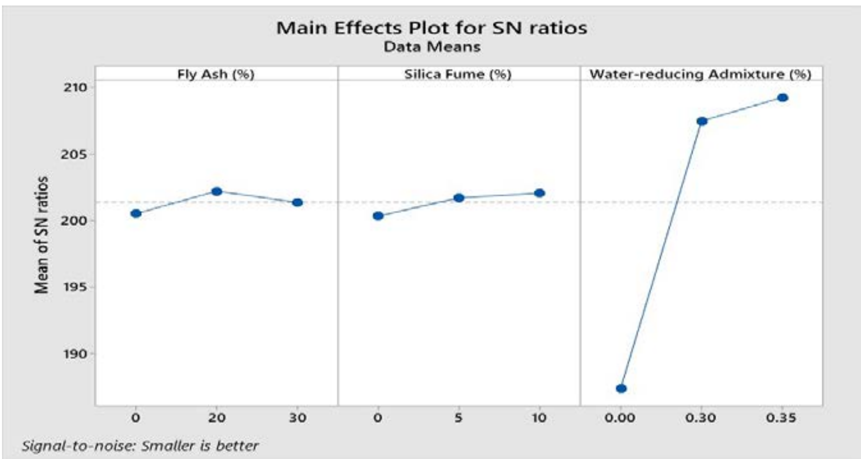

Figure 5. Graph of the influence of the additives according to 3 levels on the permeability coefficient of concrete at 60 days old.

From the graph above, we can see that concrete with plasticizer admixture reduced the permeability coefficient strongly. Water-reducing admixture was ranked No. 1 due to having the greatest impact. When the ratio of the water-reducing additive used was in the range of 0–0.3 %, the permeability coefficient dropped sharply. This coefficient continued to decrease, albeit not significantly, when the ratio of the water-reducing additives was ranging between 0.3 % and 0.35 %. This result is entirely reasonable because the more plasticizer additives the sample uses, the lower the W/B ratio is: the evaporation of excess water makes less penetration pores.

The decrease of the permeability coefficient was still apparent when the concrete used mineral additives. Silica fume and fly ash were ranked 2nd and 3rd, respectively. This result can be explained by the sample nests using silica fume to promote filling in small pores between cement particles, increasing the density of the microstructure, thus improving the waterproofing capacity, reduces the permeability coefficient.

Besides, the results as shown in Table 4 indicate that samples with additive phase have a value of the permeability coefficient ranging from $3*10^{-11}$ cm/s to $5.3*10^{-10}$ cm/s, which is lower than that of conventional concrete with the permeability coefficient ranging from $7.1 * 10^{-11}$ cm/s to $1.5 * 10^{-9}$ cm/s for the concrete grade at 30 MPa [33, 34].

3.2.4. Abrasion

Abrasion of concrete continues to be evaluated with the Smaller-is-better criterion, the impact factors can be seen in Table 8 and Figure 6.

Table 8. Response Table for Signal to Noise Ratios. (Smaller is better).

Level	Fly Ash	Silica Fume	Water-reducing Admixture
1	-15.02	-15.01	-15.50
2	-14.78	-14.88	-14.85
3	-14.81	-14.70	-14.25
Delta	0.24	0.31	1.25
Rank	3	2	1

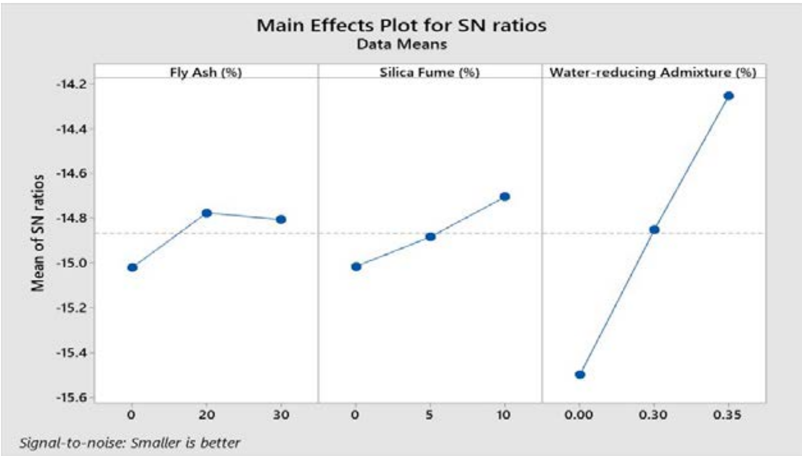

Figure 6. Graph of the influence of additives according to 3 levels on the abrasion of concrete at 60 days old.

As it can be seen from the data in Table 8, the water-reducing admixture was ranked the first in affecting abrasion. Abrasion decreased dramatically, as shown in Figure 6, when the water-reducing additive was used in the range of 0–0.3 % and up to 0.35%. Similarly, from the data in Figure 6, abrasion is affected when the concrete contained silica fume, but to a lesser extent than with water-reducing admixtures. Silica fume was ranked the second.

There was a significant difference with the fly ash content between 20 and 30 %, because abrasion did not follow the Smaller-is-better trend. Contrary to the use of 20% fly ash, the abrasion was markedly reduced. At this level, fly ash is effective in reducing abrasion of concrete. This is explained by the properties of fly ash that significantly improve concrete properties such as increased mobility, increased backfill, and increased C-S-H. However, using too much does not provide any significant advantage to this property of concrete.

These results differ in case of using a mineral additive in the mixture to improve concrete properties, as the study only used fly ash mineral additive [31]. Meanwhile, a number of other studies combining similar FA, SF and slag showed outstanding results in compressive strength and abrasion resistance as well [8, 14, 23, 30]. The law of changing abrasion is similar to the law of varying intensity, consistent with the theory; that is, the higher the concrete strength, the better its resistance to wear.

4. Conclusions

The present study used Taguchi method to examine the effects of concrete admixtures on the aspects of compressive strength at 28 days old, and durability (including absorption, permeability coefficient, and abrasion) at 60 days old. We contribute additional evidence and draw some conclusions to confirm previous findings as follows:

– Using additives significantly improves the properties of the concrete;

– Recommended fly ash content to enhance concrete properties is 20 %, which is more efficient than the total binder mass;

– Silica fume content should be at 5–10 %, which will also significantly improve concrete properties in aggressive environments when 10 % of silica fume is used;

– Water-reducing additive significantly improved the properties of concrete in the aggressive environment, when its content was in the range of 0.3–0.35 %;

– To achieve the best values of compressive strength and absorption, permeability coefficient, and abrasion, it is necessary to select the additives in the following order of priority: water-reducing additives, silica fume, fly ash.

However, several limitations to this pilot study need to be acknowledged. The sample size is still small, and several other properties for the evaluation of the concrete durability are neglected.

References

1. Kumar, M.P. Concrete in the Marine Environment. Elsevier Science Publisher, 1991.
2. Mehta, P. Durability-Critical Issues for the Future. Concrete International. 1997. 19(7). Pp. 27–33.
3. Malhotra, V.M. Supplementary cementing materials for concrete. National government publication, Ottawa, Canada, 1987.
4. Malhotra, V.M., Kumar, M.P. Pozzolanic and Cementitious Materials. Gordon and Breach Publishers. 1996.
5. Malhotra, V.M., Mehta, P.K. High performance, high volume fly ash concrete for building Sustainable and Durable Structures. Supplementary Cementing Materials for Sustainable Development Inc., Ottawa, Canada, 2008.
6. Gro, M., Steen, R., Oskar, K. Guide for the use of stainless steel reinforcement in concrete structures. Norwegian Building Research Institute, 2006.
7. Bremner, T.W., Bilodeau, A., Malhotra, V.M. Performance of Concrete in Marine Environment – Long Term Study Results. International Centre for Sustainable Development of Cement and Concrete (ICON/CANMET), 2003.
8. Dotto, J.M.R., De Abreu, A.G., Dal Molin, D.C.C., Muller, I.L. Influence of silica fume addition on concrete physica properties and on corrosion behavior of reinforcement bars. Cement and Concrete Composites. 2004. 26. Pp. 31–39.
9. Bhanj, S., Sengupta, B. Influence of silica fume on the tensile strength of concrete. Cement and Concrete Research. 2005. 35. Pp. 743–747.
10. Tarun, R.N., Shiw, S.S., Mohammad, M.H. Abrasion resistance of high strength concrete made with class C Fly Ash. Center for By-Products Utilization, University of Wisconsin-Milwaukee-Wisconsin, USA.
11. Shamsad, A., Walid, A.A.K., Omar, S.B.A.A., Mohammad, M. Compliance criteria for quality concrete. Construction and Building Materials. 2008. 22(6). Pp. 1029–1036.
12. Umesh, S.D.R. Effect of Fly Ash on the Properties of Cement. International Journal of Research in Engineering and Technology. 2013. 2(1). Pp. 5–10.
13. Steve, W.M.S., Faiz, U.A.S. Durability properties of high volume fly ash concrete containing nano-silica. Materials and Structures. 2014. 48. Pp. 2431–2445.
14. Alaa, M.R., Hosam, E.D.H., Seleem, A.F.S. Effect of Silica Fume and Slag on Compressive Strength and Abrasion Resistance of HVFA Concrete. International Journal of Concrete Structures and Materials. 2014. 8(1). Pp. 69–91.
15. Nguyen, T.T.N., Doan, L.P. Overview of some types of mineral admixtures in manufacture of concrete. Vietnam Road and Bridge Magazine. 2018. 10. Pp 22-31
16. Truong, H.C. Research on the erosion of civil and industrial construction works in coastal areas of Da Nang city and propose solutions for prevention and control. Project Report, University of Technology Da Nang faculty. 2017.
17. Truong, H.C., Tran, V.Q., Nguyen, P.P., Huynh, Q. Research and survey of the current destructive corrosion status of reinforced concrete buildings and the erosion potential of works in coastal areas of Da Nang city. Journal of Science and Technology. 2008. 6. Pp. 77–85

18. Vietnam Standard 9901: 2014, Irrigation works – Technical requirements for marine dyke design. 2014.
19. Karna, S. Application of Taguchi Methode in Indian Industry. 2012.
20. Design of Experiments (DOE) Using the Taguchi Approach, www.nutek-us.com/DOE_topicOverviews35Pg.pdf.
21. Phadke, S. Quality Engineering Using Robust Design, PTR Printice – Hall, Inc. 1989.
22. Nguyen, T.T.N. Research of using by-products of Vung Ang I thermal power plant to make construction material for rural road. Vietnam Road and Bridge Magazine. 2018. 9. Pp18-25
23. Nguyen, T.T.H. Research on solutions to improve the stability for concrete - steel reform of the structure protection of the night and coastal of Vietnam. Doctoral thesis, University of Transport Technology, 2016.
24. EN 12390-8:2009. Testing Harden Concrete. Part 8- Depth of Penetration of Water under Presure. 2009.
25. Standard Test Method for Abrasion Resistance of Concrete (Underwater Method). 2016.
26. ASTM C1138-05. Standard Test Method for Abrasion Resistance of Concrete (Underwater Method). 2005.
27. Vietnam Ministry of Construction. Technical instructions for choosing concrete components of all kinds. Construction Publishing House, 2012.
28. Ngo, V.T., Lam, T.Q.K., Do, T.M.D., Nguyen, T.C. Increased plasticity of nano concrete with steel fibers. Magazine of Civil Engineering. 2020. 93(1). Pp. 27–34. DOI: 10.18720/MCE.93.3
29. Do, T.M.D, Lam, T.Q.K. Design parameters of steel fiber concrete beams. Magazine of Civil Engineering. 2021. 102(2). Article No. 10207. DOI: 10.34910/MCE.102.7
30. Ayoob, N.S., Abid, S.R., Hilo, A.N., Daek, Y.H. Water-impact abrasion of self-compacting concrete. Magazine of Civil Engineering. 2020. 96(4). Pp. 60–69. DOI: 10.18720/MCE.96.5
31. Sharma, U., Rastogi, D. Effect of Fly Ash on the Properties of Cement. International Journal of Research in Engineering and Technology, 2013, 2(1). Pp. 5–10.
32. Nguyen, C.T., Nguyen, V.T., Pham, H.H., Nguyen, T.L. Research on fabricating super high quality concrete using a combination of silica fume mineral additives and fly ash available in Vietnam. Journal of Construction Science Construction, Institute of Construction Science and Technology IBST, No. 2, 2013. Pp24-31
33. Neville, A.M. Properties of concrete. Fourth and Final. Edition. Harlow, England; New York: Prentice Hall/Pearson Education, 2009.
34. Hoang Pho Uyen, et al. Research to determine the relationship between the permeability coefficient and the waterproofing marks of concrete of irrigation projects. Ministry of Agriculture and Rural Development, Ministerial-level thesis, 2009.

Contacts:

***Anh Tuan Nguyen**, PhD*
E-mail: tuanna@utt.edu.vn

Thi Thu Nga Nguyen
ORCID: https://orcid.org/0000-0002-9613-6011
E-mail: ngantt@utt.edu.vn

***Thanh Quang Khai Lam**, PhD*
ORCID: https://orcid.org/0000-0003-3142-428X
E-mail: lamthanhquangkhai@gmail.com

Van Thuc Ngo
ORCID: https://orcid.org/0000-0001-8101-4698
E-mail: nvthuc34@gmail.com

***Quoc Vuong Vu**, PhD*
E-mail: vuongvlxd@tlu.edu.vn

Received 31.08.2020. Approved after reviewing 26.07.2021. Accepted 27.07.2021.

Magazine of Civil Engineering. 2022. 112(4). Article No. 11205

Magazine of Civil Engineering

ISSN 2712-8172

journal homepage: http://engstroy.spbstu.ru/

Research article
UDC 625
DOI: 10.34910/MCE.112.5

Asphalt pavement rutting model in seasonal frozen area

***L.N. Zhang*[a], *D.P. He*[a] ✉, *Q.Q. Zhao*[b]**

[a] *Northeast Forestry University, Harbin, Heilongjiang, China*

[b] *Northeast Agricultural University, Harbin City, Heilongjiang Province, China*

✉ *hdp@nefu.edu.cn*

Keywords: deterioration, pavement maintenance, design model

Abstract. Effective prediction of rutting diseases in seasonal frozen area is helpful for comprehensive evaluation of asphalt pavement performance. In this paper, based on the Mechanical-Experienced Pavement Design Guide (MEPDG) theory, the rutting prediction model of asphalt pavement in the seasonal frozen area is established by using the measured rutting data of 9 typical highways in the seasonal frozen area of China. The research results show that the traffic volume, climate, and asphalt layer thickness of the pavement structure are directly proportional to the change in rutting. The proposed correction coefficients for the prediction model of asphalt pavement rutting in the seasonal frozen area are $\beta_{1r} = 2$, $\beta_{2r} = 1.03$ and $\beta_{3r} = 0.93$. The normal distribution map and P-P map of the rutting prediction model conform to the normal distribution. The fit between the predicted data of the prediction model and the measured data is high. The fitting value between the predicted data and the measured data before correction is $R^2 = 0.9357$. The fitting value between the revised predicted data and the measured data is $R^2 = 0.9925$. The research results are of great significance for the prediction of rutting and maintenance of asphalt pavement in the seasonal frozen area.

Citation: Zhang, L.N., He, D.P., Zhao, Q.Q. Asphalt pavement rutting model in seasonal frozen area. Magazine of Civil Engineering. 2022. 112(4). Article No. 11205. DOI: 10.34910/MCE.112.5

1. Introduction

With the rapid development of heavy-duty transportation, rutting disease has become the most important form of damage to asphalt pavement. The climate characteristics of the seasonal frozen area are the huge temperature difference between winter and summer, and the freeze-thaw cycle repeating many times in spring and autumn, which will further aggravate the rutting problem of asphalt pavement in the seasonal frozen area of China. Therefore, it is very important to accurately predict the rutting value. Research scholars at home and abroad have proposed a variety of rutting prediction methods for different highway grades. R. Tarefder et al. [1] conducted a local calibration of the Mechanical-Experienced Pavement Design Guide (MEPDG) lines, and the calibrated model can eliminate the prediction deviation of rutting and improve the accuracy of prediction accuracy. Z. Wu et al. [2] Used the design software (MEPDG), the PCC performance of Portland cement concrete (PCC) and asphalt mixture overlay on an unbonded base was analyzed by comparing the evaluation performance of a typical Louisiana rigid pavement structure. A new design method is proposed. M. Mubaraki [3] selected and analyzed to investigate the relationship between International Roughness Index (IRI) and pavement damage including cracking, rutting, and raveling; J. Saha et al. [4] analyzed the sensitivity of the influence of total climate road rutting and international roughness index; W.S. Mogawer et al. [5] used the Mechanical-Empirical Pavement Design Guide (MEPDG) damage prediction equation to predict the mixture performance as a function of density, which only aimed at the influence of hot mix asphalt mixture fatigue crack and rutting performance; Gulfam-E-Jannat, X.X. Yuan [6] could predict IRI and rutting depth for calibration, but the applicability of the model is only for Ontario in the United States.

Rutting will lead to poor smoothness of the pavement, reduce the performance of the pavement, affect the service life of the pavement and even endanger traffic safety. In the seasonal frozen area, the accurate prediction of rutting can effectively improve the performance of the pavement, thereby extending the service life of the highway. Based on the continuous rutting observation data of typical highways in the seasonal frozen area of China, and based on MEPDG theory, this paper establishes a rutting prediction model of asphalt pavement in the seasonal frozen area, so as to predict the rutting depth of asphalt pavement more accurately. Accurate prediction of rutting depth can take effective control measures for asphalt pavement rutting, thereby improving the highway performance in the seasonal frozen area and extending the service life of highways, providing a maintenance reference for asphalt pavement. Therefore, this study has very important practical significance, social and economic benefits.

2. Methods

2.1. MEPDG rutting prediction model

Through the observation, investigation and arrangement of the long-term road performance of more than 2200 test roads in various states of the United States, American Association of State Highway and Transportation Officials (AASHTO), the and the National Cooperative Highway Research Project, (NCHRP), launched the Mechanistic-Empirical Pavement Design Guide, MEPDG [7–15], which is suitable for local climatic conditions in the United States in 2004. MEPDG's prediction model of asphalt pavement rutting, such as formula (1)-(4):

$$\Delta p\left(HMA\right)=\varepsilon_{p(HMA)}h_{HMA}=\beta_{1\gamma}k_Z\varepsilon_{\gamma(HMA)}10^{k_{1\gamma}}n^{k_{2\gamma}\beta_{2\gamma}}T^{k_{3\gamma}\beta_{3\gamma}}, \tag{1}$$

$$k_Z=\left(C_1+C_2D\right)0.328196D, \tag{2}$$

$$C_1=-0.1039\left(H_{HMA}\right)^2+2.4868H_{HMA}-17.342, \tag{3}$$

$$C_2=0.0172\left(H_{HMA}\right)^2-1.7331H_{HMA}+27.428, \tag{4}$$

where $\Delta p\left(HMA\right)$ is accumulated permanent or plastic vertical deformation in the HMA layer/sublayer, in., $\varepsilon_{p(HMA)}$ is accumulated permanent or plastic axial strain in the HMA layer/sublayer, in/in., h_{HMA} is thickness of the HMA layer/sublayer, in., k_Z is depth confinement factor, $\varepsilon_{\gamma(HMA)}$ is resilient or elastic strain calculated by the structural response model at the mid-depth of each HMA sublayer, in/in., $k_{1\gamma}$, $k_{2\gamma}$, $k_{3\gamma}$ are global field calibration parameters (from the NCHRP 1-40D recalibration; $k_{1\gamma}=-3.35412$, $k_{2\gamma}=0.4791$, $k_{3\gamma}=1.5606$), and $\beta_{1\gamma}$, $\beta_{2\gamma}$, $\beta_{3\gamma}$ are local or mixture field calibration constants; for the global calibration, these constants were all set to 1.0., n is number of axle-load repetitions, T is mix or pavement temperature, °F, D is depth below the surface, in., and H_{HMA} is total HMA thickness, in.

Through the model [16–21], it can be judged that traffic volume, climate condition and pavement structure are important parameters that affect the rutting of asphalt pavement. Therefore, in order to put forward the rutting prediction model of asphalt pavement in the seasonal frozen area, it is necessary to verify whether there is a correlation between rutting and n, T, H_{HMA}.

2.2. Analysis of parameters affecting rutting performance

In order to reflect the climatic characteristics of the seasonal frozen area, nine typical highways are selected to fully cover the climatic conditions of the seasonal frozen area in China. The names and geographical locations of all typical highways are shown in Fig. 1. The selected typical highway has a great difference in longitude and latitude, which can more fully reflect the climatic characteristics of the seasonal frozen area in China. In order to reflect the climatic characteristics of the seasonal frozen area, 6 typical highways were selected in Northeast China.

Figure 1. Geographic location of typical highways.

2.2.1 Traffic load parameters

In order to verify whether there is a correlation between rutting and climate in the seasonal frozen area, Jian-Ji Highway and Jian-Hei Highway are selected for comparison. The pavement structure parameters and climate parameters of the two highways are similar, but there are significant differences in traffic volume. Compare the uplink and downlink traffic volume of the K45+000~K91+495 section of Jian-Ji Highway and the K168+485~K217+905 section of Jian-Hei Highway, as shown in Fig. 2, and the data in the figure shows the comparison of the total number of vehicles on the two roads in 2018. The total number of uplink vehicles in Jian-Ji Highway is 9623, of which 3410 are heavy trucks, and the total number of downlink vehicles is 9752, of which 3464 are heavy trucks. The total number of uplink vehicles in Jian-Hei Highway is 7896, of which 2784 are heavy trucks, and the total number of downlink vehicles is 9047, of which 3154 are heavy trucks. The total number of vehicles can not see the damage to the actual road surface caused by the traffic volume, because the impact of extra heavy vehicles on the road surface far exceeds the general axle load. Therefore, by comparing the axle load distribution of several observation sections with similar number of vehicles, the traffic parameters of several observation sections can be reflected in more detail. The American Standard 9 and 10 cars passed by each observation section are taken as the research object, because these two kinds of vehicles cover most of the double-axle and all three-axle models.

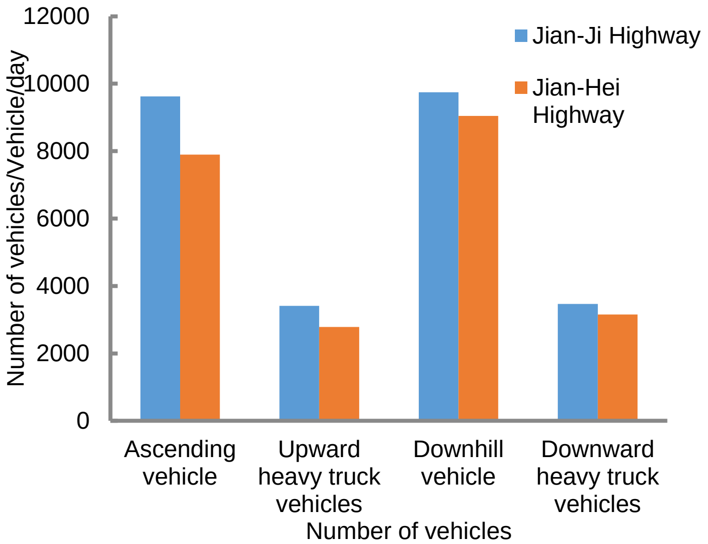

Figure 2. Comparison of the number of vehicles and heavy vehicles in different road sections.

The axle load distribution is shown in Fig. 3 and 4. It can be seen from the figure that the axle load of Jian-Ji Highway is obviously larger than that of Jian-Hei Highway, and the asphalt pavement of Jian-Ji Highway bears heavier traffic load.

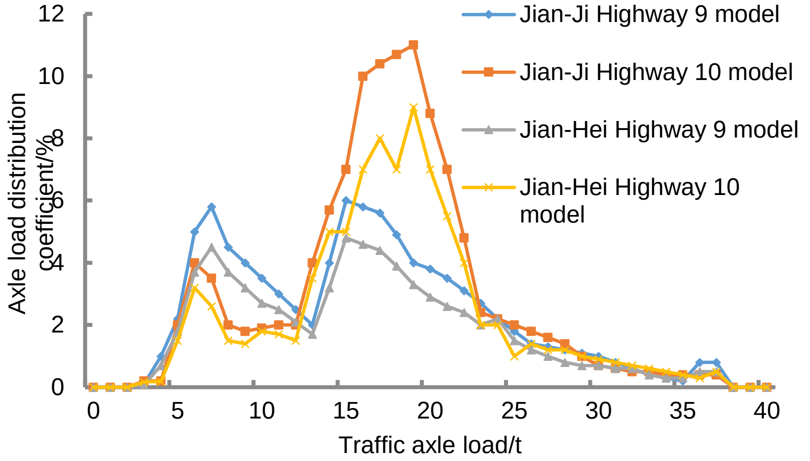

Figure 3. Comparison of axle load distribution of double couplings of overweight vehicles in different road sections.

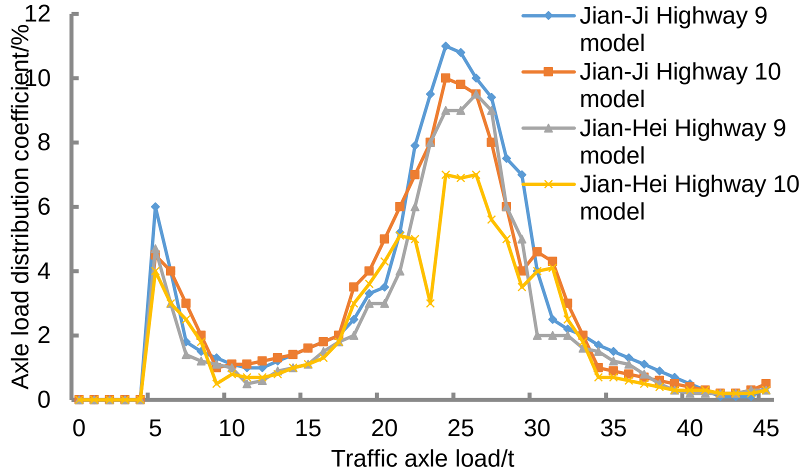

Figure 4. Comparison of axle load distribution of triple axles of overweight vehicles in different road sections.

Between 2014 and 2018, the growth rate of Jian-Ji Highway's rutting value was 33.4 %. The growth rate of Jian-Hei Highway was 26.6 %, with an average annual growth rate of 8.35 % and 6.65 %, respectively, as shown in Fig. 5. According to the analysis of the reasons, both Jian-Ji Highway and Jian-Hei Highway are located in Heilongjiang Province, China. The climate temperature of the two highways is similar and the pavement structure is the same, but the large traffic volume of Jian-Ji Highway leads to a faster increase in rutting value.

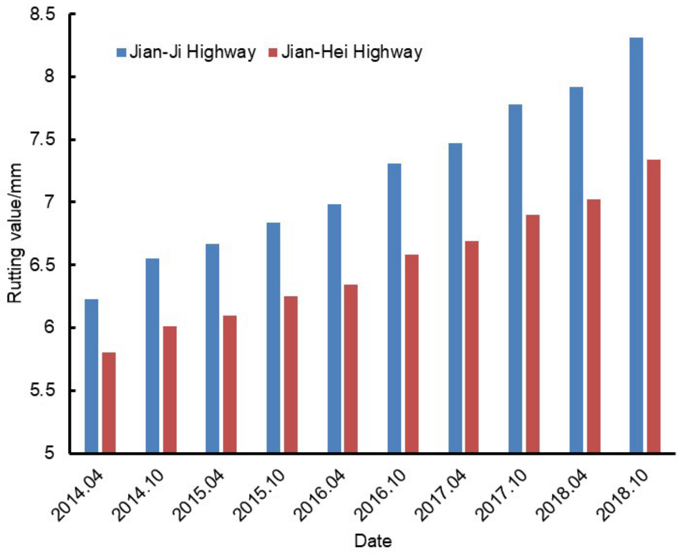

Figure 5. Comparison of rutting values between Jian-Ji Highway and Jian-Hei Highway.

2.2.2 Climatic parameters

In order to verify whether there is a correlation between rutting and climate in the seasonal frozen area, the influence on rutting is verified by selecting air temperature, average annual freezing index and average annual precipitation from the climatic conditions. The monthly mean temperature curve, freezing depth curve and precipitation distribution curve corresponding to four typical highways such as Jian-Ji Highway (Yanggang to Mishan Section), Zhang-Shi Highway (Zhangjiakou Section), Lian-Huo National Highway (Kuitun-Wusu Section) and 110 National Highway (Hubao section) are drawn respectively, as shown in Fig. 6–8.

As the temperature in the seasonal frozen area is lower than 0 °C, from October to March of the following year, the time for a complete freeze-thaw process is set from October of 2017 to October of 2018. The influence of temperature on asphalt pavement is compared and analyzed. As can be seen from Fig. 6, there is a gap in the monthly average temperature of the cities where the four highways are located. The month with the largest temperature difference is February 2018. The monthly mean temperature difference between Jian-Ji Highway and Zhang-Shi Highway cities is 10 °C, and the air temperature difference is 3 times. Among the four typical highways, Lian-Huo National Highway has the lowest temperature in winter. The average temperature in January 2018 is –18 °C, and the temperature in summer is the highest. The average temperature in July 2018 is 27.5 °C, which is the year-round among the four typical highways. The road with the largest temperature difference has a temperature difference of 45.5 °C throughout the year. Zhang-Shi Highway has the smallest temperature difference throughout the year. The monthly minimum temperature of the four typical highways appeared in January 2018. The monthly average temperature difference between Lian-Huo National Highway and Zhang-Shi Highway is 9 °C, and the difference in temperature value is 2 times. The highest monthly average temperature occurred in July 2018. The monthly average temperature difference between Lian-Huo National Highway and 110 National Highway is 4.5 °C, and the difference in temperature value is 0.83 times.

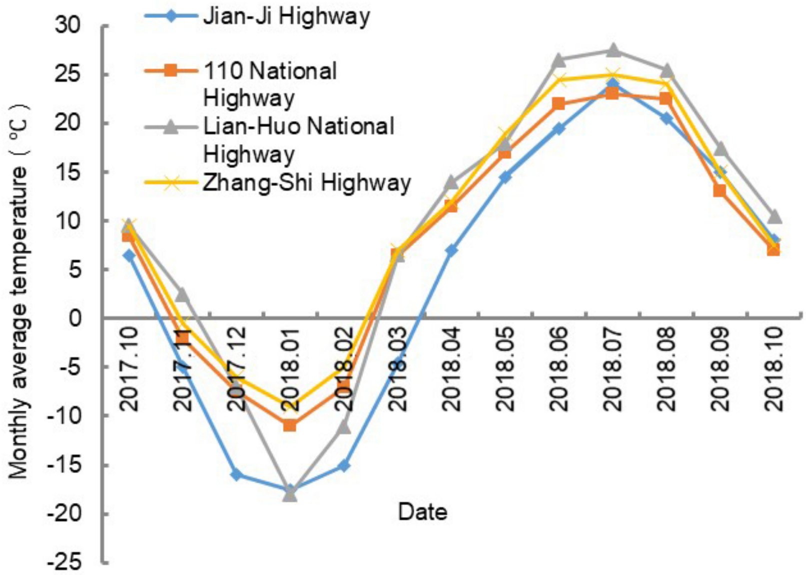

Figure 6. Change of monthly mean temperature curve.

Fig. 7 shows the precipitation distribution curve of four typical highways from January to December 2018. The season with the highest rainfall on the four highways occurs in July, in which Jian-ji Highway is the largest and Lian-Huo National Highway is the smallest. The month in which the maximum precipitation occurs is also in line with the actual characteristics of climatic precipitation in the seasonal frozen area. The highway with the largest annual precipitation is Jian-Ji Highway, with an annual precipitation of 407 mm, accounting for 5.28 %, 24.69 %, 62.04 % and 7.99 % of the annual precipitation in spring, summer, autumn and winter, respectively. The precipitation of Zhang-Shi Highway is 397.3 mm, and spring, summer, autumn and winter account for 4.3 %, 30.4 %, 58.07 % and 7.22 % of the annual precipitation, respectively. The precipitation of Lian-huo National Highway is 175.5 mm, accounting for 12.82 %, 39.66 %, 28.72 % and 18.8 % of the annual precipitation, respectively. The precipitation of 110 National Highway is 402.3 mm, and spring, summer, autumn and winter account for 5.1 %, 25.98 %, 59.98 % and 8.93 % of the annual precipitation, respectively. As can be seen from Fig. 7, January to March 2018 and October to December of 2018 are the periods when the precipitation of the four typical highways is relatively less, which is due to the fact that the four highways have entered winter one after another.

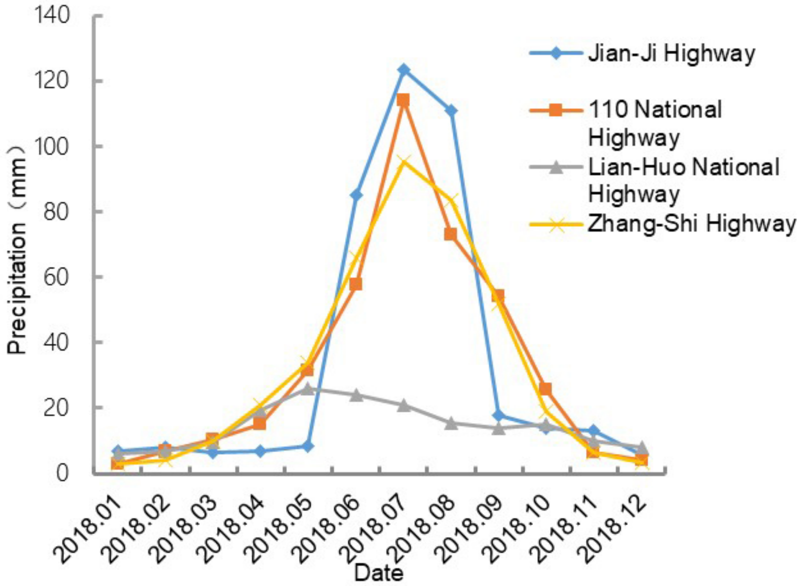

Figure 7. Precipitation distribution curve.

Fig. 8 shows the freezing depth curves of four typical highways. Since the freezing time of roads in the seasonal frozen area is from October to April of the following year, the freezing depth values of the four curves are basically 0 cm from May 2018 to September 2018. The maximum freezing depth of the four typical highways appeared in February 2018. Among them, the maximum freezing depth of Jian-Ji Highway, in northeastern China was 217 cm, followed by Lian-Huo National Highway, in northwestern China, 164 cm. The third is 110 National Highway in northern China, whose maximum deep value is 152 cm. The sminimum freezing depth is Zhang-Shi Highway, whose maximum freezing depth is 110 cm. The difference between the maximum freezing depth and the minimum freezing depth is 107 cm. The reason is that in February 2018, the temperature difference between Jian-Ji Highway and Zhang-Shi Highway is 3 times, and the precipitation difference is 1.95 times. Under the coupling action of precipitation and temperature, the difference in freezing depth is significant.

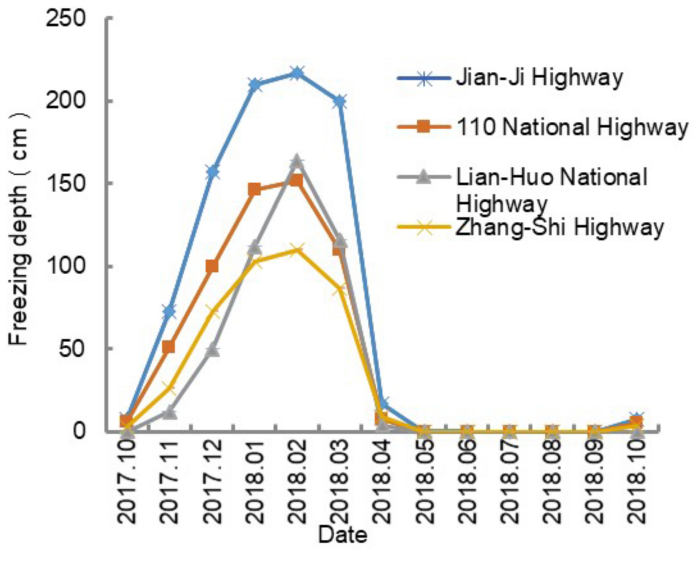

Figure 8. Freezing depth curve.

In order to further analyze the influence of climatic factors on the rut disease of asphalt pavement, the rutting depth curves of four highways from 2014 to 2018 are established, as shown in Fig. 9. In Fig. 9, the rutting values of the four highways change with time, and the change law is linear growth. For example, the rutting depth of Zhang-Shi highway increased by 0.29 mm in October 2014 compared with April 2014, and 0.13 mm in April 2015 compared with October 2014. The rutting depth of the same highway in October every year is greater than that in April. According to the analysis of the reasons, the temperature began to rise in April, the highway in the seasonal frozen area began to thaw, and the rutting disease of the pavement developed rapidly under the repeated action of external loads. The rutting depth in October has experienced many times of freezing and thawing in spring and hot high temperature in summer, so the rutting depth measured in October varies greatly. From April 2014 to April 2018, the change rate of

Lian-Huo Highway rutting depth is 59.5 %, which is the largest among the four highways, followed by 110 National Highway, whose rut depth change rate is 35.3 %. The third is Jian-Ji Highway, whose rutting depth change rate is 33.3 %. The slowest development of rutting disease is Zhang-Shi Highway, whose rutting depth change rate is 30.8 %. According to the analysis of the reasons, the freezing depth and rainfall of the highway in the seasonal frozen area are not the decisive factors affecting the rutting value, but the air temperature is the main factor affecting the rutting disease of the highway in the seasonal frozen area. The higher the temperature is, the faster the rutting disease develops.

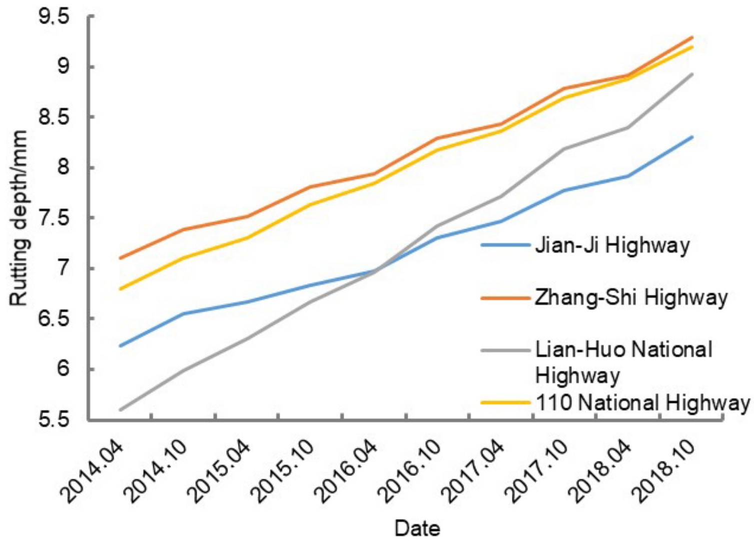

Figure 9. Rutting depth variation curve.

2.2.3 Analysis of pavement structure parameters

In order to verify whether the correlation between rutting and H_{HMA} accur in the seasonal frozen area, four highways with similar traffic volume and climatic conditions but different asphalt thickness of pavement structure are selected: Hei-Da Highway, Sui-Man Highway, Qi-Zha Highway, and Jia-Lin Highway. The effects of asphalt thickness of different pavement structures on rutting are compared. The proportion of rutting on the four highways is compared in Fig. 10. According to the analysis of Fig. 10, the thickness of the asphalt layer of Hei-Da Highway is the largest, which is 240 mm. The rutting disease of the highway develops most rapidly, and the rutting depth is concentrated between 5~12 mm, in which the rutting depth of 5~8 mm is 39 %, and the rutting ratio of 8 mm to 12 mm is 38 %. The thickness of the asphalt layer of Sui-Man Highway is 180 mm and the rutting ratio of 5 mm to 8 mm is 35 % to that of 8~12 mm. The asphalt layer thickness of Qi-Zha Highway is 150 mm, the proportion of rutting is 31 %, and the proportion of rutting of 8~12 mm is 32 %. The asphalt layer thickness of Jia-Lin Highway is 120 mm, the rutting ratio of 5~8 mm is 26 %, and the rutting ratio of 8~12 mm is 31 mm. For the typical highway in the seasonal frozen area, the transverse crack is one of the main disease characteristics of the asphalt pavement. The thicker the asphalt layer of the asphalt pavement is, the faster the rutting disease develops.

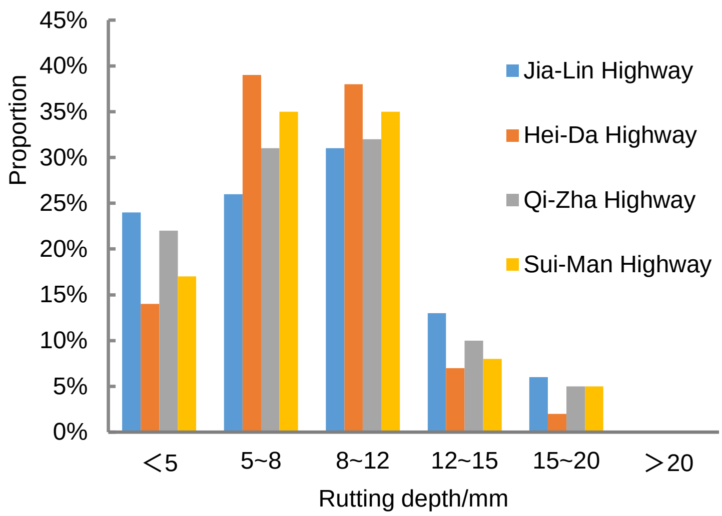

Figure 10. Rutting ratio of four highways.

From the above analysis of the rutting value of the asphalt pavement, the disease of the asphalt pavement in the seasonal frozen area is mainly rutting, and the rutting value increases with the increase of the thickness of the pavement structure when the climate condition and traffic volume are basically the same. And the development form is mainly transverse temperature shrinkage cracks.

2.3. Processing of measured rutting data

In order to establish a rutting prediction model suitable for asphalt pavement in seasonal frozen area, the rutting values of typical highways in seasonal frozen area are measured in situ. The measured time is from 2014 to 2018. The rutting values of 9 typical highways in the seasonal frozen area of China are collected by road multi-function monitoring vehicles and calibrated manually. They are measured and calibrated four times a year, and 10m per lane is measured once. In this paper, the lane with the largest rutting value is used for data analysis.

MEPDG rutting prediction model uses 90 % design reliability to calculate rutting, so the measured rutting data of typical highways are processed based on normal distribution, and the measured rutting data of corresponding 90 % frequency ratio are used. The measured rutting values of different stations should be random variables that meet the normal distribution, which ensures the rationality of the selected data.

3. Results and Discussion

3.1. Construction of rutting prediction model based on MEPDG theory

The advantage of the rutting prediction model proposed by MEPDG theory is that the factors considered in the calculation process are more comprehensive, which can reflect the actual use of the pavement more closely, and has higher accuracy. However, because the rutting prediction model proposed by MEPDG theory is based on the climatic conditions of the United States and the measured data of thousands of local test sections, the model has regional limitations. Therefore, this paper intends to modify the rutting prediction model of asphalt pavement in the seasonal frozen area according to the climatic conditions of the seasonal frozen area in China and the measured rutting values of 9 typical highways.

In the process of modifying the MEPDG rutting prediction model, firstly, the default local correction coefficient of the system, that is, $\beta_{1r} = \beta_{2r} = \beta_{3r} = 1,$ is adopted, from which the formula (5) is obtained:

$$\Delta p\left(HMA\right) = \varepsilon_{p(HMA)} h_{HMA} = k_Z \varepsilon_{\gamma(HMA)} 10^{-3.35412} n^{0.4791} T^{1.5606} h_{HMA}. \quad (5)$$

In the formula, Δp_H is the predicted value of rutting after correction, and n is the number of repeated loads, which is obtained by equivalent conversion of axle load spectrum.

By dividing (1) by (5), a relationship (6) before and after the correction of MEPDG rutting prediction model can be obtained, that is:

$$\Delta p_H / \Delta p_Q = \beta_{1\gamma} n^{0.4791\left(\beta_{2\gamma}-1\right)} T^{1.5606\left(\beta_{3\gamma}-1\right)}. \quad (6)$$

In the formula, $\Delta p_Q,\ \Delta p_H$ are the predicted values of rut before and after correction, n is the number of repeated loads, which is obtained by indoor repeated loading triaxial permanent deformation test, and T is the road surface temperature (°F), which is the average value of the annual maximum temperature in the seasonal frozen area of China in the past 10 years.

Formula (6) is used as the relation function in the solution of Excel programming. By using the function of "data analysis" in Excel programming solving method, the nonlinear model can be transformed into linear model, and the transformed multivariate nonlinear model can be analyzed by regression and verify its validity and feasibility. Based on the rut measurement data of 9 highways above, the rutting prediction model of the seasonal frozen area based on MEPDG theory is established. Some of the operation data are shown in Table 1. In the process of creating the model, use Excel Solver to establish constraint conditions for the variable cell values in the Solver model. The constraint conditions are formulas 1-4. By changing the MEPDG rut value before correction, the rut prediction after correction is determined.

The three values of local correction coefficients are calculated based on the rut prediction value before correction and the rut prediction value after correction. Because all the calculation data are calculated based on the road detection data in the seasonal frozen area, according to formula 1-4. Using matlab to perform background calculations and solutions. Therefore, it is concluded that the three coefficients are local correction coefficients. In order to verify that their calculations are accurate, they are tested by the sum of squared errors (SSE). SSE is the sum of squared deviations within the group, which is used to test errors caused by errors. The value of the squared error in the article is only 3.89641, which is very small, which proves that the local correction coefficient obtained is accurate.

$$SSE = \sum_{i=1}^{k} \sum_{j=1}^{n_i} \left(x_{ij} - \overline{x_i} \right)^2 . \quad (7)$$

In the formula, SSE is the sum of squared deviations within the group, which is the variation caused by sampling error; k is the level number of the control variable; x_{ij} is the j-th sample value under the i-th level of the control variable; n_i is the control variable The sample size at the i-th level; $\overline{x_i}$ is the sample mean of the observed variable at the i-th level of the control variable.

Table 1. Determination of coefficients of rutting prediction model based on MEPDG theory according to planning solution. (The measured data of rutting of typical highways in the seasonal frozen area of China).

Serial number	Measured value of rutting/mm	MEPDG rutting prediction value / mm		Local correction coefficient	Target value (Sum of squares of errors)
		Before correction	After correction		
1	8.1	7.7	8.0	2.00	3.89641
2	4.2	4.5	4.1	1.03	
3	5.4	5.8	5.2	0.93	
4	7.1	7.6	7.0		
5	4.3	4.7	4.2		
6	7.5	7.0	7.4		
7	6.3	6.0	6.2		
8	6.1	6.5	5.9		
9	5.8	5.4	5.7		
10	6.3	6.6	6.2		
11	7.7	8.1	7.6		
12	5.2	5.7	5.1		
13	8.1	8.5	8.0		
14	7.6	7.3	7.5		
15	6.9	7.2	6.7		
16	…	…	…		

It can be seen from Table 1 that the correction coefficients of the seasonal frozen area of MEPDG rutting prediction model obtained by using planning solution method are $\beta_{1r} = 2,$ $\beta_{2r} = 1.03,$ $\beta_{3r} = 0.93.$ The modified seasonal frozen area correction coefficient is brought into the formula (1), and the modified MEPDG rutting prediction model is obtained as the formula (8):

$$\Delta p\left(HMA\right) = \varepsilon_{p(HMA)} h_{HMA} = \\ = 2k_Z \varepsilon_{\gamma(HMA)} 10^{-3.35412} n^{0.49235985} T^{1.45366232} h_{HMA}. \quad (8)$$

3.2. Model verification

The measured data of asphalt pavement rutting are fitted with the rutting prediction value based on MEPDG theory, and the normal distribution map and P-P diagram are used to verify whether the model has universal applicability in statistics. The distribution of the difference (residual) between the measured value and the measured value of the MEPDG rutting prediction model is normally distributed as shown in Fig. 11. It is always assumed that the residual is consistent with the normal distribution in the process of regression using SPSS [22]. From the histogram and normal curve distribution of the regression residual of Fig. 11(a), we can see that the sample size is large enough and the residual distribution obviously obeys the normal distribution. This shows that the regression prediction model has universal applicability in statistics, and there is no autocorrelation and multiple collinearity among variables, so it proves the accuracy of MEPDG rutting prediction model. Fig. 11(b) is the P-P diagram of the regression normalized residual of the rutting prediction model, and the residual P-P diagram between the cumulative probability of the actual measured value and the cumulative probability of the expected estimated result. It can be seen from Fig. 11(b) that the distribution curve of the residual is distributed around the specified straight line and changes around the straight line, indicating that the distribution of the residual P-P diagram can satisfy the pre-set normal distribution and the equation has practical significance. To sum up, the MEPDG rutting prediction model has passed various tests, and the fitting effect is well.

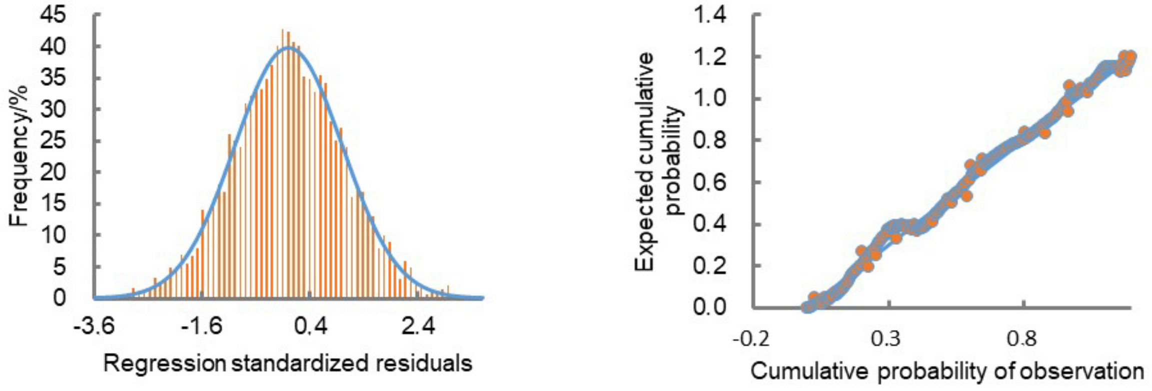

(a) Residual histogram **(b) Residual regression PMI P diagram**

Figure 11. Rutting prediction residual histogram and residual regression P-P chart.

The modified results of the rutting prediction model based on MEPDG theory [23–27] are fitted and verified, as shown in Fig. 12. Fig. 12(a), the result before correction represents the prediction result based on MEPDG theory. Fig. 12(b), the revised result is the prediction result of this revised model. It can be seen from Fig. 12 that the fitting coefficient between the predicted rutting value of MEPDG before correction and the measured value of rutting over the years is R^2 = 0.9357, and the fitting coefficient between the predicted value of modified MEPDG and the measured value is R^2 = 0.9925. It can be concluded that the modified MEPDG rutting prediction model has higher accuracy.

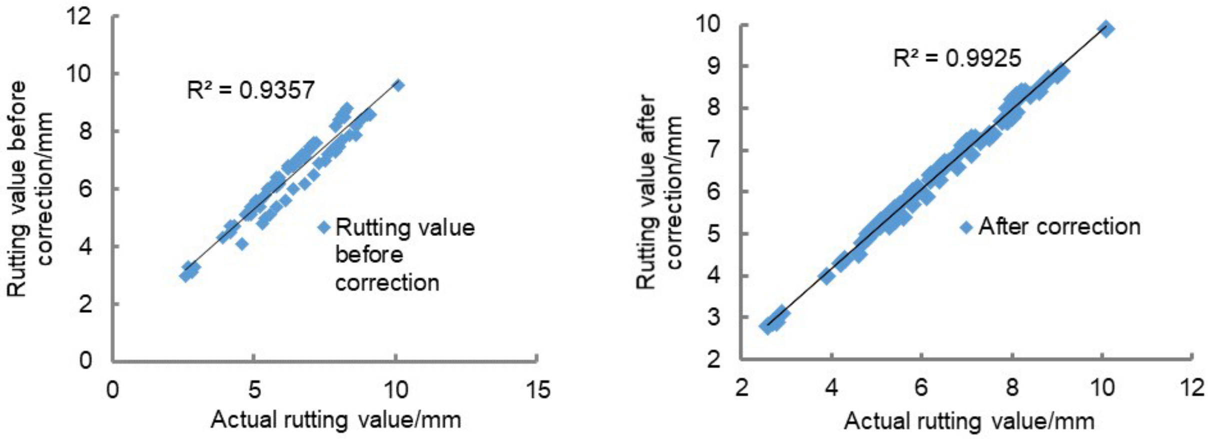

(a) Before correction **(b) After correction**

Figure 12. Correction effect of MEPDG rutting prediction model.

4. Conclusion

1. The traffic volume, climate and the thickness of asphalt layer of pavement structure are the key factors that affect the rutting change in the seasonal frozen area, and they are proportional to each other.

2. A rutting prediction model for asphalt pavement in the seasonal frozen area is proposed. Among them, β is the correction coefficient of the seasonal frozen area, and the modified coefficients are $\beta_{1r} = 2,\ \beta_{2r} = 1.03,\ \beta_{3r} = 0.93,$ respectively.

3. The normal distribution map and P-P map of the rutting prediction model accord with the normal distribution, which is generally applicable in statistics.

4. The prediction accuracy of rutting prediction model is higher. The fitting value between the predicted data and the measured data before correction is obtained, and the fitting value between the modified predicted data and the measured data is R^2 = 0.9357, and the fitting value between the modified predicted data and the measured data is R^2 = 0.9925. This shows that there is a higher degree of fit between the revised predicted data and the measured data.

References

1. Tarefder, R., Rodriguez-Ruiz, J.I. Local calibration of MEPDG for flexible pavements in New Mexico. Journal of Transportation Engineering. 2013. 139(10). Pp. 981–991. DOI: 10.1061/(ASCE)TE.1943-5436.0000576
2. Wu, Z., Xiao, D.X., Zhang, Z., Temple, W.H. Evaluation of AASHTO Mechanistic-Empirical Pavement Design Guide for designing rigid pavements in louisiana. International Journal of Pavement Research and Technology. 2014. 7(6). Pp. 405–416. DOI: 10.6135/ijprt.org.tw/2014.7(6).405
3. Mubaraki, M. Highway subsurface assessment using pavement surface distress and roughness data. 8th International Conference on Maintenance and Rehabilitation of Pavements, MAIREPAV 2016. 9(5). Pp. 393–402. DOI: 10.3850/978-981-11-0449-7-329-cd
4. Saha, J., Nassiri, S., Bayat, A., Soleymani, H. Evaluation of the effects of Canadian climate conditions on the MEPDG predictions for flexible pavement performance. International Journal of Pavement Engineering. 2014. 15(5-6). Pp. 392–401. DOI: 10.1080/10298436.2012.752488
5. Mogawer, W.S., Austerman, A.J., Daniel, J.S., Zhou, F., Bennert, T. Evaluation of the effects of hot mix asphalt density on mixture fatigue performance, rut performance and MEPDG distress predictions. International Journal of Pavement Engineering. 2011. 12(2). Pp. 161–175. DOI: 10.1080/10298436.2010.546857
6. Gulfam-E-Jannat, Yuan, X.X., Shehata, M. Development of regression equations for local calibration of rut and IRI as predicted by the MEPDG models for flexible pavements using Ontario's long-term PMS data. International Journal of Pavement Engineering. 2016. 17(1-2). Pp. 166–175. DOI: 10.1080/10298436.2014.973024
7. Caliendo, C. Local calibration and implementation of the mechanistic-empirical pavement design guide for flexible pavement design. Journal of Transportation Engineering. 2012. 138(3).Pp. 348–360. DOI: 10.1061/(ASCE)TE.1943-5436.0000328
8. Zhang, C., Wang, H., You, Z., Ma, B. Sensitivity analysis of longitudinal cracking on asphalt pavement using MEPDG in permafrost region. Journal of Traffic and Transportation Engineering (English Edition). 2015. 2(1). Pp. 40–47. DOI: 10.1016/j.jtte.2015.01.004
9. Li, Q., Xiao, D.X., Wang, K.C.P., Hall, K.D., Qiu, Y. Mechanistic-empirical pavement design guide (MEPDG): A bird's-eye view. Journal of Modern Transportation. 2011. 19(2). Pp. 114–133. DOI: 10.3969/j.issn.2095-087X.2011.02.007
10. Kim, S., Ceylan, H., Gopalakrishnan, K., Smadi, O. Use of pavement management information system for verification of mechanistic-empirical pavement design guide performance predictions. Transportation Research Record. 2010. 2153. Pp. 30–39. DOI: 10.3141/2153-04
11. El-Basyouny, M., Jeong, M.G. Prediction of the MEPDG asphalt concrete permanent deformation using closed form solution. International Journal of Pavement Research and Technology. 2014. 7(6). Pp. 397–404. DOI: 10.6135/ijprt.org.tw/2014
12. Cooper, S.B., Elseifi, M., Mohammad, L.N., Hassan, M. Performance and Cost-Effectiveness of Sustainable Technologies in Flexible Pavements Using the Mechanistic-Empirical Pavement Design Guide. Journal of Materials in Civil Engineering. 2012. 24(2). Pp. 239–247. DOI: 10.1061/(ASCE)MT.1943-5533.0000376
13. Solatifar, N., Kavussi, A., Abbasghorbani, M., Katicha, S.W. Development of dynamic modulus master curves of in-service asphalt layers using MEPDG models. Road Materials and Pavement Design. 2019. 20(1). Pp. 225–243. DOI: 10.1080/14680629.2017.1380688
14. Pierce, L.M., Ginger, M. Implementation of the AASHTO Mechanistic-Empirical Pavement Design Guide and Software. 2014.
15. El-Badawy, S., Bayomy, F., Awed, A. Performance of MEPDG dynamic modulus predictive models for asphalt concrete mixtures: Local calibration for Idaho. Journal of Materials in Civil Engineering. 2012. 24(11). Pp. 1412–1421. DOI: 10.1061/(ASCE)MT.1943-5533.0000518
16. Allan Reese, R. R for SAS and SPSS Users. Journal of the Royal Statistical Society: Series A (Statistics in Society). 2009. 172(3).Pp. 697–698. DOI: 10.1111/j.1467-985x.2009.00595_7.x
17. Hayes, A.F., Matthes, J. Computational procedures for probing interactions in OLS and logistic regression: SPSS and SAS implementations. Behavior Research Methods. 2009. 41(3). Pp. 924–936. DOI: 10.3758/BRM.41.3.924
18. Sandra, A.K., Sarkar, A.K. Development of a model for estimating International Roughness Index from pavement distresses. International Journal of Pavement Engineering. 2013. 14(7-8). Pp. 1–10. DOI: 10.1080/10298436.2012.703322
19. Guenther, A.B., Jiang, X., Heald, C.L., Sakulyanontvittaya, T., Duhl, T., Emmons, L.K., Wang, X. The model of emissions of gases and aerosols from nature version 2.1 (MEGAN2.1): An extended and updated framework for modeling biogenic emissions. Geoscientific Model Development. 2012. 5(22). Pp.1471–1492. DOI: 10.5194/gmd-5-1471-2012
20. Morozova, T.F., Tyanfu Khe, Petrova, Y.M. Building side area minimization at the expense of optimization the schedule of movement of workers. Magazine of civil engineering. 2011. 25(7). Pp. 1944–1949. DOI: 10.5862/mce.25.11
21. Eyring, V., Bony, S., Meehl, G.A., Senior, C.A., Stevens, B., Stouffer, R.J., Taylor, K.E. Overview of the Coupled Model Intercomparison Project Phase 6 (CMIP6) experimental design and organization. Geoscientific Model Development. 2016. 9(5). Pp. 1937–1958. DOI: 10.5194/gmd-9-1937-2016
22. Preacher, K.J., Hayes, A.F. SPSS and SAS procedures for estimating indirect effects in simple mediation models. Behavior Research Methods, Instruments, and Computers. 2004. 36(4). Pp. 717–731. DOI: 10.3758/BF03206
23. Baus, R.L., Stires, N.R. Mechanistic-Empirical Pavement Design Guide Implementation. The South Carolina Department of Transportation and the Federal Highway Administration. 2010.
24. Fediuk, R.S., Mochalov, A.V., Bituev, A.V., Zayakhanov, M.E. Structuring Behavior of Composite Materials Based on Cement, Limestone, and Acidic Ash. Inorganic Materials. 2019. 55(10). Pp. 1079–1085. DOI: 10.1134/S0020168519100042

25. Fediuk, R., Smoliakov, A., Muraviov, A. Mechanical Properties of Fiber-Reinforced Concrete Using Composite Binders. Advances in Materials Science and Engineering. 2017. DOI: 10.1155/2017/2316347
26. Zhao, Q., Cheng, P., Wang, J., Wei, Y.U. Damage prediction model for concrete pavements in seasonally frozen regions. Magazine of Civil Engineering. 2018. 84(8). DOI: 10.18720/MCE.84.6
27. Zhao, Q., Zhang, H., Fediuk, R.S., Wang, J., Fu, Q. Freeze-thaw damage model for cement pavements in seasonal frost regions. Magazine of Civil Engineering. 2021. 104(4). DOI: 10.34910/MCE.104.6

Information about authors:

***Lina Zhang**, PhD*
ORCID: https://orcid.org/0000-0002-2024-3806
E-mail: 53860470@qq.com

Dongpo He
ORCID: https://orcid.org/0000-0003-2427-1086
E-mail: hdp@nefu.edu.cn

***Qianqian Zhao,** PhD*
ORCID: https://orcid.org/0000-0002-0209-4181
E-mail: 492954791@qq.com

Received 29.09.2020. Approved after reviewing 21.07.2021. Accepted 12.08.2021.

Magazine of Civil Engineering. 2022. 112(4). Article No. 11206

Magazine of Civil Engineering

ISSN 2712-8172

journal homepage: http://engstroy.spbstu.ru/

Research article

UDC 69.04

DOI: 10.34910/MCE.112.6

The shear behavior of anchored groove RC beams

R. Al-Rousan

Jordan University of Science and Technology, Irbid, Jordan

rzalrousan@just.edu.jo

Keywords: reinforced concrete, anchored, shear strength, fiber reinforced polymer, experimental

Abstract. The purpose of this research is to find an effectual technique to anchor reinforced concrete (RC) beams that are strengthened with fiber-reinforced polymers (FRP) composites. Eighteen reinforced-with-CFRP beams were designed. The specimens were split into three groups consisting of: 1) eight externally-reinforced-by-CFRP beams, with no anchoring grooves; 2) eight beams similar to the first group, but with anchoring grooves; 3) and control beams, which were left without anchoring. In order to explore their behavior, all of the beam specimens underwent a four-point bending, and were compared to the control beams. The study's focus was on exploring the relationship between the specimens' modes of failure and their displacements due to the applied loads. The obtained results showed that the anchoring technique had a great effectiveness; whereas, the specimens with CFRP and anchor encountered a failure in the form of a separation in the concrete cover, unlike the un-anchored ones, which failed due to premature de-bonding. The study showed that the anchoring grooves had changed the mode of failure to a safer one. The anchoring technique enhanced the capacity of carrying the load, and reduced, to different extents, the mid-span deflection. In addition, the study found that reinforcing the beams by CFRP composites had enhanced the shear capacity of the area of anchorage, leading to an enhancement in the systematic efficiency of anchoring. Overall, the study concluded that the performance of the specimens was highly improved by utilizing the CFRP composite combined with anchored grooves. For much improved RC structural designs, it is of utmost importance to further develop the anchored groove technique to prevent, rather than delay, unpredictable de-bonding of CFRP.

Funding: The author gratefully acknowledges the financial support from Deanship of Scientific Research at Jordan University of Science and Technology under Grant number 2019/507.

Citation: Al-Rousan, R. The shear behavior of anchored groove RC beams. Magazine of Civil Engineering. 2022. 112(4). Article No. 11206. DOI: 10.34910/MCE.112.6

1. Introduction

As it is well-known, the externally-bonded fiber reinforced polymer (FRP) materials are used to repair concrete elements, and enhance their shear and flexure capacities. The beams have been subjected, frequently, to failure in de-bonding, prematurely. Therefore, there has to be a way to strengthen the FRP-concrete bond to delay, or even prevent, the de-bonding issue. The mechanical anchorage technique has been introduced to solve the threat of ill-timed de-bonding, and further strengthen the plain FRP reinforcements. The anchorage technique, although proven to be efficient, still suffers the lack of knowledge and experience among the designers and engineers. Therefore, the anchorage method needs to be further researched, experimentally and numerically, to be more familiar with it, and expand its usages.

A number of researchers reported that it had been so common for the beams, strengthened by externally-bonded FRP, to encounter an ill-time de-bonding failure mode in the FRP-concrete bond. This type of failure has constrained the usages of the FRP reinforcements [1–9]. The FRP external strengthening are most commonly known to be exposed to fail due to the peeling at the end of the FRP plate and mid-span de-bonding. The plate peeling mode of failure results from the shear stresses' conveyance from the reinforcement material to concrete. As a result, a concrete layer is detached from the reinforcing FRP material, leaving an amount of hanging concrete ranging from few millimeters to the entire concrete cover. It is worth mentioning that the discontinuity of the beam's sectional geometry, at the end of the plate, is the main cause of the shear stresses. This failure mode is brittle; and it has been noticed to take place, mostly, in the beams that are equipped with short plates [10]. As for the mid-span de-bonding, it is created by two causes: the conveyance of shear stresses to the concrete from the plate of FRP; and it begins to emerge of flexure crack close to the area of the load concentration, in the zone of the extreme bending capacity. The generation of the shear stresses is due to the inclination of the plate strain, consequential from deviations in the moment diagram contiguous to the steel reinforcement yielding in tension side and the concentrated load. The mid-span de-bonding failure mode is ductile, unlike the other type. The reason of this is that the beam’s behavior is improved in terms of tensile steel yielding, which permits higher deflections [11].

Anchoring the externally-bonded FRP materials, in RC elements, is vital for the optimization of fiber utilization before de-bonding, prematurely. Several researches have been conducted to explore the effectiveness of the anchorage devices in the strengthening of FRP [12–14], and the mechanical anchorage systems [15-23]. The previous studies introduced four methods of anchoring: (i) fasteners of metallic [32–33]; (ii) anchored FRP [25–26]; (iii) FRP composites [27]; (iv) metal plates with nails [28], (v) anchored steel bolted plate [29]; and (vi) Continuous Reinforcement Embedded at Ends (CREatE) [30].

Anchorage systems have shown a great success in delaying, or even avoiding, the de-bonding failure, converting this type of failure, which is brittle, to a less serious one. As a result, it enhances the efficiency of the method of reinforcement using FRP.

This study has been conducted aiming to find an effective, reliable mechanical anchorage technique to strengthen the FRP-reinforced beams. Based on the analysis of the previous researches conducted in this regard, a novel mechanical anchorage method has been introduced, in this work, to treat the de-bonding issue. For the purposes of this study, the structural behavior has been evaluated, experimentally, study on: 8 un-anchored beams strengthened with externally-bonded CFRP; another 8 beams that are strengthened with a combination of externally-bonded CFRP and anchoring grooves; while, lastly, 2 beams were left unanchored, as control beams.

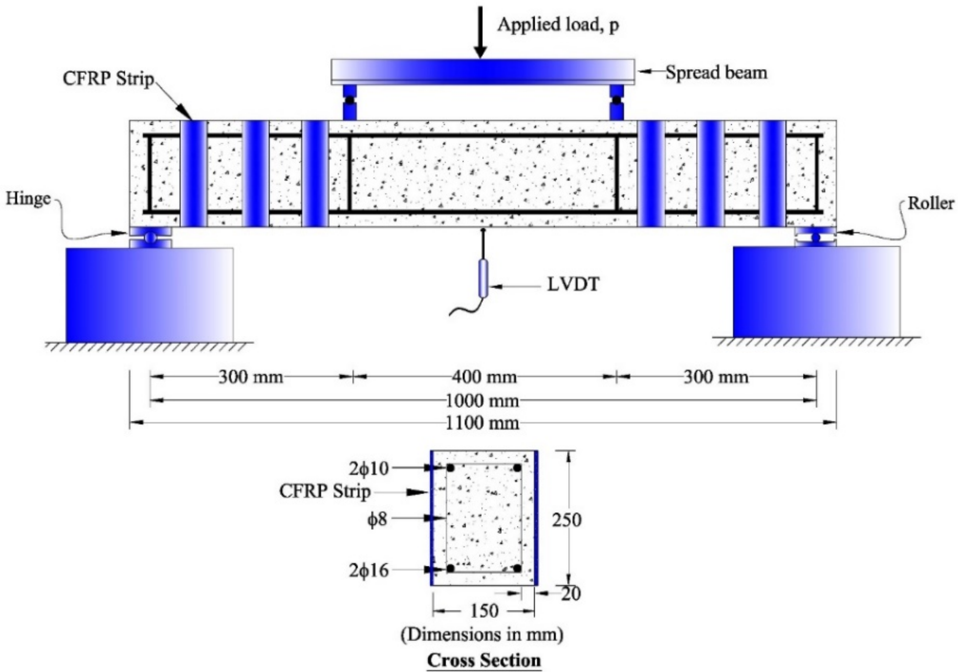

Figure 1. Setup and reinforcement details of the beams.

Table 1. The details of failure of tested shear beams.

Specimen	CFRP Configuration	P_u, kN	Δ_u, mm	ε_f, με	ε_{CFRP}
SB0	RC beams was unanchored and left as a control	55.7	4.7	---	---
SB1-1S	RC beams external strengthened with 1 Strip of FRP without anchored groove technique	68.4	5.3	5132	$0.31\varepsilon_{fu}$
SB1-2S	RC beams external strengthened with 2 Strips of FRP without anchored groove technique	81.1	5.6	5416	$0.32\varepsilon_{fu}$
SB1-3S	RC beams external strengthened with 3 Strips of FRP without anchored groove technique	95.0	6.0	5727	$0.34\varepsilon_{fu}$
SB1-4S	RC beams external strengthened with 4 Strips of FRP without anchored groove technique	108.5	6.2	5986	$0.36\varepsilon_{fu}$
SB2-1S-G	RC beams external strengthened with 1 Strip of FRP with anchored groove technique	88.0	5.8	6361	$0.38\varepsilon_{fu}$
SB2-2S- G	RC beams external strengthened with 2 Strips of FRP with anchored groove technique	108.5	6.1	6765	$0.41\varepsilon_{fu}$
SB2-3S- G	RC beams external strengthened with 3 Strips of FRP with anchored groove technique	132.5	6.5	7066	$0.42\varepsilon_{fu}$
SB2-4S- G	RC beams external strengthened with 4 Strips of FRP with anchored groove technique	158.5	7.0	7538	$0.45\varepsilon_{fu}$

Note: T is temperature, P_u is ultimate load, Δ_u is ultimate deflection, ε_f is CFRP strain, ε_{CFRP} is the strain in CFRP strips and ε_{fu} is the ultimate strain in CFRP strips of 16700 με.

2. Method

2.1. Experimental Work Review

Eighteen beam specimens (2 as control, 8 strengthened with FRP with no grooves, and 8 strengthened with FRP and grooves) were built and experimented, as simply supported under four points' loading, as explicated in Fig. 1. All of the specimens were dimensioned as: 1100 mm long and 150×250 mm in cross-section. The study parameters were: the number of CFRP strips (1, 2, 3, or 4), and the existence of anchored grooves (yes, no). The mid-section of the CFRP sheets along with the both ends of the grooved specimens were anchored, perpendicularly, with 50 mm-long, 150 mm-wide grooves filled with epoxy, as illustrated in Table 1. For the ease of reference, the specimens' designations and data are listed, in brief, in Table 1; and depicted in Fig. 1.

2.2. Mix design

The concrete mixture, Table 2, consisted of the following ingredients (percentage by weight): water (0.61); Ordinary Portland cement (Type I) (1.00); Coarse aggregates (Crushed limestone) (2.98), with a maximum size of 12.5 mm, an absorption ratio of 2.3 %, and a specific gravity of 2.62; fine aggregates (2.62) with fineness modulus of 2.69, an absorption ratio of 1.9 %, and specific gravity of 2.65. To enhance the concrete mix's efficiency and produce a 50 mm-slump, a superplasticizer was added as a percent of the cement weight was.

Table 2. Design proportions for concrete mix.

Ingredient	Quantity (kg/m^3)
Water	158
Cement	269
w/c	0.40
Super- plasticizer	8
Fine aggregate	834
Coarse aggregate	891

The specimens casting procedures were as follows: to begin with, the internal surface of the 0.15 m^3-in-capacity tilting drum mixer was soaked with water. Then, the coarse aggregates with some of the water were added while the mixer was turning. The next step was to add, gradually, to the mix each of the cement, water, in addition to the fine aggregates. The later step was to add the super-plasticizer with the remained used water to the concrete mixture. Lastly, all the added components had been mixed for five minutes before was poured into molds, made of wood with inner dimensions of (150×250×1100 mm). Finally, the mixture is compacted with an electrical vibrator. Twenty-four hours post casting, the whole beams were removed from the molds, and-then-cured in lime-saturated water tank for 28 days. At age of 28 days, the cylinders' average value of the compressive strength was 25.0 MPa, while their tensile strength was 3.0 MPa.

2.3. Bonding of CFRP sheets to the concrete beams

As mentioned in the previous section, the test beams had been molded for 24 hours before they were casted and cured, for 28 days, in a lime-saturated water tank. Grooves, 5 mm wide and 50 mm long, were, then, drilled in the surfaces of the prepared beams, at the end and the middle of bonded area. Later, the drilled grooves were completely cleaned, utilizing a vacuum cleaner and a volatile liquid, aiming to get a well-dried surface for better and stronger adhesion (Fig. 2). Then, a steel wire cup brush was used to brush the to-be-bonded area, and make it rougher. This step was done to ensure having leveled contact area between the surface of the concrete and the CFRP material (Fig. 2). The dust and lose particles, resulted from the brushing, were cleaned up, using air vacuum cleaner. Then, the to-be-bonded area was marked, while the remaining area was plastered with a tape, to keep it away from epoxy (Fig. 2). For the study purposes, the CFRP sheets were cut into various lengths, with a standard width of 50 mm. The following step was to prepare the adhesive epoxy material by, slowly, mixing the two the compounds of epoxy (i.e.: part A and B) in a low-speed electric drill for at least 3 minutes, to ensure the homogeneity of the epoxy. Later, the first layer of the prepared epoxy was placed, equally, onto the marked area of bonding; and, then, the CFRP composite sheet (thickness of 0.166 mm, the tensile strength of 4900 MPa, elastic modulus of 230 GPa, and elongation at break of 2.1 %) was put on the epoxy, and was rolled over, with a plastic roller, to kick out any entrapped air bubbles. Finally, the epoxy second layer was placed on the CFRP strips so as to ensure the well epoxy distribution (Fig. 2).

Marking the area of CFRP sheets bonded using plastering tape

Drilling the grooves

Applying the first layer of epoxy onto CFRP sheets surface

Applying the two layers of epoxy onto CFRP sheets surface

Figure 2. Attachment of CFRP strips.

2.4. Testing Setup

All of the beam specimens were simply supported span of 1000 mm (Fig. 1) and experimented under four-point loading, with. The two supports included a hinge and a roller. The points of loading were a steel type to avoid deformation at ultimate load stages. A hydraulic testing machine was used to applied the load with a displacement loading rate of 0.1 mm/sec. To be able to take the values of the mid-span deflections, at the beams' bottom side, a vertical linear variable displacement transducer (LVDT) was utilized (Fig. 1). In addition, a strain gauge was installed to record the tensile strain of the CFRP material. The data acquisition system was utilized to plot the obtained results on load-deflection curves and the CFRP strain. Whereas, the patterns of the cracking and the modes of failure were attained visually.

3. Results and Discussion

3.1. Failure Mode

Fig. 3 and 4 illustrate the modes of failure encountered by the whole beam specimens, including the control beams. The modes of failure were deliberately set to be with inclined planes, and took place inside the shear span. This was intended for the ease of evaluating the role of the CFRP strips in enhancing the concrete's shear capacity.

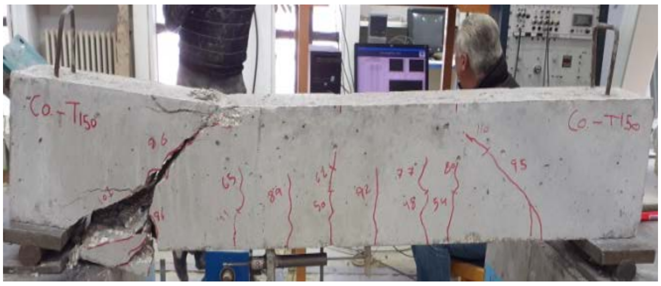

Figure 3. Typical failure mode of control beams.

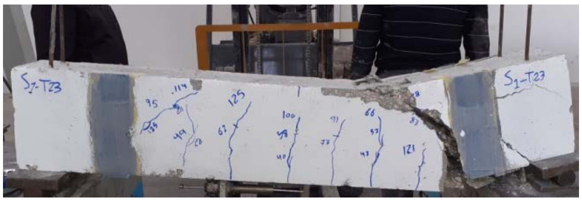


(a-1) 1 CFRP strip **(a-2) 2 CFRP strips**

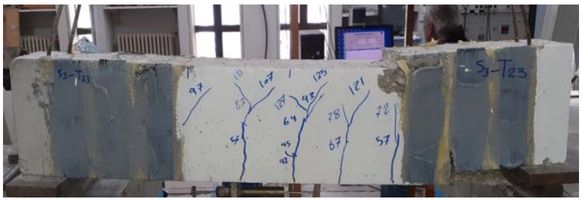


(a-3) 3 CFRP strips **(a-4) 4 CFRP strips**

(a) Without grooves

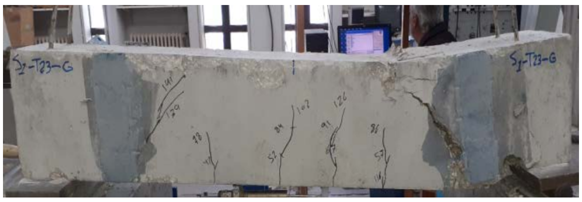


(b-1) 1 CFRP strip **(b-2) 2 CFRP strips**

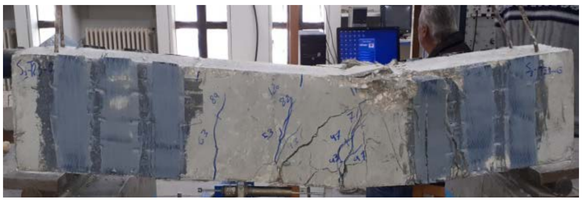


(b-3) 3 CFRP strips **(b-4) 4 CFRP strips**

(b) With grooves

Figure 4. Typical failure mode of strengthened beams.

The emergence of web-shear cracks began through the loading process. Moreover, when the load was raised, the web-shaped cracks lengths, widths, and number increased too. When the ultimate value of loading had been reached, an enormous number of web-shaped cracks emerged, followed by an abrupt crushing inside the shear span. It had been found that the strips of CFRP had a great role in the element's resistance to shear, resulting in a variation in the ultimate values of loads, at which concrete crushing took place. When a failure occurred, a considerable amount of shear-span splintered concrete was observed, occasionally. The failure in shear, usually, happens abruptly, with a big sound, resulting in the appearance of big inclined cracks. The usual place, at which the shear failure occurs, is at either ends of the beam; that is caused by either the post-deflection loading or a very light change in the beam. It has been found that the anchored specimen's shear span had less shear cracks than the control beam; while the internal core stayed almost unharmed. The reason of this is that the utilization of the CFRP strips with anchorage system shows a great success in alleviating the developed shear stresses and cracking.

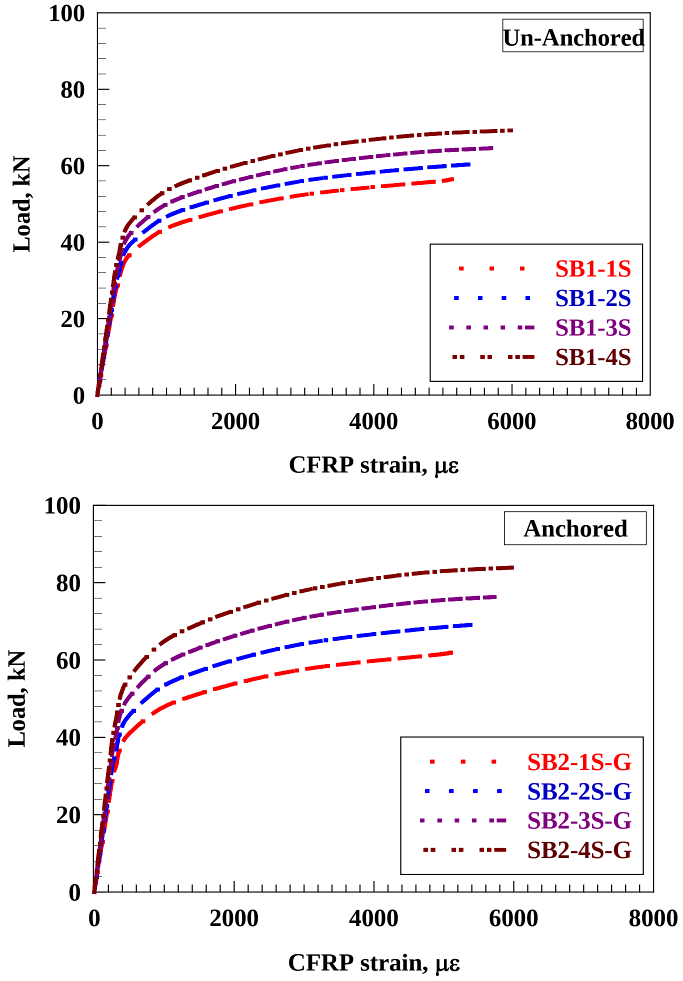

Figure 5. Typical load-CFRP strain curve.

3.2. CFRP strain

The typical curve that represents the relation between the load and the CFRP strain, for all of the tested beams, is illustrated in Fig. 5. Considering this graph, it is found that the initial appearance of in-concrete diagonal crack, resulted from the shear force, leads to developing tensile stresses in the CFRP material. In addition, it is noticed that the ultimate tensile stresses have appeared near the mid-section of the CFRP element, and crossed the diagonal cracks, close to the beam' cross-section mid-height point, as explicated in Fig. 6. It is, also, observed that all of the experimented specimens had a CFRP strain value less than 16400 με, as illustrated in Table 1. Referring to this table, Table 1, the number of CFRP strips has, greatly, affected the efficiency of the CFRP strips, in the beams without anchoring, as follows: 31 % of the CFRP' ultimate strain when one strip was installed, 32 % when using two strips, 34 % when three strips were used, and 36 % when 4 strips. On the other side, the anchored specimens showed the following ratios: 38 % of the CFRP's ultimate strain when using one strip, 41 % when using 2 strips, 42 % when 3 strips were used, and 45 % when using 4 strips. The shown percentages indicated that the strains of the anchored beams improved by 122 % of the un-anchored ones.

The strains of the CFRP strips do not exist before the appearance of diagonal crack. When the shear strength of concrete is exceeded by the shear strength, diagonal shear cracks emerge in the shear span, while the CFRP strain keeps rising, in a rapid rate, until failure, as illustrated in Fig. 5. Also, it has been noticed that the more the area of the bonded surface, the higher the rate of the increase in the CFRP's strain. Overall, the obtained results show that grooving 4 strips of CFRP has had the best effect on the beam's behavior.

Table 3. Characteristics of load deflection behavior.

Specimen	Elastic stiffness (kN/mm)	Toughness (kN.mm^2)	SF	DF	PF	SF
SB0	12.5	139	1.00	1.00	1.00	1.00
SB1-1S	14.5	186	1.07	1.12	1.19	1.07
SB1-2S	16.5	223	1.14	1.17	1.34	1.14
SB1-3S	18.5	269	1.22	1.27	1.55	1.22
SB1-4S	20.0	301	1.31	1.30	1.71	1.31
SB2-1S-G	16.0	230	1.17	1.22	1.44	1.17
SB2-2S- G	20.0	282	1.31	1.28	1.67	1.31
SB2-3S- G	24.0	347	1.44	1.37	1.97	1.44
SB2-4S- G	27.5	433	1.59	1.48	2.35	1.59

Note: SF is strength factor, DF is ductility factor, PF is performance factor = SFxDF, STF is stiffness factor

3.3. Load-deflection behavior

Table 3 illustrates the load vs. the mid-span deflection responses and the characteristics (stiffness and roughness) of the three groups of the specimens, i.e.: the un-anchored, the anchored, and the control. The initial stiffness ($k = P/\delta$) is demarcated as “the slope of linear elastic portion of load-deflection response”; whereas the toughness is defined as “the area underneath the load-deflection response until ultimate load capacity”. The load-deflection curves, Fig. 6 have three sections: a) the linear section, from the starting point till the emergence of the first flexural crack; b) the transitional section, extends from the end of the previous section till the emergence of the diagonal shear crack; and c) the after-cracking section, up to ultimate beam capacity. Fig. 6 and Table 3 show, explicitly, that the anchoring method has impacted the load-deflection characteristics curve, in terms of: ultimate deflection, ultimate load, stiffness, and toughness. In addition, it has been found that the anchored specimens performed better with the increase in the CFRP bonded area.

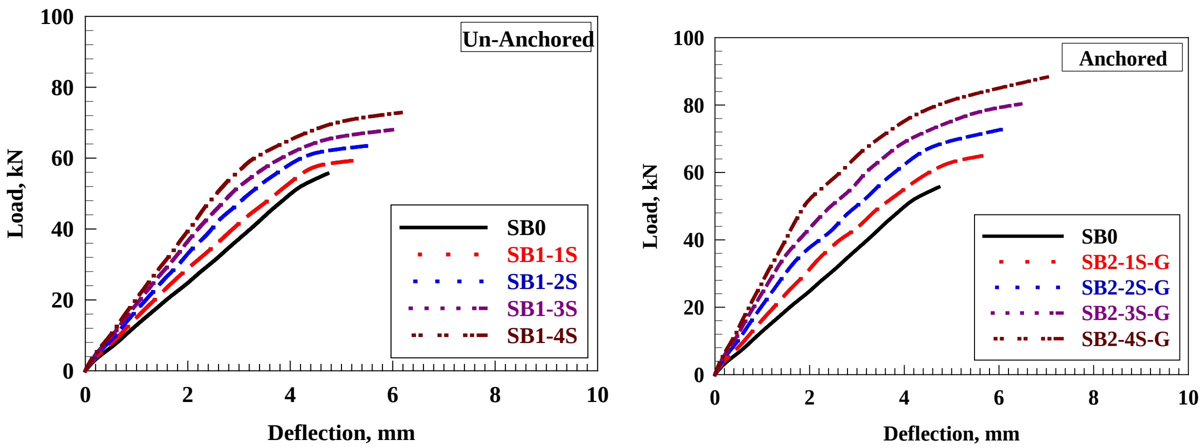

Figure 6. Load-deflection curves for the tested beam.

3.4. Ultimate load capacity and corresponding deflection

Upon evaluating the specimens’ load capacity and the resulting deflection, it has been found that the structures performed very well. In the reinforced members, the deflection is associated with the structural serviceability; where the ultimate load capacity can be connected to ultimate load limit states, as seen in Table 3. The percentages of the load capacity are determined by dividing the ultimate load capacity of the strengthened beam by the ultimate load capacity of the control beam; while the deflection can have determined by dividing the strengthened beam's ultimate deflection by the load capacity of the control beam, as explicated in Fig. 7. The term (deflection) is an indicator of the reinforced beam's capability of enduring deformations, without the occurrence of failure. The deflection percentage can be specified by dividing the strengthened beam's ultimate deflection by the ultimate deflection of the control beam (undamaged beam), as explicated in Fig. 8.

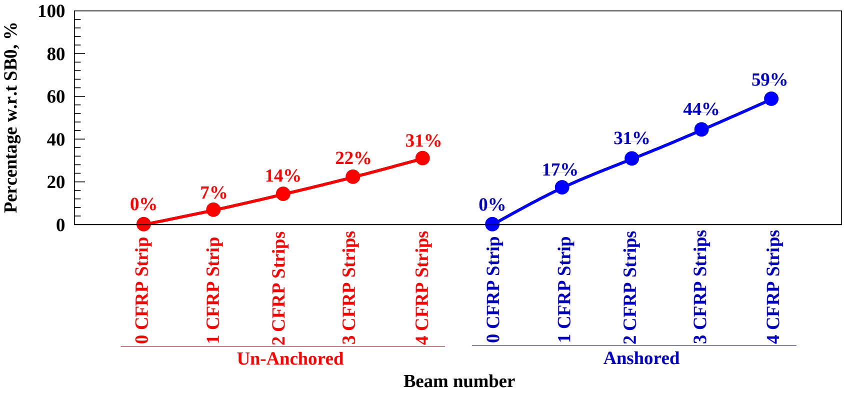

Figure 7. Ultimate load capacity enhancement percentage with respect to control beam.

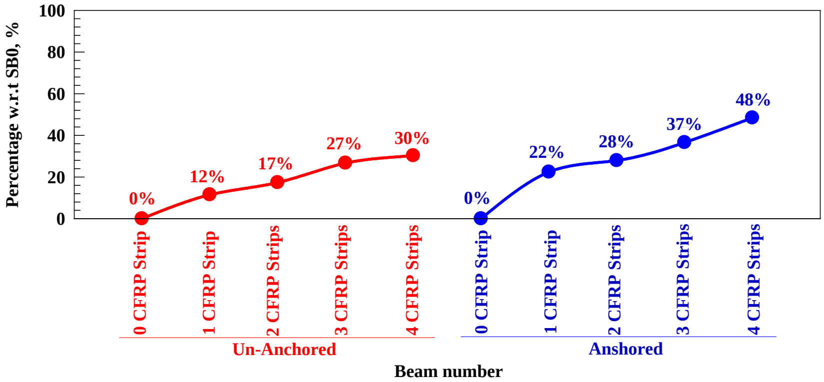

Figure 8. Ultimate deflection enhancement percentage with respect to control beam.

3.5. Elastic stiffness

The elastic stiffness determines the crystal's response when exposed to external forces, e.g.: stress or strain. Also, it is a clear indicator of the bonding's quality and stability, mechanically and structurally. In the load vs. deflection curve, the elastic stiffness is represented by the slope of the pre-cracking section. For the ease of comparison, every strengthened-beam's elastic stiffness was normalized with respect to the un-strengthened control beam, as illustrated in Fig. 9. It has been found that the more the CFRP strips, the higher the percentage of the elastic stiffness. The percentages of the un-anchored beams' elastic stiffness (Fig. 10) are: 17 % when 1 strip of CFRP is used, 33 % for 2 strips, 47 % for 3 strips, and 59 % for 4 strips; showing an enhancement average of 39 %. As for the reinforced beams with anchorage, the ratios of the elastic stiffness (Fig. 9) have reached to: 26 % upon using 1 strip of CFRP, 61 % when 2 strips, 91 % with 3 strips, and 117 % with 4 strips, with an enhancement average of 74 %. The enhancement in the anchored beams' stiffness is 1.90 times better than those without anchoring.

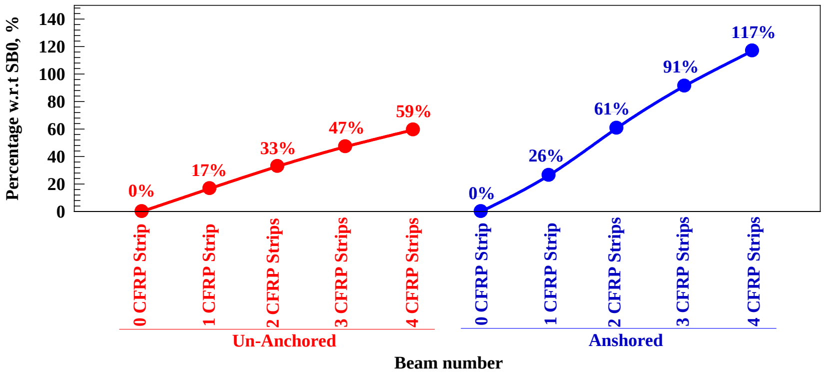

Figure 9. Stiffness enhancement percentage with respect to control beam.

3.6. Toughness

Toughness indicates the material's capability of absorbing energy and deforming, plastically, without being broken. It can be defined as the material's energy absorption (per unit volume) before breaking down. Toughness can be mathematically found by calculating the total area beneath the load vs. deflection curve.

It must be noticed that each strengthened-by-CFRP beam's toughness has been normalized with respect to the control beams, as explicated in Fig. 10. It has been shown in Fig. 10 that increasing the strips of CFRP results in raising the beam's toughness, considerably. For the beams with no anchoring, the toughness (Fig. 10) has reached to: 34 % when using 1 CFRP strip, 61 % when 2 strips are used, 94 % when using 3 strips, and 117% when using 4 strips, with an enhancement of 77 %. As for the beams with anchorage, the percentages of toughness (Fig. 10) has reached to: 66 % when using 1 strip of CFRP, 103 % when using 2 strips, 150 % when using 3 strips, and 212 % when using 4 strips, with an enhancement of 133 %. This result shows that toughness percentage of the anchored specimens is 1.73 times more than the un-anchored ones.

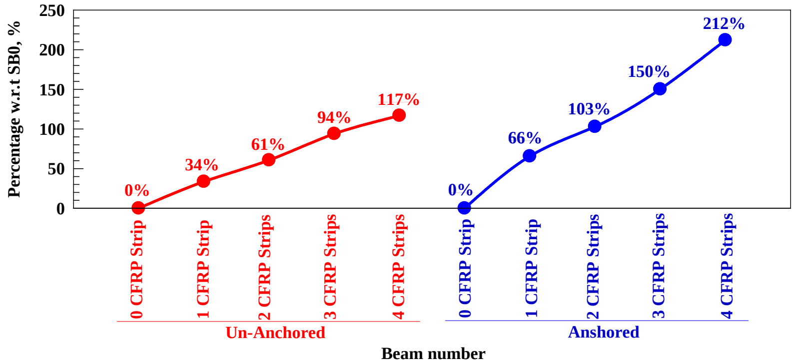

Figure 10. Toughness enhancement percentage with respect to control beam.

3.7. Performance of Tested Beams

To explore the impact of the CFRP material on the reinforced RC beams, the following factors have been evaluated: the strength factor (SF), the deformability factor (DF), and the performance factor (PF), making sure that the beams are normalized with respect to the control beams. All of the factors act together to for the total performance of a structure, as illustrated in Fig. 11. As it is explicated in Fig. 11, increasing the area of bonding, results in raising the whole factors (DF, SF, and PF). Further, raising the area of bonding results in a significant improvement in the beam’s performance, close to control beams, and prevented brittle shear failure. The anchored strengthened-with-CFRP beams exhibited much better performance than the un-anchored ones. Thus, it can be concluded that utilizing the CFRP sheets to reinforcing the beams has proven to be much more effective and showed remarkable results than the CFRP strips on the web.

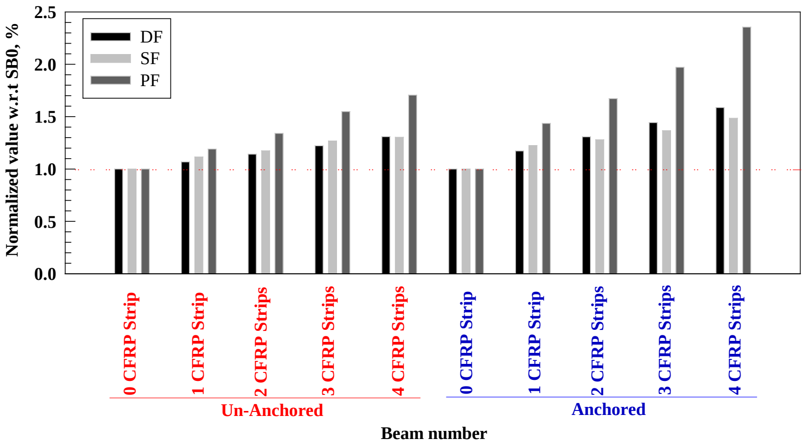

Figure 11. Normalized performance characteristic factors.

3.8. Profitability Index of the Number of CFRP Strips

Table 5 demonstrates: the concrete shear strength (V_c), CFRP shear strength (V_f), and the ultimate load capacity, obtained from experimenting RC beam specimens, that were reinforced with different methods- using CFRP composites. In addition, Table 4 shows that adding more strips of CFRP or enlarging the bonding surface has resulted in an increase in the (V_f). The indices of profitability had to be calculated to be able to assess the effectiveness of several methods of reinforcement using CFRP materials, regarding the consumed quantity of CFRP. It must be mentioned that the profitability index expresses the ratio of CFRP contribution in shear within the shear span to the total CFRP bonded area. Table 4 demonstrates the values of the profitability indices, for a number of reinforcing techniques. From Table 4, it is shown that the un-anchored beams have a profitability index of (in MPa): 1.15 when using 1 strip of CFRP, 1.10 when using 2 strips, 1.05 for 3 strips, and 1.00 for 4 strips. On the other side, the anchored beams have the following values of profitability index (in MPa): 2.56 using 1 strip of CFRP, 2.28 using 2 strips, 2.19 using 3 strips, and 2.18 using 4 strips. This shows that the anchored beams' index of profitability is 2.2 times more than the un-anchored ones.

Table 4. Profitability index of CFRP strips.

Beam number	V_c, kN	V_f, kN	V_u, kN	V_f/A_f, MPa
SB0	55.7	0.0	55.7	---
SB1-1S	55.7	3.8	59.4	1.15
SB1-2S	55.7	7.9	63.6	1.10
SB1-3S	55.7	12.4	68.0	1.05
SB1-4S	55.7	17.2	72.9	1.00
SB2-1S-G	55.7	9.6	65.3	2.56
SB2-2S- G	55.7	17.1	72.8	2.28
SB2-3S- G	55.7	24.7	80.3	2.19
SB2-4S- G	55.7	32.7	88.3	2.18

Note: V_c is the concrete shear strength, V_f is the CFRP shear strength, A_f is the total CFRP bonded area

3.9. Comparison of experimental results with the ACI model

or the sake of comparison, the obtained results have been compared with ACI model [1]. The guidance for the general design was attained from the experimental data, and they were solely valid for the external FRP reinforcement. Fig. 12 depicts the predicted values of the ACI model ($V_{f,\ experimental}/V_{f,ACI}$ [1]), and a comparison among them. It must be noted that the ACI model is adjusted to use for CFRP; therefore, extreme caution must be taken when using this model for other composites, as illustrated in Fig. 12. The overall ACI model's [1] predictions have been overvalued, with a mean $V_{f,\ experimental}/V_{f,ACI}$ value of 1.11 and a coefficient of variation (COV) of 26 %. It must be noted, also, that the obtained values, from the ACI model, are overrated, and based on the values of parameters extracted from the experimental data of the strengthened-by-FRP-laminates beams. However, the ACI model is not valid for all case. Further, the ACI model has a, vastly, broad range of experimental/theoretical failure load ratios from 0.80 to 1.46, as explicated in Fig. 12.

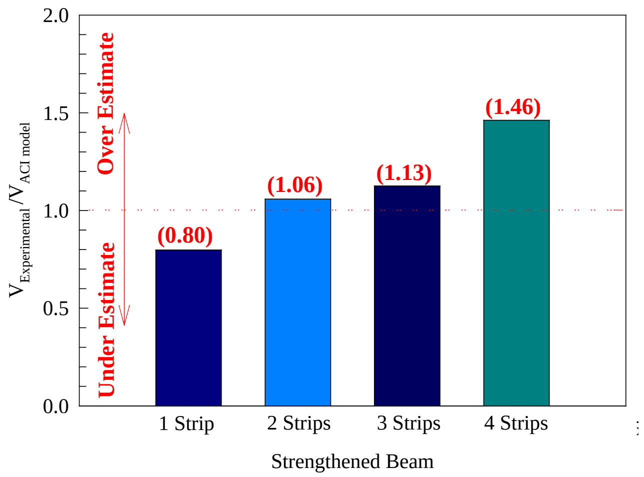

Figure 12. The ratio of experimental FRP shear force to calculated one using ACI model [1].

4. Conclusions

1. The ill-timed de-bonding issue is frequently encountered by the unanchored strengthened-by-FRP beams; unlike the anchored ones, which have a less serious failure mode, which is concrete cover separation.

2. The technique of the anchored grooves converted the dangerous modes of failure, i.e.: separation of concrete cover or in-between-surfaces de-bonding, to a less serious mode. This has enhanced the performance quality of the traditional techniques of FRP-reinforcement.

3. The method of anchored grooves has proven a great efficiency in strengthening RC beams because it enlarges the shear capacity of the anchorage region.

4. The anchored grooves method enhanced the RC beams' capacity of load-carrying, and minimized, considerably, the mid-span vertical deflection, compared with the control un-strengthened beam.

5. In contrast to the control beams, the anchored grooves method enhanced the RC beams': ultimate load capacity, stiffness, toughness; while it reduced the deflections. Also, this method availed an improved structural performance factor.

6. All of the predictions of the ACI model [1] have been overrated, where the mean value reaching 1.11, and the coefficient of variation (COV) of 26 %.

References

1. ACI Committee 440. Design and Construction of Externally Bonded FRP Systems for strengthening Concrete Structures. *ACI440.2R-02. 2002. American Concrete Institute, Farmington Hills, Mich.: 45 pp. DOI: 10.1061/40753(171)159. ISBN: 9780870312854
2. Wenwei, W., Guo, L. Experimental study and analysis of RC beams strengthened with CFRP laminates under sustained load. International Journal of Solids and Structures. 2006. 43(1). Pp. 1372–1387. DOI: 10.1016/j.ijsolstr.2005.03.076
3. Aram, M.R., Czaderski, C., Motavalli, M. Debonding failure modes of flexural FRP-strengthened RC beams. Composites: Part B. 2008. 39(1). Pp. 826–841. DOI: 10.1016/j.compositesb.2007.10.006
4. Thomsen, H., Spacone, E., Limkatanyu, S., Camata, G. Failure Mode Analyses of Reinforced Concrete Beams Strengthened in Flexure with Externally Bonded Fiber-Reinforced Polymers. Journal of Structural Engineering-ASCE. 2004. 2(123). Pp. 1090–0268. DOI: 10.1061/(ASCE)1090-0268(2004)8:2(123)
5. El-Ghandour A. Experimental and analytical investigation of CFRP flexural and shear strengthening efficiencies of RC beams. Construction and Building Materials. 2011. 25(1). Pp. 1419–1429. DOI: 10.1016/j.conbuildmat.2010.09.001
6. Rajai, Z. Al-Rousan, Mohammad, F. AL-Tahat. Consequence of surface preparation techniques on the bond behavior between concrete and CFRP composites. Construction and Building Materials. 2019. 212(1). Pp. 362–374. DOI: 10.1016/j.conbuild-mat.2019.03.299
7. Pham, H., Al-Mahaidi, R. Experimental investigation into flexural retrofitting of reinforced concrete bridge beams using FRP composites. Composite Structures. 2004. 66(1). Pp. 617–625. DOI: 10.1016/j.compstruct.2004.05.010
8. Al-Rousan, R. Behavior of CFRP Strengthened Columns Damaged by Thermal Shock. Magazine of Civil Engineering. 2020. 5(97). Pp. 90–100. DOI: 10.18720/MCE.97.5
9. Al-Rousan, R. Behavior of strengthened concrete beams damaged by thermal shock. Magazine of Civil Engineering. 2020. 94(2). Pp. 93–107. DOI: 10.18720/MCE.94.2
10. Travush, V.I., Konin, D.V., Krylov, A.S. Strength of reinforced concrete beams of high-performance concrete and fiber reinforced concrete. Magazine of Civil Engineering. 2018. No. 77(1). Pp. 90–100. DOI: 10.18720/MCE.77.8
11. Al-Rousan, R., Abo-Msamh, Isra'a. Bending and Torsion Behaviour of CFRP Strengthened RC Beams. Magazine of Civil Engineering. 2019. 92(8). Pp. 62–71. DOI: 10.18720/MCE.92.8
12. Mohammad, A. Alhassan, Rajai, Z. Al-Rousan, Ahmad M. Abu-Elhija. Anchoring holes configured to enhance the bond-slip behavior between CFRP composites and concrete. Construction and Building Materials. 2020. 250(1). Pp. 118905. DOI: 10.1016/j.conbuildmat.2020.118905
13. Ayman, S. Mosallam, Swagata Banerjee. Shear enhancement of reinforced concrete beams strengthened with FRP composite laminates. Composites Part B Engineering. 2007. 38(5-6). Pp. 781–793. DOI: 10.1016/j.compositesb.2006.10.002
14. Anil, O., Belgin, C.M. Anchorages effects on CFRP-to-concrete bond Strength. Journal of Reinforced Plastic and Composites. 2010. 29(1). Pp. 539–557. DOI: 10.1177/0731684408100259
15. Diab, H., Wub, Z., Iwashita, K. Short and long-term bond performance of prestressed FRP sheet anchorages. Engineering Structures. 2009. 31(1). Pp. 1241–1249. DOI: 10.1016/j.engstruct.2009.01.021
16. Smith, S.T., Hua, S., Kim, S.J., Seracino, R. FRP-strengthened RC slabs anchored with FRP anchors. Engineering Structures. 2011. 33(1). Pp. 1075–1087. DOI: 10.1016/j.engstruct.2010.11.018
17. El Maaddawy, T., Soudki, K. Strengthening of reinforced concrete slabs with mechanically-anchored unbonded FRP system. Construction and Building Materials. 2008. 22(1). Pp. 444–455. DOI: 10.1016/j.conbuildmat.2007.07.022
18. Ceroni, F., Pecce, M., Matthys, S., Taerwe, L. Debonding strength and anchorage devices for reinforced concrete elements strengthened with FRP sheets. Composites: Part B. 2008. 39(1). Pp. 429–441. DOI: 10.1016/j.compositesb.2007.05.002
19. Bank, L., Arora, D. Analysis of RC beams strengthened with mechanically fastened FRP (MF-FRP) strips. Composite Structures. 2007. 79(1). Pp. 180–191. DOI: 10.1016/j.compstruct.2005.12.001
20. Al-Mahmoud, F., Castel, A., François, R., Tourneur, C. Anchorage and tension-stiffening effect between near-surface-mounted CFRP rods and concrete. Cement and Concrete Composites. 2011. 33(1). Pp. 346–352. DOI: 10.1016/j.cemconcomp.20-10.10.016
21. Kalfat, R., Al-Mahaidi, R, Smith, S.T. Anchorage Devices used to improve the Performance of Reinforced Concrete Beams Retrofitted with FRP Composites: A-State-of-the-Art-Review. Journal of Composites for Construction. 2013. 17(1). Pp. 14–33. DOI: 10.1061/(ASCE)CC.1943-5614.0000276
22. Hugo, C. Biscaia, Rui Micaelo, João Teixeira, Carlos Chastre. Numerical analysis of FRP anchorage zones with variable width. Composites Part B: Engineering. 2014. 67(1). Pp. 410–426. DOI: 10.1016/j.compositesb.2014.07.031
23. Lamanna, A.J., Bank, L.C., Scott, D.W. Flexural Strengthening of Reinforced Concrete Beams Using Fasteners and Fiber-Reinforced Polymer Strips. ACI Structural Journal. 2001. 98(3). Pp. 368–676. DOI: 10.14359/10225
24. Spadea, G., Bencardino, F., Swamy, R.N. Structural behavior of composite RC beams with externally bonded CFRP. Journal of Composite Construction. 1998. 2(3). Pp.132–137. DOI: 10.1061/(ASCE)1090-0268(1998)2:3(132)

25. Lam, L., Teng, J.G. Strength of RC cantilever slabs bonded with GFRP strips. Journal of Composite Construction. 2001. 5(4). Pp. 221–227. DOI: 10.1061/(ASCE)1090-0268(2001)5:4(221)
26. Micelli, F., Rizzo, A., Galati, D. Anchorage of composite laminates in RC flexural beams. Structural Concrete. 2010. 11(3). Pp. 117–126. DOI: 10.1680/stco.2010.11.3.117
27. Wu, Y.F., Huang, Y. Hybrid bonding of FRP to reinforced concrete structures. Journal of Composite Construction. 2008. 12(3). Pp. 266–273. DOI: 10.1061/(ASCE)1090-0268(2008)12:3(266)
28. Biscaia, H.C., Chastre, C. Design method and verification of steel plate anchorages for FRP-to-concrete bonded interfaces. Composite Structures. 2018. 192(1). Pp. 52–66. DOI: 10.1016/j.compstruct.2018.02.062
29. Pellegrino, C., Modena, C. Flexural Strengthening of Real-Scale RC and PRC Beams with End-Anchored Pretensioned FRP Laminates. ACI Structural Journal. 2009. 106(3). Pp. 319–328. DOI: 10.14359/56496
30. Biscaia, H.C,. Chastre, C., Cruz, D., Franco, N. Flexural Strengthening of Old Timber Floors with Laminated Carbon Fiber–Reinforced Polymers. Journal of Composites for Construction. 2019. 21(1). Pp. 04016073. DOI: 10.1061/(ASCE)CC.1943-5614.0000731

Information about authors:

Rajai Al-Rousan, PhD
ORCID: https://orcid.org/0000-0001-6981-7420
E-mail: rzalrousan@just.edu.jo

Received 09.10.2020. Approved after reviewing 06.04.2021. Accepted 06.04.2021.

Magazine of Civil Engineering

ISSN 2712-8172

journal homepage: http://engstroy.spbstu.ru/

Research article

UDC 691

DOI: 10.34910/MCE.112.7

Mechanical properties of ceramic powder based geopolymer mortars

M. Kaya

Yozgat Bozok University, Yozgat, Turkey

✉ *mehmet.kaya@yobu.edu.tr*

Keywords: mechanical properties, mortar, geopolymer, ceramic powder, binder, optimization

Abstract. In this study, the properties of geopolymer mortars produced by activating ceramic powder with Sodium Hydroxide (NaOH) and Sodium Silicate (Na_2SiO_3) were investigated. Activator mixture was prepared by mixing NaOH containing 11 %, 13 % and 15 % sodium in proportion to the binder weight and Na_2SiO_3 in different proportions. The silicate modulus of the activator mixtures were set at ratios ranging from 0 to 0.3. Geopolymer samples were prepared by mixing ceramic powder with activator, water and sand in a standard cement mixer. After fresh mortar mixtures were placed in the molds, they were cured at 105 °C for 24 hours. The samples were taken out of the molds after curing. They were kept at room temperature for up to 28 days. Then, the samples underwent unit weight test, apparent porosity, water absorption ratio, ultrasound pulse velocity, flexural and compressive strength tests. As a result of the tests, compressive strength between 10.42 MPa and 41.53 MPa, flexural strength between 2.34 MPa and 10.38 MPa were determined. Optimum mixing ratio and strength values were determined.

Citation: Kaya, M. Mechanical properties of ceramic powder based geopolymer mortars. Magazine of Civil Engineering. 2022. 112(4). Article No. 11207. DOI: 10.34910/MCE.112.7

1. Introduction

The properties of the geopolymer such as mechanical strength, acid resistance, high temperature resistance, low shrinkage, low thermal conductivity and relatively low cost have attracted the attention of researchers in recent years [1–6]. With the production of geopolymer, the emission during traditional portland cement production is reduced by 70 %. The geopolymer is therefore known to be environmentally friendly [7]. Geopolymer concrete is considered as an alternative binder to conventional concrete in the construction industry due to its advantages such as low emission, energy saving, reduction of storage area problem, conservation of natural resources and relatively low cost [8]. In geopolymer production, industrial wastes such as fly ash [9], blast furnace slag [10], ceramic waste [11], palm oil clinker [12], rice husk ash [13] agricultural wastes and clay [14], kaloin [15] and lime-based natural materials are used as binders. For activation of the binders, NaOH, glass water [9], potassium hydroxide [16], potassium silicate [17] etc. activators are needed. Geopolymer synthesis is described as a simplified pathway such as dissolution of aluminosilicate precursor in alkali activator, final polycondensation of monomers, polymer network and solid state conversion [18].Variables such as binder type, binder amount, activator type, activator ratio, curing temperature, water/binder ratio are important in geopolymer strength. SiO_2/Na_2O ratio, known as silicate modulus (Ms), is important in gaining strength of the geopolymer. Increase of silicate module up to a certain value causes an increase in strength [19]. In recent years, ceramic powder or waste has also been used extensively in geopolymer production [11, 17, 20–22]. Ceramic is a building material widely used in the construction industry. A large amount of ceramic waste is generated during ceramic production and destruction. It is stated that ceramic production has reached 13.552 million m^2 as of 2017. However, it is reported that 1 m^2 of ceramics creates about 1.9 kg of waste, in which case 25.75 million tons of ceramic waste comes out [23]. Rapid development in the ceramic industry causes more waste and limits sustainable development as well as negative effects on the environment [24–26]. Ceramic waste also creates a storage problem by covering a large area [27]. For this reason, it is important to recycle ceramic powder by using it in geopolymer production. Ceramic powder used in geopolymer studies is primarily in the form of calcined clay as ceramic raw material [17]. The other method is obtained by grinding the waste ceramic into powder [11]. Activation of waste ceramics with alkalis by pulverizing is a common method, and studies with raw ceramic powder are limited. Huseien et al. [28] prepared mortar samples by activating mixtures of ceramic powder, fly ash and blast furnace slag with NaOH and $Na_2SİO_3$. In their studies examining the bond strength of the mixtures, it was determined that alkali activated mortars containing high amounts of ceramics and fly ash show good performance against acid attack [11]. Martin Kepperta et al. [20] stated that the geopolymers they produced using two different red-clay ceramic powders had satisfactory mechanical properties. Abdollahnejad et al. [29] produced steel fiber, PVA fiber and polypropylene fiber mortar samples by activating the ceramic powder and slag mixture with Na_2SiO_3. They found that the fiber addition improves the mechanical properties. Kovárˇík et al. [17] determined that the geopolymer samples produced by using metakaolin, potassium silicate ceramic aggregate have approximately 12 MPa flexural strength and 90 MPa compressive strength after 1000 °C temperature effect. Amin et al. [30] found that the geopolymeric bricks they produced using ceramic powder waste, slaked lime and NaOH increased the 28-day geopolymerization degree. Huseien et al. [31] exposed the samples produced by the activation of fly ash, furnace slag and high amount of waste ceramic powder to 900 °C high temperature, the samples containing 70 % waste ceramic powder 20 % blast furnace slag and 10 % fly ash have optimum resistance to high temperature. In another study, they produced alkali activated mortar using high amounts of ceramic powder, fly ash and blast furnace slag, and they found that with the increase in the amount of fly ash from 0 % to 40 %, the compressive strength increased and the resistance against acids and sulphates increased. They stated that drying shrinkage increased and freeze-thaw performance decreased with the increase of blast furnace slag in the mixture [28]. Shoaei et al. [32] the mortar samples they produced by activating the waste ceramic powder with a mixture of NaOH and Na_2SiO_3 cured at different temperatures. They determined the optimum curing temperature as 90 °C and the alkali solution/binder ratio as 0.6. They stated that 27.9 MPa compressive strength and 6.65 MPa flexural strength were achieved in samples of 28 days. In this study, physical and mechanical properties of geopolymer mortars produced by alkali activation of raw ceramic powder used in ceramic production were investigated. The aim of this study is to pioneer the studies for the production of geopolymer ceramics with higher strength than traditional tiles and ceramics by alkali activation of ceramic powder.

2. Materials and Methods

2.1. Materials

2.1.1. Ceramic powder

In this study, raw ceramic powder used in ceramic production was used. The chemical content of ceramic powder is given in Table 1.

Table 1. Chemical content of ceramic powder.

Compound	$SİO_2$	Al_2O_3	Fe_2O_3	CaO	MgO	SO_3	Na_2O	K_2O	P_2O_5
Mass %	54.58	22.02	0.91	8.89	0.21	0.05	0.21	0.81	0.26

The ceramic powder used in the study is shown in Fig. 1.

Figure 1. Ceramic powder used in the study.

The SEM (Scanning Electron Microscope) images of the ceramic powder is given in Fig. 2.

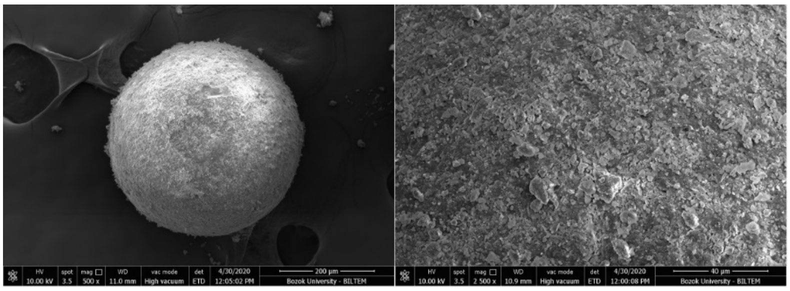

Figure 2. SEM images of ceramic powder.

The X Ray diffraction Analysis (XRD) of the ceramic powder is given in Fig. 3.

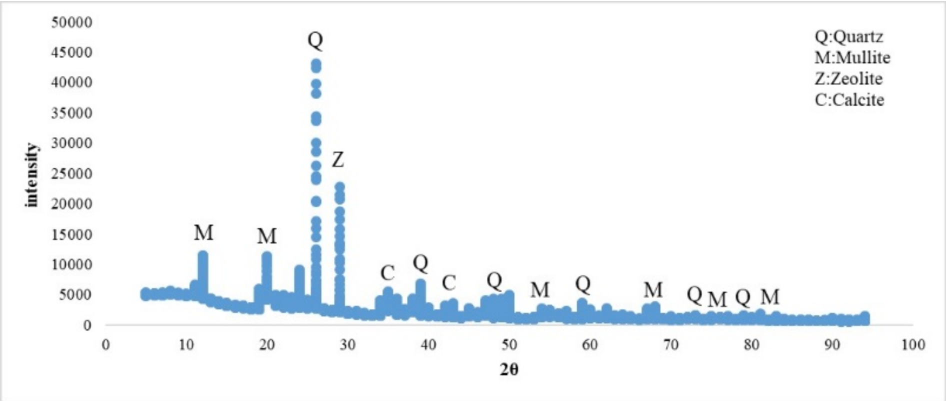

Figure 3. XRD analysis of ceramic powder.

2.1.2. Sodium Hydroxide (NaOH)

The properties of NaOH used in the study are given in Table 2.

Table 2. Properties of Sodium Hydroxide (NaOH).

Chemical Name	Sodium hydroxide
Chemical Formula	NaOH
Molecular weight	40 g/mol
Asidimetric	≥97
Na_2CO_3	≤1
Cl	<0,01
SO_4	≤0,01
Heavy metal	≤0,002
Al	≤0,002
Fe	≤0,002

2.1.3. Sodium Silicate (Na_2SiO_3)

The properties of Sodium silicate used in the study are given in Table 3.

Table 3. Properties of Sodium Silicate (Na_2SiO_3).

Chemical Name	Sodium Silicate
Chemical Formula	$Na_2SiO_3nH_2O$
Molecular weight	122.06 g/mol
Density	1.39 g/cm^3 (20 °C)
Molecular Module SiO_2/Na_2O	2.07
Na_2O	%11.71
SiO_2	%23,46
Fe	39 ppm
Cl	%0.01
SO_4	%0.01

2.1.4. Aggregate

Basalt origin aggregate with a maximum grain size of 4 mm and a specific gravity of 2.83 g/cm^3 was used in the study.

2.1.5. Water

Tap water was used to prepare the mortar mixes.

2.2. Methods

In this study, mortar samples with a water/binder (W/B) ratio of 0.40, 0.45 and 0.50 and containing 11 %, 13 %, 15 % Sodium (Na) by weight and silicate modulus (Ms) of 0, 0.1, 0.2 and 0.3 were prepared. Mixing ratios of the samples are given in Table 4.

First of all, NaOH and Na_2SiO_3 were mixed with the required amount of water and kept until it came to room temperature. Aggregate and ceramic powder were mixed in a standard cement mixer for 60 seconds. Then, by adding a mixture of activator and water, it was mixed for 120 seconds. The prepared mixtures were placed in standard molds of 40×40×160 mm. Shoei et al.[32] applied a cure between 60 °C and 105 °C in the geopolymer production they made with ceramic powder and determined the optimum temperature as 90 °C. They stated that the compressive strength increased with the increase in curing temperature. In different studies, 105 °C curing temperature was used during the production of geopolymer [33–34]. All of the samples produced in this study were kept in an oven at 105 °C for 24 hours. Samples removed from the oven were cured at room temperature for up to 28 days. At the end of 28 days, unit weight (UW), apparent porosity (AP), water absorption (WA) ratio, ultrasound pulse velocity (UPV), flexural strength (FS) and compressive strength (CS) tests were performed on the samples. Flexural and compressive test device is given in Fig. 4.

Table 4. Mixing ratio of samples.

No	Sample code	Na/binder (%)	water/binder (W/B)	Ms=SiO_2/Na_2O	binder/ aggregate
1	N11ST40MS0	11	0.40	0	1/3
2	N11ST40MS1	11	0.40	0.1	1/3
3	N11ST40MS2	11	0.40	0.2	1/3
4	N11ST40MS3	11	0.40	0.3	1/3
5	N11ST45MS0	11	0.45	0	1/3
6	N11ST45MS1	11	0.45	0.1	1/3
7	N11ST45MS2	11	0.45	0.2	1/3
8	N11ST45MS3	11	0.45	0.3	1/3
9	N11ST50MS0	11	0.50	0	1/3
10	N11ST50MS1	11	0.50	0.1	1/3
11	N11ST50MS2	11	0.50	0.2	1/3
12	N11ST50MS3	11	0.50	0.3	1/3
13	N13ST40MS0	13	0.40	0	1/3
14	N13ST40MS1	13	0.40	0.1	1/3
15	N13ST40MS2	13	0.40	0.2	1/3
16	N13ST40MS3	13	0.40	0.3	1/3
17	N13ST45MS0	13	0.45	0	1/3
18	N13ST45MS1	13	0.45	0.1	1/3
19	N13ST45MS2	13	0.45	0.2	1/3
20	N13ST45MS3	13	0.45	0.3	1/3
21	N13ST50MS0	13	0.50	0	1/3
22	N13ST50MS1	13	0.50	0.1	1/3
23	N13ST50MS2	13	0.50	0.2	1/3
24	N13ST50MS3	13	0.50	0.3	1/3
25	N15ST40MS0	15	0.40	0	1/3
26	N15ST40MS1	15	0.40	0.1	1/3
27	N15ST40MS2	15	0.40	0.2	1/3
28	N15ST40MS3	15	0.40	0.3	1/3
29	N15ST45MS0	15	0.45	0	1/3

No	Sample code	Na/binder (%)	water/binder (W/B)	Ms=SiO_2/Na_2O	binder/ aggregate
30	N15ST45MS1	15	0.45	0.1	1/3
31	N15ST45MS2	15	0.45	0.2	1/3
32	N15ST45MS3	15	0.45	0.3	1/3
33	N15ST50MS0	15	0.50	0	1/3
34	N15ST50MS1	15	0.50	0.1	1/3
35	N15ST50MS2	15	0.50	0.2	1/3
36	N15ST50MS3	15	0.50	0.3	1/3

Figure 4. Compressive and flexural test device.

3. Results and Discussion

3.1. Unit weight (UW) test results

Unit weight values of the samples are given in Fig. 5. The unit weights of the samples vary between 1.66 g/cm^3 and 2.22 g/cm^3. The lowest unit weight was observed as 1.66 g/cm^3 in the sample coded N11ST45MS3 containing 11 % Na, silicate modulus Ms = 0.3 and produced with 45 % water.

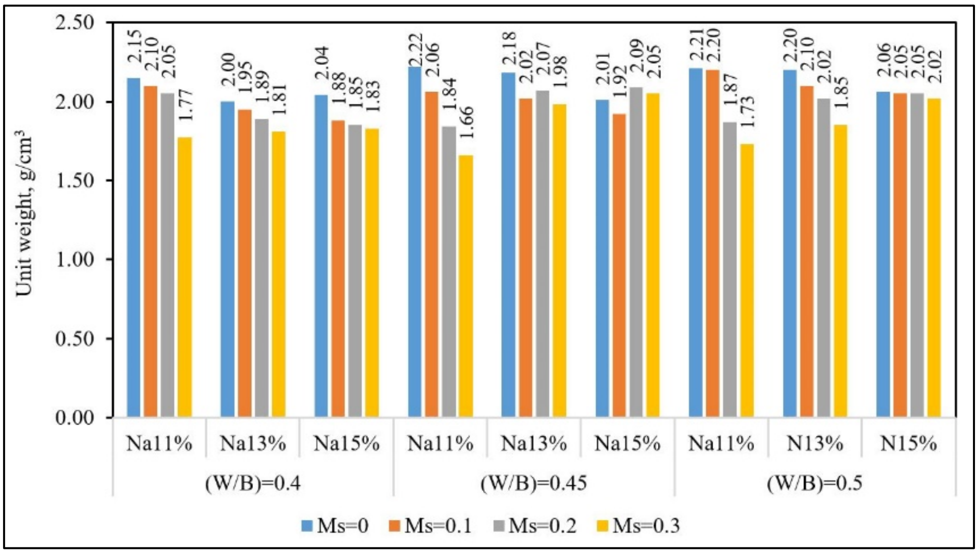

Figure 5. Unit weights of the samples.

The largest unit weight was observed in N11ST45MS0 sample with 11 % Na and silicate module Ms = 0. It was determined as 2.22 g/cm^3. It is observed that the unit weight values of all samples decrease with the increase of silicate modulus. Average unit weights were determined as 1.94 g/cm^3, 2.01 g/cm^3, 2.03 g/cm^3 for water/binder (W/B) ratio 0.40, W/B = 0.45, and W/B = 0.50 respectively. Unit weight values showed an insignificant increase with the increase in the amount of water in the mixture. In a study where geopolymer mortar was produced by alkali activation of waste ceramic powder, it was determined that the unit weight of samples produced by curing at 105 °C and having a W/B ratio of 0.40 was 1.849 g/cm^3. In samples with a W/B ratio of 0.5, it was found to be 1.861 g/cm^3 [32]. In another study where alkali activated mortar was produced by mixing ceramic tile wastes with fly ash and blast furnace slag, the unit weight of the alkali activated mortar produced using completely ceramic powder was determined to be 2.20 g/cm^3 at the end of 28 days [35]. It is known that the unit weight decreases as the curing temperature increases in geopolymer mortars [19, 32]. In this study, unit weight change is not significant since all samples are cured at 105 °C at constant temperature. In a study where fabricated geopolymer brick was produced with alkali activation of waste ceramic powder, it was stated that bulk density increased with 0.50 % increase in NaOH concentration. Unit weight increased in samples with high W/B ratio with the increase in $Ca(OH)_2$ ratio in the mixture [30].

3.2. Apparent porosity (AP) and water absorption (WA) test results

Determination of AP and WA ratio was made according to ASTM C642-3 standard [36]. AP values of the samples vary between 2.19 % and 21.63 %. The lowest AP was observed as 2.19 % in N15ST40MS1 sample. The highest AP was observed as 21.63% in N13ST40MS3 sample. It is observed that the porosity increases with the increase the silicate modulus in mixtures. The porosity generally decreases with the increase in the sodium (Na) content in the samples. The WA ratio of the samples ranges from 1.06 % to 11.74 %. While the lowest WA ratio was observed as 1.06 % in N15ST40MS1 sample, the highest WA ratio was found as 11.74 % in N13ST40MS3 sample. It is observed that WA ratios increase with the increase of silicate modulus. With the increase of Na content in samples, WA ratio generally decrease. In a study investigating the effect of ceramic powder additive in slag pastes, it is stated that ceramic powder additive reduces the WA ratio in 28-day samples. The WA ratio is observed around 17 % in samples without ceramic powder. The WA ratio decreases to approximately 13 % by increasing the ceramic powder in the mixture to 50 % [37]. In a study where waste ceramic powder and blast furnace slag were evaluated as self compacted concrete as a result of alkali activation, the WA ratio was 6.8 % in samples produced only with blast furnace slag (BFS). It was determined that it was 10.1 % in samples replaced with 50 % ceramic powder, and 14.1 % in samples replaced with 80 % ceramic powder [38]. This situation is explained by the fact that the particles that do not react due to the size of the particles of the waste ceramic powder increase the WA feature [39]. In a study in which an alkali activated paste was produced using ceramic powder and slag, it was stated that the ceramic powder additive reduced to workability [37]. In another study where geopolymer was produced by adding waste ceramic powder into fly ash and BFS, it is stated that the waste ceramic powder additive reduces the WA ratio [35]. On the other hand, it is known that increasing the silicate modulus decreases the workability in the mixture. For this reason, it is observed that the porosity and the WA ratio increase with the increase of silicate modulus in the samples. With the increase in the activator ratio in the mixture, some workability increases, so the porosity and WA ratio decrease. Curing temperature also has an effect on the porosity ratio and WA ratio. It is known that the porosity increases due to the loss of water in the sample with the increase of the curing temperature [19, 30, 40]. AP and WA ratios of the samples are given in Fig. 6.

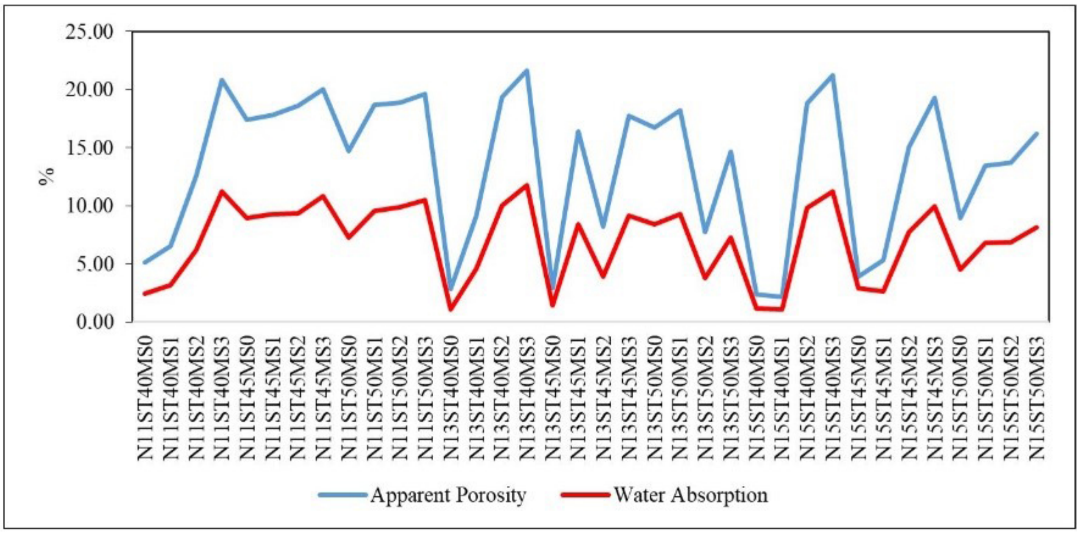

Figure 6. AP and WA ratios of the samples.

3.3. Ultrasound pulse velocity (UPV) test

The ultrasound pulse velocities of the samples were measured with a device called pundit (portable ultrasonic non-destructive digital indicating tester) according to EN 12504-4 [41]. UPV is a non-destructive testing method. It is a method used to identify voids and cracks and to determine the relative quality of concrete. UPV is used to determine properties such as void structure and cracks, and indirectly in estimation of compressive strength [42–44]. UPV values of the samples are given in Fig. 7. The UPV of the samples vary between 2108 m/s and 3661 m/s. The lowest UPV was determined as 2108 m/s in

N11ST45MS3 sample. The highest UPV was determined as 3361 m/s in N11ST50MS0 sample. A decrease in UPV was observed due to the increase in the void structure with the increase of silicate modulus in the samples. In a study in which waste brick dust and ceramic powder were activated with NaOH and Na_2SiO_3 to produce geopolymer paste, the UPVof the samples for 28 days were determined between 2635 m/s and 3724 m/s [45]. In another study where geopolymer was produced with ceramic powder, fly ash and BFS, a decrease was observed in UPV values with the increase in the amount of waste ceramic powder in the mixture [31]. In a study examining the strength and durability properties of self compacting concrete produced with Alkali activated waste ceramic powder and BFS, it is stated that the increase in ceramic dust in samples reduces the amount of loss in UPV after acid attacks [38].

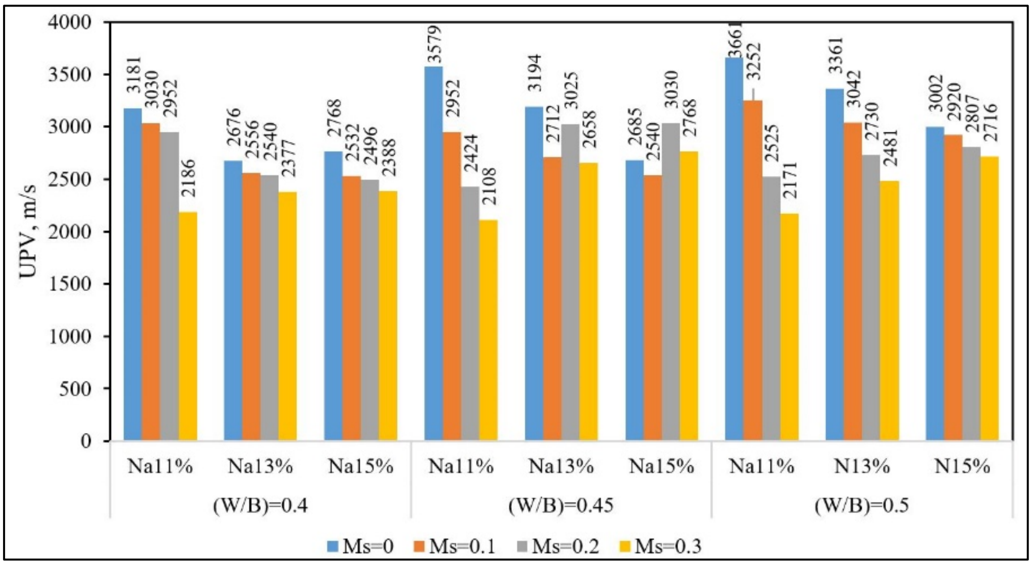

Figure 7. UPV values of samples.

3.4. Flexural Strength (FS) Test Results

The geopolymer samples produced within the scope of the study were loaded from a single point with a 100 mm support opening in accordance with EN 1015-11, 2000 [46]. Flexural strength test result are given in Fig. 8.The FS of the samples varies between 1.89 MPa and 10.38 MPa. The lowest FS was observed as 1.89 MPa in N13ST40MS3 sample produced with Ms = 0.3 with 0.40 W/B containing 13 % Na, while the highest FS was determined as 10.38 MPa in N15ST40MS0 sample produced with 0.40 W/B containing 15 % Na. In samples containing 15 % Na and 0.40 W/B the FS decreased by 77.4 % as the silicate modulus increasing to 0.3. In samples with 15 % Na and W/B ratio 0.50, the FS decreased from 5.52 MPa to 5.51 MPa with the silicate modulus increasing to 0.3. In samples produced with 0.40 and 0.45 W/B, a significant decrease in FS is observed with the increase of silicate modulus. Besides, in samples with a W/B ratio of 0.50, the decrease in FS with the increase of silicate modulus is not significant. With the increase in the W/B ratio in the mixture, it causes an increase in workability and an increase in porosity. The increase in Na_2SiO_3 in the mixture has a negative effect on workability. For this reason, the differences between the FS in mixtures with W/B 0.50 are not significant. In a study where ceramic powders of various gradations are used as aggregates and metakaolin based geopolymer is produced, it is stated that the FS of the samples varies between 9 MPa and 12 MPa [47]. In another study where geopolymer was produced by adding waste ceramic powder into fly ash and BFS, it is stated that the waste ceramic powder additive reduces the FS [35]. Shoaei et al. [32] stated that in geopolymer mortars produced with waste ceramic powder (WCP), FS increases with the increase of curing temperature. They stated that the 28-day FS of the samples cured at 105 °C increased from 4.88 MPa to 6.25 MPa with the increase in W/B ratio from 0.40 to 0.50. In this study, it is seen that the average FS increased from 5.34 MPa to 5.50 MPa with the increase of water ratio in samples from 0.40 to 0.50 ratio. It is observed that the FS is affected by 105 °C, which is kept constant in sample production. The FS increases a little with the increase in the amount of water. Some studies indicate that moisture is required to produce a good geopolymer [45–48]. Huseien et al [38] in their geopolymer study with a mixture of BFS and waste ceramic powder, found that the FS decreased with the increase in the amount of waste ceramic powder in the mixture. The samples produced with BFS stated that while the FS was 2.1 MPa, the FS decreased to 1.2 MPa with 80 % WCP replacement. It is stated that this situation is caused by the fact that WCP is larger than BFS and therefore the amount of ceramic powder involved in activation is low [39].

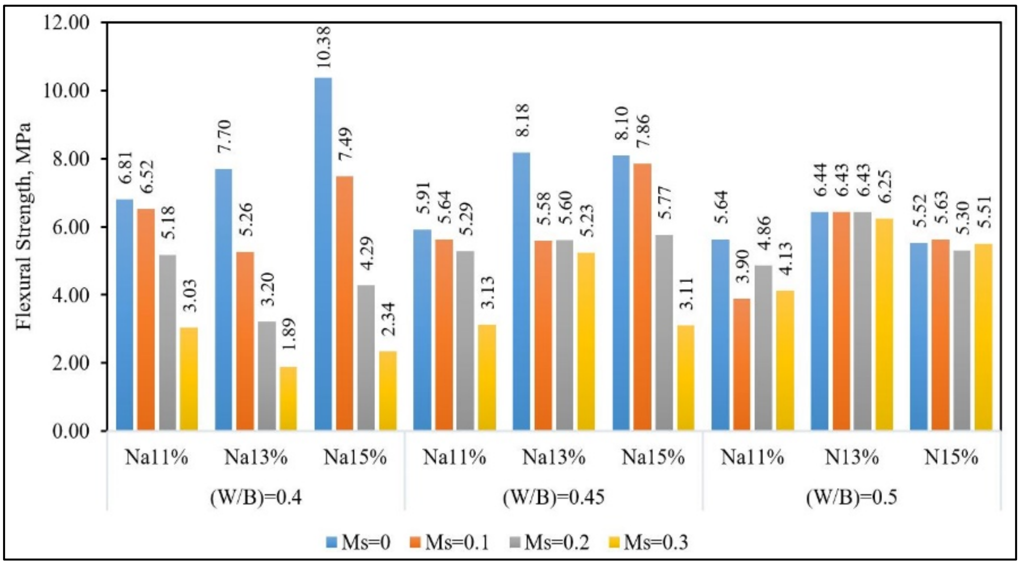

Figure 8. FS of the samples.

3.5. Compressive Strength (CS) Test Results

CS test is done according to EN 1015-11, 2000 standard [46]. CS of the samples are given in Fig. 9.The CS of the samples ranged from 10.42 MPa to 41.53 MPa. The lowest CS was observed as 10.42 MPa in N13ST40MS3 sample with Ms = 0.3 produced with 0.40 W/B containing 13 % Na. The highest CS was determined as 41.53 MPa in the sample N15ST40MS0 with Ms = 0 produced with 0.40 W/B containing 15 % Na. In samples containing 15 % Na and 0.40 W/B, the CS decreased by 70.8 % with the silicate modulus increasing from 0 to 0.3. In samples with 15 % Na and W/B ratio of 0.50, the CS decreased by 7 % with the silicate modulus increasing from 0 to 0.3. In samples with W/B ratios of 0.40 and 0.45, significant decreases in CS are observed with the increase of the silicate modulus. The difference in compressive strength is not significant for samples with a ratio of W/B 0.50. In a study where geopolymer was produced by adding waste ceramic powder (WPC) into fly ash and BFS, it was determined that the 28-day CS decreased from 70.4 MPa to 34.8 MPa with the increase of WPC in the samples from 50 % to 70 % [37]. This situation is explained by the decrease in the amount of calcium in the environment and the increase in the amount of silicon [35, 49]. Hwang et al. [45] found that the CS develops with time in geopolymer samples, which are cured at ambient temperature and contain different amounts of waste brick dust. WPC and BFS. Ca^{+} ions of Cao content and Si^{4+} and Al^{3+} ions rich in alkali cause the formation of C-S-H gel and C-A-S-H gel [33–34]. In this study, it was determined that the average CS of the samples cured at 105 °C at constant temperature was 24.47 MPa, W/B = 0.40. 25.11 MPa for W/B = 0.45, 24.54 MPa for W/B = 0.50. Average compressive strengths were determined as 22.86 MPa, 24.86 MPa and 26.38 MPa for 11 % Na, 13 % Na and 15 % Na values for all samples, respectively. With the increase in the Na ratio in the samples, an increase was observed in the CS. In geopolymer mortars, it is known that the CS increases with the increase of the sodium ratio in the mixture, and the porosity and CS decrease with the increase of the silicate module [40, 44]. Shoaei et al. [32] stated that the CS increases with the increase of curing temperature in geopolymer mortars produced with WPC. They stated that the 28-day CS of the samples cured at 105 °C increased from 23 MPa to 26.4 MPa with the increase in W/B ratio from 0.40 to 0.50. Regarding the effect of alkaline solution-binder (S/B) ratio, S/B increased values improve CS.They found that it reached its maximum value at S/B = 0.6. They also stated that 28-day samples had good strength within the age groups of the samples. Similarly, a certain amount of water increase in the CS as in the FS positively affects the strength [44, 48]. Generally, the strength development in ceramic powder based geopolymers is not very high compared to BFS and FA origin geopolymers due to the chemical composition of the ceramic powder [35, 50–51]. Rashad et al. [34] found that the compressive strength increases with the increase in the amount of WPC in the mixture in alkali activated pastes produced with ceramic powder and slag. They stated that with the increase of the amount of WPC in the mixture to 50 %, the 28-day CS increased 1.53 times. In the literature, it is stated that temperature curing increases the strength as well as the durability [52]. The increase in the $NaOH/Na_2SiO_3$ ratio causes a decrease in the CS [4, 53–54]. When the $NaOH/Na_2SiO_3$ ratio is exceeded the optimum value, the strength is negatively affected [19, 40].

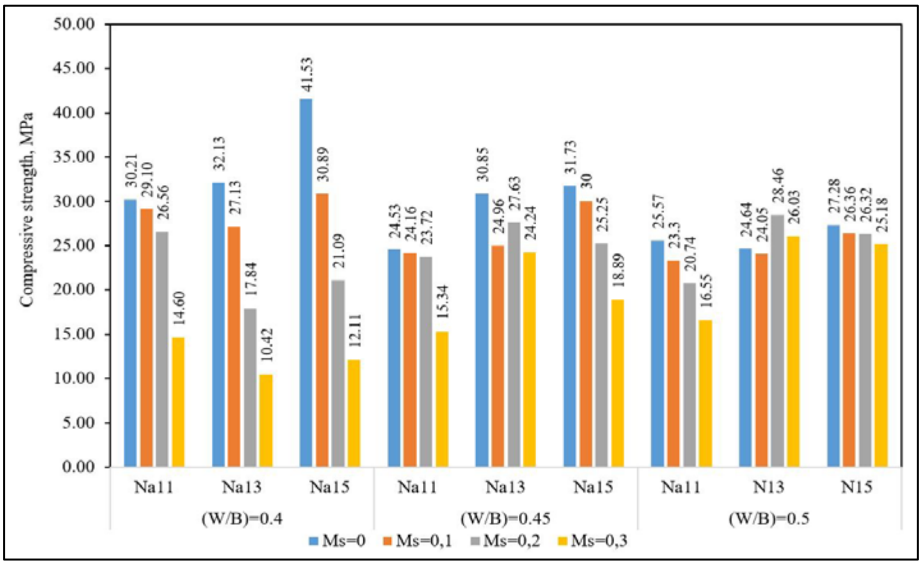

Figure 9. CS of the samples.

3.6. Relationships between some properties

The relationship between UPV-CS and AP-CS of samples are given in Fig. 10. All correlations in graphs are given exponential. It is observed that UPV values increase and AP values decrease with the increase of CS in all sodium ratios. It was determined that there is a strong relationship between UPV and CS with $R^2 = 0.96$. Hwang et al. [45]. found a correlation of $R^2 = 0.91$ between UPV and CS in alkali activated waste tile and ceramic powder pastes. It is seen that the CS increases with the decrease of AP. The correlation between AP and CS was determined as $R^2 = 0.79$. The relationship between UW and CS of samples are given in Fig. 11. The correlation between UW and CS was determined as $R^2 = 0.94$. It was observed that the CS increased with the increase in UW. The correlation between FS and CS of all samples are given in Fig. 12. In the correlation between FS and CS of all samples, a relation such as $R^2 = 0.83$ was observed. Huseien et al. [35] found a correlation of $R^2 = 0.9435$ between FS and CS for 28 days in their geopolymer studies with waste ceramic additives.

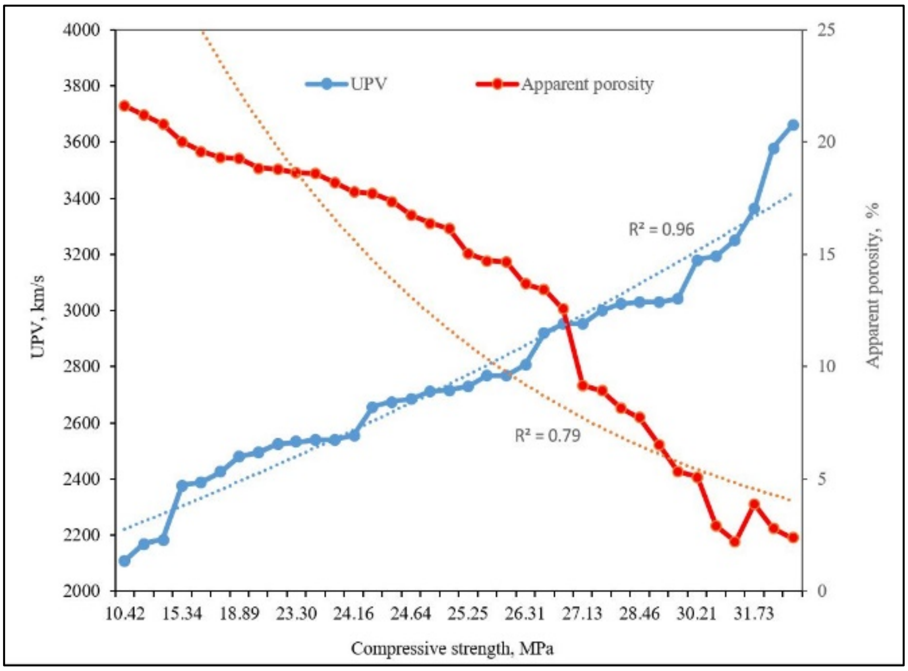

Figure 10. Relationship between UPV-CS and AP-CS of the samples.

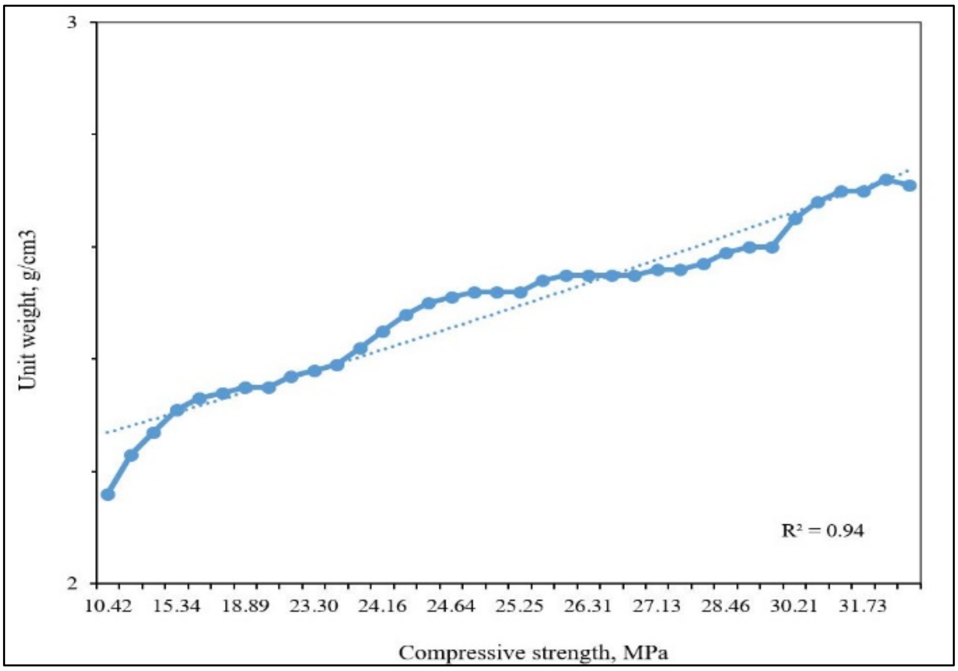

Figure 11. Relationship between UW-CS of the samples.

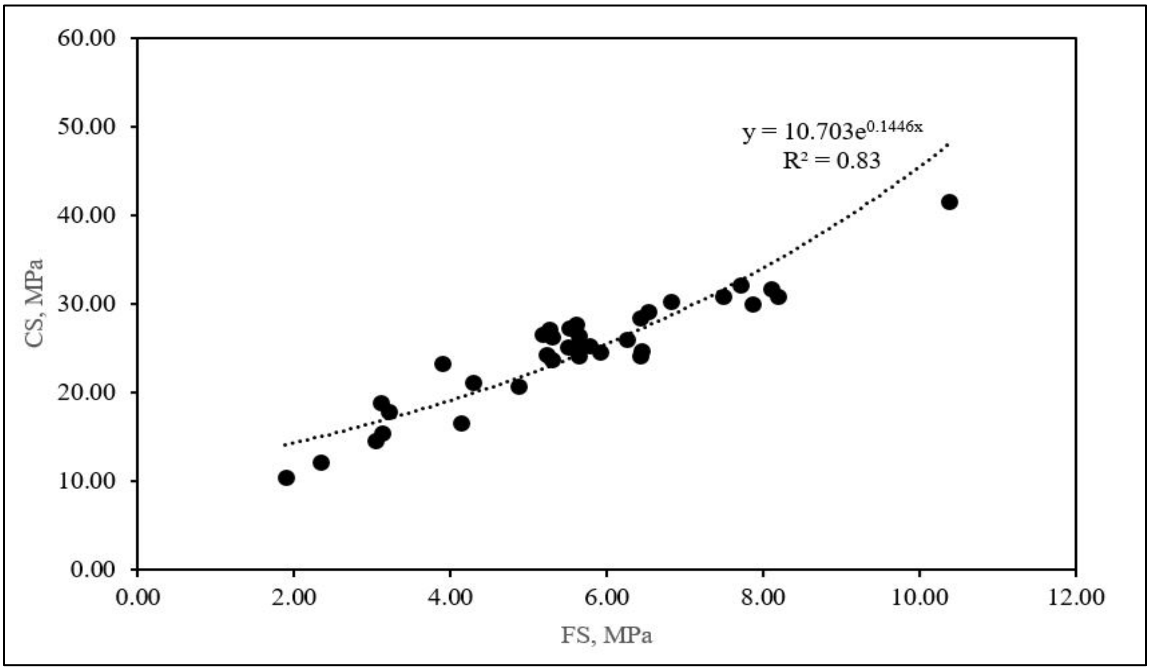

Figure 12. Correlation between CS and FS of all samples.

3.7. Experimental Design and Optimization

Response surface method (RSM) is a method consisting of mathematical and statistical techniques. Empirical models and first presented by Box and Wilson44 in 1951. Then RSM, It has been used in modeling numerical experiments [55–57]. In this study, flexural strength (FS) and compressive strength (CS) test results are designed with RSM. Water/binder W/B, activator/binder Na (%), silicate module is coded with Ms. FS codes were used for flexural strength and CS codes for compressive strength. The independent variables in this study are W/B, Na (%) and Ms values. In this study, optimum values were determined by response surface method by using 11 %, 13 % and 15 % Na ratio, 0, 0.1, 0.2, 0.3 Ms ratio and 0.40, 0.45, 0.50 W/B independent variables. In order to obtain a response surface, 27 data for each response were used for variance analysis. The response surfaces of FS and CS as a function of Na%, W/B ratio and M_S values are given in Fig. 13 and Fig. 14, respectively. Equations obtained from regression models for FS and CS are given in Equation (1) and Equation (2). Regression coefficient was found as R^2 =0.77 for FS and R^2 =0.73 for CS.

$$FS = 27.98 - 0.45(Na) - 64.37(W/B) - 81.49(Ms) + \\ + 2.35\left[(Na \times W/B)\right] - 1.71(Na \times Ms) + 211.25\left[(W/B) \times Ms\right], \quad (1)$$

$$CS = 167.69 - 6.66978(Na) - 360.19(W/B) - 236.37(Ms) + \\ + 18.89\left[Na \times (W/B)\right] - 6.21(Na \times Ms) + 637.08\left[(W/B) \times Ms\right] \quad (2)$$

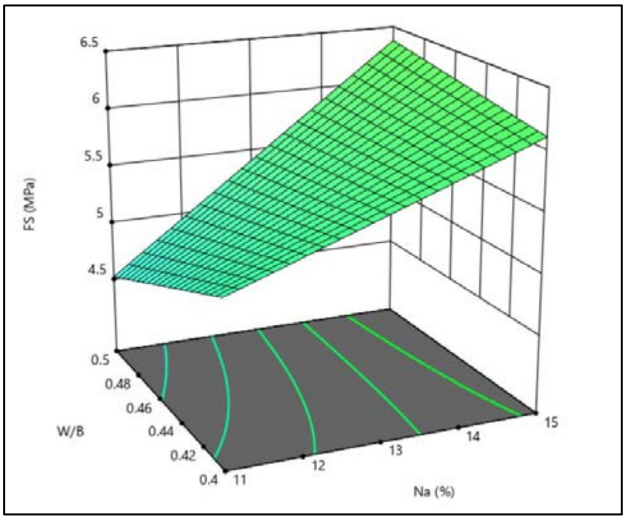

Figure 13. Respose surface for FS.

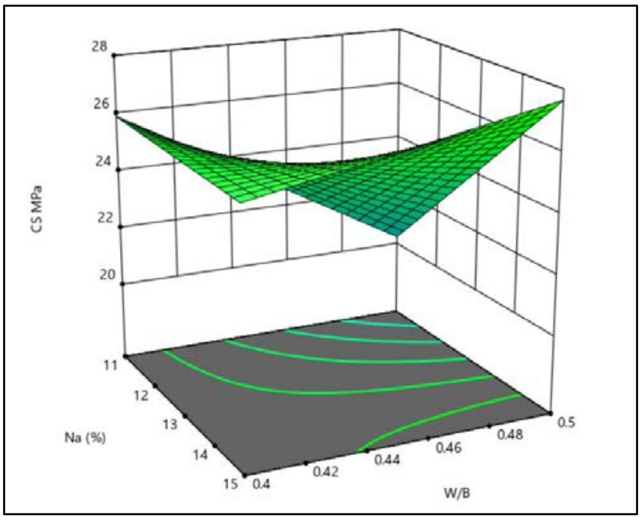

Figure 14. Respose surface for compressive strength (CS).

The numerical optimization technique proposed by Derringer and Suich [58] to simultaneously optimize the responses for a desirability is given as functions (di). A desirability function for each answer ranges from 0 ≤ di ≤ 1. A multipurpose optimization problem the single compound given in Equation 3 is resolved using the response or general desirability (Dis) which is the geometric mean of individual desirabilities.

$$Dis = (d1 \times d2 \times d3 \times \ldots dn)^{(1/n)}, \quad (3)$$

n represents the number of response surfaces in the optimization. Suitable regions used in this study are:

$$\%11 \le Na \le \%15,$$
$$0.40 \le (W/B) \le 0.50,$$
$$0 \le Ms \le 0.30.$$

In order to obtain high strength, FS and CS strength must be high. Activator is seen as an important cost element in the production of geopolymer. Therefore, n = 4 in the equation to minimize the activator while maximizing flexural and compressive strength.

$$Dis = \left(d1 \times d2 \times d3 \times d4\right)^{\left(1/4\right)}.$$

The optimum solution for this modeling result is given in Table 5.

Table 5. The optimum solution for this modeling result.

		Contraints		
		Lower Limit	Upper Limit	Optimum Solution
Na (%)	Minimum	11	15	12.67
W/B	Minimum	0.4	0.5	0.425
Ms	Minimum	0	0.3	0.12
FS (MPa)	Maximum	2.34	10.38	5.97
CS (MPa)	Maximum	12.11	41.53	26.75

The desirability level resulting from the modeling of the samples and the optimum flexural (FS) and compressive strength (CS) values are shown in Fig. 15. In Fig. 13, with the increase of Na ratio, an increase in flexural strength is observed. With the increase of W/B at low Na ratios, the flexural strength decreased. With the increase of W/B at high Na ratios, the flexural strength increased. Fig. 14 shows an increase in compressive strength with the increase of Na ratio. Similar to the flexural strength, the compressive strength decreased with the increase of W/B at low Na ratios, while it increased significantly at high Na ratios. The optimum solution was determined as 12.67 % Na, 0.425 W/B 0.12 Ms, and the flexural strength as 5.97 MPa and 26.75 MPa. Mermerdas et al. [59] In their optimization study for geopolymer produced with blast furnace slag and fly ash, determined that the optimum curing temperature was between 9 and 24 hours at 60 °C. Zhang and Yue [60] made use of the optimization technique in their study where they produced glass powder doped slag based geopolymer. Regarding the flexural and compressive strengths, they found that the optimal values were 14.57 % glass powder content for 8.31 % Na_2O. They stated that the Response Surface methodology (RSM) is an efficient and useful method for optimizing design parameters of the following.

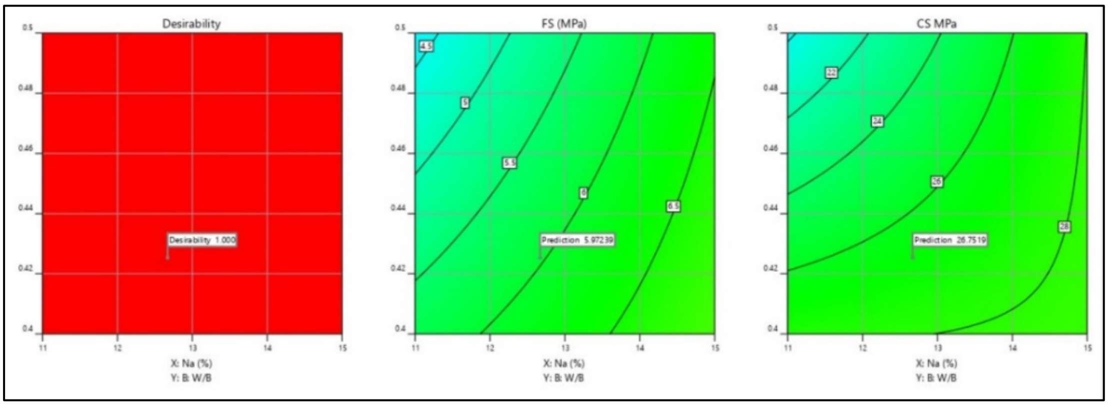

Figure 15. Desirability, optimum FS and CS.

4. Conclusions

The following results have been obtained from the experimental studies:

- 28-day flexural strength of mortar samples produced by alkali activation of ceramic powder varies between 2.34–10.38 MPa and compressive strength between 10.42–41.53 MPa. The highest compressive strength was determined as 41.53 MPa for samples containing 40 % water/binder, 15 % Na and Ms = 0.
- With the increase of silicate modulus in all samples, decreases in flexural and compressive strength were detected. Using only NaOH for alkali activation of ceramic powder gives good results in terms of strength.

- With the increase in the Na ratio by weight in the samples with low water content, the flexural and compressive strengths increased significantly. On the other hand, this increase in strength is not evident in samples with high water content. In samples with W/B ratios of 0.40 and 0.45, significant decreases in compressive strength are observed with the increase of the silicate modulus. The difference in compressive strength is not significant for samples with a ratio of W/B 0.50.
- As a result of the optimization, it has been determined that the optimum mixture of 12.67 % Na, 0.425 W/B and 0.12 Ms can achieve a flexural strength of 5.97 MPa and a compressive strength of 26.75 MPa.

High strength geopolymer can be produced by alkali activation of ceramic powder. It is thought that this geopolymer material can be used in the production of high strength ceramics.

References

1. Atis, C.D., Görür, E.B., Karahan, O., Bilim C., Ilkentapar, S., Luga. E. Very high strength (120 MPa) class F fly ash geopolymer mortar activated at different NaOH amount, heat curing temperature and heat curing duration. Constr. Build Mater. 2015. No. 96. Pp. 673–678 (). https://doi.org/10.1016/j.conbuildmat.2015.08.089
2. Zhuanga, H.J., Zhanga, H.Y., Xua, H. Resistance of geopolymer mortar to acid and chloride attacks, Procedia Engineering. 2017. No. 210. Pp. 126–131.
3. Lahoti, M., Tan, K.H., Yang, E. A critical review of geopolymer properties for structural fire-resistance applications, Construct Build Mater. 2019. No. 221. Pp. 514–526. https://doi.org/10.1016/j.conbuildmat.2019.06.076
4. Mermerdas, K., Algın, Z., Ekmen, S. Experimental assessment and optimization of mix parameters of fly ash-based lightweight geopolymer mortar with respect to shrinkage and strength, Journal of Building Engineering. 2020. No. 31. 101351 https://doi.org/10.1016/j.jobe.2020.101351
5. AinJayaa, N., Yun-Ming, L., Cheng-Yong, H., Abdullah, M.M.A., Hussin. K. Correlation between pore structure, compressive strength and thermal conductivity of porous metakaolin geopolymer, Constr. Build Mater. 2020. No. 247. 118641. https://doi.org/10.1016/j. conbuildmat.2020.118641
6. Villaquirán-Caicedo, M.A., Mejía de Gutiérrez, R. Synthesis of ceramic materials from ecofriendly geopolymer precursors. Materials Letters.2018. No. 230. Pp. 300–304. https://doi.org/10.1016/j.matlet.2018.07.128
7. Weil, M., Dombrowski, K., Buchwald, A.: Life-cycle analysis of geopolymers. In J.L. Provis, J.S.J. Van Deventer (Eds.). Geopolymers: Structures, Processing, Properties and Industrial Applications, Woodhead Publishing Limited, Cambridge, England. 2009. Pp. 194–210.
8. Provis, J.L., Palomo, A., Shi, C.: Advances in understanding alkali-activated materials. Cem. Concr. Res. 2015. No. 78. Pp. 110–125. https://doi.org/10.1016/ j.cemconres.2015.04.013
9. Atabey, İ.İ., Karahan, O., Bilim, C., Atiş, C.D. The influence of activator type and quantity on the transport properties of class F fly ash geopolymer. Constr. Build Mater. 2020. No. 264. 120268.
10. Gupta, A., Gupta, N., Saxena, K.K., Goyal, S.K. Investigation of the strength of ground granulated blast furnace slag based geopolymer composite with silica füme. Materials Today: Proceedings. 2020. https://doi.org/10.1016/j.matpr.2020.06.010
11. Shah, K.W., Huseien, G.F. Bond strength performance of ceramic, fly ash and GBFS ternary wastes combined alkali-activated mortars exposed to aggressive environments. Constr. Build Mater. 2020. No. 251. 119088. https://doi.org/10.1016/j.conbuildmat.2020.119088
12. Alamgir Kabir, S.M., Alengaram, U.J., Jumaat, M.Z., Yusoff, S., Sharmin, A., Bashar, I.I. Performance evaluation and some durability characteristics of environmental friendly palm oil clinker based geopolymer concrete. J.Clean. Prod. 2017. No. 161. Pp. 477–492. https://doi.org/ 10.1016/j.jclepro.2017.05.002
13. Freire, A.L., Moura-Nickel, C.D., Scaratti, G., Rossi, A., Peralta, R.F., Moreira, M. Geopolymers produced with fly ash and rice husk ash applied to CO_2 capture, J.Clean. Prod. 2020. No. 273. 122917. https://doi.org/10.1016/j.jclepro.2020.122917
14. Phetchuay, C., Horpibulsuk, S., Suksiripattanapong, C., Chinkulkijniwat, A., Disfani, M.M. Calcium carbide residue: Alkaline activator for clay–fly ash geopolymer. Constr. Build Mater. 2014. No. 69. Pp. 285–294. https://doi.org/ 10.1016/j.conbuild-mat.2014.07.018
15. Matalkah, F., Aqel, R., Ababneh, A. Enhancement of the Mechanical Properties of Kaolin Geopolymer Using Sodium Hydroxide and Calcium Oxide. Procedia Manuf. 2020. No. 44. Pp. 164–171. https://doi.org/10.1016/j.promfg.2020.02.218
16. Merabtene, M., Kacimi, L., Clastres, P. Elaboration of geopolymer binders from poor kaolin and dam sludge waste. Heliyon. 2019. No. 5. e01938. https://doi.org/10.1016/ j.heliyon. 2019.e01938
17. Kovárˇík, T., Krˇenek, T., Rieger, D., Pola, M. et al. Synthesis of open-cell ceramic foam derived from geopolymer precursor via replica technique. Mat. Lett. 2017. No. 209. Pp. 497–500. https://doi.org/10.1016/j.matlet.2017.08.081
18. Yun-Ming, L., Cheng-Yong, H., Al Bakri, M.M., Hussin, K. Structure and properties of clay-based geopolymer cements: a review. Prog. Mater. Sci. 2016. No. 83. Pp. 595–629. https://doi.org/10.1016/j.pmatsci.2016.08.002
19. Kaya, M. Examination of Mechanical And Durability Properties of Various Types Of Fly Ash Produced By Using Alkali Activated Mortars. Sakarya University, The Graduate School of Natural and Applied Science. PhD Thesis. 2016 (in Turkish).
20. Keppert, M., Vejmelková, E., Bezdička, P., Doleželová, M., Černý, R. Red-clay ceramic powders as geopolymer precursors: Consideration of amorphous portion and CaO content, App. Clay Sci. 2018. No. 161. Pp. 82–89. https://doi.org/10.1016/j.clay.2018.04.019
21. Luoa, Y., Maa, S., Liua, C., Zhaoa, Z., Zhenga, S., Wanga, X. Effect of particle size and alkali activation on coal fly ash and their role in sintered ceramic tiles. Journal of the European Cer. Soc. 2017. No. 37. Pp. 1847–1856. https://doi.org/10.10-16/j.jeurceramsoc. 016.11.032
22. Wanga, H., Lib, H., Wanga, Y., Yana, F. Preparation of macroporous ceramic from metakaolinite-based geopolymer by calcination, Cer. Inter. 2015. No. 41. Pp. 11177–11183. https://doi.org/10.1016/j.ceramint.2015.05.067

23. Yun-hong, C., Huang, F., Liu. R., Hou, J., Guanh-Iu, L. Test research of effects of waste ceramic polishing powder on the permeability resistance of concrete. Mater. Struct. 2016. No. 49. Pp. 729–738. https://doi.org/10.1617/s11527-015-0533-6

24. Senthamarai, R.M., Devadas, P., Manoharan, P.D., Gobinath, D. Concrete made from ceramic industry waste: durability properties Constr. Build Mater. 2011. No. 25. Pp. 2413–2419. https://doi.org/10.1016/j.conbuildmat.2010.11.049

25. Pereira-de-Oliveira, L.A, Castro-Gomes J.P., Santos P. The potential pozzolanic activity of glass and red-clay ceramic waste as cement mortars components. Constr. Build Mater.2012. No. 31. Pp. 197–203. https://doi.org/10.1016/j.conbuild-mat.2011.12.110

26. Higashiyama, H., Yamauchi, K., Sappakittipakorn, M., Sano, M., Takahashi, O. A visual investigation on chloride ingress into ceramic waste aggregate mortars having different water to cement ratios, Constr. Build Mater. 2013. No. 40. Pp. 1021–1028. https://doi.org/10.1016/ j.conbuildmat.2012.11.078

27. Li, L.G., Zhuo, Z.Y., Zhu, J., Chen, J.J., Kwan, A.K.H. Reutilizing ceramic polishing waste as powder filler in mortar to reduce cement content by 33 % and increase strength by 85 %, Powder Technol. 2019. No. 355. Pp. 119–126. https://doi.org/10.1016/ j.powtec.2019.07.043

28. Huseien, G.F., Sam, A.R.M., Shahb, K. et al Evaluation of alkali-activated mortars containing high volume waste ceramic powder and fly ash replacing GBFS. Constr. Build Mater. 2019. No. 210. Pp. 78–92. https://doi.org/10.1016/j.conbuild-mat.2019.03.194

29. Abdollahnejad, Z., Mastali, M., Luukkonen, T., Kinnunen, P., Illikainen, M. Fiber-reinforced one-part alkali-activated slag/ceramic binders. Ceram. Inter. 2018. No. 44. Pp. 8963–8976. https://doi.org/10.1016/j.ceramint.2018.02.097

30. Amin, Sh.K., El–Sherbiny, S.A., El–Magd, A.A.M.A., Belal, A., Abadir, M. Fabrication of geopolymer bricks using ceramic dust waste. Constr. Build Mater. 2017. No. 157. Pp. 610–620. https://doi.org/10.1016/j.conbuildmat.2017.09.052

31. Huseien, G.F., Sam, A.R.M, Mirza, J., Tahir, M.M. et al. Waste ceramic powder incorporated alkali activated mortars exposed to elevated Temperatures: Performance evaluation, Constr. Build Mater. 2018. No. 187. Pp. 307–317. https://doi.org/10.1016/ j.conbuildmat.2018.07.226

32. Shoaei, P., Musaeei, H.R., Mirlohi, F., Narimani, S. et al. Waste ceramic powder-based geopolymer mortars: Effect of curing temperature and alkaline solution-to-binder ratio. Constr. Build Mater. 2019. No. 227. 116686. https://doi.org/10.1016/j.con-buildmat. 2019.116686

33. Ismail, I., Bernal, S.A., Provis, J.L., Nicolas, R.S., Hamdan, S., Deventer. J.S.J. Modification of phase evolution in alkali-activated blast furnace slag by the incorporation of fly ash, Cem. Concr. Compos. 2014. No. 45. Pp 125–135. https://doi.org/10.1016/ j.cemconcomp.2013.09.006

34. Rashad, A.M., Bai, Y., Basheer, P.A.M., Milestone, N.B: Collier NC. Hydration and properties of sodium sulfate activated slag. Cem. Concr. Compos. 2013. 37 20–29. https://doi.org/10.1016/j.cemconcomp.2012.12.010

35. Huseien, G.F., Sam, A.R.M., Shah, K.W., Asaad, M.A, et al. Properties of ceramic tile waste based alkali-activated mortars incorporating GBFS and fly ash, Constr. Build Mater. 2019. No. 214. Pp. 355–368. https://doi.org/10.1016/j.conbuild-mat.2019.04.154

36. ASTM C642–13, Standard Test Method for Density, Absorption, and Voids in Hardened Concrete

37. Rashad, A.M., Essa. G.M.F. Effect of ceramic waste powder on alkali-activated slag pastes cured in hot weather after exposure to elevated temperature. Cem. Concr. Compos. 2020. No. 111. 103617. https://doi.org/10.1016/j.cemcon-comp.2020.103617

38. Huseien, G.F., Sam, A.R.M, Shah, K.W, Mirza, J. Effects of ceramic tile powder waste on properties of self-compacted alkali-activated concrete. Constr. Build Mater. 2020. No. 236. 117574.

39. Kubba, Z., Huseien, G.F., Sam, A.R.M., Shah, K. et al. Impact of curing temperatures and alkaline activators on compressive strength and porosity of ternary blended geopolymer mortars. Case Stud. Constr. Mater. 2018. No. 9. e00205. https://doi.org/10.1016/ j.cscm.2018.e00205

40. Atabey, I. Investigation of Durability Properties of F Class Fly Ash Geopolymer Mortar. Erciyes University. The Graduate School of Natural and Applied Science. PhD Thesis. 2017 (in Turkish)

41. EN 12504-4. Concrete tests-part 4: Determination of ultrasonic pulsed wave velocity. Ankara, Turkey: Turkish Standards Institution, 2012

42. Bogas, J.A., Gomes, M.G., Gomes, A. Compressive strength evaluation of structural lightweight concrete by non-destructive ultrasonic pulse velocity method. Ultrasonics. 2013. No. 53. 962–972. https://doi.org/10.1016/j.ultras.2012.12.012

43. Huynh, T.P., Vo, D.H., Hwang, C.L. Engineering and durability properties of ecofriendly mortar using cement-free SRF binder. Constr. Build. Mater. 2018. No. 160. 145–155. https://doi.org/10.1016/j.conbuildmat.2017.11.040

44. Kaya, M., Uysal, M., Yılmaz, K., Karahan, O., Atiş, C.D. Mechanical properties of class C and fly ash geopolymer mortars. Gradevinar. 2020. No. 72. Pp. 297–309. https://doi.org/10.14256/JCE.2421.2018

45. Hwang, C.L., Yehualaw, M.D., Vo, D.H., Huynh T.P. Development of high-strength alkali-activated pastes containing high volumes of waste brick and ceramic powders, Constr. Build Mater. 2019. No. 218. Pp. 519–529. https://doi.org/10.1016/ j.conbuildmat.2019.05.143

46. EN 1015-11. Methods of test for mortar for masonry-Part 11:Determination of flexural and compressive strength of hardened mortar. Ankara, Turkey: Turkish Standards Institution, 2013.

47. Kovárˇík, T., Rieger, D., Kadlec, J., Krˇenek, T. et al. Thermomechanical properties of particle-reinforced geopolymer composite with various aggregate gradation of fine ceramic filler, Constr. Build Mater. 2017. No. 143. Pp. 599–606. https://doi.org/10.1016/ j.conbuildmat.2017.03.134

48. Chindaprasirt, P., Chareerat, T., Sirivivatnanon, V. Workability and strength ofcoarse high calcium fly ash geopolymer, Cem. Concr. Compos. 2007. No. 29. Pp. 224– 229. https://doi.org/10.1016/j.cemconcomp.2006.11.002

49. Huseien, G.F., Ismail, M., Tahir, M.M., Mirza, J., Khalid, N.H.A., Asaad, M.A. et al: Synergism between palm oil fuel ash and slag: Production of environmentalfriendly alkali activated mortars with enhanced properties. Constr. Build. Mater. 2018. No. 170. Pp. 235–244 (2018). https://doi.org/10.1016/j.conbuildmat.2018.03.031

50. Kannan, D.M., Aboubakr, S.H., EL-Dieb, A.S., Taha, M.M.R. High performance concrete incorporating ceramic waste powder as large partial replacement of Portland cement, Constr. Build. Mater. 2017. No. 144. Pp. 35–41. https://doi.org/10.1016/j.conbuildmat. 2017.03.115

51. Huseien, G.F., Ismail, M., Tahir. M., Mirza, J., Hussein, K.N.H., Sarbini, N.N. Performance of sustainable alkali activated mortars containing solid waste ceramic powder. Chem. Eng. Trans. 2018. No. 63. Pp. 673–678 (2018). https://www.aidic.it/cet/18/63/113.pdf

52. Maochieh, C. Effects of dosage of alkali-activated solution and curing conditions on the properties and durability of alkali-activated slag concrete, Construct. Build. Mater. 35. 240–245 (2012). https://doi.org/10.1016/j.conbuildmat.2012.04.005

53. Vora, P.R., Dave, U.V. Parametric studies on compressive strength of geopolymer concrete. Procedia Eng. 2013. No. 51. Pp. 210–219. https://doi.org/10.1016/j.proeng. 2013.01.030

54. Kamhangrittirong, P., Suwanvitaya, P., Witayakul, W., Suwanvitaya, P., Chindaprasirt, P. Factors influence on shrinkage of high calcium fly ash geopolymer paste, Adv. Mater. Res. 2013. No. 610. Pp. 2275–2281. https://www.scientific.net/AMR.610-613.2275

55. Box, G.E.P., Draper, N.R. Emprical Model Building and Response Surfaces. New York: John Wiley, 1987.

56. Myers, R.H., Montgomery, D.C. Response surface methodology: Process and product optimization using designed experiments. New York, NY: John Wiley & Sons. Inc. 1995.

57. Whitcomb, P.J., Anderson, M.J. RSM Simplified: Optimizing Processes Using Response Surface Methods for Design of Experiments. Taylor & Francis, New York. 2004.

58. Derringer, G., Suich R. Simultaneous optimization of several response variables. J Qual Technol. 1980. No. 12 (4). Pp. 214–219.

59. Mermerdas, K., Algın, Z., Oleiwi, S.M., Nassani, D.E. Optimization of lightweight GGBFS and FA geopolymer mortars by response surface method. Const. and Buil. Mater. 2017. No. 139. Pp 159–171. https://doi.org/10.1016/j.conbuild-mat.2017.02.050

60. Zhang, L., Yue, Y. Influence of waste glass powder usage on the properties of alkali-activated slag mortars based on response surface methodology. Const. and Buil. Mater. 2018. No. 181. Pp. 527–534. https://doi.org/10.1016/j.conbuild-mat.2018.06.040

Information about authors:

Mehmet Kaya, PhD
ORCID: https://orcid.org/0000-0002-8116-0123
E-mail: mehmet.kaya@yobu.edu.tr

Received 07.11.2020. Approved after reviewing 18.11.2021. Accepted 24.11.2021.

Magazine of Civil Engineering. 2022. 112(4). Article No. 11208

Magazine of Civil Engineering

ISSN 2712-8172

journal homepage: http://engstroy.spbstu.ru/

Research article

UDC 624

DOI: 10.34910/MCE.112.8

Effect of Na^+ on hydration degree of alkali activated metakaolin polymer

Y. Zhao, H. Wang ✉***, Y. He, L. Yang, H. Wu***

Northeast Forestry University, Xiangfang District, Harbin, China

✉ *wanghongguang@zoho.com*

Keywords: geopolymers, chemical activation, hydration, materials testing, scanning electron microscopy, X-ray diffraction

Abstract. In recent years, geopolymeric gel materials have become a hot research issue due to their good mechanical properties, durability and excellent chemical stability. In this paper, Na^+-metakaolin soil polymer was prepared by activating metakaolin with a combination of NaOH and sodium silicate. Taking Na's influence on the hydration degree of alkali-activated metakaolin soil polymer as the goal, we selected Na_2O equivalent and the modulus of the alkali activator, two most important factors for Na^+ content in the system, as the object of our studies. The effect of Na_2O equivalent and modulus on the degree of hydration of geopolymers was analyzed by testing the compressive strength of metakaolin land polymers and microscopic SEM, FT-IR and XRD. The results show that the optimal activation environment for metakaolin is 18 % Na_2O equivalent and 1.5 modulus. When the Na_2O equivalent is less than 18 %, as the Na_2O equivalent increases, the degree of hydration of the metakaolin land polymer deepens. When it is greater than 18 %, with the Na_2O equivalent, the first stage of the geopolymer hydration reaction is suppressed and the degree of kaolin hydration is partially weakened. When the modulus is less than 1.5, as the modulus increases, the rate of the first stage of geopolymerization is accelerated, and the degree of hydration is deepened. When the modulus is greater than 2.0, as the modulus increases, the geopolymerization hydration reaction is suppressed during the second and third stages, the formation rate of geopolymeric gel is slowed down and the degree of hydration is weakened.

Funding: The research in this paper was supported by the National Natural Science Foundation of China (Grant No. 51708092), China Postdoctoral Science Fund Project (Grant No. 2018M631894), and Fundamental Research Funds for the Central Universities of China (Grant No. 2572019BJ01).

Citation: Zhao, Y., Wang, H., He, Y., Yang, L., Wu, H. Effect of Na^+ on hydration degree of alkali activated metakaolin polymer. Magazine of Civil Engineering. 2022. 112(4). Article No. 11208. DOI: 10.34910/MCE.112.8

1. Introduction

In the past few decades, geopolymer cementitious materials prepared by alkali activated aluminosilicate materials have become a hot research area. Compared with ordinary Portland cement, geopolymer cementitious materials have the same excellent compressive strength and excellent durability, high temperature resistance, shrinkage and chemical stability. At the same time, due to their low emission and low energy consumption preparation technology, geopolymers are considered the most promising building material to replace OPC in the 21th century at the world market [1].

Kaolin in the aluminosilicate precursors as the most pure natural ingredient has attracted researchers' attention. Alkaline activated solution plays an important role in the geopolymer reaction or hydration degree of metakaolin geopolymer, which greatly affects its mechanical properties. In recent years, some researchers carried out experimental observation by isothermal calorimetry (ICC) and thermogravimetric analysis (TGA). The effect of alkaline activator (type, modulus and ionic concentration) on the formation process of geopolymer was revealed gradually. The results showed that alkaline sodium silicate solution had good activation effect on metakaolin. The content of Na^+ and Si^{4+} in the activation system played an important role in the degree of hydration and mechanical strength of geopolymers [2–5].

Researchers have basically reached a consensus on the formation process of geopolymers in metakaolin, which can be divided into three stages: 1) dissolution and reconstruction of aluminosilicate in metakaolin, 2) the regenerated silicon tetrahedron and aluminum oxide tetrahedron are condensed to form small geopolymer gels, 3) the small aggregates of small gels are continuously aggregated to form highly polymerized geopolymers [6–9].

J.P. Gevaudan's studies have shown that alkali content affects the amount of silica used in geopolymer water and the process, determines the type and structure of final polymer formation, and affects the overall properties of geopolymers, such as permeability and porosity [10]. They believed that the increase of pH value promoted the dissolution of aluminosilicate in the first stage, and Na^+ played an important role in the second stage. At the same time, the higher the concentration of the activator, the higher the rate of condensation of tetrahedron and the higher the order of the structure. Based on this study, clear relationships were found between the reaction processes and chemical deformations. Furthermore, a conceptual model of the reaction processes and corresponding chemical deformation is proposed based on experimental results and theoretical calculations [11]. The effect of alkaline cation on the compressive strength of metakaolin polymer was studied. The results showed that the compressive strength of metakaolin polymer was highly dependent on the metal cation of the activator. Na^+ polymer had higher compressive strength than the K^+ polymer at the same Si/Al ratio and alkali metal ion concentration with higher concentration of Na^+ observed; higher compressive strength of the geopolymer is formed [10, 11].

In this paper, we consider the influence of Na^+ on the hydration degree of alkali activated metakaolin geopolymer, selecting two factors controlling the content of Na^+ in the geopolymer system as the object. The factors were the modulus of basic sodium silicate and the Na_2O equivalent. In addition, we analyzed the role of Na^+ in the three stages of the geopolymerization and the effect on the overall hydration degree.

2. Methods

2.1. Raw materials

This experiment uses metakaolin produced by ASUS mineral products company of Lingshou, China as raw material for preparing metakaolin polymer. Its chemical composition is shown in Table 1. The activator is composed of NaOH and sodium silicate composite activator, of which sodium silicate is industrial grade sodium silicate produced by Harbin Qiang Li sodium silicate factory (50 Bo Mei degree). NaOH provides analytical pure sodium hydroxide (NaOH, purity 96 %) for China National Pharmaceutical Group Chemical Reagent Co., Ltd.

Table 1 Chemical composition of metakaolin (weight%).

SiO_2	Al_2O_3	TiO_2	Fe_2O_3	MgO	GaO	Na_2O	K_2O
52	45	1.5	0.5	0.5	0.2	0.2	0.1

2.2. Preparation of metakaolin polymer

In this paper, the preparation method of the metakaolin polymer is made of paste, and its preparation method is strictly referenced to the national standard cement mortar strength testing method (IOS method). The local test procedure has been adjusted because of the particularity of the metakaolin polymer paste.

1. Solid analytical pure sodium hydroxide was added the sodium silicate to produce a solution complying with the modulus requirements of of the test. In this process, the problem of exothermic heat will occur, so after adding sodium hydroxide to stir and dissolve it, we need to seal it with plastic film and keep it for 24 hours.

2. The water consumption (deionized water) was added to the quantitative sodium silicate in the experiment, so that it can be mixed evenly and placed at normal temperature (not placed in the control group).

3. The metakaolin solution and the solution in second step was added into the mortar mixer (planetary cement mortar mixer). The mix process took 240 seconds, and then the mixture was stirred slowly for 60 s, and quickly for 180 s.

4. The colloid obtained in the third step was supplied into the mortar test mold of 40 cm×40 cm×160 cm, because the geopolymer paste is thicker than the cement paste, so it is necessary to manually compact the polymer paste and then place it on the sand shaking table for 60 s.

5. Polyethylene plastic film was used to seal the surface of the mould to prevent the water from evaporating rapidly, and then the trial mould was put into the curing box for maintenance.

The specimen composition is shown in Table 2.

Table 2 Specimen composition table.

Paste number	modulus	Na_2O equivalent	Water solid ratio	Paste number	modulus	Na_2O equivalent	Water solid ratio
M_{1-8}	1	8	0.5	$M_{2.0-8}$	2.0	8	0.5
M_{1-12}	1	12	0.5	$M_{2.0-12}$	2.0	12	0.5
M_{1-18}	1	18	0.5	$M_{2.0-18}$	2.0	18	0.5
M_{1-24}	1	24	0.5	$M_{2.0-24}$	2.0	24	0.5
M_{1-30}	1	30	0.5	$M_{2.0-30}$	2.0	30	0.5
$M_{1.5-8}$	1.5	8	0.5	$M_{2.5-8}$	2.5	8	0.5
$M_{1.5-12}$	1.5	12	0.5	$M_{2.5-12}$	2.5	12	0.5
$M_{1.5-18}$	1.5	18	0.5	$M_{2.5-18}$	2.5	18	0.5
$M_{1.5-24}$	1.5	24	0.5	$M_{2.5-24}$	2.5	24	0.5
$M_{1.5-30}$	1.5	30	0.5	$M_{2.5-30}$	2.5	30	0.5

2.3. Mechanical properties of metakaolin polymer

The mechanical properties test of the metakaolin polymer is strictly referenced to the national standard GB/T17671-1999 cement mortar strength detection method (IOS method). Compressive strength and flexural strength of metakaolin polymer slurry at the ages of 3 days, 7 days and 28 days are tested by compressive strength test machine and bending strength tester respectively. The average value of the same three specimens is taken as the corresponding compressive and flexural strength.

2.4. Microscopic characterization of metakaolin polymer

At the same time, mechanical tests were carried out to collect the microscopic test samples of the polymer mortar of the mountain ridge. The size of the specimen was about 50–5000 cm^2. The specimen was chosen from the naturally shedding polymer parts after the strength test, and was selected for scanning electron microscope (SEM) for the Korean company EM-30 plus.

After the strength test, the samples of 1 cm^3 were selected for infrared spectrum and X-ray diffraction test. The samples were processed before the test, and the collected samples were ground in the mortar to make the particle diameter of the sample as small as possible.

3. Result and Discussion

3.1. Effect of Na_2O equivalent on compressive strength of metakaolin polymer

Na_2O equivalent and strength effect of MK geopolymer is shown in Fig. 1. The results show that the compressive strength increases first and then decreases with the increase of Na_2O equivalent in the case of a given alkali activator modulus, and reaches the peak value at 18 %, with the increase of Na_2O equivalent to 24 %. The strength of 3 days and 7 days can be observed approximately in the same direction, but the rate of change is obvious. In the case of low modulus, the compressive strength varies significantly with the change of Na_2O equivalent. When Na_2O equivalence is in the range of 8–12 % and 24–30 %, the intensity change rate is extremely high.

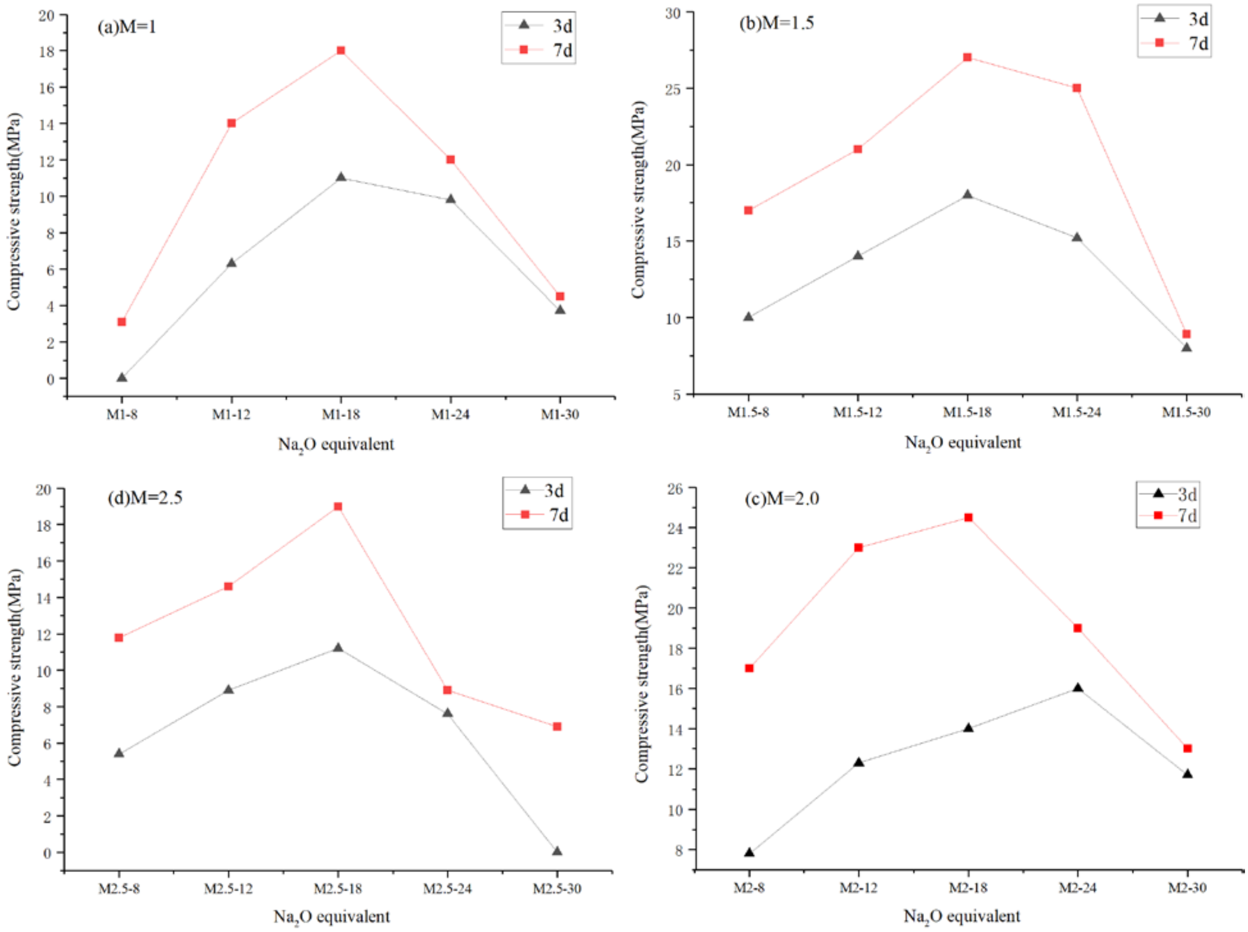

Figure 1. Relationship between the Na2O equivalent and strength of MK geopolymer.

High compressive strength of the metakaolin polymer is due to its dense three-dimensional network shape and state and its stable high polymerization framework, sodium aluminosilicate gel (NASH) [11–15]. Therefore, the compressive strength of metakaolin geopolymer can also reflect the process of metakaolin polymerization. In the same geopolymerization system, the higher the degree of hydration of metakaolin geopolymer, the more complete the geopolymerization, the more complete the NASH structure, the higher the degree of polymerization. By analyzing the effect of different Na_2O equivalent of alkali activator on the compressive strength of the metakaolin polymer, it is known that Na_2O equivalence has an important effect on the hydration degree of the kaolin polymer. When Na_2O equivalence is less than 18 %, the degree of hydration of the metakaolin polymer is increasing with the increase of Na_2O equivalent. It has a positive effect. When Na_2O equivalence is greater than 18 %, with the increase of Na_2O equivalent, the degree of hydration of the metakaolin polymer decreases and has inhibitory effect.

In Fig. 1, the 18 % of the Na_2O equivalent is the optimum activation environment for the hydration reaction of metakaolin. The Na_2O equivalence is less than 18 %. The Na^+ content in the metakaolin land polymerization system is insufficient to support the geopolymerization of metakaolin. Studies have shown that the three-dimensional structure skeleton of geopolymer is obtained through oxygen bridge linking silicon oxygen and aluminum oxide. The Al^{3+} ions in the framework can replace Si^{4+}, which leads to the generation of negative charges, and the negative charge needs to be balanced by metal cations in the alkaline activator [16–18]. The concentration of Na^+ plays an important role in the condensation of second phase silicon oxy tetrahedron with aluminum oxide tetrahedron in the reaction of metakaolin.

The empirical formula of geopolymer is shown in Fig. 2 [19]. Na^+ ion concentration is too low to meet the need of the second stage equilibrium charge, which will result in the termination of the reaction. At the same time, the Na^+ guiding role is also needed in the third stage of conversion from oligomeric to high polymer state. For example, the concentration of Na^+ is insufficient, and the polymerization degree of metakaolin polymer decreases, the polymerization chain shortens, and the structure is missing. The content of silicon in activator increases with the increase of Na_2O equivalent, thus increasing the number of available silicon and accelerating the hydration process of metakaolin. As the three stages of the geopolymerization occur at the same time, when the Na_2O equivalent is greater than 18 %, the reaction in the second and third stages will occur rapidly, and the polymer with low or high polymer will rapidly form on the surface of metakaolin. The metakaolin raw material is wrapped so that it can not be dissolved in contact with the alkaline solution, thus inhibiting the hydration degree of the metakaolin polymer.

$$M_n(-(SiO_2)_Z-AlO_2)_n,\omega H_2O \quad \text{(Inspection structure)}$$

$$n(Si_2O_5,Al_2O_2)+2nSiO_2+4H_2O \xrightarrow{KOH,NaOH} n(OH)_3\text{-Si-O-Al-O-Si-}(OH)_3$$

$$\text{(Oligomer formation)}$$

$$n(OH)_3\text{-Si-O-Al-O-Si-}(OH)_3 \xrightarrow{KOH,NaOH} (Na,K)(\text{-Si-O-Al-O-Si-O-})$$

$$+4nH_2O \text{(Transition from low poly to high poly)}$$

Figure 2 The empirical formula of geopolymer.

3.2. Effect of modulus on compressive strength of metakaolin polymer

As shown in Fig. 3, the effect of modulus of alkali activator on the compressive strength of metakaolin polymer is studied. The results show that the compressive strength of the metakaolin polymer increases with the increase of the modulus of the alkali activator at the given Na_2O equivalent, and reaches the peak value from 1.5 to 2, when the modulus is greater than 2. The strength clearly decreases when the Na_2O equivalence is at 12 % and 24 % (as shown in a_2 and a_4 in Fig. 3), the inflection point of 3 days and 7 days compression strength curve is not consistent. At 12 %, the compressive strength of 3 days reaches a peak at 1.5 modulus and then decreases; at 24 %, the compressive strength reaches the peak value of 7 days at 2 modulus and then decreases. On the surface of $M_{1\text{–}8}$, it is obvious that the water accumulated, and the surface of $M_{2.5\text{–}30}$ has hardened and formed a layer of sodium silicate shell, but the interior has not yet solidified. It is found that when the modulus is greater than 2, with the increase of modulus, the development of early strength will slow down or even stagnate.

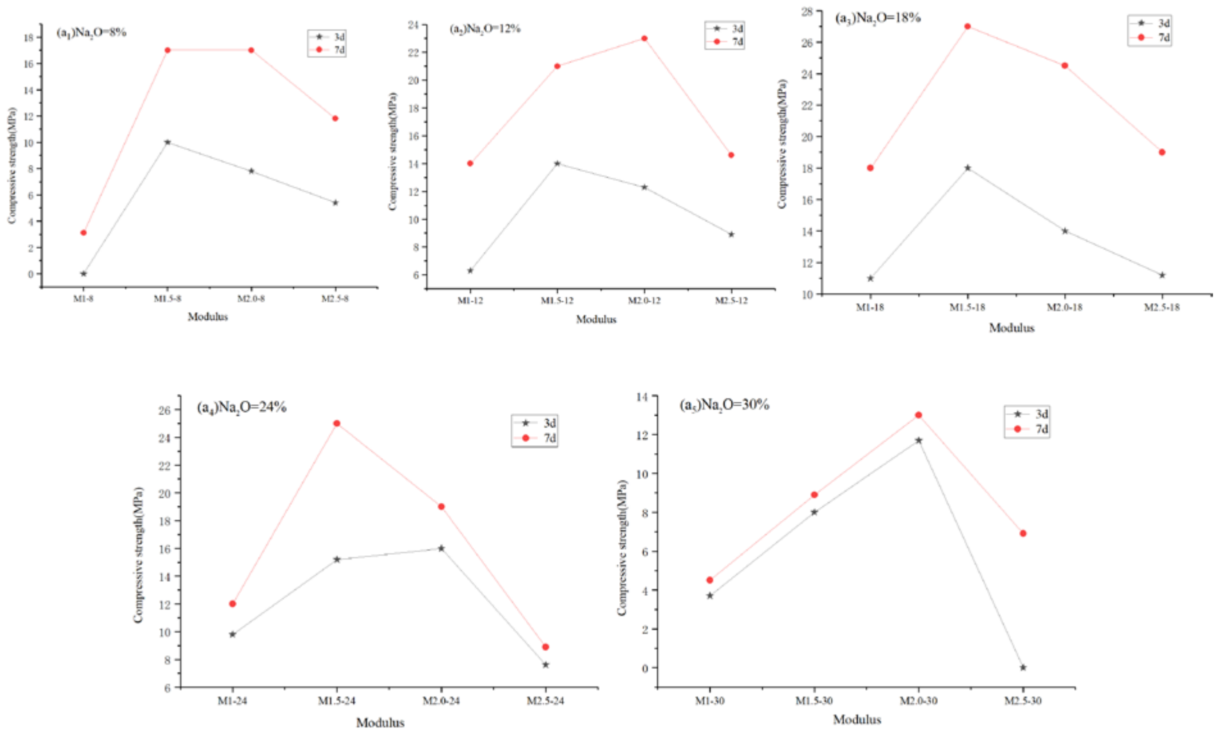

Figure 3. Effect of modulus on the aggregation strength of metakaolin land.

By analyzing the effect of different moduli of alkali activator on the compressive strength of metakaolin polymer, the modulus has an important effect on the degree of hydration of the metakaolin polymer. When the activation modulus is less than 1.5, the hydration degree of metakaolin increases with the increase of modulus. When the activation modulus is greater than 2, the hydration degree of metakaolin can be inhibited as the modulus increases.

Studies have shown that the first stage of hydration reaction of metakaolin is aluminosilicate dissolved into silicon aluminum monomer. During this process, when the modulus of the activator is too low, less than 1.5, the initial Na^+ concentration will be very high, which will accelerate the reaction rate of the 2nd or 3rd stage and inhibit the dissolution of aluminosilicate. The amount of silicon available in the geopolymerization system is reduced. However, when the modulus is greater than 2, the aluminum dissolution from metakaolin will tend to react with SiO_3^{2-} in the alkaline activator and hinder the dissolution of silicon in metakaolin [11]. The rate of dissolution of silicon monomer in metakaolin is slowed down [20]. The composition and quantity of Nash gel formed in the process of geopolymerization depend on the degree of reaction of precursors [21]. Therefore, the degree of hydration of metakaolin is high if the precursor material is dissolved sufficiently. On the contrary, the residual amount of precursor material is high, and the degree of hydration is low.

In the first stage of the dissolution of aluminosilicate, the aluminum monomer will first be dissolved, because the bond length of Al-O is 1.75 Å, the bond length of Si-O is 1.61 Å, and the electronegativity of aluminum is small, so the binding force of Al-O is smaller than that of Si-O bond [22]. It inhibited the precipitation of silicon monomer, when the modulus of the alkali activator was greater than 2, the Na^+ decreased with the increase of the modulus. Therefore, the reaction rate of the 2nd or 3rd phases would be reduced, resulting in slower consumption of aluminum monomer, restricting the dissolution of silicate and inhibiting the hydration degree of metakaolin [15]. At the same time, due to the increase of modulus, the concentration of OH^- in geopolymer system is reduced, so that metakaolin does not completely dissolve, and there will be remnants, resulting in lower degree of hydration of metakaolin.

When alkali activator modulus is too large, due to the low alkalinity in the reaction environment and low content of OH^-, the dissolution of aluminosilicate in metakaolin is less, and the formation of Si/Al monomer is insufficient, resulting in lower hydration degree of metakaolin. However, when the activator modulus is too small, the aluminosilicate in the metakaolin is completely dissolved, but the remaining components in the activator fill in the gap. The activator is easily soluble in water and easily destroys the structure of polymer.

3.3. SEM analysis

The specimens were scanned simultaneously by scanning electron microscope (SEM) after the compressive strength test. Fig. 4 shows the SEM images of metakaolin geopolymer with different moduli, when the Na_2O equivalent was 18 %. By comparing a, b, c, d, we can see that B showed the most complete form of polymer gelation, of which Na-G indicated that the gel was of uniform texture and good morphology of polymerization. The results are consistent with the test results of compressive strength.

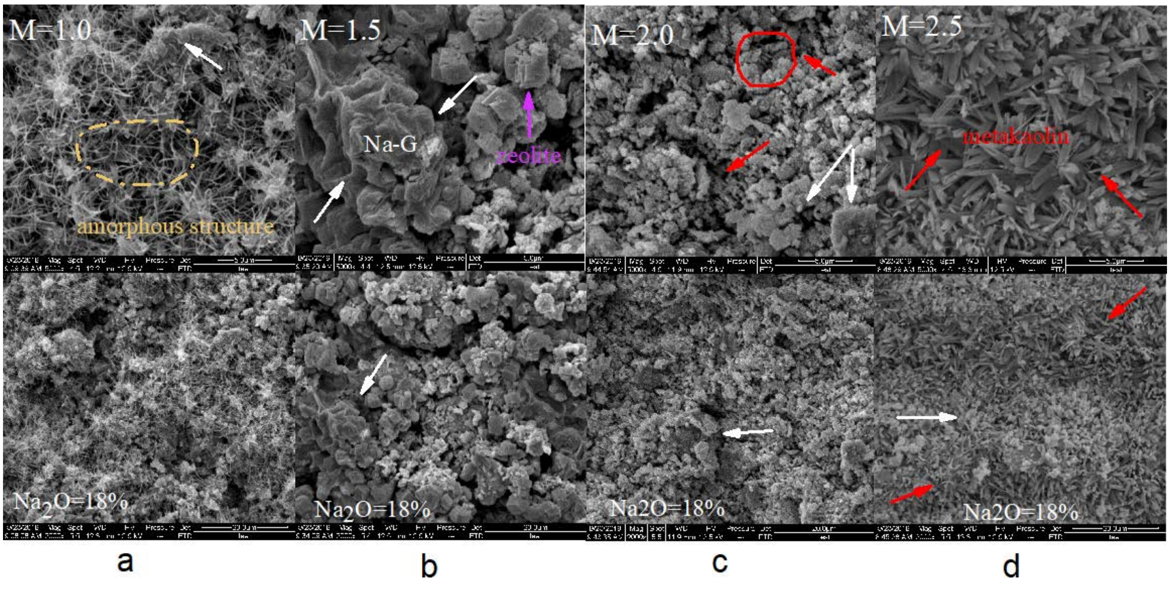

Figure 4. SEM images of metakaolin polymers with different modulus at 18% Na_2O equivalent.

At the same time, the existence of zeolites was observed in the B diagram, such as the purple arrow. Some studies have shown that the formation of NASH gel will be accompanied by the formation of some by-product zeolite crystals [10], for example, zeolite ZSM-3, zeolite A, zeolite P, sodium carbonate, zeolite 5p and so on. Some studies also suggest that NASH can be transformed into zeolites in time or some other external conditions to form a more stable structure [23].

In Fig. 4a, it could be seen clearly that there are long hairy or silk flocculent amorphous substances on the surface of NASH gel. This phenomenon is observed in three images of b, c and d. However, Fig. 5a$_1$ and 5a$_2$ show a similar phenomena, but the number is less than that of the map. The amorphous length of hairy or floc is very short. We think that the amorphous structure is made up of two parts. The first part is the ionic group formed by ions in the activator remaining in the hydrated system of metakaolin. The second part is the silicon aluminum monomer, which is used in the uncondensed reaction. The dissolution reaction of metakaolin aluminosilicate is quite complete at this time. The concentration of Si/Al monomer is very high, and at this time, because the concentration of Na^+ is not enough to support such a high concentration of Si/Al monomer to form small geopolymer gels (Si-O-Al-O, Si-O-Al-O-Si-O), the Si/Al monomer will adhere to the surface of geopolymer to form a hairy or silk flocculent amorphous structure.

Fig. 4c and 4d clearly demonstrates that the degree of polymerization of the geopolymer in metakaolin is reduced, the particle size is small, the geopolymer formed is small gel structure, the skeleton is relatively small, the structure is incomplete, the porosity is high, and there are a large number of unreacted kaolin precursors. This conclusion is consistent with the test results of compressive strength. When the concentration of Na_2O is too high, the dissolution of aluminosilicate in metakaolin can be inhibited, the number of unresponsive metakaolin increases, and the degree of hydration of metakaolin decreases.

In Fig. 4, it is obvious that the degree of polymerization of a_2 and a_4 metakaolin polymer is lower than the polymerization degree of a_3. When Na_2O equivalence is less than 18 %, the degree of polymerization of metakaolin polymer is increasing with the increase of Na_2O equivalent, and the texture is more uniform and ordered. When the a is greater than 18 %, the degree of polymerization of metakaolin decreases continuously, from large gel group to small gel particle, and at the same time the unresponsive metakaolin precursor begins to appear. In Fig. 5a_5, the particles of unresponsive metakaolin can be observed clearly. This conclusion can further confirm the strength test results of the metakaolin polymer.

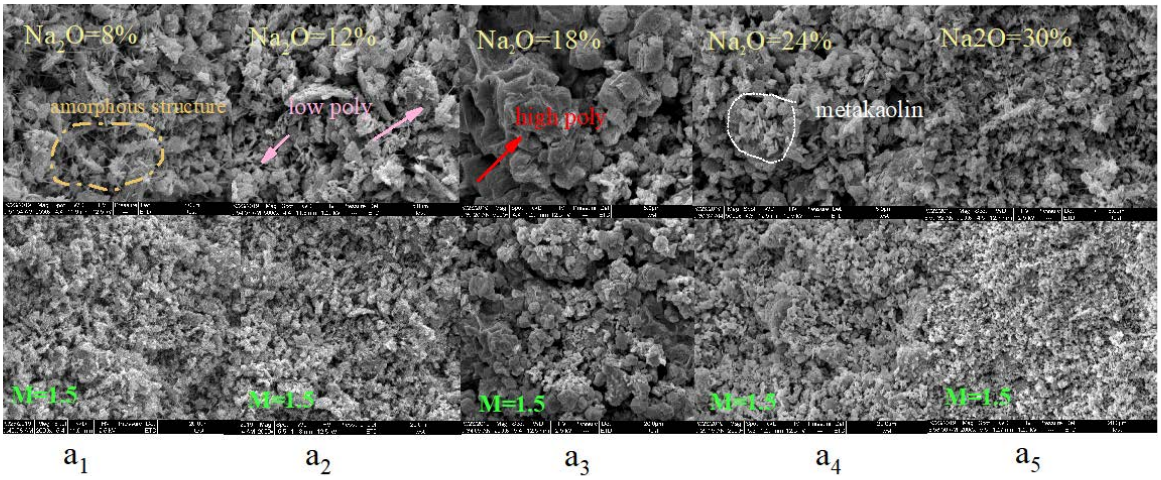

Figure 5. SEM images of metakaolin polymers with different Na_2O equivalents at 1.5 modulus.

3.4. FT-IR and XRD analysis

The FTIR spectra of metakaolin and metakaolin polymers are shown in Fig. 6. The FT-IR spectra of metakaolin polymer are selected by 3 days and 7days of $M_{1.5–18}$ specimens. In the infrared spectra of metakaolin, the wide peaks between 1000 $cm^{–1}$ and 1100 $cm^{–1}$ are considered to be asymmetrical tensile vibrations of silicon tetrahedron and alumino oxygen tetrahedron [24–26]. By comparing the FT-IR spectra of 3 days and 7 days, the spectra of metakaolin polymer can be found to be basically the same, mainly at 700 $cm^{–1}$. The FT-IR spectrum of 7 days has a weak absorption peak between 600 $cm^{–1}$ to 700 $cm^{–1}$ [24]. 3 days and 7 days of $M_{1.5-18}$ FT-IR spectra show strong absorption peaks at 900 $cm^{–1}$ to 1000 $cm^{–1}$. Judging by other analyzed references, it seems to be caused by the asymmetric tensile vibration of Si-O-T [26]. Compared with metakaolin, this absorption peak shifts to the left, which we think is the cause of the formation of NASH [26].

The XRD images of metakaolin and metakaolin geopolymer are shown in Fig. 7. The geopolymer test samples are $M_{1.5–18}$ and $M_{2.5–30}$. It is mainly considered that the strength results can be interpreted and verified. Comparing the XRD images of metakaolin precursor materials, $M_{1.5–18}$ and $M_{2.5–30}$, we can see that the width of the peak between diffraction angle (20° – 40°) of $M_{1.5–18}$ specimen is obviously larger than that of $M_{1.5–18}$ and metakaolin because of the dissolution of aluminosilicate crystals in metakaolin under the action of alkaline activator. Then, the NASH gel was formed by geopolymerization. The gel was a high polymer and an amorphous structure [22]. At the same time, $M_{2.5–30}$ display the characteristics of quartz and halloysite in this interval. Therefore, $M_{2.5–30}$ can be considered to have low dissolution rate of aluminosilicate in the process of polymerization, resulting in its early compressive strength being particularly low. In the XRD image of $M_{1.5–18}$, the characteristics of Zeolite A were observed, but no phase characteristics of calcite were found. There is also the existence of halloysite and quartz.

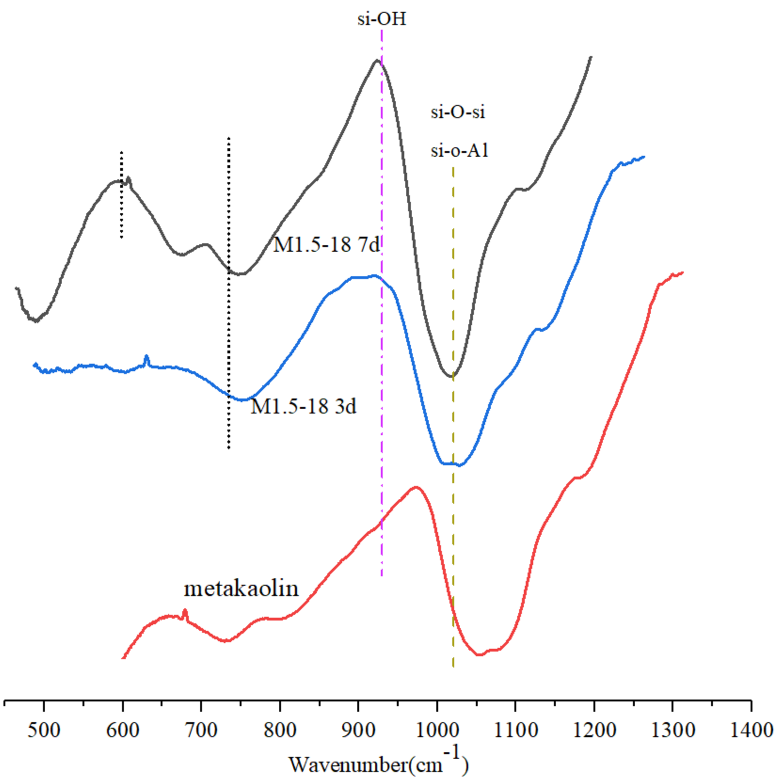

Figure 6. FT-IR spectra of metakaolin and metakaolin land polymer.

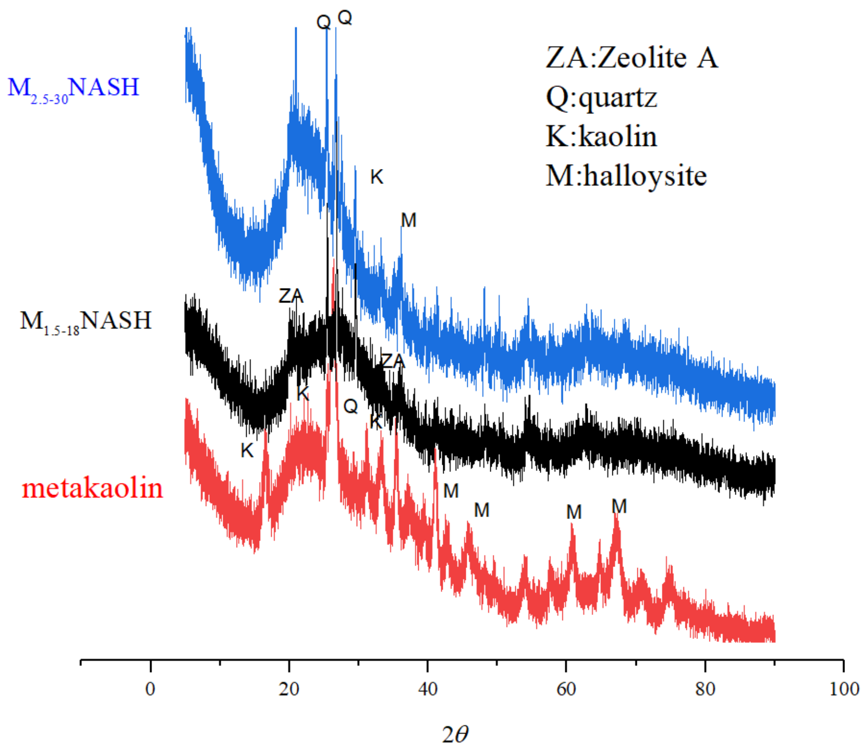

Figure 7. XRD pattern of metakaolin and geopolymer.

4. Conclusion

This paper studied the effect of Na^+ on the hydration degree of alkali activated metakaolin polymer. The effects of Na_2O equivalent and the modulus of alkali activator on the strength and microstructure of the kaolin polymer were demonstrated. The results of the study led to the following conclusions:

1. 18 % Na_2O equivalent is the activation environment for the highest degree of hydration of metakaolin geopolymer. When Na_2O equivalence is less than 18 %, the degree of hydration of metakaolin geopolymer increases with the increase of Na_2O equivalent. When the Na_2O content is greater than 18 %, as the Na_2O equivalent increases, it will inhibit the hydration reaction of the geopolymer reducing its degree of hydration.

2. When the modulus of alkali activator is 1.5, the maximum hydration degree of the geopolymer can be achieved. When the modulus is less than 1.5, the rate of polymer reaction will accelerate and the hydration degree will be accelerated with the increase of the modulus. When the modulus is greater than 2, the reaction of the first stage of the metakaolin hydration process will be inhibited with the increase of modulus, and the hydration degree of metakaolin will be reduced.

3. When Na_2O equivalence is less than 18 %, the degree of polymerization of metakaolin polymer is increasing with the increase of Na_2O equivalent, and the texture is more uniform and structured. $M_{2.5–30}$ has low dissolution rate of aluminosilicate in the process of polymerization, resulting in its early compressive strength being particularly low.

References

1. Asghari, A., Khorrami, M.K., Kazemi, S.H. Hierarchical H-Zsm5 Zeolites Based on Natural Kaolinite as a High-Performance Catalyst for Methanol to Aromatic Hydrocarbons Conversion. Scientific Reports. 2019. No. 9. No. 1. Pp. 17526. http://dx.doi.org/10.1038/s41598-019-54089-y
2. Belmokhtar, N., Ammari, M., Brigui, J., Ben Allal, L. Comparison of the Microstructure and the Compressive Strength of Two Geopolymers Derived from Metakaolin and an Industrial Sludge. Construction and Building Materials. 2017. No. 146. Pp. 621–29. http://dx.doi.org/10.1016/j.conbuildmat.2017.04.127
3. Cheng-Yong, H., Yun-Ming, L., Abdullah, M.M., Hussin, K. Thermal Resistance Variations of Fly Ash Geopolymers: Foaming Responses. Scientific Reports. 2017. No. 7. Pp. 45355. http://dx.doi.org/10.1038/srep45355
4. Deng, G., Yongjia, H., Linnu, L., Shuguang, H. The Effect of Activators on the Dissolution Characteristics and Occurrence State of Aluminum of Alkali-Activated Metakaolin. Construction and Building Materials. 2020. No. 235. DOI: 10.1016/j.conbuildmat.2019.117451
5. Gao, K., Lin, K.L., Wang, D., Hwang, C.L., Shiu, H.S., Chang, Y.M., Cheng, T.W. Effects Sio_2/Na_2o Molar Ratio on Mechanical Properties and the Microstructure of Nano-Sio2 Metakaolin-Based Geopolymers. Construction and Building Materials. 2014. No. 53. Pp. 503–10. http://dx.doi.org/10.1016/j.conbuildmat.2013.12.003
6. Gevaudan, J.P., Campbell, K.M., Kane, T.J., Shoemaker, R.K., Srubar, W.V. Mineralization Dynamics of Metakaolin-Based Alkali-Activated Cements. Cement and Concrete Research. 2017. No. 94. Pp. 1–12. http://dx.doi.org/10.1016/j.cemconres.2017.01.001
7. Hou, L., Li. J., Lu, Z.-Y. Effect of Na/Al on Formation, Structures and Properties of Metakaolin Based Na-Geopolymer. Construction and Building Materials. 2019. No. 226. Pp. 250–58. http://dx.doi.org/10.1016/j.conbuildmat.2019.07.171
8. Jaya, N.A., Liew, Y.-M., Heah, C.-Y., Abdullah, M.M.A.B., Hussin, K. Correlation between Pore Structure, Compressive Strength and Thermal Conductivity of Porous Metakaolin Geopolymer. Construction and Building Materials. 2020. No. 247. Pp. 118641. http://dx.doi.org/https://doi.org/10.1016/j.conbuildmat.2020.118641
9. Król, M., Rożek, P., Chlebda, D., Mozgawa, W. Atr/Ft-Ir Studies of Zeolite Formation During Alkali-Activation of Metakaolin. Solid State Sciences. 2019. No. 94. Pp. 114–19. http://dx.doi.org/10.1016/j.solidstatesciences.2019.06.004
10. Lahoti, M., Narang, P., Tan, K.H., Yang, E.H. Mix Design Factors and Strength Prediction of Metakaolin-Based Geopolymer. Ceramics International, 2017. Vol. 43. No. 14. Pp. 11433–41. http://dx.doi.org/10.1016/j.ceramint.2017.06.006
11. Li, Z., Zhang, S., Zuo, Y., Chen, W., Ye, G. Chemical Deformation of Metakaolin Based Geopolymer. Cement and Concrete Research. 2019. No. 120. Pp. 108–18. https://doi.org/10.1016/j.cemconres.2019.03.017
12. Longhi, M.A., Walkley, B., Rodríguez, E.D., Kirchheim, A.P., Zhang, Z., Wang, H. New Selective Dissolution Process to Quantify Reaction Extent and Product Stability in Metakaolin-Based Geopolymers. Composites Part B: Engineering. 2019. No. 176. Pp. 10.1016/j.compositesb.2019.107172
13. Medpelli, D., Seo, J.M., Seo, D.K. Geopolymer with Hierarchically Meso-/Macroporous Structures from Reactive Emulsion Templating. Journal of the American Ceramic Society. 2014. Vol. 97. No. 1. Pp. 70–73. http://dx.doi.org/10.1111/jace.12724
14. Park, S., Pour-Ghaz, M. What Is the Role of Water in the Geopolymerization of Metakaolin? Construction and Building Materials, 2018. No. 182. Pp. 360–70. http://dx.doi.org/10.1016/j.conbuildmat.2018.06.073
15. Riahi, S., Nemati, A., Khodabandeh, A.R., Baghshahi, S. The Effect of Mixing Molar Ratios and Sand Particles on Microstructure and Mechanical Properties of Metakaolin-Based Geopolymers. Materials Chemistry and Physics. 2020. No. 240. DOI: 10.1016/j.matchemphys.2019.122223
16. Rocha, T.d.S., Dias, D.P., França, F.C.C., Guerra, R.R.D.S., Marques, L.R.D.C.D.O. Metakaolin-Based Geopolymer Mortars with Different Alkaline Activators (Na^+ and K^+). Construction and Building Materials. 2018. No. 178. Pp. 453–61. https://doi.org/10.1016/j.conbuildmat.2018.05.172
17. Shi, Z., Shi, C., Wan, S., Zhang, Z. Effects of Alkali Dosage and Silicate Modulus on Alkali-Silica Reaction in Alkali-Activated Slag Mortars. Cement and Concrete Research. 2018. No. 111. Pp. 104–115. http://dx.doi.org/10.1016/j.cemconres.2018.06.005
18. Sun, Z., Vollpracht, A., an der Sloot, H.A. Ph Dependent Leaching Characterization of Major and Trace Elements from Fly Ash and Metakaolin Geopolymers. Cement and Concrete Research. 2019. No. 125. DOI: 10.1016/j.cemconres.2019.105889.
19. Tchuente, F.M., Tchakouté, H.K., Banenzoué, C., Rüscher, C.H., Kamseu, E., Andreola, F., Leonelli, C. Microstructural and Mechanical Properties of (Ca, Na)-Poly(Sialate-Siloxo) from Metakaolin as Aluminosilicate and Calcium Silicate from Precipitated Silica and Calcined Chicken Eggshell. Construction and Building Materials. 2019. No. 201. Pp. 662–75. https://doi.org/10.1016/j.conbuildmat.2018.12.219
20. Wan, Q., Rao, F., Song, Sh., García, R.E., Estrella, R.M., Patiño, C.L., Zhang, Y. Geopolymerization Reaction, Microstructure and Simulation of Metakaolin-Based Geopolymers at Extended Si/Al Ratios. Cement and Concrete Composites, 2017. No. 79. Pp. 45–52. https://doi.org/10.1016/j.cemconcomp.2017.01.014

21. Wianglor, K., Sinthupinyo, S., Piyaworapaiboon, M., Chaipanich, A. Effect of Alkali-Activated Metakaolin Cement on Compressive Strength of Mortars. Applied Clay Science. 2017. No. 141. Pp. 272–79. http://dx.doi.org/10.1016/j.clay.20-17.01.025
22. Zhang, F., Zhang, L., Liu, M., Mu, Ch., Liang, Y.N., Hu, X. Role of Alkali Cation in Compressive Strength of Metakaolin Based Geopolymers. Ceramics International. 2017. Vol. 43. No. 4. Pp. 3811–17. http://dx.doi.org/10.1016/j.ce-ramint.2016.12.034
23. Zhang, M., Zhao, M.X., Zhang, G.P., El-Korchi, T., Tao, M.J. A Multiscale Investigation of Reaction Kinetics, Phase For-mation, and Mechanical Properties of Metakaolin Geopolymers. Cement & Concrete Composites. 2017. No. 78. Pp. 21–32. http://dx.doi.org/10.1016/j.cemconcomp.2016.12.010
24. Zhang, M., Zhao, M., Zhang, G., El-Korchi, T., Tao, M. A Multiscale Investigation of Reaction Kinetics, Phase Formation, and Mechanical Properties of Metakaolin Geopolymers. Cement and Concrete Composites. 2017. No. 78. Pp. 21–32. https://doi.org/10.1016/j.cemconcomp.2016.12.010
25. Zhang, Z., Wang, H., Provis, J.L., Bullen, F., Reid, A., Zhu, Y. Quantitative Kinetic and Structural Analysis of Geopolymers. Part 1. The Activation of Metakaolin with Sodium Hydroxide. Thermochimica Acta. 2012. No. 539. Pp. 23–33. https://doi.org/10.1016/j.tca.2012.03.021
26. Zibouche, F., Kerdjoudj, H., de Lacaillerie, J.-B.d'E., van Damme, H.. Geopolymers from Algerian Metakaolin. Influence of Secondary Minerals. Applied Clay Science. 2009. Vol. 43. No. 3-4. Pp. 453–58. http://dx.doi.org/10.1016/j.clay.2008.11.001

Information about authors:

***Yagebai Zhao**, D.Sc.*
E-mail: 270286835@qq.com

***Hongguang Wang**, PhD*
ORCID: https://orcid.org/0000-0002-7620-614X
E-mail: wanghongguang@zoho.com

Yao He
E-mail: 1436287817@qq.com

Lanjie Yang
E-mail: yanglanjie@nefu.edu.cn

Hao Wu
E-mail: 2111566167@qq.com

Received 17.06.2020. Approved after reviewing 08.10.2021. Accepted 09.10.2021.

Magazine of Civil Engineering

ISSN 2712-8172

journal homepage: http://engstroy.spbstu.ru/

Research article
UDC 627.832
DOI: 10.34910/MCE.112.9

Telescopic water intake with stilling well

A.A. Lipin

Azerbaijan SPU of Hydro technique and melioration, Baku, Azerbaijan

dorian.lipin@gmail.com

Keywords: water, structure, calculation, CFX, finite element method, improvement.

Abstract. Telescopic water intake structures have an important role in the water management system. Telescopic water intake has high mobility and wide field of application; at the same time, it is very simple and convenient to operate. But despite these advantages, there is no structural solution for flow energy dissipation in the downstream, no exact calculation method of flow energy dissipating structure, no structural solution to prevent floating objects entering inside the water intake structure, and no structural solution to stop water intake operation. In this regard, the purpose of this research is to improve the design of the existing telescopic water intake, to develop the design and calculation method for the stilling well. Structural solution for flow energy dissipation by means of stilling well is proposed. To protect the water intake from the ingress of floating objects and debris, protective mesh is designed. A shutter is provided to stop water intake operation of the unit. Methodology for analytical hydraulic calculation of a stilling well has been developed. In order to verify above mentioned calculation methodology, analytical calculations and numerical modeling of specific example were performed. The following results of analytical calculation of the main parameters of stilling well were obtained: length and depth. The results of numerical modeling demonstrated effective energy dissipation in the stilling well and acceptable flow velocity at the entrance to the channel.

Citation: Lipin, A.A. Telescopic water intake with stilling well. Magazine of Civil Engineering. 2022. 112(4). Article No. 11209. DOI: 10.34910/MCE.112.9

1. Introduction

In water management, water supply, energy and other areas of the economy, water intake structures with different designs and operating principles are used to draw water from different sources. In the vast majority, depending on topographic, geological and geographical conditions, frontal, side, bottom and tower intakes are used [1–11]. Each type of water intake structure has specific features and disadvantages. The main disadvantages of these water intake structures are the following:

1. When the water level in the sources fluctuates, their productivity (consumption) changes;

2. In springs filled with melt and spring waters, as well as waters of mountain rivers, the lower horizons have low temperatures compared to the upper ones. The water taken from these sources and supplied for irrigation has a detrimental effect on soil fertility and crop productivity. When the water temperature drops below 20 °C, the yield of agricultural crops in arid zones decreases by 30–40 %, and when the water temperature drops below 15 °C, agricultural crops completely die [12–15]. Along with this, when the temperature of the irrigation water drops below the temperature of the soil, its biological activity deteriorates, the process of nitrification and humification is disrupted;

3. When water is taken by known water intake structures, the purity and clarity of the taken water is not maintained, since during operation, suspended and bottom sediments are supplied to them.

In the middle of the last century in Japan, surface water intakes of various designs were developed under various names [16–20]. Analyzing the principle of operation and design features, as well as the identified shortcomings of known surface water intake structures and devices, a new telescopic water intake device was developed [21].

Developed telescopic water intake contains a float, an inlet funnel, telescopically connected pipes tapering downward, an elbow with a discharge pipe and connecting elements. In order to prevent cavitation, a cone-shaped air supply pipe with a protrusion directed towards the inlet funnel is installed in the middle part of the float. To ensure the automatic movement of the float downward until the inlet funnel is closed in case of water absence (or liquid) or upon reaching a dead volume of water in the source, springs are installed in the lower part of the connecting elements (Fig. 1).

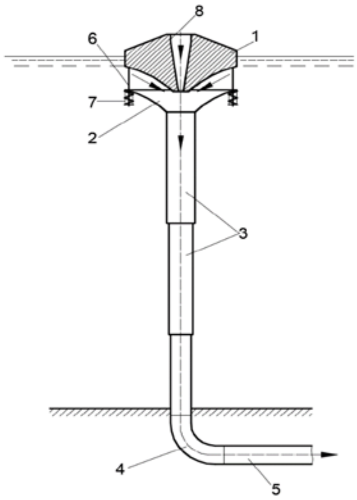

Figure 1. Construction of surface water intake:
1 – float, 2 – inlet funnel, 3 – telescopically connected pipes, 4 – elbow,
5 – outlet pipe, 6 – connecting element, 7 – springs, 8 – air-supply confuser.

The float, keeping the inlet funnel in the water immersed, provides a constant pressure at its inlet. In this case, water from the upper layers enters the funnel, and from there into the telescopically connected pipes, then through the elbow into the outlet pipeline.

When the water level in the source drops, telescopically connected pipes, funnel and float go down, and when the water level rises, they go up. Thanks to this, an automated water intake and a constant flow rate are provided, regardless of the effective pressure in the source. The water intake is carried out from the upper horizons, therefore, more clarified, cleaner and at the same time warmer water, heated by direct sunlight, enters the water intake.

When water enters the inlet funnel, the flow narrows and its speed increases, due to which vacuum and cavitation are formed. Air is sucked into the vacuum zone through the air supply pipe and the process of cavitation is prevented, characterized by the release of vapor-gas bubbles from the flow, causing crackling, noise and vibration, and ultimately erosion and destruction of the device. In the absence of water or reaching the dead volume in the source, the springs installed under the connecting elements ensure automatic closure of the inlet funnel.

Developed telescopic water intake has high mobility, wide field of application, at the same time, it is very simple and convenient to operate in comparison with known ones. Despite these advantages of water intake, it has several disadvantages. The telescopic water intake has high velocities at the exit from the outlet pipeline. In fact, when water is transported in an open way, i.e. by means of open canal, high entrance velocity to the canal leads to its erosion and destruction. The known device does not provide an element for stopping water intake in emergency situations, a stilling well for energy dissipation in the downstream and protective element to prevent floating and foreign objects from entering the inlet funnel, and then into the water intake. In addition, exact method for calculating a stilling structure is lacking.

In this regard, the purpose of this research is to improve the design of the existing telescopic water intake, to develop the design and calculation method for the stilling well.

2. Methods

In this research, structure of vertical telescopic water intake equipped with stilling well was analyzed by means of analytical calculations and numerical modeling [22–26].

If water intake is intended for water supply and transportation is carried out over long distances using a pipeline, then in this case there is no need for a stilling well.

When using a telescopic water intake, a sufficiently high working head is formed at the outlet of the outlet pipeline, and thus kinetic energy, which can be used to generate electrical energy by installing reactive electric turbine on the line at any convenient place in the outlet pipeline.

Thus, the water leaving the vertical telescopic water intake into the open channel at the outlet expands. The water leaving the diffuser gradually expands and at the end of the jet's flight reaches its maximum value. The jet expansion angle (θ_g) is equal to the diffuser taper angle (θ_d).

The diameter obtained at the end of the jet's flight can be taken as the depth of the water in the stilling well. In general, it is determined by the conjugate depth of the transporting channel [27, 28]:

$$a = h_2 - h_b, \tag{1}$$

where a is the depth of the stilling well (m); h_2 is conjugate depth (m); h_b is depth of water in the channel (m).

$$h_2 = D + 2L\text{tg}\frac{\theta}{2}, \tag{2}$$

The length of the flight of the jet leaving the diffuser (L) is determined depending on the speed and acceleration of gravity by the following equation [11, 14]:

$$L = v\sqrt{\frac{2(Z+0.5D)}{g}}, \tag{3}$$

where v is the speed of the jet leaving the diffuser, m/s; Z is the difference between the upstream and downstream pressures m; D is diameter at the outlet of the diffuser, m; g = 9.81 m/s^2 is acceleration of gravity.

The velocity of the jet leaving the diffuser (v) is calculated using the following equation:

$$v = \frac{4Q}{\pi D^2}, \tag{4}$$

where Q is the water intake flow rate, m^3/s; $\omega = \pi D^2 / 4\pi$ is area of the outlet part of the diffuser, m^2.

3. Results and Discussion

3.1. Analytical calculation

To prevent foreign floating objects from entering the water intake, cylindrical removable protective grid is installed around the connecting elements on the inlet funnel. To stop or regulate the flow rate of water taken from the source, a gate (valve) is installed in the downstream on the outlet pipeline, and a stilling well is built behind it to dissipate water energy [27] and prevent local erosion [30] (Fig. 2).

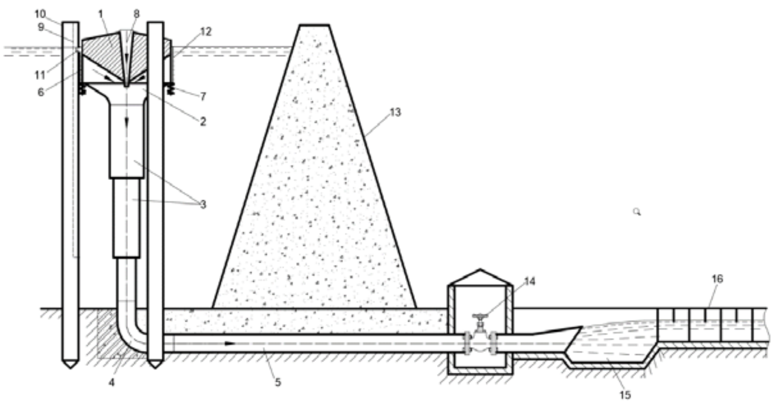

Figure 2. Scheme of telescopic water intake: 1 – float; 2 – entrance funnel; 3 – telescopically connected pipes; 4 – elbow; 5 – outlet pipeline; 6 – connector; 7 – release springs; 8 – air supply confuser; 9 – guide slot; 10 – piles; 11 – T-shaped ledge; 12 – lattice; 13 – dam; 14 – shutter; 15 – stilling well; 16 – channel.

The length of the stilling well is determined only by the length of the jet's flight. Therefore, the length of the jet flight determined by the equation (3) is taken as the length of the stilling well. Let us consider the hydraulic calculation of the proposed telescopic water intake using a specific example.

Example: Let us say the following parameters are set on the basis of the project:

- Estimated flow rate of the intake structure Q = 10 m³/s;
- The length of the outlet pipeline l = 20 m;
- Difference of upstream and downstream pressures Z = 10 m;
- Channel slope coefficient m = 1.5;
- Channel slope i = 0.001;
- channel roughness coefficient n = 0.017.

It is required to define the following parameters:

1. Diffuser diameter D;
2. The diameter of the outlet pipeline d;
3. Length of diffuser l;
4. Parameters of the drainage channel, including the bottom width b and the water depth in the channel h;
5. Average speed of water movement in the channel v;
6. The depth of the stilling well a;
7. The length of the stilling well L.

Solution. First, we take the system flow coefficient $\mu = 0.8$ and define the outlet diameter of the diffuser:

$$D = \sqrt{\frac{4Q}{\mu\pi\sqrt{2gZ}}} = \sqrt{\frac{4 \cdot 10}{0.8 \cdot 3.14\sqrt{2 \cdot 9.81 \cdot 10}}} \approx 1.1\,\text{m}.$$

Now we take the value of the vacuum in the system h_v = 6.5 m.w.s. and calculate the diameter of the outlet pipeline:

$$d = \sqrt{\frac{4Q}{\mu\pi\sqrt{2g\left(Z + h_v\right)}}} = \sqrt{\frac{4 \cdot 10}{0.8 \cdot 3.14\sqrt{2 \cdot 9.81(10 + 6.5)}}} = 0.94\,\text{m}.$$

We accept the taper angle of the diffuser 7° and calculate its length using the equation:

$$1 = \frac{D - d}{2\text{tg}\dfrac{\theta}{2}} = \frac{1.1 - 0.94}{2\text{tg}\dfrac{7}{2}} = 1.33\,\text{m}.$$

According to [29], we determine the hydraulically most favorable radius of the channel.

In accordance with the slope coefficient of the channel m = 1.5, we determine the slope characteristic:

$$m_o = 2\sqrt{1 + m^2} - m = 2\sqrt{1 + 1.5^2} - 1.5 = 2.106.$$

In accordance with the slope of the channel (i = 0.001), the flow rate (Q = 10 m³/s) and the slope characteristic of the channel (m_o = 2.106), we calculate the function of the most advantageous hydraulic radius using the equation:

$$F\left(R_{\Gamma.\text{H}}\right) = \frac{Q}{4m_o\sqrt{i}} = \frac{10}{4 \cdot 2.106\sqrt{0.001}} = 37.6\,\text{m}^3/\text{s}.$$

According to the tables given in the literature, for example [28] table A.16.6, in accordance with the values of the roughness coefficient n = 0.017 and $F(R_{г.н})$ = 37.6 m³/s, we find $R_{г.н}$ = 0.84 m.

With σ = 1, we determine the ratios $b/R_{г.н}$ =1.40 and $h/R_{г.н}$ = 2. Whence h = 2·0.84 = 1.68 m and b = 1.4·0.84 = 1.18 m.

We find free cross-section area of the channel by equation:

$$\omega = \left(b + mh\right)h = \left(1.18 + 1.5 \cdot 1.68\right) = 6.22\ \text{m}^2.$$

To determine the average speed of water movement in the channel from the above table No. P.16.6, we determine the value in accordance with the radius $R_{г.н}$ = 0.84 and the roughness coefficient n = 0.017, $C\sqrt{R} = 52.67$ m/s.

We determine the average speed of water movement in the channel by equation:

$$v = C\sqrt{R}\sqrt{i} = 52.67 \cdot \sqrt{0.001} = 1.67\ \text{m/s}.$$

We determine the bandwidth of the channel by the equation:

$$Q_k = \omega v = 6.22 \cdot 1.67 = 10.4\ \text{m}^3/\text{s}.$$

Control: The flow rate of the intake structure is Q = 10 m³/s, the throughput of the canal is Q_k = 10.4 m³/s, i.e. $Q_k \geq Q$. This means that the canal can transport the flow of water entering it with buffer.

To determine the depth of the stilling well, we determine the mating depth h_2. For this purpose, using equation (4), we determine the water velocity at the outlet from the diffuser:

$$v = \frac{4Q}{\pi D^2} = \frac{4 \cdot 10}{3.14 \cdot 1.1^2} = 10.5\ \text{m/s}.$$

Then, using equation (3), we determine the length of the jet flight:

$$L = v\sqrt{\frac{2\left(Z + 0.5D\right)}{g}} = 10.5\sqrt{\frac{2\left(10 + 0.5 \cdot 1.1\right)}{9.81}} = 15.4\ \text{m}.$$

The jet expansion angle $\left(\theta_j\right)$ is taken to be equal to the diffuser taper angle $\left(\theta_j = \theta = 7^\circ\right)$ and the mating depth $\left(h_2\right)$ is determined by the equation (2):

$$h_2 = D + 2L\text{tg}\frac{\theta}{2} = 1.1 + 2 \cdot 15.4\text{tg}\frac{7^\circ}{2} = 2.95\ \text{m}.$$

The depth of the stilling well is determined by equation (1):

$$a = h_2 - h = 2.95 - 1.44 = 1.51 \approx 1.5\ \text{m}.$$

We accept the length of the stilling well equal to the length of the jet flight $l_q = L$ = 15.4 m.

3.2. Computer simulation

For computer modeling, ANSYS CFX software package was used. This module allows to solve complex hydraulic tasks.

A model of vertical telescopic water intake structure equipped with a stilling well has been assembled at a scale of 1:1. The initial dimensions for modeling are taken from the above given analytical calculations.

In order to perform hydraulic simulation, the same hydraulic characteristics and boundary conditions were used as in the above example.

Fig. 3 shows the diagram of the velocities distribution in the longitudinal section of the structure. This section cut was done along the center line of the structure.

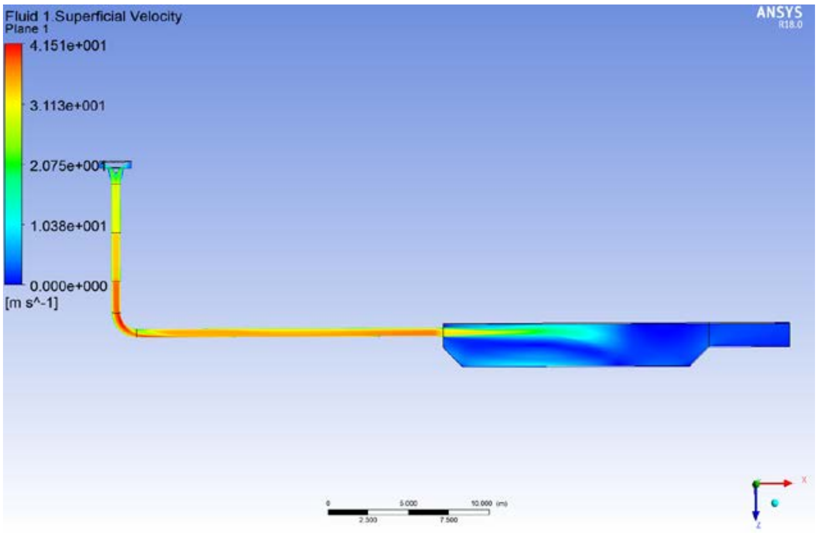

Figure 3. Diagram of water velocities distribution in the longitudinal section of the structure

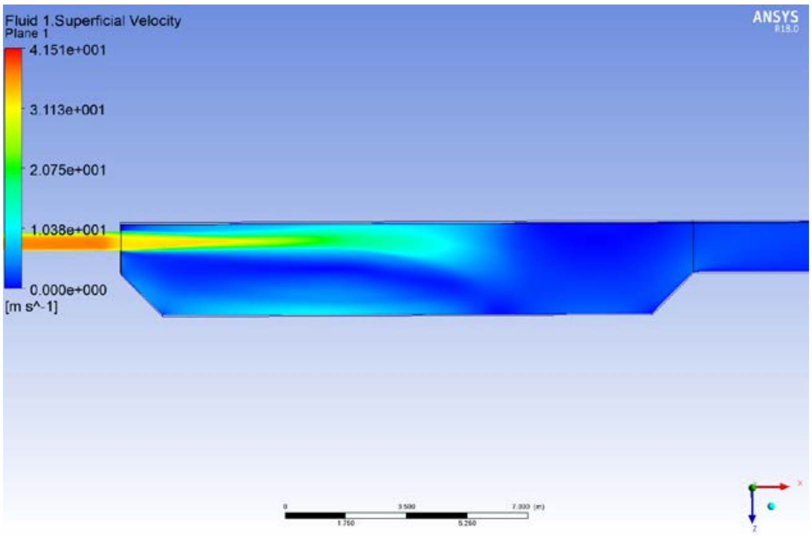

Figure 4. Diagram of water velocities distribution in the longitudinal section of a stilling well

The calculation results show that the maximum velocity in the outlet pipeline reaches 37 m/s (Fig. 3). In the diffuser, the flow expands and the speeds decrease. In (Fig. 4) it can be seen that the flow velocity at the edges of the diffuser is much less than in the center. Along the length of stilling well flow speed reduces and kinetic energy of the flow dissipates. At the exit of the stilling well, the speed is about 1.5–1.6 m/s. At the entrance to the main channel, the speed is 2 m/s.

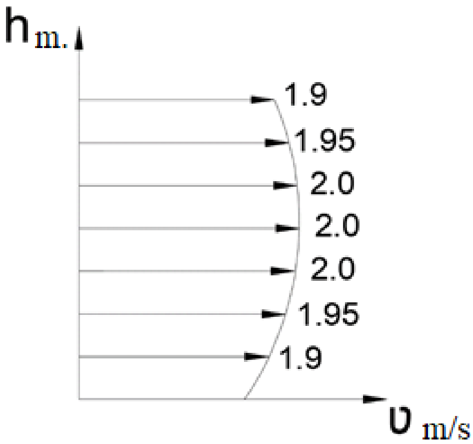

Figure 5. Velocity diagram in longitudinal section at the channel entrance:
h – channel depth; v – flow velocity.

4. Conclusion

In this work, design of vertical telescopic water intake and energy dissipation of the downstream flow in case of transportation by means of open way were studied. The following main conclusions were obtained:

1. Protective mesh is proposed to prevent floating objects from entering inside the water intake.
2. A shutter is proposed to stop water intake operation.
3. Design of stilling well is proposed for energy dissipation in the downstream.
4. The main parameters of stilling well have been established and analytical method for its calculation has been developed. Results of analytical calculations were verified by numerical modeling. Velocity diagrams obtained from numerical modeling demonstrated effective energy dissipation in the stilling well.
5. As a result of numerical modeling, velocity distribution diagram at the entrance to the channel was obtained.

References

1. Urishev, A. Current use of water intake structures of reservoirs. January 2021, IOP Conference Series Materials Science and Engineering 1030:012119. DOI: 10.1088/1757-899X/1030/1/012119
2. Progulny, V., Hurinchyk, N., Grachov, I., Borysenko, K. Porous constructions of water intake structures. Bulletin of Odessa State Academy of Civil Engineering and Architecture, 2020, no. 81, Pp. 149–155. DOI: 10.31650/2415-377X-2020-81-149-155
3. Gabl, R., Gems, B., Birkner, F., Hofer, B, Aufleger, M. Adaptation of an Existing Intake Structure Caused by Increased Sediment Level. Water 2018, 10, p. 1066. DOI: 10.3390/w10081066
4. Herrmann, H., Bucksch, H. water intake, Dictionary Geotechnical Engineering/Wörterbuch GeoTechnik, DOI: 10.1007/978-3-642-41714-6_230502
5. Alawadhi, A.A., Sajwani, Z.Y., Salman, F.H., Kayani, F.A., Alteneiji, Sh.M., Emad Alras, Z.M. Water intake among Sharjah. International Journal of Recent Scientific Research. 2018. Vol. 9. No. 10(D). Pp. 29331–29334. DOI: 10.24327/ijrsr.2018.0910.2840
6. Missimer, T.M., Watson, I.C. Conventional Surface Water Intake Designs. Water Supply Development for Membrane Water Treatment Facilities. Pp. 47–55. DOI: 10.1201/9781351077637-7
7. Budzilo, B. Reliability subsystem of surface water intakes. Water Engineering and Management 146 (7). Pp. 18–21.
8. Cole, J.A., Hawker, P.J., Lawson, J.D., Montgomery, H.A.C. Pollution Risks and Countermeasures for Surface Water Intakes. Water and Environment Journal 2 (6). Pp. 603–625. DOI: 10.1111/j.1747-6593.1988.tb01349.x
9. Bazarov, D.R., Mavlyanova, D.A. Numerical studies of long-wave processes in the reaches of hydrosystems and reservoirs. Magazine of Civil Engineering. 2019. 87 (3). Pp. 123–135. DOI: 10.18720/MCE.87.10
10. Averkiev, A.G. Damless water intake facilities. I.V.Averkiev, I.I. Makarov, V.I.Sinotin. L. Energy, 1969. p. 164.
11. Worrall, R.J. The Effect Of Irrigation Water Temperature On The Germination And Growth Of Plants, Acta Horticulturae. April 1978. DOI: 10.17660/ActaHortic.1978.79.16
12. Nxawe, S., Laubscher, C.P., Ndakidemi, P.A. Effect of regulated irrigation water temperature on hydroponics production of Spinach (Spinacia oleracea L), African Journal of Agricultural Research Vol. 4 (12), pp. 1442–1446. http://www.academic-journals.org/AJAR
13. Brockwell, J., Gault, R.R., Effects of irrigation water temperature on growth of some legume species in glasshouses, Australian Journal of Experimental Agriculture 16 (81). DOI: 10.1071/EA9760500
14. Bezdnina S. Ya. Optimal parameters of soil reclamation regime. Hydrotechnics and melioration. 1986. No. 11; Pp. 58-63.
15. Japanese application No. 53-39697, M.cl. EO2 B 9/04, 1978.
16. Japanese application No. 53-43728, M.cl. EO2 B 9/04, EO2 B 13/00, 1978.
17. Japanese application No. 57-40294, M.cl. EO2 B 7/032, 5/08, 1983.
18. Japanese application No. 57-43686, M.cl. EO2 B 7/32, 1986.
19. Tadao Fukushima, Junsheng Gao, Masayuki Fujihara. Selective Intake from Middle-High Water Flow in a Small River. Design Concept of Settling Basin and Surface Water Intake. Journal of Rainwater Catchment Systems 6 (2). Pp. 39–42. DOI: 10.7132/jrcsa.KJ00003257877
20. Hasanov, S.T. Water intake device. USSR patent by application N0 4883468/15 (111716), M. Kl5E02 B5 / 08, 1991.
21. Podverbny, V.A., Podverbnaya, O.V., Pachema, A.L. Calculation of the depth of a water well constructed at fast current. Science and education for transport. 2018. No. 2. Pp. 153–159.
22. Moldashev, N.R., Smagulova, A.S., Sultanova, B.K., Moldash, Y.A. Modeling of hydraulic jump dissipation in the downstream of a structure, Actual problems of modern science. 2017. No. 6 (97). Pp. 110–114.
23. Podverbny, V.A., Podverbnaya, O.V., Pachema, A.L. Calculation of the depth of a water well constructed at fast current. Science and education for transport. 2018. No. 2. Pp. 153–159.
24. Jin, J., Liu, H., Feng, B., Shao, G. Calculation on discharge of a modified vertical stilling well, International Agricultural Engineering Journal 27 (3). Pp. 23–31.
25. Roozbeh Aghamajidi, Report Of Stilling Basin, December 2020. DOI: 10.13140/RG.2.2.36236.33929
26. Amany, A. Habib. JET STILLING BASIN. Journal of Engineering Sciences. Assiut University, Vol. 40, No. 3, Pp. 657–672. DOI: 10.21608/jesaun.2012.114401
27. Shterenlikht, D.V. Hydraulics, 3rd ed., M.: KolosS, 2004. p. 656.

28. Mikhalev, M.A. Calculation of main channels. Engineering magazine. 2013. No. 4 (39). Pp. 83–93.

29. Tiwari, H. L., Gahlot, V.K. Stilling basins below outlet works – an overview. International Journal of Engineering Science and Technology, Vol. 2 (11), 2010, pp. 6380–6385. https://www.researchgate.net/publication/50366312

Information about authors:

Andrey Lipin
ORCID: https://orcid.org/0000-0003-0564-9928
E-mail: dorian.lipin@gmail.com

Received 21.01.2021. Approved after reviewing 02.09.2021. Accepted 03.09.2021.

Magazine of Civil Engineering

ISSN 2712-8172

journal homepage: http://engstroy.spbstu.ru/

Research article
UDC 691.335
DOI: 10.34910/MCE.112.10

Fluoroanhydrite based composites with the thermoplastic additive

***A.N. Gumeniuk*[a] ✉, *I.S. Polyanskikh*[a], *A.F. Gordina*[a], *G.I. Yakovlev*[a], *I.K. Averkiev*[b], *F.E. Shevchenko*[a]**

[a] *Kalashnikov Izhevsk State Technical University, Izhevsk, Russia*

[b] *Udmurt Federal Research Center of the Ural Branch of the Russian Academy of Sciences, Izhevsk, Russia*

✉*aleksandrgumenyuk2017@yandex.ru*

Keywords: compressive strength, hydration, energy utilization, recycling, binders, sulfur compounds, calcium compounds, optimization, environmental impact

Abstract. The article represents the results of using industrial sulfur as an additive to a fluoroanhydrite based binder and the estimation of its influence on mechanical and physicochemical properties. Waste generated by human activities on an industrial scale, such as industrial sulfur and fluoroanhydrite, pose a serious environmental problem in terms of storage and disposal. Moreover, industrial sulfur and fluoroanhydrite have particular properties to form composite material with required properties. A number of studies have been carried out on using industrial waste as components of building materials, performance properties of the products obtained being improved and the functional use of the products being expanded. In order to study changes in the mechanical properties and physicochemical composition of material based on synthetic fluoroanhydrite, conventional testing methods accompanied by modern methods including scanning electron microscopy and X-ray analysis and infrared spectroscopy, were used. According to the obtained results compressive strength of composition modified with 10 % of thermoplastic additives was 35.77 MPa, water resistance was 0.68. This increase in mechanical properties is due to an interaction between chemically reactive polymorphic types of sulfur which are formed by transformation of α- type to β- and fluoroanhydrite binder. The results of the presented study prove the possibility of creating a building material, the composition of which is fully represented by industrial waste and the characteristics of which are not inferior to its analogues in terms of technical and economic properties.

Funding: Research was supported by the Grant of Russian President (grant MK-3391.2022.4). SEM study was performed using Thermo Fisher Scientific Quattro S microscope in the Center of Shared Facilities “Surface and new materials” of UdmFRC UB RAS supported by Russian Ministry of Science and Higher Education (project № RFMEFI62119X0035).

Citation: Gumeniuk, A.N., Polyanskikh, I.S., Gordina, A.F., Yakovlev, G.I., Averkiev, I.K., Shevchenko, F.E. Fluoroanhydrite based composites with the thermoplastic additive. Magazine of Civil Engineering. 2022. 112(4). Article No. 11210. DOI: 10.34910/MCE.112.10

1. Introduction

The world oil and gas processing complex annually produces more than 70 million tons of industrial sulfur in the form of solid and liquid waste. In addition, this waste is generated by the activities of various sectors of the mining and chemical industries. Currently, conducting scientific research in the field of finding new methods of disposal and reducing the level of environmental impact from by-products is of great importance [1, 2].

Sulfur compositions are used in various sectors of the construction industry, in industrial and transportation engineering. Sulfur-based composite materials are used mainly in those conditions where traditional materials based on Portland cement quickly lose the required properties, for example, when operating in acidic and alkaline environments [3–5]. Varying the content of industrial sulfur in the composition of traditional compositions made it possible to achieve an increase in a number of physicotechnical and physicochemical properties of products (increased impact strength, heat, electrical, and sound insulation, shielding from natural radiation and anthropogenic electromagnetic background) [6].

In addition, it is necessary to consider that, according to expert estimates, more than 300 million tons of synthetic gypsum are produced annually in the world, 20 million tons of which are fluorogypsum, titanium gypsum, etc., and the rest is phosphogypsum. In recent years, the annual increase in the volume of gypsum-containing by-products of the chemical industry is on average 7–8 %. Currently, synthetic gypsum is used in small quantities in agriculture and insignificantly in construction; the main part of gypsum-containing waste is usually stored in open dumps or dumped into water bodies [7, 8].

The limited use of fluoroanhydrite is due to the low quality of products made directly from raw synthetic materials [9, 10]. Most of the research in the field of using fluoroanhydrite has been focused on varying the mechanical treatment and mechanical activation of the binder as well as on selecting effective curing catalysts and various mineral modifying additives [11–13].

As practice shows [14], the use of additives containing sulfate ions can accelerate the setting time of a synthetic binder by increasing the solubility of calcium sulfate. Sulfates do not affect the water demand of the fluoroanhydrite binder, the crystallization of calcium sulfate from the solution accelerating, which has a significant effect on the rate of formation of the nuclei of the hydrate phase [15].

Many Russian and foreign researchers [15–17] have found that sodium sulfate has a significant effect on the setting time of sulfate-containing binders (Na_2SO_4). Research has shown [18] that with the amount of sodium sulfate exceeding 4 %, the setting time of the binder is shortened due to an increase in the solubility of anhydrite. Some research results [19] show that for the production of dry mortars based on fluoroanhydrite binder a dosage of 2–3 % is recommended.

Products based on fluoroanhydrite are known for their fire resistance and heat and sound insulation properties. At the same time, due to its low water resistance and mechanical strength, the use of fluoroanhydrite is limited in the production of materials and structures for humid conditions [20].

A review of literary sources has demonstrated insufficient information on the issue of the integrated use of industrial sulfur, sulfate activator, and synthetic anhydrite in the production of composite building materials.

The scientific research of rational ways of recycling industrial wastes such as industrial sulfur and fluoroanhydrite is a paramount importance in case of preserving sustainable environment [2, 3].

Currently, the main direction of research in the field of the use of synthetic gypsum is the development of methods for increasing the hydrophobic properties of products [21, 22]. The need for this research is also driven by the demand in developing countries' markets for quality and cost-effective building materials.

The main aim of the research is to design proper composite material based on fluoroanhydrite activated by water solvable additive and thermally activated industrial sulfur.

Following tasks should be achieved during this research:

A. To estimate the proper use of man-made waste materials and find out the way of adding sulfur contained waste for composite formation.

B. To research characteristics of sulfur behavior under temperature treatment and following cooling.

C. To estimate the influence of thermoplastic additive on mechanical and performance characteristics.

2. Methods

2.1. Raw materials and experiment method

To study the effect of industrial sulfur on the physicochemical and physicomechanical properties of products based on synthetic anhydrite (fluoroanhydrite), a series of experiments was carried out to modify the binder with a pretreated dispersed sulfur additive.

Thermoplastic sulfur additive was obtained as a result of a two-stage process described in the studies [23]. The processed industrial sulfur was introduced at the stage of mixing the main components, and the hardening activator was introduced together with the mixing water. The resulting mixture was put into metal molds and removed after 2 hours, followed by heat treatment of the samples.

Fluoroanhydrite. Fluoroanhydrite (from Galogen LLC, Perm) was used in the study. This is a homogeneous low-density material with a constant chemical composition, whose particle sizes range from 1 to 20 mm. The raw material is laboratory-milled and sifted through a 0.4 mm sieve until less than 13 wt% residue is left, producing a white powder. In the process of mixing with water until standard consistency is reached (spreading on the Suttard viscometer 180 mm), it forms a dough of normal density at W/G = 0.33. Setting times are: start 0 h 21 min. end 0 h 41 min. The component composition is presented in Table 1.

Table 1. Component composition of fluoroanhydrite, %.

$CaSO_4$		CaF_2	H_2SO_4	HF
γ – $CaSO_4$	β – $CaSO_4$			
20	78	1 – 1.8	1 – 1.2	–

Sodium sulfate. Based on the research results [18], sodium sulfate corresponding to Russian State Standard GOST 21458-75, crystallization sodium sulfate, was taken as a hardening activator. The optimal introduction rate was determined based on researches [18].

Industrial sulfur. Industrial sulfur of grade 9998 corresponding to Russian State Standard GOST 127.1-93 was used as the main component of the thermoplastic sulfur additive. The content of the thermoplastic additive varied in the range from 0 to 10 % by weight of the binder, in increments of 2 %. The concentration range of sulfur additive was selected in accordance with the hypothesis discussed earlier in [24]. Physicomechanical and physicochemical properties are presented in Table 2.

Table 2. Specifications of sulfur, grade 9998 [24].

Name	Particle shape	Bulk density	Mass fraction of sulfur	Mass fraction of ash	Mass fraction of organic matter	Mass fraction of water
Unit	–	g/cm³	%	%	%	%
Value	Hemispherical	1.3	99.99	0.005	0.005	0.01

2.2. Experiment method

In order to study changes in the physicochemical composition of artificial stone based on synthetic fluoroanhydrite, both scanning electron microscopy and additional informative research methods, including X-ray analysis and infrared spectroscopy, were used. Scanning electron images of the microstructure were obtained using a Thermo Fisher Scientific Quattro S scanning electron microscope at the “Surface and New Materials” shared knowledge center at the Udmurt Federal Research Center of the Ural Branch of the Russian Academy of Sciences. Infrared spectra were obtained using an IRAffinity-1 spectrometer. Images and spectra are presented without additional processing (except for adjusting the brightness and contrast of images). The compressive and flexural strength was measured using a PGM-100MG4-A hydraulic press.

To study the complex changes in the physicochemical composition, the method of differential thermal analysis of samples of the control and modified composite material modified with a thermoplastic additive was used, including thermogravimetric analysis (TGA). In addition, differential thermogravimetry (DTG) and differential scanning calorimetry (DSC) methods were used. Laboratory studies were carried out on a TGA/DSC1 thermal analyzer produced by Mettler-Toledo Vostok. Shooting conditions: measurement interval 50–1100°C, heating rate 10 deg/min, platinum crucibles, working medium – air.

3. Results and Discussion

Comparative evaluation of the samples was carried out according to changes in the compressive and flexural strength of the modified and control compositions. The composition containing fluoroanhydrite and 2 % of the catalyst by weight of the binder was taken as a control sample.

The tests were carried out on beams with dimensions of 40×40×160 mm. The samples were kept under normal conditions for 2 hours after stripping, then placed in a drying cabinet 80-01 SPU for heat treatment at 180 °C for 60 minutes [25]. At the same time, to prevent dehydration of water in the mineral matrix, the samples were sealed during the whole time of heat treatment. After the heat treatment, the samples were cooled to room temperature in a drying oven. Afterwards, the samples were kept under normal conditions for 7, 14, and 28 days; the required characteristics were measured on the control dates. The experimental compositions are presented in Table 3.

Table 3. Component composition of produced samples.

Composition	Fluoroanhydrite, g	Dosage of catalyst, %	Industrial sulfur, %	Treatment temperature(°C)
Control	1200	2	0	180
C-1			2 %	
C-2			5 %	
C-3			7 %	
C-4			10 %	

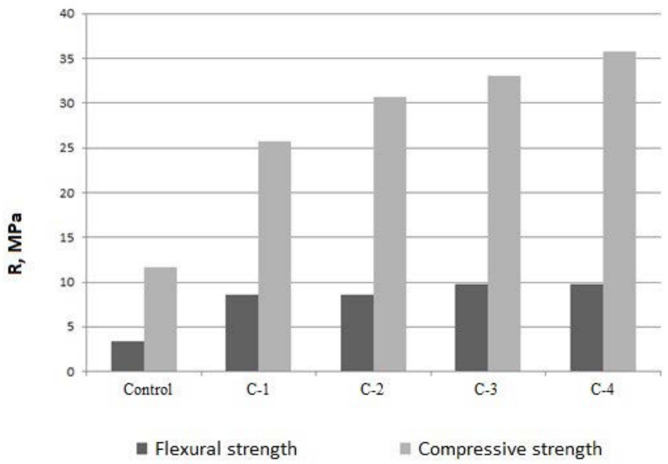

Figure 1. Strength of modified fluoroanhydrite-based products at 28 days (Note to Fig. 2. The value of the coefficient of variation in determining the strength of the hardened binder samples was V = 4.5 %).

The index of compressive strength with the introduction of 10 % of thermoplastic additive on the 28th day of hardening is on average 35.77 MPa (Fig. 1), which significantly exceeds the strength indicators of the control composition. Water resistance determined by the value of the softening coefficient of the fluoroanhydrite composition on the 28th day of hardening was 0.68 % for the composition C-4. Results are also higher than the indicators reported in studies [8, 12, 13].

As the study of physical and mechanical properties show, the optimal dosage of modified industrial sulfur is 10 %. At the same time, the dynamic of the growth of mechanical characteristics makes it possible to increase the concentration of sulfur in the composition, counting on a further increase in performance indicators; however, for the purposes of this study, the optimal content of the additive is 10 %.

At the same time, the increase in strength is due to the conditions of chemical interaction between various reactive polymorphic modifications of sulfur formed as a result of the transition of α sulfur to β sulfur with components of the fluoroanhydrite structure during its thermal activation in the matrix structure. It should also be noted that the growth of the physical and mechanical parameters of the material is due to the formation of polymer sulfur during polymerization in the temperature range from 70 °C to 206 °C. The extremum is observed at 189 °C. The transition energy corresponds to ΔE_p polymerization – 19.35 J/g. Previous research [1, 5, 6, 25] confirms this.

When comparing the microstructure of the control and the modified samples, dense, homogeneous formations were found in the structure of the modified artificial stone with an increased adhesion of the anhydrite matrix to the polymer component observed.

Structural changes are shown in Fig. 2, and the analysis of the modified sample revealed the formation of an amorphous and dense structure, in which the content of the crystalline typical phase of hydrated fluoroanhydrite is practically absent. In addition, the energy dispersive X-ray spectroscopy of the control and modified sample of the composition C-4 with reference to the analyzed area presented in Fig. 2 and 3 demonstrates the comparative changes in the component composition presented in Table 4.

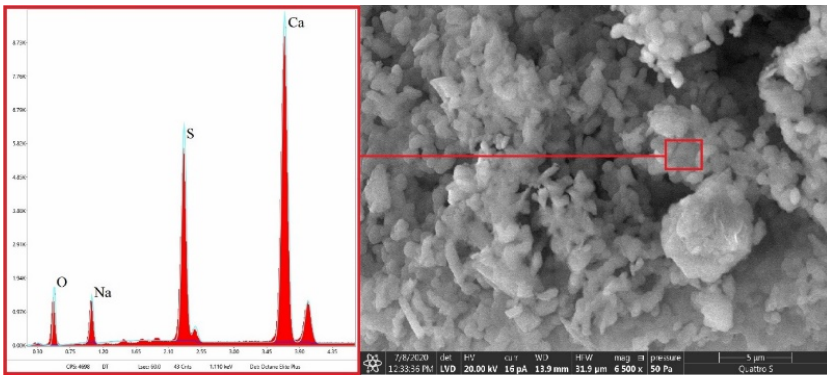

Figure 2. Microanalysis and microstructure of the control sample.

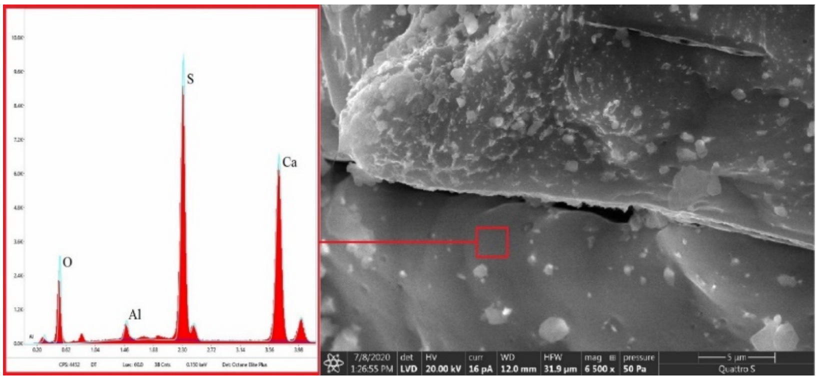

Figure 3. Microanalysis and microstructure of the modified sample (sample C-4).

The elemental composition shows an increased intensity reflecting the content of sulfur, which may presumably indicate its structuring role in the component composition.

Table 4. Component composition of the control and modified samples according to the results of X-ray spectroscopy.

Element	C-4				Control			
	Weight %	Atomic %	Error %	Net Int.	Weight %	Atomic %	Error %	Net Int.
O	54.5	72.5	11.4	227.97	0.0	0.0	0.0	124.1
Al	1.9	1.5	10.3	75.8	–	–	–	–
Na	–	–	–	–	15.2	22.6	10.9	126.6
S	20.96	13.9	4.8	1389.8	24.2	25.8	5.4	863.2
Ca	22.7	12.1	3.6	1141.5	60.6	51.6	3.7	1642.1

Analysis of the IR spectra of the control and modified compositions (Fig. 4) showed that with the addition of the modified industrial sulfur, the nature of the peaks of the main functional groups of the material changes and new wavenumbers appear (Table 5). This may be due to the formation of new polymer forms of sulfur and the change in the anhydrite crystallization conditions.

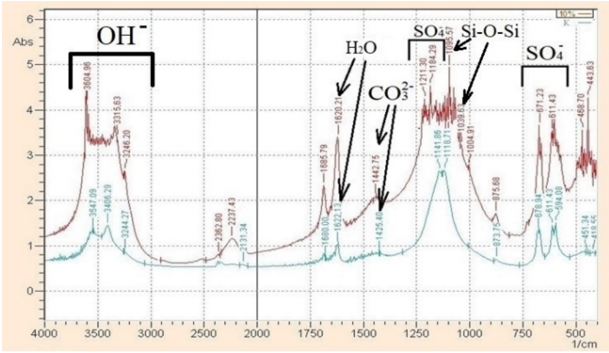

Figure 4. Comparison of IR spectra of the control (red) and modified (turquoise) samples with the introduction of 10 % of industrial sulfur.

Table 5. Change in wavenumbers when comparing infrared spectra.

Ion	Wavenumbers cm^{-1}, control sample	Wavenumbers cm^{-1}, modified sample
SO_4^{2-}	594.08; 611.43; 679.94;1141.86; 1118.71	611.43;671.23;1184.29;1211.30
CO_3^{2-}	1442.75; 873.5	1425.40; 875.68
Si-O-Si	–	1095.57; 1039.63
OH^-	3547.09; 3406.29; 3244.27	3604.96; 3315.63; 3246.20
H_2O	1620.21	1622.13

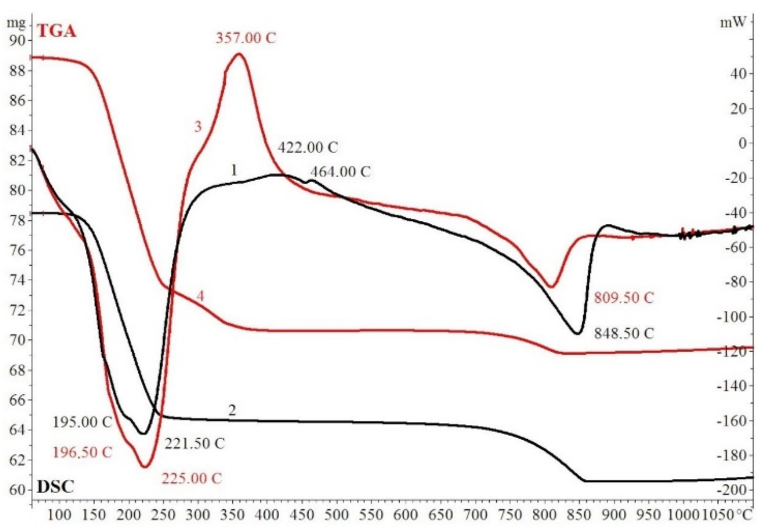

Figure 5. Differential scanning calorimetry spectra: control sample (1, 2), C-4 sample of modified industrial sulfur (3, 4).

The derivatogram of the control sample (Fig. 5, isotherms 1 and 2) of fluoroanhydrite with a hardening activator shows a double endothermic effect of 195 and 221.5°C typical for the removal of crystallization water as well as an endothermic effect of 848.5, the area typical for calcite dissociation into calcium oxide and carbon dioxide and partial dissociation of calcium sulfate and low-basic calcium hydrosilicates in an insignificant volume. The effects in the range of 420–470°C are associated with the rearrangement of the crystal lattice with the formation of insoluble anhydrite. Fluoroanhydrite, in its turn, is represented by a combination of anhydrite, calcium carbonate, and gypsum.

When modifying fluoroanhydrite with a hardening activator and 10 % (Fig. 5, isotherms 3 and 4) of processed industrial sulfur, a slight endothermic effect was noted in the region of 90–150°C associated with a change in the phase state of sulfur, namely, the transition from the alpha form to the beta form. A shift in temperatures corresponding to the removal of crystallization water up to 196.5 and 225.0 degrees, respectively, was noted, which indirectly confirms the change in the hydration conditions of fluoroanhydrite in the direction of acceleration and completeness of the reaction. A strong exothermic effect was noted in the temperature range of 340–370°C, which is associated with the burnout of sulfur in air with the formation of SO_2 and SO_3, while the effect manifests itself in a significant volume smoothing out the concomitant effects of the rearrangement of the crystal lattice of the binder, preventing them from being identified. An endothermic effect in the region of 800°C associated with the dissociation of calcium sulfate and low-basic calcium hydrosilicates was also noted.

Thus, the spectral data are consistent with the results of the microstructural analysis, indicating the formation of a matrix of increased density including amorphous structures based on the sulfur component. The change in the size and intensity of the peaks of the main wave numbers and/or typical reactions confirms the hypothesis about the influence of a man-made additive on the conditions for the structure formation of fluoroanhydrite.

4. Conclusions

The influence of industrial sulfur on the structure formation of the mineral binder has been analyzed. The results of the research are as follows:

1. As a result of the research it was found that the composite material based on industrial sulfur (Taneco, PJSC) and fluoroanhydrite binder (Galogen, Ltd) has the increased physical and technical indicators. With 10 % of modified industrial sulfur introduced, the flexural strength increases by 55.6 %, the compressive strength by 2 times, and the softening coefficient is 0.68 %.

2. The introduction of a thermoplastic additive based on industrial sulfur has a significant effect on the physicochemical properties of artificial stone-based man-made anhydrite. A comparative analysis of the results of energy dispersive X-ray spectroscopy showed that in the process of modifying the anhydrite matrix, a high-density amorphous structure is formed possibly due to changes in hydration conditions confirmed by the results of IR spectral analysis and the appearance of oscillations in the region of 1184.29 and 1211.30 wavenumbers corresponding to SO_4^{2-}.

3. The results obtained confirm the possibility of rational use of man-made waste and the prospects for thermal activation of sulfur in the structure of the mineral matrix in order to improve the performance characteristics and expand the area of application of products based on man-made anhydrite.

References

1. Shafiq, I., Shafique, S., Akhter, P., Yang, W., Hussain, M. Recent developments in alumina supported hydrodesulfurization catalysts for the production of sulfur-free refinery products: A technical review. Catalysis Reviews – Science and Engineering. 2020. DOI: 10.1080/01614940.2020.1780824
2. Wagenfeld, J.G., Al-Ali, K., Almheiri, S., Slavens, A.F., Calvet, N. Sustainable applications utilizing sulfur, a by-product from oil and gas industry: A state-of-the-art review 2019. DOI: 10.1016/j.wasman.2019.06.002
3. Moon, J., Kalb, P.D., Milian, L., Northrup, P.A. Characterization of a sustainable sulfur polymer concrete using activated fillers. Cement and Concrete Composites. 2016. DOI: 10.1016/j.cemconcomp.2015.12.002
4. Galdina, V.D. Serobitumnyye vyazhushchiye: monografiya [Serobitumen binders: monograph]. – Omsk: SibADI, 2011. 124 p. (rus)
5. Grabowski, Ł., Gliniak, M., Polek, D. Possibilities of use of waste sulfur for the production of technical concrete. E3S Web of Conferences. 2017. DOI: 10.1051/e3sconf/201712301032
6. Kiselev, D.G., Korolev, E.V., Smirnov, V.A. Structure formation of sulfur-based composite: The model. Advanced Materials Research. 2014. DOI: 10.4028/www.scientific.net/AMR.1040.592
7. Liu, S., Ouyang, J., Ren, J. Mechanism of calcination modification of phosphogypsum and its effect on the hydration properties of phosphogypsum-based supersulfated cement. Construction and Building Materials. 2020. DOI: 10.1016/j.conbuildmat.2020.118226
8. Yakovlev, G., Polyanskikh, I., Fedorova, G., Gordina, A., Buryanov, A. Anhydrite and gypsum compositions modified with ultrafine man-made admixtures. Procedia Engineering. 2015. DOI: 10.1016/j.proeng.2015.06.195
9. Singh M., Garg M. Making of anhydrite cement from waste gypsum. Cement and Concrete. 2000. DOI: 10.1016 / S0008-8846 (00) 00209-X
10. Gracioli, B., Angulski da Luz, C., Beutler, C.S., Pereira Filho, J.I., Frare, A., Rocha, J.C., Cheriaf, M., Hooton, R.D. Influence of the calcination temperature of phosphogypsum on the performance of supersulfated cements. Construction and Building Materials. 2020. DOI: 10.1016/j.conbuildmat.2020.119961
11. Anikanova, L.A., Volkova, O.V., Kudyakov, A.I., Kurmangalieva, A.I. Mechanically Activated Composite Fluoroanhydrite Binder. Stroitel'nye Materialy. 2019. DOI: 10.31659/0585-430x-2019-767-1-2-36-42
12. Singh, N.B. The activation effect of K2SO4 on the hydration of gypsum anhydrite, CaSO4(II). Journal of the American Ceramic Society. 2005. DOI: 10.1111/j.1551-2916.2004.00020.x
13. Magallanes-Rivera, R.X., Escalante-García, J.I. Anhydrite/hemihydrate-blast furnace slag cementitious composites: Strength development and reactivity. Construction and Building Materials. 2014. DOI: 10.1016/j.conbuildmat.2014.04.056

14. Kramar, L.Y., Trofimov, B.Y., Chernykh, T.N. Properties and modification of anhydrite binder from technogenic raw materials. Innovative materials and technologies KNAUF – GARANT of quality and safety in modern construction. Collection of reports of the fifth scientific conference LLC KNAUF GIPS – Chelyabinsk, 2012, 58 p.
15. Garg, M., Pundir, A. Energy efficient cement free binder developed from industry waste – A sustainable approach. European Journal of Environmental and Civil Engineering. 2017. DOI: 10.1080/19648189.2016.1139510
16. Nizevičienė, D., Vaičiukynienė, D., Vaitkevičius, V., Rudžionis. Effects of waste fluid catalytic cracking on the properties of semi-hydrate phosphogypsum. Journal of Cleaner Production. 2016. DOI: 10.1016/j.jclepro.2016.07.037
17. Anikanova, L.A., Kurmangalieva, A.I., Volkova, O.V., Pervushina, D.M. Gas-gypsum materials properties modified by plasticizing agents. Vestnik Tomskogo gosudarstvennogo arkhitekturno-stroitel'nogo universiteta. Journal of Construction and Architecture. 2020. DOI: 10.31675/1607-1859-2020-22-1-106-117
18. Budnikov, P.P., Zorin, S.P. Angidritovyy tsement [Anhydrite cement]. M.: Promstroyizdat, 1954. 90 p. (rus)
19. Gazdič, D., Fridrichová, M., Kalivoda, K., Stachová, J. Study of the kinetics of hydration process of anhydrite using external exciters. Advanced Materials Research. 2014. DOI: 10.4028/www.scientific.net/AMR.838-841.2342
20. Yakovlev, G.I., Kalabina, D.A., Pervushin, G.N., Drochytka, R., Bazhenov, K.A., Gordina, A.F., Ginchitskaya, J.N. Efficient heat-insulating material based on technogenic anhydrite. IOP Conference Series: Materials Science and Engineering. 2019. DOI: 10.1088/1757-899X/660/1/012052
21. Kurmangalieva, A.I., Anikanova, L.A., Volkova, O.V., Kudyakov, A.I., Sarkisov, Y.S., Abzaev, Y.A. Activation of hardening processes of fluorogypsum compositions by chemical additives of sodium salts. Izvestiya Vysshikh Uchebnykh Zavedenii, Seriya Khimiya i Khimicheskaya Tekhnologiya. 2020. DOI: 10.6060/ivkkt.20206308.6137
22. Fedorchuk, Y.M., Zamyatin, N.V., Smirnov, G.V., Rusina, O.N., Sadenova, M.A. Prediction of the properties anhydrite construction mixtures based on neural network approach. Journal of Physics: Conference Series. 2017. DOI: 10.1088/1742-6596/881/1/012039
23. Yakovlev, G.I., Polyanskih, I.S., Gordina, A.F., Gumeniuk, A.N. Using technical sulfur as a structuring additive for mineral binders based on calcium sulfate. Engineering Structures and Technologies. 2020. DOI: 10.3846/est.2019.11948
24. Certificate of quality No. 448N date: 18th of February 2016. Sera tekhnicheskaya gazovaya granulirovannaya, sort 9998 [Sulfur technical gas granulated, grade 9998]. (rus)
25. Paturoyev, V.V. Polimerbetony [Polymer concretes]. Moscow: Stroyizdat, 1987. 285 p. (rus)

Information about authors

Aleksandr Gumeniuk
ORCID: https://orcid.org/0000-0002-2880-8103
E-mail: aleksandrgumenyuk2017@yandex.ru

***Irina Polyanskikh**,*
PhD in Technical Science
ORCID: https://orcid.org/0000-0003-1331-9312
E-mail: irina_maeva@mail.ru

Anastasiya Gordina,
PhD in Technical Science
ORCID: https://orcid.org/0000-0001-8118-8866
E-mail: afspirit@rambler.ru

Grigorij Yakovlev,
Doctor in Technical Science
ORCID: https://orcid.org/0000-0002-2754-3967
E-mail: gyakov@istu.ru

Igor Averkiev,
ORCID: https://orcid.org/0000-0001-9952-8363
E-mail: virgilio.007@yandex.ru

Filipp Shevchenko,
ORCID: https://orcid.org/0000-0002-7109-0686
E-mail: gism56@mail.ru

Received 22.01.2021. Approved after reviewing 23.08.2021. Accepted 23.08.2021.

Magazine of Civil Engineering

ISSN 2712-8172

journal homepage: http://engstroy.spbstu.ru/

Research article
UDC 624
DOI: 10.34910/MCE.112.11

Structural performance of corroded RC beams without shear reinforcement

N.T. Nguyen ✉, ***T.K. Nguyen***, ***H.G. Nguyen***

Hanoi University of Civil Engineering, Hanoi city, Vietnam

✉ *tannn@huce.edu.vn*

Keywords: reinforced concrete beams, reinforcement corrosion, shear strength, modeling, finite element method

Abstract. In this paper, a total of eight medium-scale RC beams with the dimensions of 150×200×1100 mm were fabricated without shear reinforcements. These beams were subjected to an accelerated corrosion test and then to a four-point loading shear test. The key test variables were various degrees of corrosion introduced in the tension reinforcements (0 %, 3.13 %, 4.11 %, and 4.93 % by mass loss). Even though all tested beams collapsed in shear failure, corroded beams exposed to 3 % and 4 % corrosion degrees showed a clear upward trend of approximately 7 % of maximum capacity compared to control beams. In contrast, corroded beams having a 5 % corrosion degree showed a 10 % decrease in shear strength with distinguished cracking patterns and load-carrying mechanism because of the significant loss of bond strength due to corrosion. Furthermore, a finite element model (FEM) for the prediction of structural performance in tested beams was produced using DIANA software. This model was verified by the experimental results (e.g. load-deflection curves, cracking patterns) with good agreement. Lastly, the parametric study of different shear span-to-depth ratios was also conducted to examine the FEM capability in simulating different behavior associated with beam and tie-arched mechanisms.

Funding: The authors would like to thank the financial support from the National University of Civil Engineering (NUCE), Hanoi, Vietnam, under grant number 47-2021/KHXD.

Citation: Nguyen, N.T., Nguyen, T.K., Nguyen, H.G. Structural performance of corroded RC beams without shear reinforcement. Magazine of Civil Engineering. 2022. 112(4). Article No. 11211. DOI: 10.34910/MCE.112.11

1. Introduction

Steel reinforcement corrosion inflicts damage that induces a deterioration in the performance and significantly impairs the mechanical properties of RC structures. There should be attention paid to the fact that RC structures tend to be exposed to deteriorative agents throughout their service life. The residual strength and load-carrying mechanism of these structures must be calculated to effectively rehabilitate the degraded RC structures subjected to corrosion.

There are numerous comprehensive studies of experimental efforts assessing the flexural behavior of corroded RC structures. It has been generally accepted that the flexural capacity of corroded members is directly associated with the remaining sectional area of reinforcing rebars and that ductility is degraded by corrosion of longitudinal reinforcement [1–7]. Along with the majority of the previous studies that have investigated mainly the flexural behavior of corroded RC structures, more and more researchers focused on the shear strength of corroded beams [8–11], because the corrosion of reinforcement had altered the failure mode from bending for non-corroded beams to shear for corroded beams [5]. It means that the design of RC beams with a higher shear capacity to avoid such sudden failure is compulsory.

Recently, because of a large number of existing deteriorated structures, reliable methods that can evaluate the residual structural performance to facilitate repair and maintenance strategies are in great demand. Accurate performance evaluation of the deteriorated structures from the numerical analysis may allow the extension of service life and increase the safety level across a network of deteriorated structures [12]. Therefore, numerical approach researches from 2004 to 2020 [12–18] are necessary. However, comparatively less attention has been devoted to assessing the residual structural capacity of corroded RC beams without stirrups using the finite element method (FEM) [19, 20]. The study of Toongoenthong and Maekawa [19] on spatially localized cracking and pre-induced damage along with the longitudinal reinforcement of RC beam by simulating the corrosion effect has shown that corrosion cracking does not necessarily always bring a non-favorable effect on the structural behavior of corroded RC members because of the steel and concrete bond performance. With sufficient anchorage performance, the bond deterioration caused by corrosion cracks in the shear span may lead to tied-arch action with the increase of shear capacity. It shares the same agreement with the research work conducted by Han et al. [20], in which the tension reinforcement was properly anchored using the hook details: the RC beams constructed without stirrups subjected to less than 5 % corrosion degree showed about 40 % enhancement in shear resistance capacity due to the transfer mechanism shifting from beam action to tied-arch action, regardless of the reduction in bond performance.

Thus, the experimental and simplified modeling methodologies are addressed in this study, focusing on the bond behavior of corroded RC beams without stirrups. Corrosion-induced damages will be modeled by considering corrosion-induced cracking, changing the properties of concrete and steel, and modifying the bond between tension reinforcement and concrete. Thereafter, the FE model was validated by calibrating the test results obtained on a set of eight RC beams in an experimental program. The main parameters of the non-linear analysis consist of the relationship between load and mid-span deflection, the cracking patterns, and failure mode. Finally, a parametric study has been investigated and discussed to assess the effect of the shear span-to-depth ratio on the structural performance of corroded RC beams without stirrups.

2. Methods

2.1. Experimental method

The composition of the concrete used, consisting of Portland cement, river sand, crushed stone with a maximum diameter of 20 mm, and water, is presented in Table 1. The water-cement ratio is equal to 0.42. The compression test was performed on a sample group of three cubes with the dimensions of 150×150×150 mm at 28 days. The results show that the average concrete compressive strength is equivalent to 25.1 MPa, with a standard deviation of 0.4 MPa and a coefficient of variation of 1.5 % [21].

Table 1. Concrete mix.

Cement (kg)	Fine aggregates (kg)	Coarse aggregates (kg)	Water (liter)	W/C
439	622	1211	185	0.42

Ribbed steel rebars with a nominal diameter of 16 mm are longitudinal reinforcement inside the experimental beams. The tensile strengths of steel rebars were also calculated in the laboratory by the tension test, with the average yield tensile strength and ultimate tensile strength of 328.5 and 528.8 MPa, respectively. The length and the initial mass before corrosion have been weighted among all steel rebars. In this study, in order to investigate the influence of corroded tension reinforcement on the structural performance of the RC beams made without stirrups and to validate the finite element (FE) model, eight experimental beams with the dimensions of 150×200×1100 mm with a different configuration of steel corrosion degrees were tested under static loading. Each experimental beam was manufactured of concrete having the compressive strength of 25.1 MPa and two φ16 longitudinal steel rebars at the bottom layer as illustrated in Fig. 2(a) and without shear reinforcement (stirrups). The depth of the concrete cover is 40 mm from the bottom face of the beam.

Six beams were subjected to an accelerated corrosion test after 28 days of curing, as shown in Fig. 1. The steel rebars are wired to the power supplier's anode, while the cathode is connected to the copper rebar embedded in the 3.5 % sodium chloride solution. Only the experimental beams' bottom face is in contact with the solution. The solution depth is preserved at approximately 2 cm from the beam bottom. The steel rebars were not soaked in the solvent in order to protect exterior rebars from corrosion locally.

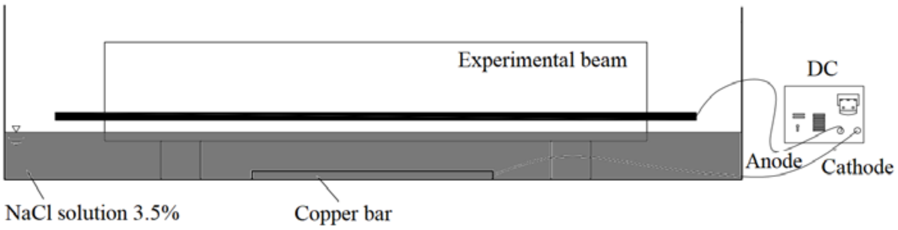

Figure 1. Detail of accelerated corrosion test.

For longitudinal reinforcement, the corrosion degree of the beam tested was determined based on the mass loss of the metal. The steel rebars were measured to assess the initial mass before doing the corrosion tests (m_o). The corroded reinforcements were separated from the beams for measurement after the corroded beams were exposed to monotonic loading for fracture. Firstly, the reinforcement was cleaned by a bristle brush to eliminate concrete adhering to the surface of the steel rebars. The reinforcement was then soaked in a 5 percent HCl solution for one day with 3.5 g hexamethylenetetramine and then cleaned to remove corrosion materials. The cleaning technique was also applied without corrosion to the non-corroded steel rebar. The procedure resulted in an insignificant loss of the control steel rebar. Therefore, to assess the remaining mass (m), the steel rebars were weighed. The corrosion degree of the reinforcement, noted c (%), is defined by Eq. (1), with m_o (g) being the steel mass before corrosion, m (g) being the steel mass after corrosion, and Δm (g) being the steel mass loss by corrosion:

$$c(\%) = \frac{m_o - m}{m_o} \times 100 = \frac{\Delta m}{m_o} \times 100. \tag{1}$$

Table 2. Determination of corrosion degrees of steel rebars.

Test group	Beam notation	Initial mass (g)	Remaining mass (g)	Mass loss (g)	Corrosion degree (%)	Average degree (%)
C0	C0-1	1987	1987	0	0	0
	C0-2	1956	1956	0	0	
C3	C3-1	1964	1909	55	3.16	3.13
	C3-2	1881	1822	59	3.10	
C4	C4-1	1993	1932	61	4.27	4.1
	C4-2	1950	1888	62	3.94	
C5	C5-1	1947	1865	82	4.99	4.93
	C5-2	1872	1797	75	4.87	

Table 2 shows the results of the determination of steel corrosion degree for all testing beams. For each corroded beam, the corrosion degree is the average value of the two corroded rebars at the bottom layer (φ16 steel rebars). The eight tested beams were divided into four groups named C0, C3, C4, and C5, respectively. Group C0 consisted of two control beams. Group C3, C4, and C5 had two corroded beams. Each experimental beam was designated with two numbers: the first number indicating the average degree of corrosion (0 %, 3.13 %, 4.1 %, and 4.93 %), whereas the second number stands for the numerical order of the beam.

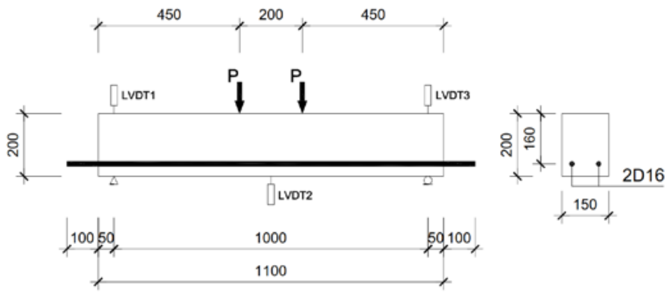

(a)

(b)

Figure 2. Details of (a) test specimen and (b) four-point loading test.

In the four-point loading test setup, the shear span and effective depth were kept constant at 400 mm and 160 mm, respectively, in order to consider a shear span to depth ratio of 2.5 for all beams. The test specimens were subjected to monotonic loading, as illustrated in Fig. 2, to investigate the structural performance following the electrochemical accelerated corrosion of corroded beams and at least 28 days of curing with non-corroded beams. Over a clear span of 1100 mm, the beams were simply supported with two concentrated loads, which were both 400 mm apart from the supports R1 and R2. In order to calculate the vertical displacement of each beam measured, three Linear Variable Deformation Transducers (LVDTs) were mounted. The displacement transducer sets (LVDT1 and LVDT3) were used to calculate the displacement of the supports. In order to measure the displacement at the mid-span of the beam, the LVDT2 displacement transducer was used. A data-logger TDS-530 and a computer were connected to all displacement transducers to automatically collect measurement data to determine the relationship between the applied load and displacement.

2.2. Finite element modeling method

In this study, the numerical simulation was carried out in the DIANA software (version 10.3). In this three-dimensional analysis, the sensitivity of mesh was considered. It was verified in the study of Maekawa et al. in 1994 [22] that the tension-softening model used for concrete is independent of the element size. It should be noted that due to the heterogeneity in the concrete material, the minimum mesh size was taken as 20 mm (considering the maximum size of coarse aggregates). Therefore, the mesh size in the three-dimensional analysis can be sufficiently large without sacrificing accuracy [23]. The concrete model was based on a total strain fixed crack model. Firstly, the damage of concrete in the tested beam due to corrosion was modeled. The volumetric expansion from corrosion products induces internal pressure leading to the formation of concrete cover crack. In addition, the considerable effect of corrosion on the reduction of concrete compressive strength in the degraded area compared with the undamaged area was experimentally inspected in the study of Shayanfar et al. [24]. Therefore, the corrosion damage on the concrete cover is considered in the FE model by modifying the stress-strain relationship of the concrete as illustrated in Fig. 3(a), which was suggested by Coronelli and Gambarova [15] and validated in a numerical study of Lim et al. [25]. Whereas the behavior of concrete in compression is modeled using a parabolic curve in DIANA 9.1 User's manual [26]. The linear-elastic response up to 30% of the compressive strength of non-corroded concrete $\left(f_c'\right)$ is considered for stress levels, while the deterioration of the concrete compressive strength can be described by Eq. (2), with $f_{c,d}'$ being the compressive strength of the corroded concrete. The post-peak response of concrete in compression is modeled using compressive fracture energy, denoted G_C, based on the recommendations in studies of Nakamura and Higai [27]. While k' being the coefficient related to rebar roughness and diameter, for the case of medium-diameter ribbed rebars, a value k' = 0.1 has been proposed by Cape [28], ε_0 being the strain at the compressive strength f_c', and ε_1 being the average smeared tensile strain in the transverse direction:

$$f_{c,d}' = f_c' \Big/ \left[1 + k'\left(\varepsilon_1/\varepsilon_0\right)\right]. \tag{2}$$

The strain ε_1 can be estimated by Eq. (3), with b_0 being the section width in the state without corrosion crack, b_f being the beam width expanded by corrosion cracking:

$$\varepsilon_1 = \left(b_f - b_0\right) \Big/ b_0, \tag{3}$$

$$b_f - b_0 = n_{bars} w_{cr}, \tag{4}$$

where n_{bars} is the number of rebars, and w_{cr} is the total crack width at a given corrosion degree. The total crack width w_{cr} can be calculated using Eq. (5) as recommended in the study of Molina et al. [29] in case of not having data from experiments:

$$w_{cr} = 2\left(v_{rs} - 1\right) X_d, \tag{5}$$

where v_{rs} is the ratio between the specific volumes of rust and steel that can be assumed to be 2. The depth of penetration attack X_d was determined by Eq. (6) as proposed in the study of Val [30], with

$i_{corr}\left(\mu A/cm^2\right)$ = 0.35 being the corrosion current density in the steel rebar and t (years) being the duration of corrosion:

$$X_d = 0.0116 i_{corr} t. \tag{6}$$

The tension softening behavior of concrete is represented using the non-linear curve of Hordijk et al., as described in DIANA 9.1 User's manual [26]. There, G_F is the tensile fracture energy, and h is the crack bandwidth taken as the square root of element area. All the input parameters, including G_F and tensile strength of concrete f_t' are obtained from CEB-FIP Mode Code [31] based on concrete compressive strength and maximum aggregate size. In this finite element simulation, the values of corroded compressive strength $f_{c,d}'$ are calculated using Eq. (2) and the reduced value of compressive fracture energy G_C is used for the concrete elements in order to model the effect of the loss of strength and ductility from the cracked concrete on the corroded tested beams.

Previous studies have indicated that corroded reinforcement strength and ductility are mainly affected by variability in the loss of steel cross-section across their lengths [32]. An alternative solution is proposed by modeling the corroded steel rebar over a length based on average cross-section loss along with empirical coefficients because of the difficulty in applying the real variability of steel corrosion in the numerical model.

In addition to the reduction attributed to the average cross-section, the use of empirical coefficients (whose values are lower than 1.0) is expected to account for the reduction in the strength and ductility of the corroded rebar due to the variable cross-sectional loss along the reinforcement length. The simplified bilinear constitutive stress-strain relationship of steel as shown in Fig. 3(b) is used without empirical coefficients, because the corrosion damage on the rebar is considered in the FE model by reducing the steel cross-sectional areas over the rebar length according to steel weight loss, where the post-yield module is presumed to be 1 percent of its elastic modulus E_s. There, the yield tensile strength and ultimate tensile strength of steel are f_y and f_{su}, while ε_y and ε_{su} are respectively the yield strain and maximum steel strain.

In the proposed model, the loss of corroded steel is represented simply by reducing the reinforcement cross-section area based on the weight loss from the experimental test. The following equations can calculate the cross-sectional area of the corroded reinforcing steel rebar:

$$A_s = \frac{\pi D^2}{4}\left(1 - \frac{c}{100}\right), \tag{7}$$

$$c = \frac{W_o - W_C}{W_o} * 100, \tag{8}$$

where W_o and W_C are the weight of the sound and corroded reinforcements, *c* represents the degree of corrosion.

Finally, the steel – concrete bond constitutive model was proposed. The amount of steel corrosion and the confinement of the reinforced concrete as indicated by the existence of stirrups are the two main factors that have tremendous effects on the bond stress-slip relationship. There is agreement on its well-defined pattern at the pre-cracking point where the bond strength initially increased with the amount of corrosion and then decreased significantly as the longitudinal corrosion cracking formed along the steel reinforcement. However, for the general design of concrete covers and stirrup quantities, bond failure in RC structures that have corroded steel rebars is often seen by the splitting mechanism. Therefore, for the deteriorated bond between steel and concrete, the residual bond stress-slip curve as proposed by Kallias et al. [12] and Maaddawy et al. [33] is used herein, and the bond stress-slip relationship in CEB-FIP Model Code [31] is used to model the good bond as shown in Fig. 3(c).

$$U_{\max,D} = R\left[0.55 + 0.24\left(c/d_b\right)\right]\sqrt{f_c} + 0.191\left(A_{st} f_{yt} / S_s d_b\right), \tag{9}$$

$$R = A_1 + A_2 m_L, \tag{10}$$

where $U_{max,\,D}$ is the residual bond strength, which can be determined by Eq. (9), with *c* being the concrete cover, d_b being the diameter of the longitudinal rebar, A_{st} being the cross-section area of the stirrup, f_{yt} being the yield strength of the stirrup, S_s being the stirrup spacing. R is the factor accountable for the residual contribution of concrete towards the bond strength as a function (Eq. (10)) of A_1 = 1.079 and A_2 = –0.0123 with the corrosion current density i_{corr} (mA/cm^2) = 0.35 [33], and m_L is the amount of steel weight loss in percentage. Eq. (9) consists of two different terms: concrete and stirrup contributions to the bond strength are related to the first and second terms, respectively. The effectiveness of this equation is that the level of confinement can be varied with the changes in the stirrup spacing and concrete compressive strength for different specimens. The proposed model of bond deterioration model is validated in the numerical studies of Saether et al. [34]. Otherwise, apart from the empirical models that have been proposed [35–40], the advantages of this bond strength model enable simulating the reduction in confinement and then bond strength of the RC beams without stirrups, including its ability to predict the experimentally observed increase of bond strength for a low degree of corrosion, e.g., the case of tested beams in group C3.

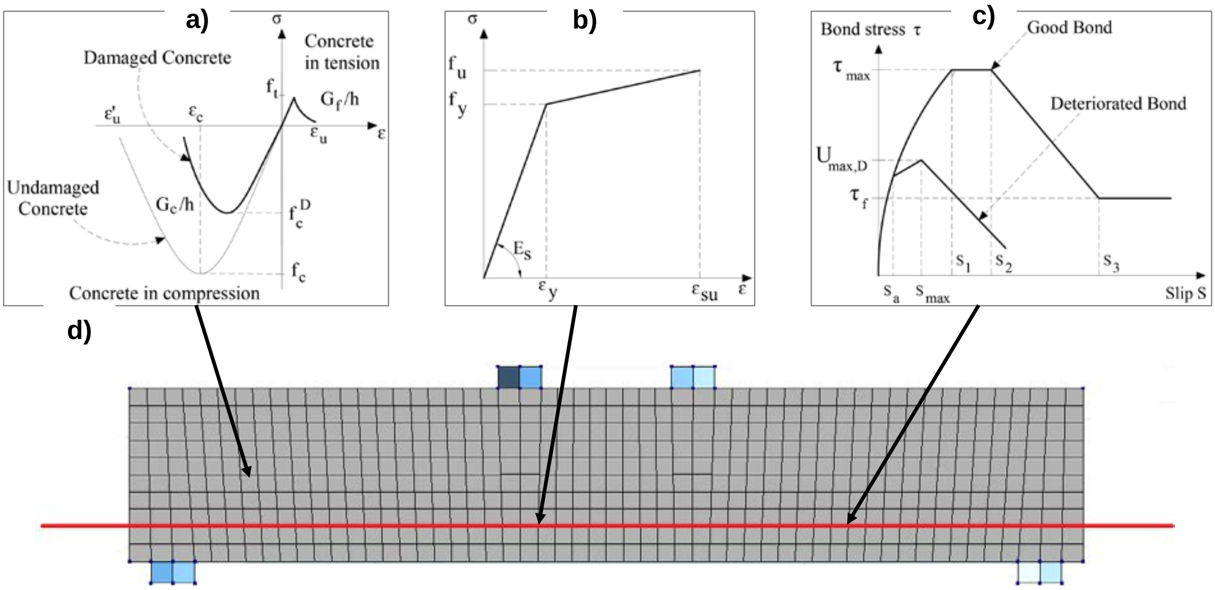

Figure 3. Constitutive models for (a) concrete in compression and tension, (b) steel, (c) bond stress-slip law, (d) mesh discretization of the beam and support conditions.

The concrete is modeled with an element mesh of 20×20×20 mm using a 20-node hexahedron solid element, as illustrated in Fig. 3(d). The compressive strength of concrete is assigned to be 20 MPa on cylinder corresponding to the value obtained from the compression test. Meanwhile, the residual compressive strength of damaged concrete in the target corrosion areas is calculated by Eq. (2) and reduced from 19.2 to 17.8 MPa when increasing the corrosion degree of longitudinal reinforcement from 3 % to 5 %. Moreover, the tensile strength of damaged concrete has remained the identical value as the undamaged concrete at 2.4 MPa. Lastly, the modulus of elasticity for damaged and undamaged concretes shown in Table 3 are calculated by the compressive strength using the formula proposed in CEB-FIP Model Code [31].

In DIANA FEA software, the steel reinforcement is modeled as bond-slip reinforcement. A line-solid interface element has been used in order to simulate the influence of bond-slip behavior because it connects slip reinforcement to the continuum element in which the line element is located. The yield and ultimate tensile strengths of steel used are also summarized in Table 3. In the present simulation, the effect of steel corrosion is modeled by reducing the cross-section of the tension reinforcement based on the corrosion degree. For non-corroded beams, the bond strength and slip parameters are selected based on CEB-FIP Model Code [31], such as the maximum bond strength τ_{max} = 10.0 MPa, the residual bond strength τ_f = 1.05 MPa, the slips S_1 = S_2 = 0.6 mm and S_3 = 2.5 mm, and the exponent coefficient α = 0.4. For corroded tension reinforcement, in order to model the splitting failure mode of unconfined RC beams without stirrups, S_1 must be taken close to S_2, and the descending branch must be sharp, reducing the value of S_3, and considering τ_f close to zero. The deteriorated bond curve, as illustrated in

Fig. 3(c), is applied, then the residual bond strength is calculated by Eq. (9) as given in Table 3. In the simulated model of beam C3 and C4, the bond strength enhancement as seen in experiments will be taken into consideration by increasing about 25 % to beam C0.

Table 3. Mechanical properties of materials for modeling tested RC beams.

Beam notation	C0	C3	C4	C5
Residual compressive strength of damaged concrete (MPa)	20	19.2	18.9	17.8
Residual tensile strength of concrete (MPa)	2.4	2.4	2.4	2.4
Young's modulus of concrete (MPa)	25760	25510	25420	25070
Yield tensile strength of steel (MPa)	328.5	328.5	328.5	328.5
Ultimate tensile strength of steel (MPa)	528.8	528.8	528.8	528.8
Elastic modulus of steel (GPa)	210	210	210	210
Maximum bond strength (MPa)	10	12.5	8	2

3. Results and Discussion

3.1. Experimental results of shear behavior

A total of eight experimental beams were fabricated and tested in the laboratory. Six beams belong to groups C3, C4, and C5 were subjected to accelerated corrosion, and the remaining two beams of group C0 were retained as non-corroded control beams. All beams were without compression and transverse shear reinforcement. Test variables included the different degrees of corrosion of 0 %, 3.13 %, 4.1 %, and 4.93 % on average. The shear responses of the experimental beams are shown in Fig. 4. For the control beams, three distinct phases will characterize the load – deflection response, as follows: (i) the first phase represents the action of an un-cracked beam with a gross inertia moment; (ii) the second phase represents the first shear crack with a reduced inertia moment; (iii) the third phase is the post-peak phase after failure. In the control beams C0-1 and C0-2, the first crack was observed at the load of approximately 7.5 kN, and shear failure occurred at the ultimate load of 34.8 and 35.1 kN, respectively. The corroded beams belong to groups C3 and C4 exhibited shear behavior similar to that of the control beams. However, in the case of the beams C3-1 and C3-2 having the target corrosion degree of 3.16 % and 3.10 %, respectively, the shear strength was increased by approximately 7 % (37.5 kN versus 35 kN on average) while in the case of the beams C4-1 and C4-2 the maximum capacity is nearly equal to the result of the control beams in group C0. These results can be explained that the bond stress between steel and concrete increases in the experimental beams having the corrosion degree smaller than 4 % regardless of the corrosion cracks that occurred along the longitudinal reinforcement that is mentioned in the literature [10, 20, 41].

In addition, the beams C5-1 and C5-2 that were attacked by more severe corrosion had lower overall initial stiffness than the other tested beam specimens. There were no apparent shear cracks but the flexural cracks in the beam web during the test. It is also stated that the width of the splitting cracks gradually increased with load increase after the splitting cracking formed along the longitudinal reinforcing rebars, and failure occurred at 32.5 kN and 30.2 kN corresponding to a decrease of 10 % in comparison with those of the control beams. This is because the bond-loss between reinforcement and concrete dominates the failure mechanism of these corroded RC beams as the corrosion degree increases before sufficient tensile forces are developed in the tension reinforcement to resist the in-plane bending moment.

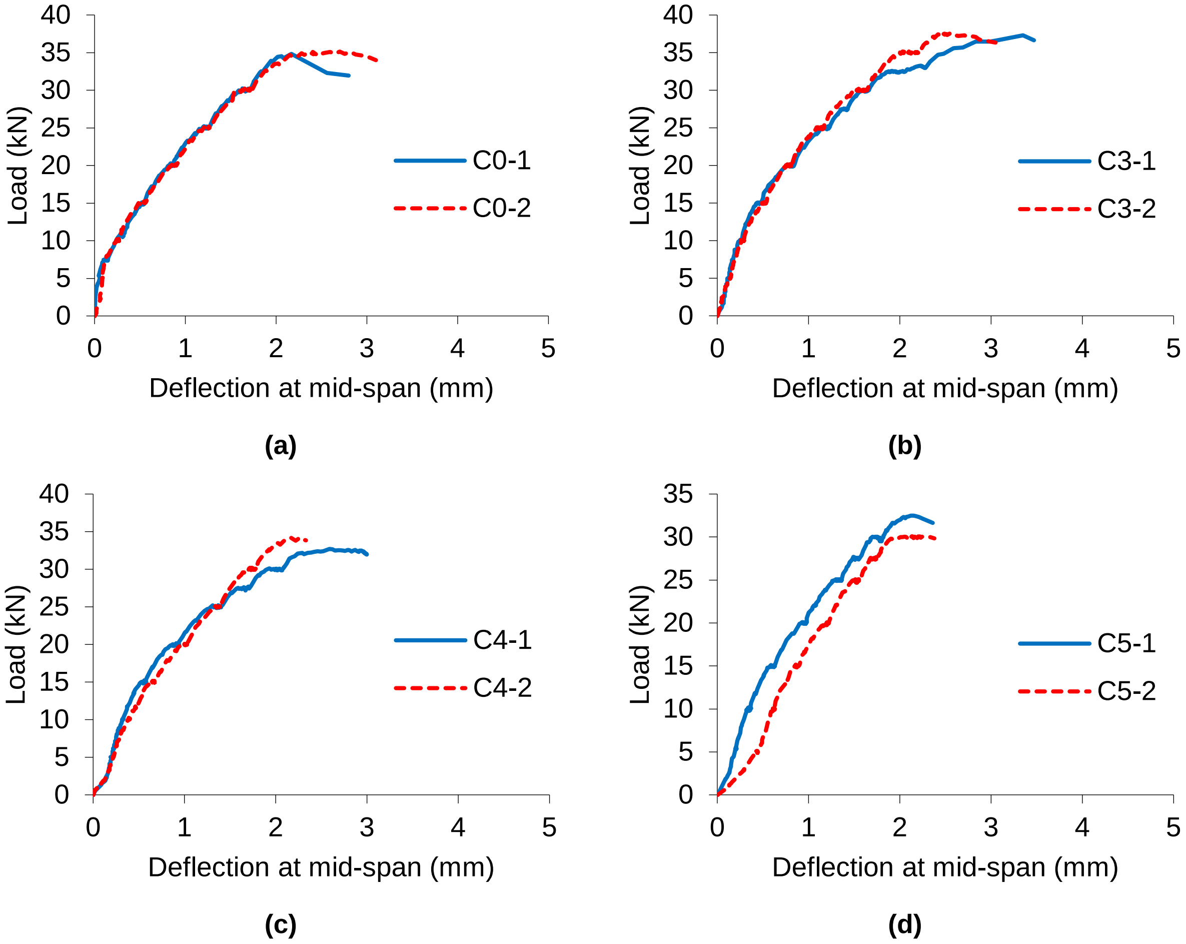

Figure 4. Load – deflection curves of the experimental beams:
(a) group C0, (b) group C3, (c) group C4, (d) group C5.

Table 4 synthesizes the main results obtained using the four-point loading test for each experimental beam, characterized by the corrosion degree of longitudinal reinforcement, ultimate load, and failure mode. For each test group, the average value of the ultimate load is calculated in order to compare the shear strength and failure modes between the beams with different degrees of corrosion.

Table 4. Summary of test results.

Beam notation	Degree of corrosion *c* (%)	Ultimate load *P* (kN)	Average ultimate load (kN)	Failure mode
C0-1	0	34.8	35.0	Diagonal tension failure
C0-2	0	35.1		Diagonal tension failure
C3-1	3.16	37.3	37.5	Diagonal tension failure
C3-2	3.10	37.6		Diagonal tension failure
C4-1	4.27	35.4	34.8	Diagonal tension failure
C4-2	3.94	34.2		Diagonal tension failure
C5-1	4.99	32.5	31.3	Shear tension failure
C5-2	4.87	30.2		Shear tension failure

3.2. FEM results of shear behavior

Fig. 5 illustrates the comparison between the results of tested beams by experimental and numerical approaches. It is confirmed that the simulation by modifying the constitutive materials shown in section 3 is capable of modeling the response of corroded RC beams with reasonable accuracy between the two approaches results for the load – deflection curves of the control beam C0 and three corroded beams C3, C4, C5. FE model can predict the ultimate flexural strength of tested beams C0, C3, and C5 with good accuracy. The beam C4 with a 4 % degree of corrosion in stirrups has the least reduction in load-carrying capacity, 34.2 kN in the test versus 31.5 kN in FEM. The ultimate load of the beam C5 in the test was 30.2 kN compared with approximately 30.5 kN at the same deflection of FEM results.

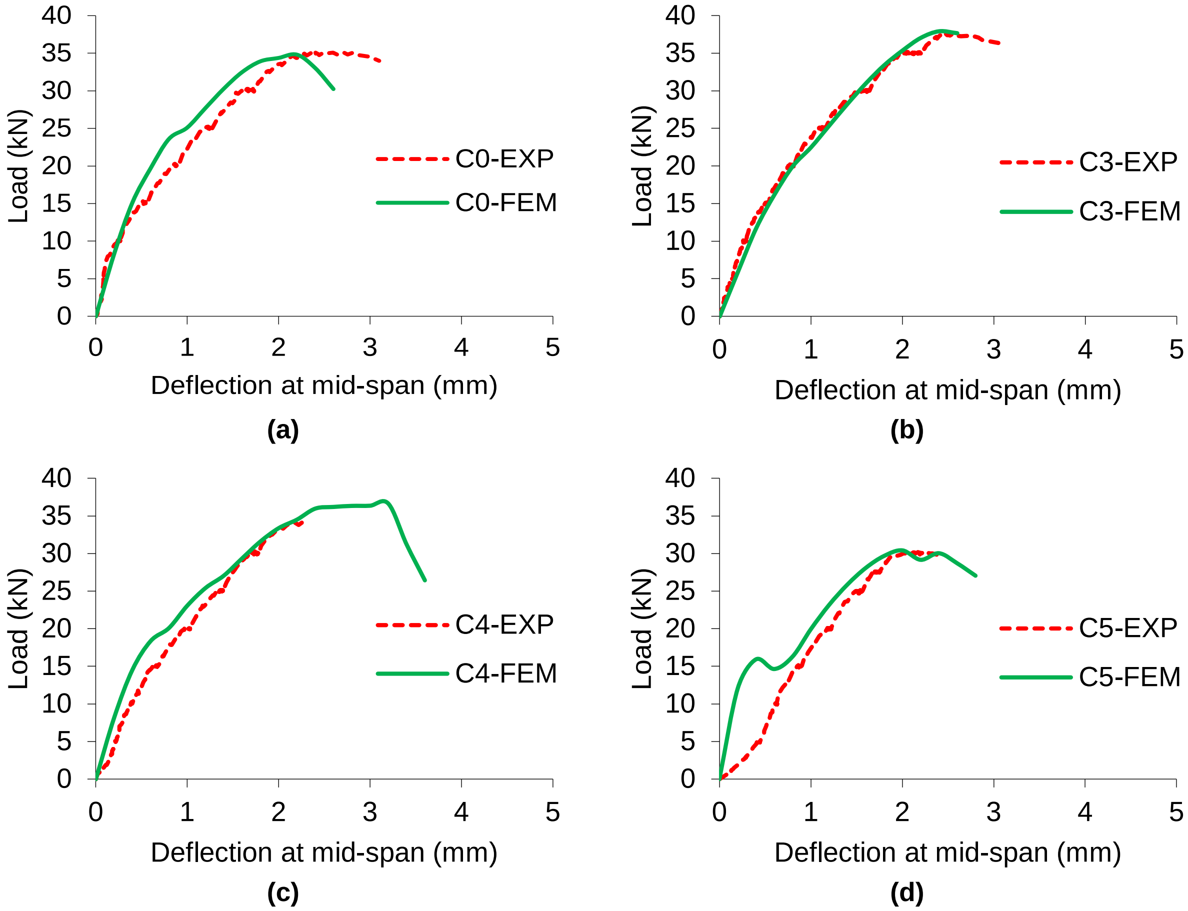

Figure 5. Load – deflection curves of corroded beams using experiment and FEM.

Due to the increasing corrosion degree of tension reinforcement of eight tested beams, the cross-sectional areas of the tension reinforcement decreased, and the concrete cover cracked, leading to a reduction of the effective cross-section. The shear strength of corroded RC beams is considerably low in all cases. The shear strength dropped rapidly after the peak load, and a small displacement increment caused a large decrease in shear strength, which is a characteristic of the shear failure mode. Small amounts of steel corrosion, prior to the development of visible concrete cracking, tend to cause an increase of bond strength between the steel rebars and concrete. Bond strength begins to deteriorate with the formation of corrosion cracking in concrete, typically along the reinforcement length.

As mentioned in the literature review, the shear strength of concrete beams without shear reinforcement is determined by the shear strength of the concrete compressive zone, the shear force due to dowel action, aggregate interlock, and bond strength with efficient anchorage condition. In the case of group C3, by sensitively increasing the maximum bond strength from 10 MPa in the case of a good bond to 12.5 MPa (cf. Table 3), the maximum capacity obtained of beam C3 from the test can be simulated by a numerical approach without considering the bond enhancement of tension reinforcement due to the dowel action as it is shown in Fig. 5.

Otherwise, in the case of group C5, FEM simulation shared the same maximum capacity as reported from the test, which is around 10 % less than those of the non-corroded beam. The differences in the initial stiffness between experimental and numerical approaches can be seen. In the test, due to the significant amount of crack forming along the tension reinforcement from the accelerated corrosion stage, the tested C5 beam shared the significantly larger deflection at 10 kN load, which indicates the lower initial stiffness than other tested beams. On the other hand, by using the FEM simulation, the maximum bond strength was decreased from 10 MPa in the case of a good bond to around 2 MPa (cf. Table 3). The performance of the simulated beam C5 is similar to beam specimens during the elastic stage. The corresponding load later shows a slight decrease before rising significantly and shared the same value at the failure stage as it is given in the experimental test. This is because the loss in bond strength between steel and concrete only has a contribution to the structural performance of the beam after the first crack occurrence, or the tensile stress in concrete surpasses its tensile strength.

In general, the results of corroded beams in FEM simulation showed the sensitive responses to the selection of the model of bond strength reduction with the corresponding parameters assigned in DIANA. The lack of a formulation for the bond strength in simulation for corroded steel rebars with varying diameters in tension reinforcement is a barrier against accurate estimation for the ductility of FEM simulated and tested beams. It can be seen by the differences in deflection at the failure stage of both methods. There was a noticeable difference in the stiffness of the FE model comparing with the experimental beams, and it can be ascribed to initial cracking in concrete before loading due to the corrosion of steel rebars when the simulated beams were considered uncracked at the onset of the FE analysis.

(a) (b)

Figure 6. Failure modes of tested beams: (a) Diagonal tension failure, (b) Shear tension failure.

The crack strain distribution obtained from FE analysis was also compared with the experimental results as shown in Fig. 6 for both types of failure modes (cf. Table 4) to confirm the applicability and accuracy of the model. As stated previously, all tested specimens exhibited shear dominant failure, and cracks mostly occurred in the zone of the beam with the maximum shear load. Fig. 7 shows the maps of concrete cracks due to loading for each tested beam, which is identified by the test and the FE model. The cracking patterns of the control beams and corroded beams are consisting of corrosion cracks marked red and loading cracks (i.e. flexural cracks in loading and shear cracks at failure). For the sample groups C0, C3, and C4, the corrosion cracks propagated for a limited length along longitudinal reinforcement, while they propagated for the total length of the corroded beams in group C5. As it is illustrated, FEM results can represent the crack pattern of the tested beams with a good correlation.

For the control beams C0-1 and C0-2, they showed typical diagonal tension failure mode, which is a sudden failure of concrete in shear. In group C3, the development of vertical cracks (flexural cracks) at the bottom of the beam due to flexural tensile stress has led to diagonal tension failure. If the load on the beam increases, as it propagates from the support point of the beam towards the loading point, these cracks expand both in width and length and bend in a diagonal direction. The beams in groups C3 and C4 exhibited a similar failure mode and shear crack pattern to those of the reference specimen. The corroded beams C5-1 and C5-2, which have higher corrosion degrees, showed a different failure mode. In particular, as the degree of corrosion reached 5 %, beam C5-2 had a shear tension failure at the final stage and illustrated a tendency that the width of the splitting cracks caused by corrosion increased significantly as the external load increased. Moreover, the diagonal cracks propagate horizontally along the rebars, it is mainly because of inadequate anchorage of the longitudinal rebars, and the specimen failed abruptly with the occurrence of the nearly vertical critical shear cracks at the maximum load-carrying capacity. While it should be noted that smeared cracking approach provides a rough estimation about stress-release resulting from cracking [42], the present finite element analysis exhibited a similar cracking pattern.

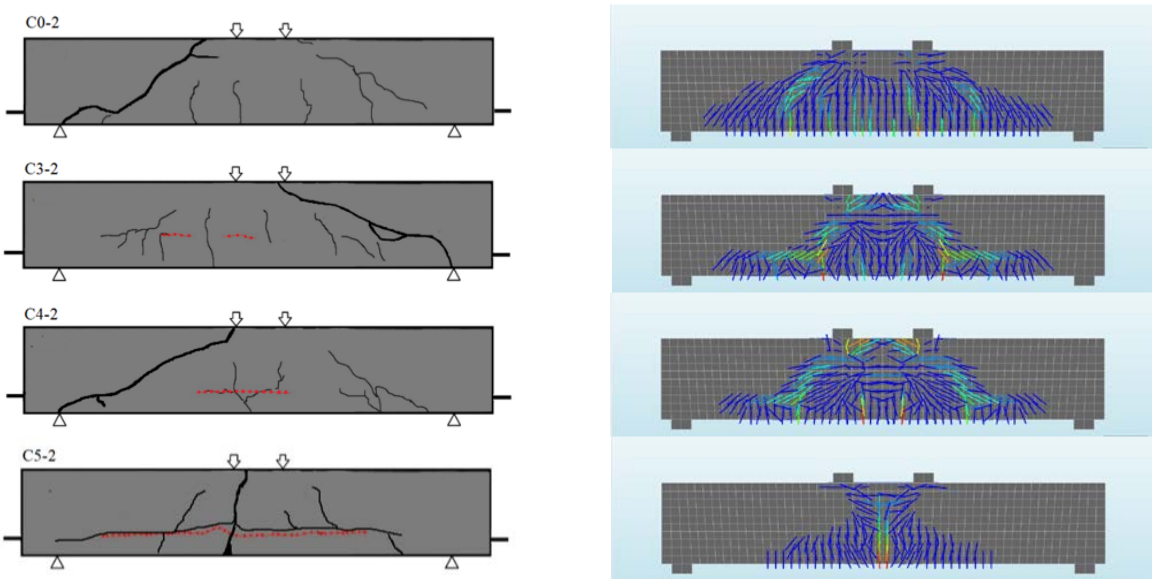

Figure 7. Cracking patterns at the failure of the beams using test and FEM.

3.3. Parametric study

According to the current design codes such as CEB-FIP Model Code 2010 [31] and ACI 318-19 [43], the beams that have the shear span-effective depth ratio (a/d) smaller than 2.0 are considered as deep beams. In general, deep beams can sustain high shear strength because of the tie-arched mechanism that distributes the load directly to the support through concrete compressive struts. This type of beam usually fails by shear compression failure, which occurs at the tip of the shear crack when the compressive strength of the concrete is exceeded in the compression area. Meanwhile, the beams with the a/d ratios greater than 2.0 are slender beams. In slender beams, the beam mechanism plays a more important role. This is because the considerably increasing distance between the loading point and the support has deteriorated the tied-arch mechanism. After the failure of the beam mechanism, the diagonal cracks propagate rapidly to the loading point with the sudden breakdown of aggregate interlock, which causes diagonal tension failure. To examine the FE model capability in simulating the different behavior associated with beam and tie-arched mechanisms, the tested beam C4 without shear reinforcement and shear span-to-depth ratios ranging from 1.0 to 6.0 are considered as illustrated in Fig. 8.

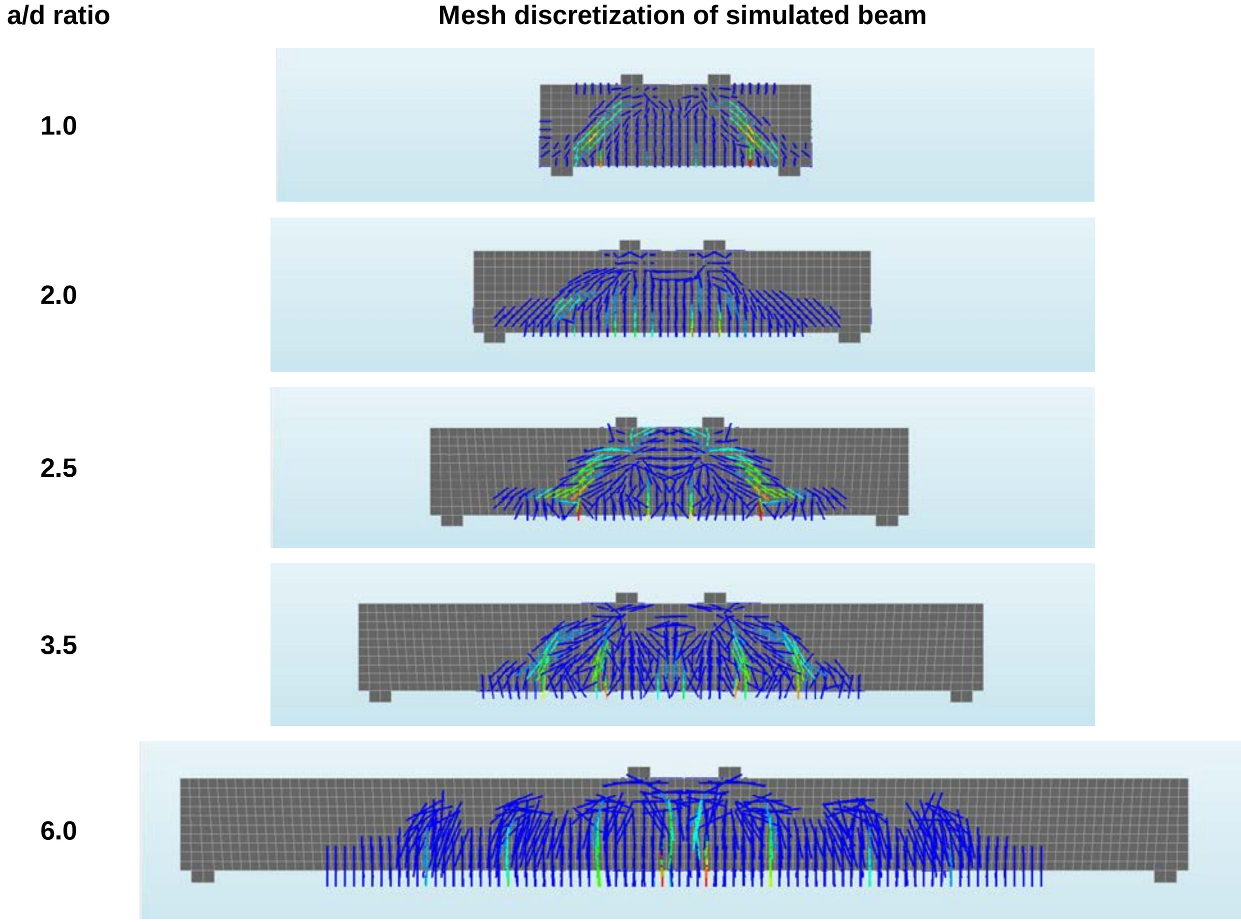

Figure 8. Crack strain distribution at the failure of simulated beams with different a/d ratios.

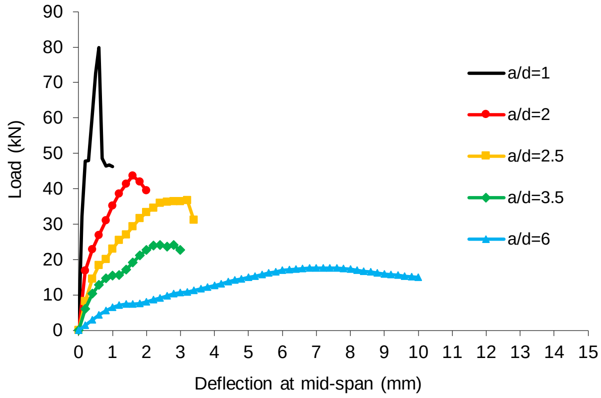

Figure 9. Load - deflection curves of simulated corroded beams with different shear span-to-depth ratios.

Fig. 8 shows the crack strain distribution at failure. The presence of a well-defined inclined strut from load point to support is evident for the a/d ratio equals to 1.0. The numerical results show that the higher strains are localized below the line connecting the load and support points. On the other hand, for the a/d higher ratios of 2.0, 2.5, 3.5, the beam action is shown by the horizontal compression chord at the top of the beam and the wide inclined compression field in the web. The failures observed are due to crack propagation which is the splitting crack starting parallel to the reinforcement, propagating diagonally across the web, and finally splitting the top concrete cover. Lastly, the crack strain distribution at the failure stage of a beam with the a/d ratio equals to 6 was observed, several vertical cracks appeared around the mid-span rather than the formation of diagonal crack, which indicates the flexural failure. Fig. 9 shows the load – deflection curves of the simulated beams having the a/d ratio ranging from 1.0 to 6.0. It indicates that the shear span-to-depth ratio is a significant factor affecting the shear strength of all simulated beams. This is because the load-carrying capacity of the beams decreased considerably with increasing the a/d ratio. The maximum shear strength of the simulated beam having the a/d ratio equals to 1 is approximately 100 %, 166 %, and 220 % larger than beams having a/d ratio equal to 2.0, 2.5, and 3.0, respectively. When a/d equals to 6, the failure mode shifted from shear failure to flexural failure having the maximum capacity of around one-third of the beam with a/d equal to 1.

4. Conclusions

In this paper, an experimental study and a 3D non-linear FE model simulation are carried out to assess the structural performance of a series of eight RC beams without shear reinforcement damaged by varying degrees of steel corrosion. The results of FE analyses were compared to the experimental results to investigate the accuracy of the numerical approach. Key parameters affecting the shear strength of tested beams are identified. These include the influence of compressive strength of concrete, impaired bond performance (due to corrosion in the tension reinforcement), and reduced cross-section area of tension reinforcement. The parametric study of different shear span-to-depth ratios was also conducted to examine the FE model capability in simulating the different behavior associated with beam and tie-arched mechanisms. The main conclusions are drawn as follows:

1. The tension reinforcement corrosion has an overall adverse effect on the shear performance of RC beams. In the corroded beams where the tension reinforcement subjected to corrosion degree smaller than 4 %, specimens showed about 7 % increase of shear strength, compared with control beams. Even when the beams were subjected to 4 % degree of corrosion in tension reinforcement, the maximum shear capacity obtained still remained the same as of the control beams because of the increase in bond stress between tension reinforcement and concrete regardless of the formation of crack openings from accelerated corrosion process.

2. The main cause for the loss of shear strength in corroded RC beams without stirrups is due to the impaired bond. While the structural behavior of experimental beams can be simulated by reducing the bond strength values, this indicates that the deterioration of bond behavior has a significant contribution to the structural performance of corroded RC beams even with the relatively small degree of corrosion, which is around 5 %.

3. The adoption of the extended finite element method has the ability to predict the load – deflection response, cracking pattern of corroded RC beams without shear reinforcement. In the case of the beams with the corrosion degree smaller than 4 %, loss of steel cross-sectional area and associated compressive strength of concrete loss in the finite element analyses were found to have a significant influence.

4. The accuracy of the FE model is validated in the parametric study. The use of such numerical models can not only serve as a tool for assessing existing structures that are designed and constructed without shear reinforcement and also as a complementary tool for planning and optimization of the experimental studies by establishing the preliminary parameter sensitivity.

References

1. Castel, A., François, R., Arliguie, G. Mechanical behaviour of corroded reinforced concrete beams – Part 1: Experimental study of corroded beams. Materials and Structures. 2000. 33. Pp. 539–544.
2. Torres-Acosta, A.A., Fabela-Gallegos, M.J., Munoz-Noval, A., Vázquez-Vega, D., Hernandez-Jimenez, J.R., Martinez-Madrid, M. Influence of corrosion on the structural stiffness of reinforced concrete beams. Corrosion. 2004. 60(9). Pp. 862–872.
3. Torres-Acosta, A.A., Navarro-Gutierrez, S., Terán-Guillén, J. Residual flexure capacity of corroded reinforced concrete beams. Engineering Structures. 2007. 29(6). Pp. 1145–1152.
4. Almusallam, A.A., Al-Gahtani, A.S., Aziz, A.R., Dakhil, F.H., Rasheeduzzafar. Effect of reinforcement corrosion on flexural behavior of concrete slabs. Journal of Materials in Civil Engineering. 1996. 8(3). Pp. 123–127.
5. Rodriguez, J., Ortega, L.M., Casal, J. Load carrying capacity of concrete structures with corroded reinforcement. Construction and Building Materials. 1997. 11(4). Pp. 239–248.
6. Soltani, M., Safiey, A., Brennan, A. A state-of-the-art review of bending and shear behaviors of corrosion-damaged reinforced concrete beams. ACI Structural Journal. 2019. 116(3). Pp. 53–64.

7. Zhu, W., François, R., Fang, Q., Zhang, D. Influence of long-term chloride diffusion in concrete and the resulting corrosion of reinforcement on the serviceability of RC beams. Cement and Concrete Composites. 2016. 71. Pp. 144–152.
8. Xu, S., Zhang, Z., Li, R., Qiu, B. Experimental study on the shear behavior of RC beams with corroded stirrups. Journal of Advanced Concrete Technology. 2017. 15(4). Pp. 178–189.
9. Higgins, C., Farrow, W.C.III. Tests of reinforced concrete beams with corrosion-damaged stirrups. ACI Structural Journal. 2006. 103(1). Pp. 133–141.
10. Lachemi, M., Al-Bayati, N., Sahmaran, M., Anil, O. The effect of corrosion on shear behavior of reinforced self-consolidating concrete beams. Engineering Structures. 2014. 79. Pp. 1–12.
11. El-Sayed, A.K., Hussain, R.R., Shuraim, A.B. Influence of stirrup corrosion on shear strength of reinforced concrete slender beams. ACI Structural Journal. 2016. 113(6). Pp. 1223–1232.
12. Kallias, A.N., Imran Rafiq, M. Finite element investigation of the structural response of corroded RC beams. Engineering Structures. 2010. 32(9). Pp. 2984–2994.
13. Biswas, R.K., Iwanami, M., Chijiwa, N., Uno, K. Effect of non-uniform rebar corrosion on structural performance of RC structures: A numerical and experimental investigation. Construction and Building Materials. 2020. 230. 116908.
14. Blomfors, M., Lundgren, K., Zandi, K. Incorporation of pre-existing longitudinal cracks in finite element analyses of corroded reinforced concrete beams failing in anchorage. Structure and Infrastructure Engineering. 2020. 1–17.
15. Coronelli, D., Gambarova, P. Structural assessment of corroded reinforced concrete beams: modeling guidelines. Journal of Structural Engineering. 2004. 130(8). Pp. 1214–1224.
16. Coronelli, D., Mulas, M.G. Modeling of shear behavior in reinforced concrete beams. ACI Structural Journal. 2006. 103(3). Pp. 372–382.
17. Huang, L., Ye, H., Jin, X., Jin, N., Xu, Z. Corrosion-induced shear performance degradation of reinforced concrete beams. Construction and Building Materials. 2020. 248. 118668.
18. Nakamura, H., Iwamoto, T., Fu, L., Yamamoto, Y., Miura, T., Gedik, Y.H. Shear resistance mechanism evaluation of RC beams based on arch and beam actions. Journal of Advanced Concrete Technology. 2018. 16(11). Pp. 563–576.
19. Toongoenthong, K., Maekawa, K. Interaction of pre-induced damages along main reinforcement and diagonal shear in RC members. Journal of Advanced Concrete Technology. 2004. 2(3). Pp. 431–443.
20. Han, S., Lee, D., Yi, S., Kim, K.S. Experimental shear tests of reinforced concrete beams with corroded longitudinal reinforcement. Structural Concrete. 2020. 21(5). Pp. 1763–1776.
21. Tan, N.N., Kien, N.T. An experimental study on the shear capacity of corroded RC beams without shear Reinforcement. Journal of Science and Technology in Civil Engineering. NUCE 2021. 15(1). Pp. 55–66.
22. Maekawa, K., Hasegawa, T. The state-of-the-art on constitutive laws of concrete. Concrete Journal. 1994. 32(5). Pp. 13–22.
23. Maekawa, K., Pimanmas, A., Okamura, H. Nonlinear mechanics of reinforced concrete. Spon Press, London, 2003.
24. Shayanfar, M.A., Barkhordari, M.A., Ghanooni-Bagha, M. Effect of longitudinal rebar corrosion on the compressive strength reduction of concrete in reinforced concrete structure. Advances in Structural Engineering. 2016. 19(6). 897–907.
25. Lim, S., Akiyama, M., Frangopol, D.M. Assessment of the structural performance of corrosion-affected RC members based on experimental study and probabilistic modeling. Engineering Structures. 2016. 127. Pp. 189–205.
26. TNO. DIANA 9.1 User's manual. TNO Building and Construction Research. Delft, 2005.
27. Nakamura, H., Higai, T. Compressive fracture energy and fracture zone length of concrete. In: Shing P., Tanabe T., editors. Modelling of inelastic behaviour of RC structures under seismic loads. American Society of Civil Engineers. 2001. Pp. 471–487.
28. Cape, M. Residual service-life assessment of existing R/C structures. MS thesis, Chalmers Univ. of Technology (Goteborg, Sweden) and Milan Univ. of Technology (Italy, Erasmus Program), 1999.
29. Molina, F.J., Alonso, C., Andrade, C. Cover cracking as a function of rebar corrosion: Part 2 – Numerical model. Materials and Structures. 1993. 26. 532–548.
30. Val, D.V. Deterioration of strength of RC beams due to corrosion and its influence on beam reliability. ASCE Journal of Structural Engineering. 2007. 133(9). Pp. 1297–1306.
31. CEB-FIP Model Code. fib model code for concrete structures 2010. fib, Berlin, Germany.
32. Du, Y.G., Clark, L.A., Chan, A.H.C. Residual capacity of corroded reinforcing bars. Magazine of Concrete Research. 2005. 57(3). Pp. 135–147.
33. Maaddawy, T.E., Soudki, K., Topper, T. Analytical model to predict nonlinear flexural behaviour of corroded reinforced concrete beams. ACI Structural Journal. 2005. 102(4). Pp. 550–559.
34. Sæther, I., Sand, B. FEM simulation of reinforced concrete beams attacked by corrosion. ACI Structural Journal. 2012. 39(2). Pp. 15–31.
35. Tran, N.L. A new shear model for fibre-reinforced concrete members without shear reinforcement. In: Hordijk D., Luković M. (eds) High Tech Concrete: Where Technology and Engineering Meet. Springer, Cham. DOI: 10.1007/978-3-319-59471-2_86
36. Tran, N.L. A mechanical model for the shear capacity of slender reinforced concrete members without shear reinforcement. Engineering Structures. 2020. 219. 110803.
37. Khan, I., François, R., Castel, A. Experimental and analytical study of corroded shear-critical reinforced concrete beams. Materials and Structures. 2013. 47(9). Pp. 1467–1481.
38. Lu, Z.-H., Li, H., Li, W., Zhao, Y.-G., Dong, W. An empirical model for the shear strength of corroded reinforced concrete beam. Construction and Building Materials. 2018. 188. Pp. 1234–1248.
39. Krishan, A., Narkevich, M., Sagadatov, A., Rimshin, V. The strength of short compressed concrete elements in a fiberglass shell. Magazine of Civil Engineering. 2020. 94(2). Pp. 3–10.
40. Kim, H.-G., Jeong, C.-Y., Kim, M.-J., Lee, Y.-J., Park, J.-H., Kim, K.-H. Prediction of shear strength of reinforced concrete beams without shear reinforcement considering bond action of longitudinal reinforcements. Advances in Structural Engineering. 2017. 21(1). Pp. 30–45.
41. Lushnikova, V.Y., Tamrazyan, A.G. The effect of reinforcement corrosion on the adhesion between reinforcement and concrete. Magazine of Civil Engineering. 2018. 4(80). Pp. 128–137.

42. An, X., Maekawa, K., Okamura, H. Numerical simulation of size effect in shear strength of RC beams. Journal of Materials, Concrete Structures and Pavement. JSCE 1997. 35. Pp. 297–316.

43. ACI 318-19. Building Code Requirements for Structural Concrete and Commentary. American Concrete Institute. 2019.

Contacts:

Ngoc Tan Nguyen, *PhD*
ORCID: https://orcid.org/0000-0002-4841-0653
E-mail: tannn@huce.edu.vn

Trung Kien Nguyen
ORCID: https://orcid.org/0000-0002-3108-6463
E-mail: kiennt2@huce.edu.vn

Hoang Giang Nguyen, *PhD*
ORCID: https://orcid.org/0000-0001-7505-2233
E-mail: giangnh@huce.edu.vn

Received 07.03.2021. Approved after reviewing 19.07.2021. Accepted 19.07.2021.

Magazine of Civil Engineering. 2022. 112(4). Article No. 11212

Magazine of Civil Engineering

ISSN 2712-8172

journal homepage: http://engstroy.spbstu.ru/

Research article

UDC 621.5

DOI: 10.34910/MCE.112.12

Flexural behavior of 60 m UHPC pre-stressed box girder

V.T. Nguyen[a] , ***V.C. Mai***[b]

[a] *Le Quy Don Technical University, Ha Noi, Viet Nam*

[b] *Kumoh National Institute of Technology, Gumi, Gyeongbuk, South Korea*

maivietchinh@lqdtu.edu.vn

Keywords: concrete damage plasticity, simulation model, box girder, four-point bending, ultra high performance concrete

Abstract. In recent years, an emerging technology of Ultra High Performance Concrete (UHPC) has become popular in the construction industry and has been applied in many countries around the world. However, this material technology is still relatively new in Vietnam. The present investigation is a study on enhancement in flexural performance and the effectiveness of UHPC box girder strengthened with pre-stressed tendons, which was adapted from the first project of a high-speed train in Vietnam. A 3D simulation model of a 60 m UHPC pre-stressed box girder was implemented using concrete damage plasticity (CDP) approach. The validity of the proposed model is ensured by comparing the simulation results with experimental data. The parametric studies were then performed using the validated finite element model to analyze the flexural behavior of the 60m UHPC pre-stressed box girder. It was concluded that the developed models can accurately capture the behavior and predicts the load-carrying capacity of the UHPC girder. The present research contributes to the development and application of advanced UHPC concrete technology in Vietnam as well as emphasizes effective designs that significantly reduce self-weight and enhance loading capacity for super long-span girders.

Citation: Nguyen, V.T., Mai, V.C. Flexural behavior of 60 m UHPC pre-stressed box girder. Magazine of Civil Engineering. 2022. 112(4). Article No. 11212. DOI: 10.34910/MCE.112.12

1. Introduction

The population explosion in the big cities around the world leads to a rapid increase in the continuous development of transportation infrastructure. And, in this particular scenario, utilizing the full capacity of the material, decreasing the self-weight, increasing the efficiency of the bearing structure, and finally optimizing construction cost, particularly, for a super long span of the structural girder, become the important tasks for structural engineers and researchers. Ultra high performance concrete (UHPC) is an advanced concrete material with superior property both in mechanical and chemical properties is the potential choice to fulfill demanding design requirements. Due to its high packing density with a very low water-to-binder ratio (w/b) and the addition of reactive mineral powder [1–3], such as silica fume, compared with normal concrete, UHPC possesses many superior properties, such as high flowability, high strength, abrasion and impact resistance, low permeability and high durability [4–11]. UHPC offers new opportunities for infrastructure works, building constructions, particularly for super long-span structures. UHPC is considered as an advanced material for the future [12] and is intensively researched in many developed countries including USA [13], Germany [14], France [15, 16], Netherlands [17], Canada [18], Austria [19], Australia [20], New Zealand [21], Republic of Korea [22, 23], and Japan [24]. According to collected data, Y.L. Voo revealed more than 200 bridges are using UHPC as the main bearing structure or the supported parts [25].

The experimental studies of flexural behavior of pre-stressed UHPC girder were implemented by Min-Seon Jeong et al [26] for segmental box girders, by Lee Seung-Jae et al [27] for UHPC pre-stressed

T-beams, by Qing-Young Guo et al [28] for segmental box shaped girders. However, abovementioned studies contribute to field of short-span UHPC girders, more studies are needed for large-scale structures. In the simulation aspect, Luaay Hussein investigated flexural behavior on three series of UHPC-NSC/HSC composite girders by simulation model in Abaqus. The proposed model was validated by experimental results. The comparison between the FE model and test for UHPC-NSC/HSC composite girder showed very close results [29]. M. Singh et al implemented experimental and numerical investigations of a 3.5 m UHPC girder. Numerical simulation was analyzed in Abaqus. The ultimate load capacity predicted by the FEM model is 4 % disparity compared to the test's result [30]. By the numerical simulation in Abaqus, Chen and Graybeal studied three different in length, pre-stressed UHPC I-girder and four different UHPC 2nd generation pi-girders. The length of I-girders is 24.4 m, 7.3 m and 9.2 m, respectively. The 2nd generation pi-girder length is 7.6 m [29]. Based on the linear complementary problem (LCP), Guo et al investigated the applicability of numerical simulation to predict the failure surface of three different UHPC-I girders and validate results by comparing experimental results and finite element analysis of DIANA software. The fracture result comparison between the LCP method and the experimental result shows a similar tendency, implying that the LCP model can capture the behavior of the UHPC girder before and after peak load [26]. According to the literature survey, more experiments and finite element studies are needed on large-scale UHPC pre-stressed girders.

Table 1. Advantages and disadvantages of some kind of box girder.

Case	Advantage	Disadvantage
Pre-stressed Concrete Box Girder	Reduces the thickness of deck and self-weight of structure Higher strength per unit concrete area Quality assurance with precast segments Reasonable cost	High cost of logistic and transportation High deflection at the mid-span after a period of operation Crack in long-span after a period of operation
Steel Composite Box Girder	Greater aerodynamic stability Support point required are less compared to conventional systems Provide better appearance and slender shape	Greater fabrication cost due to reduced scope for automated fabrication Steel girders are costly High maintenance cost, not suitable for aggressive environment
Pre-stressed UHPC Box Girder	All advantages of Pre-stressed Concrete Box Girder Higher torsional stiffness than steel composite girder Shaping is flexible Suitable design in highly aggressive environments Total lower cost	Logistical inefficiencies and transportation cost Require advanced production technology

Table 1 shows the advantages and disadvantages of UHPC box girder compared to other girders. While UHPC has been under research and development for over thirty years, it is still a relatively new material. The lack of understanding on structural behavior of UHPC elements are some of the major factors in slowing the implementation of this technology.

The objective of the paper is to investigate the flexural behavior of UHPC box girder strengthened with pre-stressed tendons. A 3D simulation model of the 60 m UHPC pre-stressed box girder, using concrete damage plasticity (CDP) approach, was implemented. Furthermore, the well-fitted constitutive models both compressive and tensile nonlinear behavior of the material, which plays an important part of numerical simulation, will be conducted in this study.

2. Methods

In terms of the existing constitutive model, the Concrete Damage Plasticity (CDP) which is based on continuum, plasticity, and damaged state for concrete, and has been implemented in ABAQUS for numerical simulation. CDP model was firstly introduced by Lubliner et al. for monotonic loading [33]. Due to the advantages of the CDP model to capture the behavior of concrete materials, in the present study, the concrete damage plasticity (CDP) model is chosen to investigate the flexural behavior of the UHPC box girder. Fig. 1 depicts tension behavior and compressive behavior in the CDP model. In the CDP model, the uniaxial tension stress-strain relation is assumed linearly elastic until failure stress of f_t^0. For uniaxial compression, the response is linear up to the initial yield f_c^0.

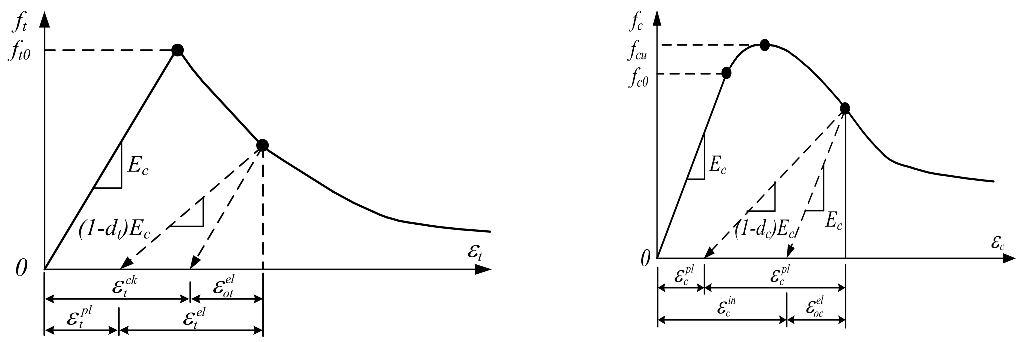

a) **b)**

Figure 1. Tension behavior (a) and Compressive behavior in the CDP model (b).

After reaching the ultimate stress in the plastic zone, the response of concrete is described by the stress hardening followed by strain softening. Stresses of the concrete element f_t and f_c determined to unload from any point on the strain are:

$$f_t = E_c\left(\varepsilon_t - \varepsilon_t^{pl}\right)\left(1 - d_t\right), \tag{1}$$

$$f_c = E_c\left(\varepsilon_c - \varepsilon_c^{pl}\right)\left(1 - d_c\right), \tag{2}$$

where E_c denotes Young's modulus of concrete. ε_t, ε_c are the strain in tension and compression. ε_t^{pl}, ε_c^{pl} define the plastic strain in tension and compression. Damage variables d_t and d_c define the degradation of the elastic stiffness. To determine the failure surface, the effective tensile $\overline{f}_t$ and compressive cohesion stresses $\overline{f}_c$ of concrete can be calculated by:

$$\overline{f}_t = \frac{f_t}{1 - d_t} = E_c\left(\varepsilon_t - \varepsilon_t^{pl}\right), \tag{3}$$

$$\overline{f}_c = \frac{f_c}{1 - d_c} = E_c\left(\varepsilon_c - \varepsilon_c^{pl}\right). \tag{4}$$

The relationship of the cracking strain and plastic strain can be expressed by:

$$\varepsilon_t^{pl} = \varepsilon_t^{ck} - \frac{d_t}{1 - d_t}\frac{f_t}{E_0}, \tag{5}$$

$$\varepsilon_c^{pl} = \varepsilon_c^{ck} - \frac{d_c}{1 - d_c}\frac{f_c}{E_0}, \tag{6}$$

where ε_t^{ck}, ε_c^{ck} present the cracking strain, which can be obtained by the total strain minus the elastic strain corresponding to the undamaged material.

3. Results and Discussion

3.1. Validation of simulation model

This section includes the validation of the FE model in Abaqus using the CDP approach to ensure that the proposed model has been correctly implemented and is thereby further used to investigate the flexural behavior of UHPC pre-stressed box girder. The proposed model is verified by comparing the results with the tests of the UHPC beam conducted by Yang et al. Fig. 2 shows the constitutive law of UHPC material in compression and tension behaviour [34]. Input parameters of the CDP model for UHPC material are presented in Table 2.

In the test of Yang, the length of the UHPC beam is 2900 mm with the dimension of cross-section 180 mm × 270 mm, is shown in Fig. 3. The NR1 beam denotes the UHPC plain specimen without the steel bar, whereas the R13 beam includes three steel bars with 13 mm diameter corresponding to the steel bar ratio of 0.9 %, using class of SD400 in Korean code. Fig. 4. shows the test setup of Yang for NR1 beam and R13 under four-point bending moment test.

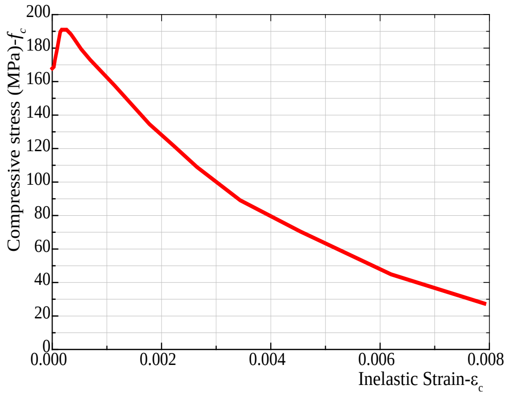

a)

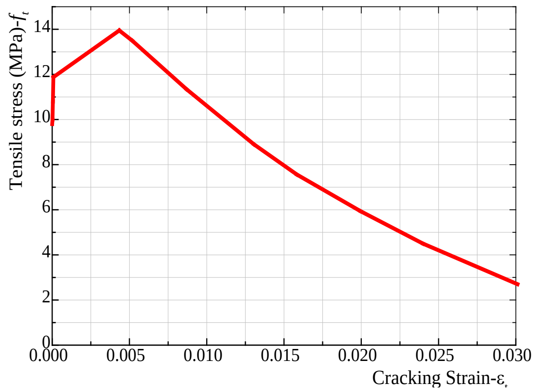

b)

Figure 2. Compressive stress – inelastic strain (a), and Tensile stress – cracking strain of UHPC.

Table 2. Input parameters of CDP model for UHPC.

Property	UHPC
Mass density (ton/mm^3)	2.45e^{-9}
Compressive strength (MPa)	190.9
Modulus of elasticity (MPa)	46418
Poisson's ratio	0.2
Dilation angle ψ (^{0})	36
Eccentricity ϵ	0.1
Stress ratio σ_{bo}/σ_{co}	1.16
Shape parameter (K_c)	0.667
Viscosity parameter μ	0

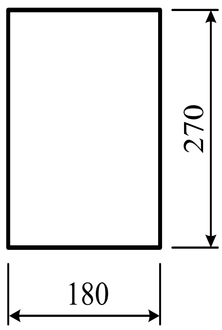

a)

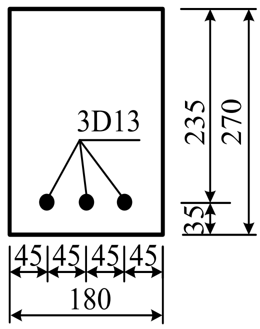

b)

Figure 3. Cross section of Beam NR1 (a), and R13 (b) (mm).

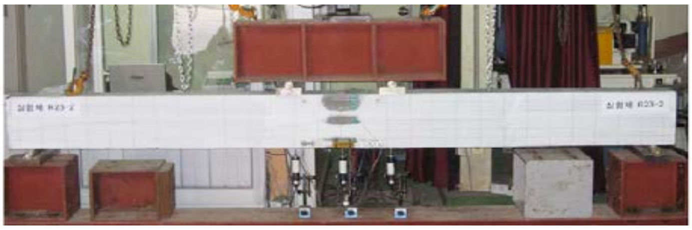

a)

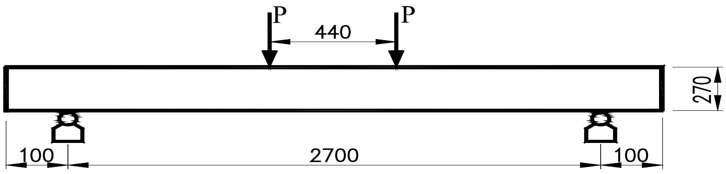

b)

Figure 4. Test setup of Yang.

Load-deflection curves in the test of Yang and simulation are shown in Fig. 5. The peak load and maximum deflection of beam NR1 and R13 according to the test of Yang and simulation result are listed in Table 3. The load-deflection curve obtained by the proposed model is generally similar to the test data, however, the maximum deflection response exhibits the disparity in both cases. The load-deflection curve in the simulation result shows stiffer behavior than the corresponding results from the test. The development of microcracks due to dry shrinkage, UHPC material curing, experimental process, and so on, could be the reason for this disparity. In addition, in the Abaqus model, the concrete–steel interaction is assumed as embedded interaction, implying an idealization interaction. This perfect interaction can also contribute to the superior stiffness in the numerical model.

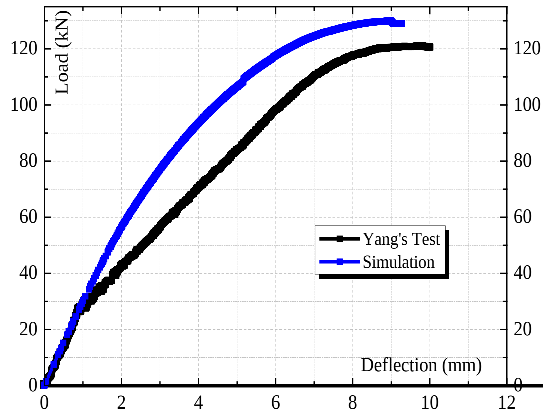

a)

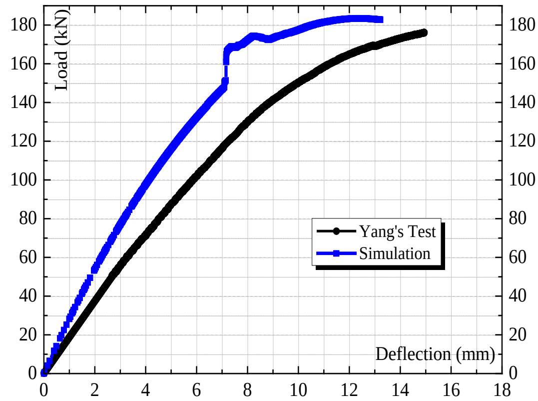

b)

Figure 5. Load-deflection curve in the test of Yang and simulation for beam NR1 (a) and R13(b).

Table 3. Peak load and maximum deflection of beam NR1 and R13.

Beam	Peak load (1)	Peak load (2)	Disparity	Max. deflection (1)	Max. deflection (2)	Disparity
NR1	120.2 kN	128.8 kN	7.2 %	10.3 mm	9.2 mm	13.1 %
R13	174.6 kN	183.7 kN	5.1 %	15.1 mm	12.8 mm	15.2 %

Note: (1) – Yang's test; (2) – Simulation's result

The crack pattern observed in the simulation model is quite similar to the test of Yang, are shown in Fig. 6. Initial, first cracks occurred at flexural zones under loading points. Later on, following the increase of applied load, newer cracks evolved as older cracks propagated wider and deeper in the flexural and shear zone. It can be seen that the CDP model and the constitutive law of material demonstrated the accuracy of the simulation of the UHPC girder under the four-point bending test. Based on the obtained result, the proposed model will be developed to investigate the flexural behavior of 60 UHPC box girder.

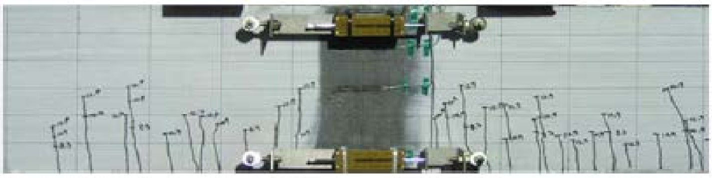

a)

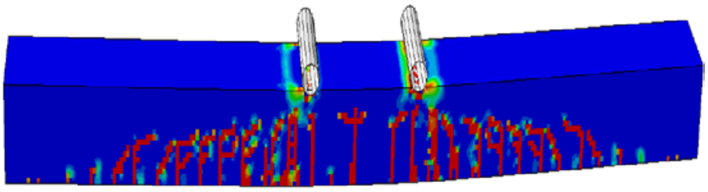

b)

Figure 6. Crack pattern in the test of Yang (a) and simulation (b).

3.2. Finite element model development for 60 m UHPC box-girder

3.2.1. Description of 60 m UHPC box girder

Detail of the UHPC box girder adapted from the first project of the high-speed train in Vietnam. Fig. 7 shows the plan and front view of the UHPC box girder. The cross-section of the girder consists of a UHPC U-shaped part, UHPC deck plate (50 mm), and high strength concrete (HSC) reinforced plate (200 mm) with compressive strength of 40 MPa. The width of the box girder changes from 1600 mm to 2600 mm corresponding to the bottom surface and upper surface. The UHPC box girder contains 2×8 pre-stressed tendons in the upper flange and 6×24 pre-stressed tendons in the lower flange. The 50 mm UHPC plate without reinforcement bar and 200 mm HSC plate with two layers of steel bar are shown in Fig. 8. Parameters of the pre-stressed tendon are taken according to Vietnamese standard and shown in Table 4, in which a tendon cluster is applied a force equivalent to 4853 kN [35].

Table 4. Pre-stressed load of tendon.

Strand	Total area (mm^2)	Ultimate stress fy (MPa)	Pre-stressed Force 0.7 fy (MPa)
24	3328.8	2100	1470

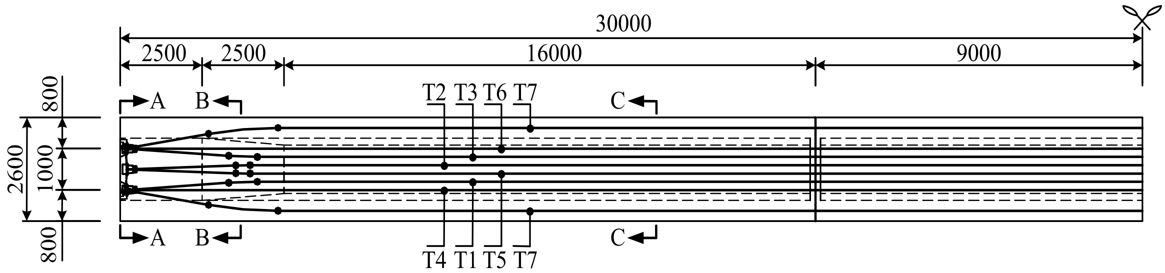

a)

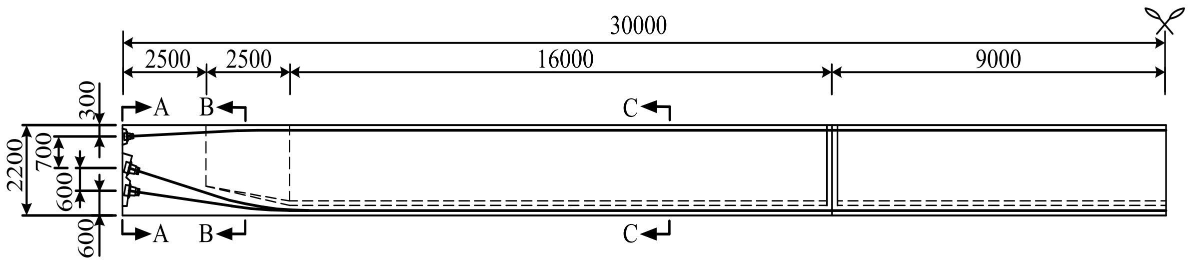

b)

Figure 7. Plan (a) and front view (b) of UHPC box girder (mm).

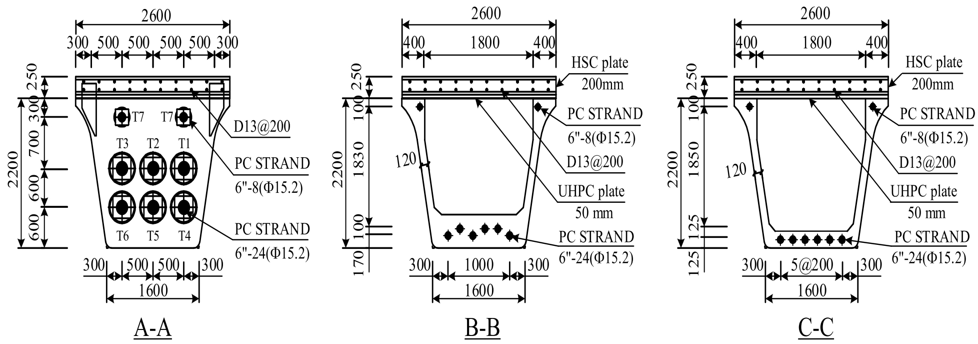

Figure 8. Cross sections of UHPC box girder.

3.2.2. Numerical Results

The input parameters for the UHPC material are adopted as the proposed model. In the Abaqus model, C3D8R and T3D2 element types are selected to simulate concrete and longitudinal bar. C3D8R element (Fig. 9) is defined as a continuum element with reduced integration and hourglass control, which can describe concrete cracking in tension and crushing in compression. T3D2 presents a two-node, three-dimensional truss element used to simulate slender and line elements. There is no moment or perpendicular force to the centerline of this element. The interaction of the UHPC-HSC plate is a tie connection while the embedded property is applied for the interaction of concrete-tendon and concrete-steel bar. The constitutive model of UHPC includes compression post-peak, tension-softening behavior is described by the stress-strain curve in the CDP model (Fig. 2). The box girder is supported by two simple rollers for each end. Three types of loads are applied including self-weight, post-tensioning, and displacement load. In the FE model, self-weight is calculated as a gravity load. To obtain the nonlinear behavior of the box girder, displacement is adopted instead of concentrated load. A pair of –80 mm displacement is applied on the top surface of the HSC plate. Fig. 10 shows the full 3D model of the UHPC box girder.

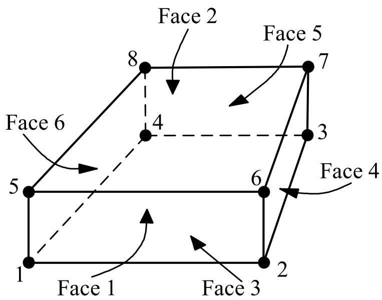

Figure 9. C3D8R element type in Abaqus modeling.

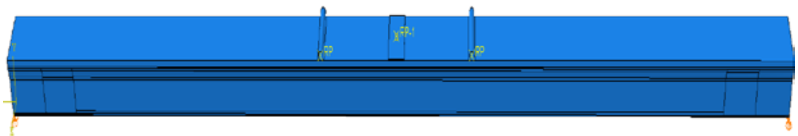

Figure 10. Full 3D model of UHPC box girder under four-point bending test Load-deflection curve.

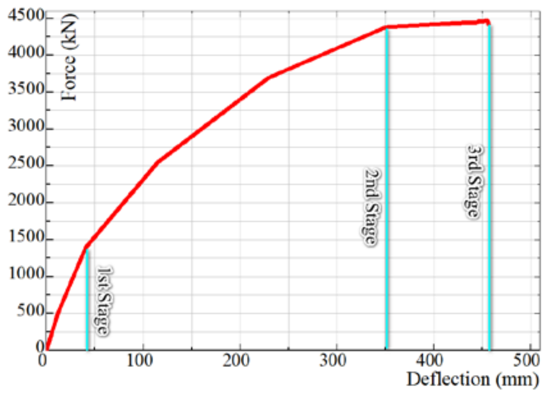

Figure 11. P-U curve of UHPC box girder.

The load-displacement curve of the UHPC box girder is depicted in Fig. 11. The load-displacement curve shows three stages. The first stage is from the beginning of the simulation process to the load of 1325.6 kN, which is nearly 29 % of the peak load (4475.2 kN). At this stage, the load-displacement curve exhibits elastic behavior. The initial crack occurs at the load of 1325.6 kN, corresponding to the deflection of 48.2 mm at the midspan. At the second stage, the applied load is observed from 1325.6 kN to 4390.4 kN, strain-hardening appeared and propagated along the surface of the box girder, concentrated under loading point and midspan. Unlike the first stage, at the second stage, the load-displacement curve shows the nonlinear behavior with the multiple crack propagation. At the load of 4390.4 kN, the observed deflection value is 350.3 mm. At the third stage, loading from 4390.4 kN reaches the maximum value of 4475.8 kN with a deflection of 455.9 mm. The P-U curve shows plasticity behavior, where load increment is considerably smaller than the previous stage. The peak load is observed in this stage at 4475.8 kN. After this moment, the P-U curve starts to the downward nonlinear trend.

Fig. 12 shows the Von-mises contour stress of the box girder. Under peak load of 4475.8 kN, the stress in the HSC plate reaches the ultimate limit of compressive strength, resulting in crushing failure, whereas the UHPC girder exhibits strain softening behavior in the tensile region. These results would seem to suggest that in order to obtain full capacity of UHPC material, the higher compressive strength of HSC material is necessary.

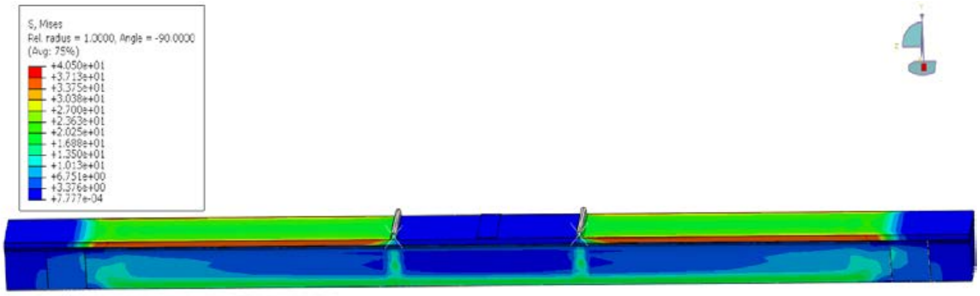

Figure 12. Stress contour in the box girder.

Strain profile

In order to measure the longitudinal strain of the UHPC box girder, the elements are extracted from the simulation model at mid span and joint sections in Fig. 13. Fig. 14a shows the strain profile of the UHPC box girder at mid-span. The initial yielding strain occurs at 1325.6 kN, in which strain values are –150.2 $\mu\varepsilon$ in compression at HSC slab (S5), –105.8 $\mu\varepsilon$ in compression at UHPC slab (S4), and 207.2 $\mu\varepsilon$ in tension at the bottom of the UHPC girder (S1), respectively. At load level of 4390 kN, HSC slab exhibits inelastic, strain hardening behavior in compression with strain value of –2507.3 $\mu\varepsilon$, while UHPC plate is under elastic behavior in compression with strain value of –1860.1 $\mu\varepsilon$. UHPC box girder has a strain value of 5507.3 $\mu\varepsilon$ in tension. At the peak load of 4475 kN, FE analysis predicts the strain values of elements increase rapidly. The HSC plate (S5) undergoes inelastic, strain hardening behavior in compression with the strain values of –2817.2 $\mu\varepsilon$, whereas the UHPC plate (S4) shows linear elastic behavior in compression with strain values of –2019.8 $\mu\varepsilon$. UHPC box girder exhibits the strain-softening behavior in the tension of 7913.8 $\mu\varepsilon$.

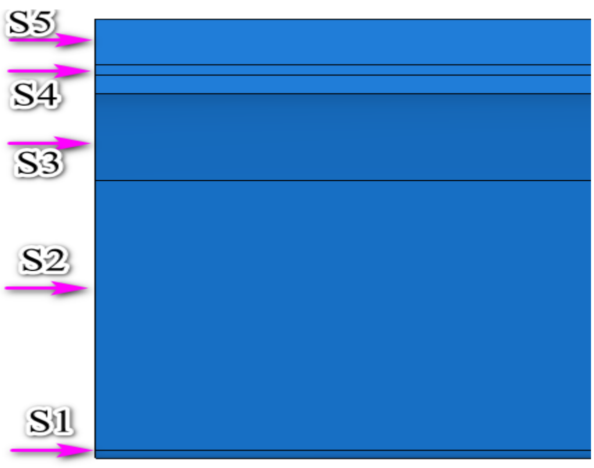

Figure 13. Position to take strain data from FE model.

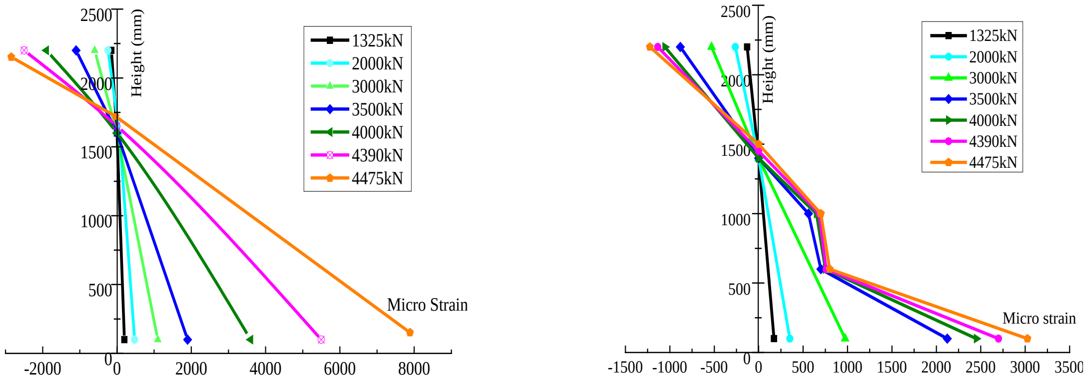

a) b)

Figure 14. Longitudinal strain profile at mid span (a) and joint section (b).

Strain at the joint section shows a similar trend to what has been reported at the mid-span of the box girder. However, strain at the joint section has a significantly smaller value than in the mid-span (Fig. 14b). For instance, at the maximum load of 4475.8 kN, HSC (S5) and UHPC (S4) slab exhibit linear elastic behavior with strain value of –1224.5 με and –920.8 με in compression, respectively. Meanwhile, the UHPC girder (S1) shows strain-hardening behavior with a strain value of 3024.4 με. The curvature difference of strain at joint section in Fig. 14b appears due to the discrete crack as increasing of applied load.

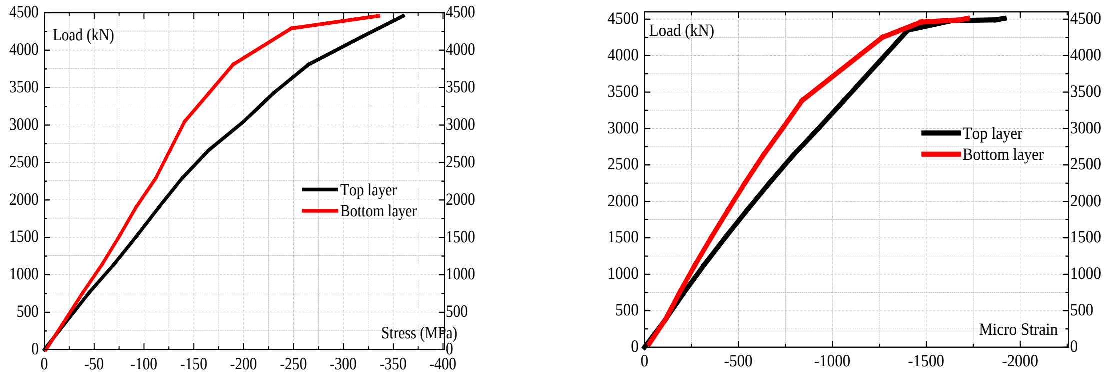

a) b)

Figure 15. Stress (a) and strain (b) versus load in longitudinal steel bars at mid span.

Fig. 15 depicts the stress and strain versus load in longitudinal steel bar of HSC plate. At the moment of first cracks appearance with the load of 1325.6 kN, stress and strain of longitudinal bar in the bottom layer is –67.9 MPa and –286.1 με, respectively. Stress and strain of longitudinal bar in the top layer are –78.3 MPa and –364.8 με. Both layers of longitudinal steel bar exhibit elastic behavior. Under the maximum load of 4475.8 kN, stress and strain in the bottom layer reach the value of –340.8 MPa and –1741.7 με, while in the top layer are –362.4 MPa and –1915.8 με. The top and bottom longitudinal steel bars show perfect plastic behavior.

Fig. 16 depicts stress and strain versus the vertical load of tendons at mid-span. Compared to lower tendons, upper tendons have smaller stress and strain. The maximum value of stress and strain in the upper tendons is 853.7 MPa and 3240.7 με, respectively. Upper tendons exhibit linear elastic behavior. On the contrary, the lower tendons show larger stress and strain than the upper tendons. The stress-strain curve consists of two stages. In the first stage from beginning to the load of 1325.6 kN, stress-strain values are 1136.4 MPa and 6283.5 με. The tendons show elastic behavior. Following the increment in applied load, there is a tremendous increase of stress and strain in lower tendons. At the peak load of 4476 kN, stress and strain reach the value of 1428.2 MPa and 12864.1 με, respectively. The lower tendons show plastic behavior.

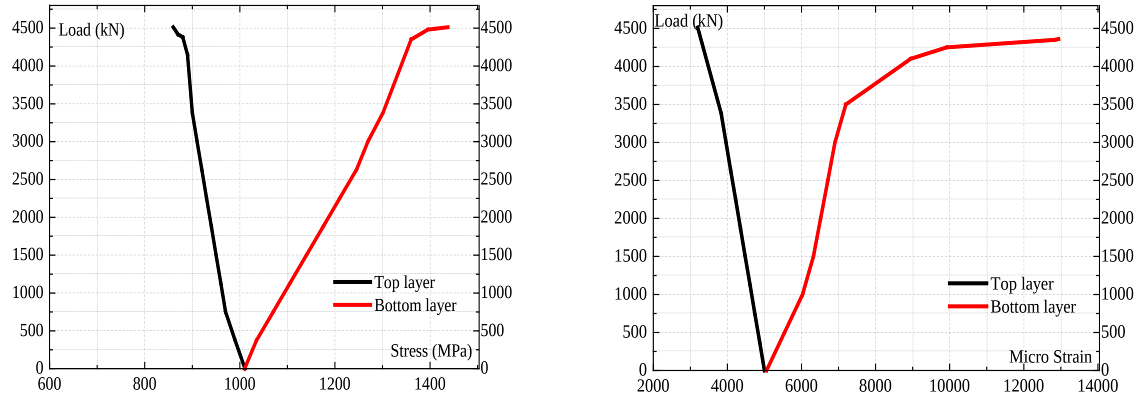

a) **b)**

Figure 16. Stress (a) and strain (b) versus load in tendons at mid span Cracking Pattern.

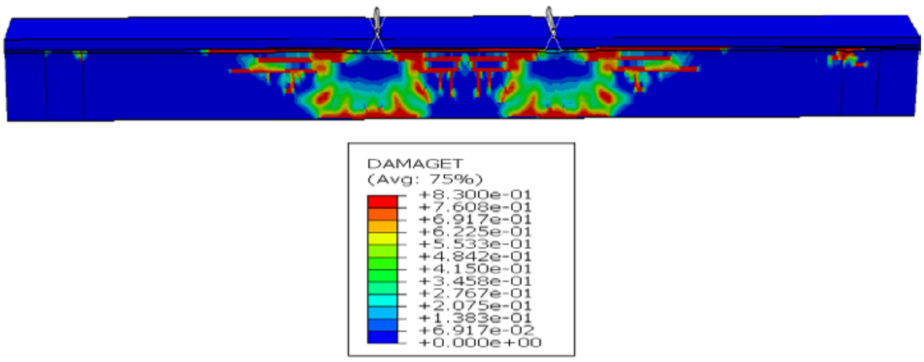

Figure 17. Crack pattern in the box girder.

Fig. 17 shows the cracking pattern of the box girder versus increasing the load. The first cracks occurred at a load of 1325.6 kN. During the increment of the vertical load until the maximum value, the crack pattern propagates rapidly along the longitudinal axis of the box girder. At the load level of 1325.6 kN, cracks are distributed along 10.2 m length at mid-span. At the peak load of 4475.8 kN, the length of the crack distribution is 15.8 m.

4. Conclusions

The study presents the structural behavior of the pre-stressed UHPC box girder. Using the CDP model, the numerical simulation determined the appropriate constitutive model in the compressive and tensile behavior of the UHPC box girder. The proposed model was proved with experimental results of the short span UHPC beam under the four-point bending moment test. Later on the model was developed to simulate 60 m pre-stressed UHPC box girder. The following conclusions are drawn:

1. The prediction of flexural behavior of the UHPC box girder shows three different stages of box girder, including: From the first point to the occurrence of initial crack, corresponding to the elastic phase of material; The initial crack to the propagation of multiple cracks, which describe the nonlinear behavior; The stage of plasticity behavior and finally downward nonlinear behavior results in failure of the girder.

2. At the maximum value of the applied load, the top and bottom longitudinal steel bars in the HSC plate show perfect plastic behavior. The prestressed tendons exhibit different behaviors depending on the location. Under applied load, the upper tendons undergo compressive stress with linear elastic behavior. In contrast to upper tendons, lower tendons are in tension stress and show plasticity behavior under maximum load.

3. First cracks occur perpendicularly to the bottom edge of the box girder at mid-span. The increment in vertical load leads to rapid formation and propagation of perpendicular and diagonal cracks along the longitudinal axis of the girder. Based on the obtained result, while the HSC plate shows failure under maximum load, stresses in UHPC girder is significantly smaller than ultimate strength. In order to utilize full capacity of UHPC material, the strength of conventional concrete in the box girder should be improved.

References

1. Wang, J.Y., Bian, C., Xiao, R.C., Ma, B. Restrained Shrinkage Mechanism of Ultra High Performance Concrete. KSCE Journal of Civil Engineering. 2019. 23(10). Pp. 4481–4492. DOI: 10.1007/s12205-019-0387-5
2. Arora, A., Aguayo, M., Hansen, H., Castro, C., Federspiel, E., Mobasher, B., Neithalath, N. Microstructural packing- and rheology-based binder selection and characterization for Ultra-high Performance Concrete (UHPC). Cement and Concrete Research. 2018. 103(February). Pp. 179–190. DOI: 10.1016/j.cemconres.2017.10.013. URL: http://dx.doi.org/10.1016/j.cemconres.2017.10.013
3. Le Hoang, A., Fehling, E. Influence of steel fiber content and aspect ratio on the uniaxial tensile and compressive behavior of ultra high performance concrete. Construction and Building Materials. 2017. 153(November). Pp. 790–806. DOI: 10.1016/j.conbuildmat.2017.07.130. URL: http://dx.doi.org/10.1016/j.conbuildmat.2017.07.130
4. Tian, H., Zhou, Z., Zhang, Y., Wei, Y. Axial behavior of reinforced concrete column with ultra-high performance concrete stay-in-place formwork. Engineering Structures. 2020. 210(February). Pp. 110403. DOI: 10.1016/j.engstruct.2020.110403.
5. Yujing, L., Wenhua, Z., Fan, W., Peipei, W., Weizhao, Z., Fenghao, Y. Static mechanical properties and mechanism of C200 ultra-high performance concrete (UHPC) containing coarse aggregates. Science and Engineering of Composite Materials. 2020. 27(1). Pp. 186–195. DOI: 10.1515/secm-2020-0018
6. He, S., Deng, Z. Seismic Behavior of Ultra-High Performance Concrete Short Columns Confined with High-Strength Reinforcement. KSCE Journal of Civil Engineering. 2019. 23. Pp. 5183–5193. DOI: 10.1007/s12205-019-0915-3
7. Mao, L., Barnett, S.J. Investigation of toughness of ultra high performance fibre reinforced concrete (UHPFRC) beam under impact loading. International Journal of Impact Engineering. 2017. 99. Pp. 26–38. DOI: 10.1016/j.ijimpeng.2016.09.014.
8. Meng, W., Valipour, M., Khayat, K.H. Optimization and performance of cost-effective ultra-high performance concrete. Materials and Structures/Materiaux et Constructions. 2017. 50(1). DOI: 10.1617/s11527-016-0896-3
9. Yoo, D.Y., Banthia, N. Mechanical properties of ultra-high-performance fiber-reinforced concrete: A review. Cement and Concrete Composites. 2016. 73. Pp. 267–280. DOI: 10.1016/j.cemconcomp.2016.08.001.
10. Wu, Z., Shi, C., He, W., Wang, D. Static and dynamic compressive properties of ultra-high performance concrete (UHPC) with hybrid steel fiber reinforcements. Cement and Concrete Composites. 2017. 79. Pp. 148–157. DOI: 10.1016/j.cemconcomp.2017.02.010.
11. Hosinieh, M.M., Aoude, H., Cook, W.D., Mitchell, D. Behavior of ultra-high performance fiber reinforced concrete columns under pure axial loading. Engineering Structures. 2015. 99. Pp. 388–401. DOI: 10.1016/j.engstruct.2015.05.009.
12. Qian, D., Yu, R., Shui, Z., Sun, Y., Jiang, C., Zhou, F., Ding, M., Tong, X., He, Y. A novel development of green ultra-high performance concrete (UHPC) based on appropriate application of recycled cementitious material. Journal of Cleaner Production. 2020. 261. Pp. 121231. DOI: 10.1016/j.jclepro.2020.121231.
13. Graybeal, B. UHPC in the US Highway Infrastructure. Designing and Building with UHPFRC. 2013. (November 2009). Pp. 221–234. DOI: 10.1002/9781118557839.ch15
14. Schmidt, M., Leutbecher, T., Piotrowski, S., Wiens, U. The German Guideline for Ultra-High Performance. UHPFRC 2017 Designing and Building with UHPFRC: New large-scale implementations, recent technical advances, experience and standards. 2017. 2(1). Pp. 545–554.
15. Toutlemonde, F., Bernardi, S., Brugeaud, Y., Simon, A. Twenty years-long French experience in UHPFRC application and paths opened from the completion of the standards for UHPFRC. 2018. URL: https://hal.archives-ouvertes.fr/hal-01955204
16. Toutlemonde, F., Généreux, G., Delort, M., Resplendino, J. Product and Design Standards for UHPFRC in France. 2016. (January). DOI: 10.21838/uhpc.2016.114
17. Schmidt, M., Fehling, E. Ultra-high-performance concrete: Research, development and application in Europe. Seventh International Symposium on the Utilization of High Strength/High-Performance Concrete. 2005. (September 2015). Pp. 51–78.
18. Graybeal, B.A. Compressive Behavior of Ultra-High-Performance Fiber-Reinforced Concrete. ACI Materials Journal. 2007. 104. Pp. 46–152.
19. Freytag, B., Heinzle, G., Reichel, M., Sparowitz, L. WILD- Bridge scientific preparation for smooth realisation. Proceeding of 3rd International Symposium on UHPC and Nanotechnology for High Performance Construction Materials. 2012. Pp. 881–888.
20. Rebentrost, M., Wight, G. Perspective on UHPCs from a specialist construction Company. ISTE, London, 2011. Pp. 189–206.
21. Rebentrost, M., Wight, G., Fehling, E. Experience and Applications of Ultra-high Performance Concrete in Asia. 2nd International Symposium on Ultra High Performance Concrete. 2008. Pp. 19–30.
22. Kim, B.-S., Joh, C., Park, S.Y., Koh, G.-T., Kwon, K., Park, J. KICT's Application of UHPC to the First UHPC Cable Stayed Roadway Bridge. 2016. Pp. 1–9. DOI: 10.21838/uhpc.2016.97
23. Lee, C., Kim, K., Choi, S. Application of Ultra high performance concrete to pedestrian cable-stayed bridges. Journal of Engineering Science and Technology. 2013. 8(3). Pp. 296–305.
24. Tanaka, Y., Maekawa, K., Kameyama, Y., Ohtake, A., Musha, H., Watanabe, N. The Innovation and Application of UHPFRC Bridges in Japan. Designing and Building with UHPFRC. 2013. (October). Pp. 149–188. DOI: 10.1002/9781118557839.ch12
25. Voo, Y.L., Foster, S., Pek, L.G. Ultra-high performance concrete – Technology for present and future 2017.
26. Guo, Q., Han, S.-M. Flexural Behavior of Ultra High Performance Fiber Reinforced Concrete Segmental Box Girder. Journal of the Korea Concrete Institute. 2014. 26(2). Pp. 109–116. DOI: 10.4334/jkci.2014.26.2.109
27. Yang, I.H., Joh, C., Kim, B.S. Flexural strength of large-scale ultra high performance concrete prestressed T-beams. Canadian Journal of Civil Engineering. 2011. 38(11). Pp. 1185–1195. DOI: 10.1139/l11-078
28. Guo, Q., Han, S.-M. Flexural Behavior of Ultra High Performance Fiber Reinforced Concrete Segmental Box Girder. Journal of the Korea Concrete Institute. 2014. 26. DOI: 10.4334/JKCI.2014.26.2.109
29. Chen, L., Graybeal, A.B. Finite element analysis of ultra-high performance concrete: Modeling structural performance of an AASHTO type II girder and a 2nd generation pi-girder 2010.
30. Singh, M., Sheikh, A.H., Mohamed Ali, M.S., Visintin, P., Griffith, M.C. Experimental and numerical study of the flexural behaviour of ultra-high performance fibre reinforced concrete beams. Construction and Building Materials. 2017. 138. Pp. 12–25. DOI: https://doi.org/10.1016/j.conbuildmat.2017.02.002.
31. Behloul, M., Lee, K.C. Seonyu footbridge. Structural Concrete. 2003. 4. Pp. 195–201.

32. Lafarge. Ductal® – Applications and References. 2020URL: http://www.ductal-lafarge.com/wps/portal/Ductal/Applications-AndReferences/
33. Lubliner, J., Oliver, J., Oller, S., Onate, E. a Plastic-Damage Model. International Journal of Solids and Structures. 1989. 25(3). Pp. 299–326.
34. Yang, I.H., Joh, C., Kim, B.S. Structural behavior of ultra high performance concrete beams subjected to bending. Engineering Structures. 2010. 32(11). Pp. 3478–3487. DOI: 10.1016/j.engstruct.2010.07.017.
35. Vietnamese Ministry of Construction, V.M. of C. Precast Prestressed concrete product – Technical requirements and acceptance test2014. 1–86 p.

Information about authors:

Van Tu Nguyen
ORCID: https://orcid.org/0000-0002-0298-5080
E-mail: nguyentu@lqdtu.edu.vn

Viet Chinh Mai, PhD
ORCID: https://orcid.org/0000-0002-2285-3034
E-mail: maivietchinh@lqdtu.edu.vn

Received 26.02.2021. Approved after reviewing 23.08.2021. Accepted 23.08.2021.

Magazine of Civil Engineering

ISSN 2712-8172

journal homepage: http://engstroy.spbstu.ru/

Research article

UDC 677.074, 677.027.62, 699.868

DOI: 10.34910/MCE.112.13

Thermal resistance of fire retardant materials

***T.A. Budykina*[a] ✉, *Y.B. Anosova*[b]**

[a] *Civil Defence Academy EMERCOM of Russia, Khimki, Moscow region, Russia*
[b] *Mendeleev Russian University of Chemistry and Technology, Moscow, Russia*

✉ *tbudykina@yandex.ru*

Keywords: fire retardant materials, fire retardant properties, fire retardant composition, building materials, thermogravimetric analysis, microstructure

Abstract. The results of thermal resistance of fire-retardant materials "OGNEBASALT" PMBOR and OGNEZA-GT sealant in the form of a mineral wool heat-insulating plate are presented. To study the behavior of fire-retardant materials, the method of TG-DSC synchronous thermal analysis (thermogravimetry in conjunction with differential scanning calorimetry) was used on a NETZSCH thermal analyzer. The incombustible properties of "OGNEBASALT" PMBOR have been confirmed, which showed a decrease in the mass of the material by 21 % when heated to 1000 °C. The thermo-expanding sealant OGNEZA-GT reduced its weight at the same heating with the fire-basalt material by 64 %. For a 10 % weight loss, the two test specimens require different temperatures of 395 and 262 °C, respectively. Time interval of "OGNEBASALT" PMBOR weight loss from 99.6 % to 77.6 % – from 12 minutes to 27 minutes of the experiment; for OGNEZA-GT sealant, from 99.8 % to 54.7 % – from 8 minutes to 18 minutes of testing. The best thermo-resistant properties have been revealed for the fire-retardant material "OGNEBASALT" PMBOR, which makes it possible to recommend its widespread use as a material for passive fire protection. The research results can be used to justify the choice of fire protection in buildings of various functional classes of fire hazard.

Citation: Budykina, T.A., Anosova, Y.B. Thermal resistance of fire retardant materials. Magazine of Civil Engineering. 2022. 112(4). Article No. 11213. DOI: 10.34910/MCE.112.13

1. Introduction

One of the elements of fire protection are refractory materials used to increase the fire resistance of building structures in the event of a fire. The objects of study were samples of refractory materials – fire retardant material "OGNEBAZALT" PMBOR (LLC "OG-NEBAZALT MSK", Moscow region, Balashikha) and fire retardant thermo-expanding sealant OGNEZA-GT in the form of a mineral wool heat-insulating plate (LLC "Ogneza", g . St. Petersburg).

A number of publications provide the results of designing and increasing the fire resistance of wood [1–12] and metal structures [13–16], studies to reduce the flammability of synthetic materials [17, 18], imparting fire retardant properties to cellulosic textile materials [19, 20]. Research work is mainly aimed at studying the properties of fire retardants, products of pyrolysis and combustion of materials, the mechanism of slowing down combustion, increasing the fire resistance of materials, assessing the flammability and fire-retardant efficiency of coatings for metal structures, intumescent fire-retardant materials [21–23]. However, data on the thermal properties of fire-resistant materials are scarce [24]. There is especially insufficient information on the properties of Russian-made refractory materials.

Purpose of the research: diagnostics of behavior under thermal influence of modern fire-resistant materials of Russian production.

Research objectives:

- study of the weight loss of fire retardant materials when exposed to temperature;
- determination of temperature ranges of sample weight loss;
- study of the microstructure of samples before and after exposure to temperature;
- determination of materials with the best heat-resistant properties.

Fig. 1 shows the investigated samples of refractory materials – the fire-protective material "OGNEBASALT" PMBOR and the fire-retardant thermally expanding sealant OGNEZA-GT in the form of a mineral wool heat-insulating plate.

a)

b)

c)

Figure 1. Investigated samples of fire retardant materials: a) side view and top view of the fire-retardant material "OGNEBASALT" PMBOR (thickness – 8 mm); b) side and top view of fire retardant thermally expanding sealant OGNEZA-GT (thickness – 30 mm); c) side view of both samples.

Fire-retardant material "OGNEBASALT" PMBOR is a fire-retardant roll-stitching material made of super-thin basalt fiber with a thickness of 5.0 to 16.0 mm, laminated with aluminum foil on one side (TU 5769-004-52876233-2009). Manufacturer – LLC "Epoch-Basalt", Bryansk region [25].

Fire-retardant basalt material PMBOR is a layer of super-thin basalt fibers, randomly arranged and bonded together in a natural way, without adding glue, but stitched with a knitting-stitching method. PMBOR is used for fire protection (building structures, air ducts) and for thermal insulation (pipelines, boilers, boiler building structures, residential and industrial buildings and structures, attic floors of houses).

The study used a sample "OGNEBASALT" PMBOR 8 mm thick. According to the manufacturer's data [25], the fire resistance limit of "OGNEBASALT" PMBOR is EI 90.

Table 1 shows the characteristics of the material "OGNEBASALT" PMBOR [25].

Table 1. Technical characteristics of the fire-retardant material "OGNEBASALT" PMBOR.

Indicator	Value
Surface density, g /m^2, no more	1800
Density, kg /m^3, no more	140
Humidity,%, nomore	2.0
Thermal conductivity, at a temperature of 25 ± 5 °C, W / (mK), no more	0.038
Application temperature, °C:	
– without lining	from –260 to +900
– covered with fiberglass	from –260 to +400
– withoutlining	NG

Fire-retardant thermally expanding sealant OGNEZA-GT in the form of a mineral wool heat-insulating plate is made on the basis of basalt rocks, has a density of 100 kg/m^3 and belongs to the fire hazard class KM0 [26]. The material is used for fire protection and thermal insulation of reinforced concrete floor slabs, for sealing expansion (structural joints), cable and ventilation ducts of communications through walls and ceilings. The principle of operation of the sealant is based on its ability to expand under the influence of high temperatures (from 200 °C) and create a dense non-combustible layer of coke, which prevents the penetration of fire and smoke into adjacent rooms.

2. Methods

To study the behavior of fire retardant materials under temperature exposure, experiments were carried out using the method of synchronous thermal analysis (STA) (Russian State Standard GOST R 55134-2012), including differential scanning calorimetry (DSC) and thermogravimetry (TG).

The thermal analyzer is a thermal balance (digital, high-sensitivity, high-resolution) with top loading of the sample and direct measurement of the temperature on the sample. In these devices, a sample of a substance (mg) is heated at a given temperature regime, at a given rate in an inert gas atmosphere, the decrease in the mass of the substance (thermogravimetric analysis, TG or TG) and exo- and endo-effects (differential thermal analysis, DTA or DTA (DSC – Differential Scanning Calorimetry)).

The study by the STA method was carried out at the Department of Fire Safety of the Federal State Budgetary Educational Institution of Higher Education "Academy of Civil Protection" on a thermal analyzer STA 449 F3 Jupiter of the German company "NETZSCH" (Fig. 2).

Figure 2. Synchronous thermal analyzer STA 449 F3 Jupiter from NETZSCH.

The main technical characteristics of the thermal analyzer are shown in Table 2.

Table 2. Specifications STA 449 F3 Jupiter.

Indicator	Value
Temperaturerange, °C	–150 – 2400
Maximumsampleweight, g	35
Heating and cooling rate, °C/min	0.001 – 50
TG resolution, μg	0.1
DTG resolution, μW (depending on the type of sensor)	< 10

The results of the analysis of the thermal analyzer are recorded in the form of a graphical dependence:

- TG (integral curve) – "change in sample mass,%, – heating duration, min";
- DSC (thermal effects) – "exo- and endo-effects, microV/mg, – heating duration, min". The latter effects can arise as a result of chemical processes, phase transitions, thermal destruction of a substance, etc. in the sample under study;
- dDSC – "rate of change in the mass of samples under thermal exposure, microV/mg/min – heating duration, min".

The method of differential scanning calorimetry (DSC) allows to study with high accuracy the properties of substances under thermal influence [27].

Characteristics of the experimental conditions:

- measurement mode – TG / DCS / dDSC;
- heating rate: 20 °C/min;
- heating – up to 1000 °C;
- atmosphere – N_2.

The microstructures of the samples of fire retardant materials before and after exposure to temperature were investigated using an electron microscope of the Department of Chemistry and Materials Science of the FGB-VOU VO "Academy of Civil Protection".

3. Results and Discussion

Fig. 3–6 show the TG /DCS /dDSC curves of the investigated fire-retardant materials, reflecting the rate of weight loss of the samples and the accompanying thermal phenomena, obtained using a NETZSCH STA 449 F3 Jupiter thermal analyzer. Fig. 3, 5 show the dynamics of the processes occurring with the samples in relation to temperature; Fig. 4, 6 – in time.

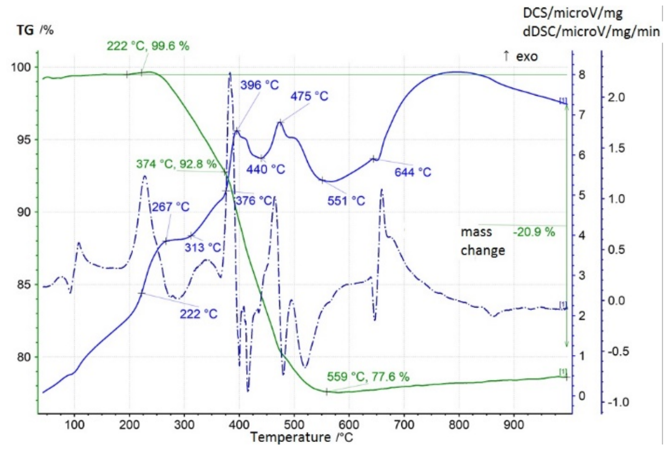

Figure 3. Thermogram of the fire retardant material "OGNEBASALT" PMBOR (by temperature).

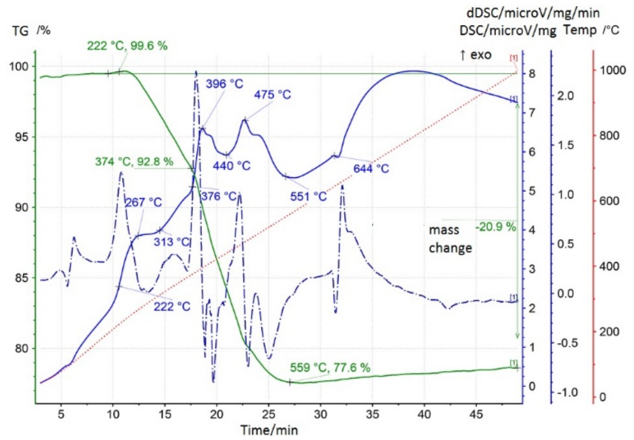

Figure 4. Thermogram of fire-retardant material "OGNEBASALT" PMBOR (by the time of temperature exposure).

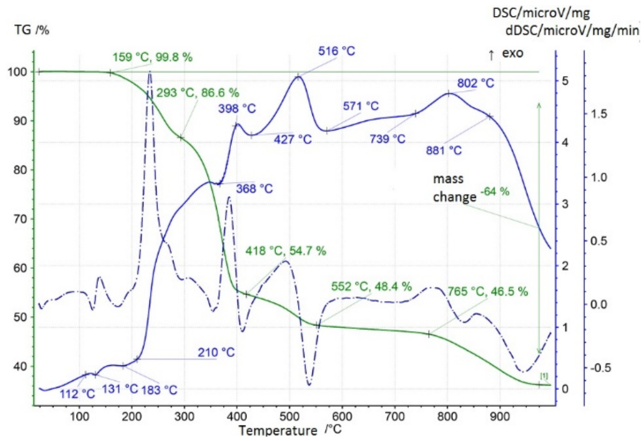

Figure 5. Thermogram of fire retardant thermally expanding sealant OGNEZA-GT (by temperature).

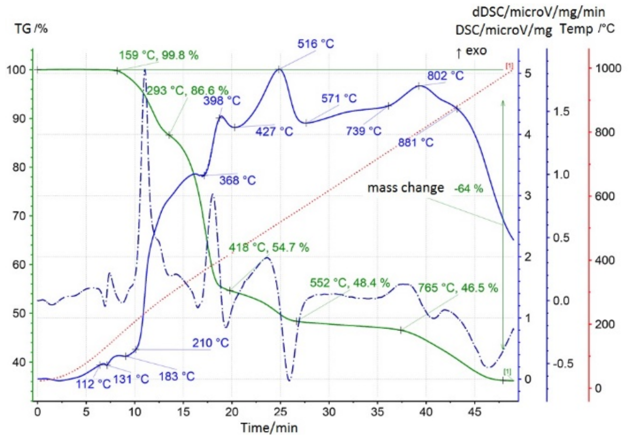

Figure 6. Thermogram of fire retardant thermally expanding sealant OGNEZA-GT (by the time of temperature exposure).

As can be seen from Fig. 3-6, the behavior of fire-retardant materials under temperature exposure differs from each other, however, the non-combustible properties of the fire-retardant material "OGNEBASALT" PMBOR, declared by the manufacturer, are confirmed as a non-combustible material, in which the mass of material when heated to 1000 °C decreases by 21 %. The thermo-expanding sealant OG-NEZA-GT reduced its weight with the same heating as the fire-basalt material by 64 %.

On the curve of the thermogram of the fire-retardant material "OGNEBASALT" PMBOR (Fig. 3), it can be seen that up to a temperature of 222 °C, the sample weight decreases by only 0.4 %, while a slight exothermic effect is observed, the maximum of which is at 267 °C. Upon further heating to a temperature of 313 °C, a series of small exo effects begins with maxima at 396 °C and 475 °C and an endo effect with a minimum at 551 °C, and then an exo effect begins at 644 °C. Thus, it can be assumed that in the temperature range of 222–559 °C, thermal oxidative destruction of the organic part of the sample occurs, followed by spontaneous ignition of its combustible part, accompanied by a decrease in mass by 21 %; however, upon further heating, no loss of mass occurs, which is due to the mineral composition of the sample (silica based material).

Fig. 4 allows you to trace the behavior of the fire-retardant material "OGNEBASALT" PMBOR under temperature exposure in time: the weight loss of the sample by 0.4 % occurs from 12 minutes of the experiment, when the temperature of 222 °C is reached, and up to 27 minutes (weight loss 22.4 %) ... By the 50th minute of the experiment, the material retains 79.1 % of its mass.

Analyzing the thermogram of the fire retardant thermally expanding sealant OGNEZA-GT (Fig. 5, 6), the following conclusions can be drawn. The sample does not lose weight until it reaches a temperature of 159 °C, while insignificant exothermic effect at 112 °C and an endothermic effect at 131 °C are observed. At 210 °C, a powerful exothermic effect begins with a decrease in weight. At 418 °C, only 54.7 % of the sample weight is retained. It can be assumed that thermal oxidative decomposition of the organic part of the material occurs in the temperature range 159 – 418 °C.

The time interval of weight loss from 0.02 % to 45.3 % was determined from 08 minutes to 18 minutes of testing, which can be presumably associated with the thermal expansion of the structure (which is consistent with [24]). Endoeffects at 427 °C and 571 °C can be explained by the consumption of heat for the process of melting substances. At a temperature of 802 °C, 39 minutes after the start of the test, an exo effect occurs, which is probably due to spontaneous ignition and burnout of an additional 15 % of the sample mass. The total decrease in the mass of the sample by the 50th minute of the experiment was 64 % when the temperature reached 1000 °C (end of the experiment).

Fig. 6 a, b show the images of the original structure of the material "OGNEBA-ZALT", obtained using an electron microscope with a magnification of 15 and 30 times. Fig. 6 c, d show the structure of material residues after a fire exposure of 1000 °C (an increase of 15 and 30 times).

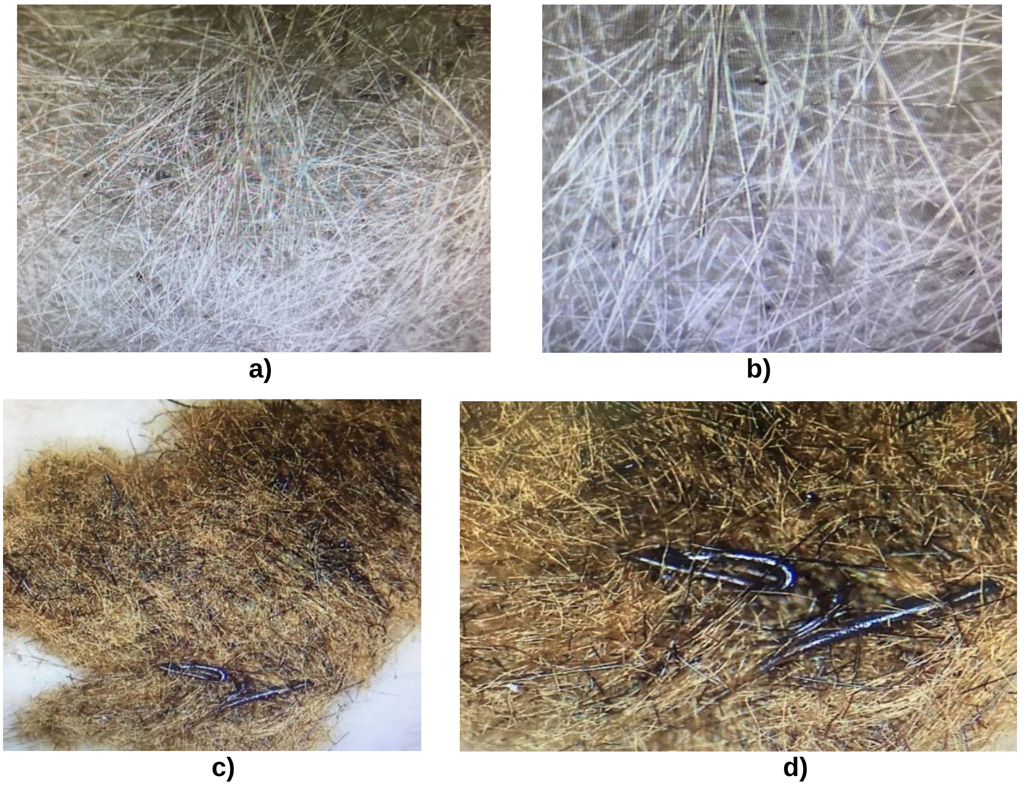

Figure 6. Micrographs of samples of fire-retardant material "OGNEBASALT" PMBOR (a, b) and their residues in the crucible after exposure to fire after (c, d): a – fire retardant material "OGNEBASALT" PMBOR (increase 15 times); b – fire-retardant material "OGNEBASALT" PMBOR (30 times increase); c – the remainder of the sample "OGNEBASALT" PMBOR after exposure to fire at 1000 °C (15 times increase); d – the remainder of the sample "OGNEBA-ZALT" PMBOR (increase in 30 times).

As can be seen from Fig. 6 a, b, the fire retardant material "OGNEBASALT" PMBOR is a chaotically located layers of fibers. After a fire exposure of 1000 °C (Fig. 6 c, d), the fibrous structure of the material is preserved, which confirms the non-combustible properties of the material. In this case, clearly expressed, few, sintered structures are formed (presumably, aluminum foil, which is lined with the original material).

OGNEZA-GT sealant is a two-layer material consisting of dense and fibrous parts. Fig. 7a shows an image of a two-layer structure of the OG-NEZA-GT sealant with an increase of 15 times; Fig. 7 b is a micrograph of the dense part of the OGNEZA-GT sealant (magnification 45 times). Fig. 7 c, e allows you to see the fibrous part of the OGNEZA-GT sealant (magnification 30 and 60 times). Fig. 7 f and e – photomicrograph of the remainder of the sealant sample after exposure to fire at 1000 °C (magnification 45 and 60 times).

Fig. 7a clearly shows the two-layer structure of the fire-retardant thermally expanding sealant OGNEZA-GT. Fig. 7 b shows the porous structure of the dense part of the sealant, presumably of organo-mineral origin. Fig. 7 c, d show the fibrous part of the sealant. After a fire exposure of 1000 °C (Fig. 7e,f), the fibrous structure of the material is preserved, providing the integrity of 36 % of the sealant structure. Presumably, the dense part of the sealant completely burned out, turning into small sintered fragments, clearly shown in Fig. 7e, f. The porous structure of the dense part of the sealant, due to its high permeability, was intensively exposed to temperature until complete burnout.

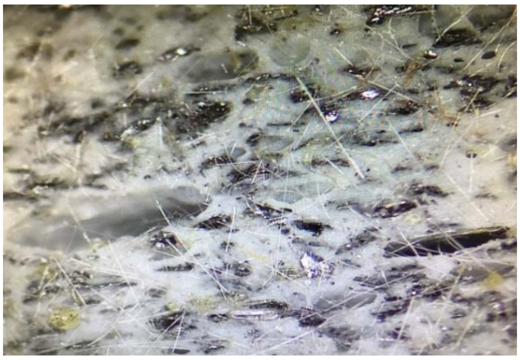

a) b)

c) d)

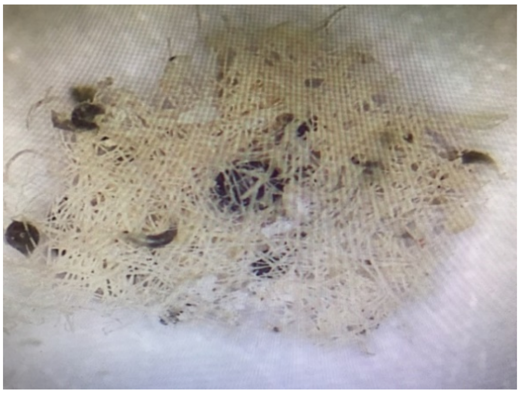

e) f)

Figure 7. Micrographs of a sample of fire retardant thermally expanding sealant OGNEZA-GT (a, b, c, d) and its remainder in the crucible after exposure to fire at 1000 °C (e, f): a – OGNEZA-GT sealant (15 times increase); b – the dense part of the OGNEZA-GT sealant (magnification 45 times); c – fibrous part of the OGNEZA-GT sealant (increase by 30 times); d – the fibrous part of the OGNEZA-GT sealant (60 times increase); f – the remainder of the sealant sample after exposure to fire (45 times increase); e – the remainder of the sealant sample after exposure to fire (60-fold increase).

Table 3 shows the reduction in the mass of the tested samples of fire retardant materials when heated.

Table 3. Characteristic of reducing the mass of the sample of the sealant under fire exposure.

	Weight loss of samples,% (upon reaching temperature, °C)									
	10	20	30	40	50	60	70	80	90	100
Fire retardant material "OGNEBASALT" PMBOR	395	481	Starting from a temperature of 559 °C, no change in mass occurs. Theoverallweightlossis 21 %.							
OGNEZA-GT sealant	262	338	364	382	516	888		No mass loss occurs. The overall weight reduction of the sample is 64 %.		

Based on the data in Table 3, it can be concluded that for a 10 % weight loss, the two test samples require different temperatures – 395 and 262 °C, respectively. For the sealant, weight loss of 20, 30, 40 % occurs with a "step" of 76, 26, 18 °C, respectively, which adversely affects the fire-retardant characteristics of the material.

4. Conclusions

1. The incombustible properties of the fire-retardant material "OGNEBASALT" PMBOR have been confirmed.

2. The material "OGNEBASALT" PMBOR, when heated to 1000 °C, reduced its weight by 21 %, the OGNEZA-GT sample – by 64 %.

3. The temperature and time intervals of changes in the properties of the investigated fire-retardant materials have been established.

"OGNEBASALT" PMBOR begins to respond to the effect of temperature by weight loss at 222 °C at the 12th minute of the test, OGNEZA-GT – at 159 °C at the 08th minute of the test.

In the temperature range of 222–559 °C (from 12 minutes of the experiment to 27 minutes), thermal oxidative destruction of the organic part of the sample "OGNEBASALT" PMBOR occurs by 21 %. With further heating, the material is resistant to heat and does not lose weight.

In the temperature range 159–418 °C (from 08 minutes of the experiment to 18 minutes), a loss of 45.3 % of the mass of the OGNEZA-GT sample occurs due to thermal oxidative destruction of the organic part. The decrease in the mass of the sample by the 50th minute of the experiment was 64 % when the temperature reached 1000 °C (end of the experiment).

4. The microstructure of materials has been investigated. "OGNEBASALT" consists of randomly arranged layers of fibers. After exposure to a temperature of 1000 °C, the fibrous structure of the material is preserved. OGNEZA-GT sealant is a two-layer material consisting of dense and fibrous parts. After exposure to 1000 °C, the fibrous structure of the material is preserved, ensuring the integrity of 36 % of the structure. Presumably, the dense part of the sealant has completely burned out.

5. The best heat-resistant properties were found in the fire-retardant material "OGNEBASALT" PMBOR, which allows us to recommend it as a material for passive fire protection. The research results can be used to substantiate the choice of fire protection in buildings of various functional classes of fire hazard.

References

1. Saknite, T., Serdjuks, D., Goremikins, V., Pakrastins, L., Vatin, N.I. Fire design of arch-type timber roof. Magazine of Civil Engineering. 2016. 64(4). Pp. 26–39. DOI: 10.5862/MCE.64.3
2. Gravit, M.V., Serdjuks, D., Bardin, A.V., Prusakov, V., Buka-Vaivade, K. Fire Design Methods for Structures with Timber Framework. Magazine of Civil Engineering. 2019. 85(1). Pp. 92–106. DOI: 10.18720/MCE.85.8
3. Suzuki, J., Mizukami, T., Naruse, T., Araki, Y. Fire resistance of timber panel structures under stand-ard fire exposure. Fire Technology. 2016. No. 52. Pp. 1015–1034. DOI: 10.1007/s10694-016-0578-2
4. Green, M., Taggart, J. Tall Wood Buildings Design, Construction and Performance. Birkhauser. 2017. 176 p. DOI: 10.1080/24751448.2018.1497379
5. O'Neill, J.W., Abu, A.K., Carradine, D.M., Moss, P.J., Buchanan, A.H. Modelling the fire performance of structural timber floors. Journal of Structural Fire Engineering. 2014. Vol. 5. No. 2. Pp. 113–124. DOI: 10.1260/2040-2317.5.2.113
6. Klippel, M., Leyder, C., Frangi, A., Fontana, M., Lam, F., Ceccotti, A. Fire Tests on Loaded Cross-laminated Timber Wall and Floor Elements. Fire Safety Science. 2014. Vol. 11. Pp. 626–639. DOI: 10.3801/IAFSS.FSS.11-626
7. Frangi, A., Fontana, M. Fire Performance of Timber Structures under Natural Fire Conditions. Fire Safety Science. 2005. Pp. 279–290. DOI: 10.3801/IAFSS.FSS.8-279
8. Wiesner, F., Bisby, L.A., Bartlett, A.I., Hidalgo, J.P., Santamaria, S., Deeny, S., Hadden, R.M. Struc-tural capacity in fire of laminated timber elements in compartments with exposed timber surfaces. Engineering Structures. 2019. Vol. 179. Pp. 284–295. DOI: 10.1016/j.engstruct.2018.10.084
9. Nedryshkin, O., Gravit, M., Grabovyy, K. Modeling fires in structures with an atrium in the FDS field model. MATEC Web of Conferences. 2018. Vol. 193. 03023. DOI: 10.1051/matecconf/201819303023
10. Schmid, J., Klippel, M., Just, A., Frangi, A., Tiso, M. Simulation of the Fire Resistance of Cross-laminated Timber (CLT). Fire Technology. 2018. Vol. 54. No. 5. Pp. 1113–1148. DOI: 10.1007/s10694-018-0728-9
11. Kinjo, H., Katakura, Y., Hirashima, T., Yusa, S., Saito, K. Deflection behavior and load-bearing period of structural glued laminated timber beams in fire including cooling phase. Journal of Structural Fire Engineering. 2018. Vol. 9. No. 4. Pp. 287–299. DOI: 10.1108/JSFE-01-2017-0009
12. Roszkowski, P., Sulik, P., Sedlak, B. Fire resistance of timber stud walls. Forestry and Wood Technology. 2015. No. 92. Pp. 368–372.
13. Gravit, M.V., Nedviga, Y.S., Vinogradova, N.A., Teplova, Z.S. Ognestoykost sborno-monolitnykh chastorebristykh plit po balkam so stalnym profilem [Fireproof of prefabricated monolithic multiribbed plate with rolled steel beam]. Construction of Unique Buildings and Structures. 2016. 51(12). Pp. 73–83. (rus)

14. Bronzova, M.K., Garifullin, M.R. Fire resistance of thin-walled cold-formed steel structures Article history. Construction of Unique Buildings and Structures. 2016. No. 3(42). Pp. 61–78.
15. Golovanov, V.I., Kuznetsova, Y.V. Effektivnyye sredstva ognezashchity dlya stalnykh i zhelezobet-onnykh konstruktsiy [Effective Means of Fire Protection for Steel and Concrete Structures]. Industrial and Civil Engineering. 2015. No. 9. Pp. 82–90. (rus)
16. Gravit, M., Dmitriev, I., Ishkov, A. Quality control of fireproof coatings for reinforced concrete struc-tures. IOP Conference Series: Earth and Environmental Science. 2017. Vol. 90. 012226. DOI: 10.1088/1755-1315/90/1/012226 103
17. Reva, O.V., Nazarovich, A.N., Bogdanova, V.V. Fixing non-toxic flame retardants on the surface of polyester fibers. Bulletin of the University of Civil Protection of the Ministry of Emergencies of Belarus. 2019. Vol. 3. No. 2. Pp. 107–115.
18. Akulova, M.V., Mochalov, A.M. About the results of the study of the effect of fire retardants based on organosiloxanes on the flammability of expanded polystyrene. Modern problems of civil protection. No. 2 (31), 2019. Pp. 48–55.
19. Takey, E., Tausarova, B.R., Vig, A. The use of sodium silicate and thiourea in the development of fire-resistant cellulose textile materials by the solgel method. Almaty tehnologii university khabarshysy. 2018. No. 3. Pp. 32–37.
20. Sycheva, A.V., Loktev, A.A., Mozharov, A.E., Sychev, V.P. Protection of building metal structures with fire retardants. Construction and Architecture. 2018. No. 2. Pp. 89–93.
21. Manich, A., Pérez-Rentero, S., Alonso, C., Coderch, L., Martí, M. Thermal analysis of healthy and ecological friendly flame retardants for textiles. KnEEngineering. 2020. Pp. 129–141. DOI: 10.18502/keg.v5i6.7028
22. Anosova, E.B., Perova, A.N., Kapranov, A.V. Modern sintetic materials as a source of fire and toxic danger under thermal exposure. Ecology and Industry of Russia. 2016. Vol. 20. No. 8. Pp. 38–43.
23. Zheng, C., Li, D., Ek, M. Improving fire retardancy of cellulosic thermal insulating materials by coating with bio-based fire retardants. Nordic Pulp and Paper Research Journal. 2019. 34. Pp. 96–106. DOI: 10.1515/npprj-2018-0031
24. Zhang, F., Wang, Y., Jin, Y., Zhang, J. Experimental Study on Thermal Diffusivity of Intumescent Fire-Retardant Materials. Advanced Materials Research. 2012. Pp. 550–553. Pp. 2749–2753. DOI: 10.4028/www.scientific.net/AMR.550-553.2749
25. Fire retardant material PMBOR [Online]. URL: https://ognebazalt.ru/catalog/ognezaschita-na-osnove-bazaltovogo-volokna/teplo--ognezaschitnye-materialy/material-ognezaschitnyy-pmbor RU (reference date: 15.02.2021).
26. Mineral wool heat-insulating plate [Online]. URL: https://ogneza.com/mineralovatnaya-plita-1000x600x50 RU (reference date: 15.02.2021).
27. Jones, J.M., Rollinson, A.N. Thermogravimetric evolved gas analysis of urea and urea so-lutions with nickel alumina catalyst. Thermochimica Acta. 2013. Vol. 565. Pp. 39–45. DOI: 10.1016/j.tca.2013/04/34

Contacts:

***Tatyana Budykina**,*
Doctor of Technical Science
ORCID: https://orcid.org/0000-0001-9571-3166
E-mail: tbudykina@yandex.ru

***Yevgenia Anosova**,*
PhD in Technical Science
E-mail: evgenia.anosowa@yandex.ru

Received 16.02.2021. Approved after reviewing 23.08.2021. Accepted 23.08.2021.

Magazine of Civil Engineering

ISSN 2712-8172

journal homepage: http://engstroy.spbstu.ru/

Research article

UDC 691.54

DOI: 10.34910/MCE.112.14

Cement grinding aid based on glycerol-waste antifreeze

***R. Jin Hyok*[a] ✉, *K. Yong Ho*[a], *H. Yong Su*[a], *K. Song Gun*[b], *Y. Ju Hyon*[a]**

[a] *University of Science, Department of Chemistry, Pyongyang, DPR Korea*

[b] *Kim Cheak University of Technology, Department of Mining Engineering, Pyongyang, DPR Korea*

✉ *rijinge@163.com*

Keywords: Cement mortar, grinding aid, waste antifreeze, clinker powder, compressive strength

Abstract. Grinding aids to increase grinding efficiency in cement production are materials that can produce large amounts of high-quality cement in a short time by reducing surface energy by preventing particle agglomeration and improving fluidity. In the paper, a grinding aid using glycerol-waste antifreeze (GAP) was prepared and its effect on the grinding properties of clinker was investigated in contrast to that without the grinding aid. The results are as follows: The angle of repose of the cement powder added with GAP decreased as the grinding time increased (decreases by 3.8 when the grinding time was 60 minutes), indicating that it increased the flowability of the powder. On the contrary, when GAP was added, the residual amount of 45 µm sieve was also significantly reduced (4.6 % decrease) and the specific surface area increased (30.5 m^2/kg), which resulted in an increase in the grinding efficiency. The zeta potential of the cement powder is greatly reduced, which lowers the surface tension of the cement particles. In the size range of 3 to 32 µm, it increases the particle content, makes the particle size distribution uniform, the 7d and 28d activity index of the powder is improved by 5 % and 6 %, respectively, and increases the compressive strength of the cement. In addition, it was confirmed that the performance of the TEA grinding aid and the grinding aid were similar, and were very effective in terms of economy.

Citation: Jin Hyok, R., Yong Ho, K., Yong Su, H., Song Gun, K., Ju Hyon, Y. Cement grinding aid based on glycerol-waste antifreeze. Magazine of Civil Engineering. 2022. 112(4). Article No. 11214. DOI: 10.34910/MCE.112.14

1. *Introduction*

Antifreeze is used for the purpose of preventing freezing of cooling water for water-cooled internal combustion engines and preventing corrosion of various devices in internal combustion engines, and its main components are monoethylene glycol or propylene glycol. The antifreeze that is discarded after use is referred to as the waste antifreeze solution. When waste antifreeze solution is treated with waste water, the chemical oxygen demand (COD) reaches about 460.000 ppm, which is equivalent to 10.000 times the discharge standard of normal waste water, so it is impossible to treat waste water. Not only is it expensive to incinerate waste liquid, but it also causes secondary air pollution during incineration.

Cement is one of the most used building materials in our lives, but during its production it consumes a lot of energy and emits carbon dioxide. Clinker baked in a cement kiln is mixed with gypsum and pulverized into powder in a ball mill to make cement. In the production of cement, the amount of energy consumed by the grinding process is almost 50 % of the previous process. When grinding the clinker powder in the ball mill, the cement grinding efficiency decreases due to cohesion between the particles, and it also negatively affects the strength of the cement [1–3].

To solve this problem, a cement grinding aid is added. The grinding aid is adsorbed between the fine cracks of the particles and provides ions or molecules in the functional stage, thereby balancing or shielding the unsaturated charges of the crack part, preventing the surface from being healed, and allowing the crack to expand more easily. In addition, molecules of the grinding aid are adsorbed on the surface of the cement particles to form an adsorption film, thereby reducing the free energy and interfacial tension of the powder surface. This prevents the particles from agglomerating with each other and acts as a dispersion, preventing them from becoming too fine. Therefore, it improves the grinding efficiency and reduces the energy consumption applied in the grinding process [4–10].

Amines such as triethylenetetramine, aminalols such as diethanolamine, glycol compounds such as ethylene glycol, phenol, and phenol derivatives, and also many more complex compounds were used as grinding aids [11–15]. Sohoni et al. reported that grinding aids such as triethanolamine, mono and diethylene glycol, oleic acid, sodium oleate, sulfite waste liquor and dodecylbenzene sulfonic acid have very good effects in grinding limestone and clinker [16]. Jeknavorian and others had identified phenol, 5-glycol, and alkanolamine compounds in cement with the test technique they found [17]. Hasegawa conducted research on grinding aids for use in ultra-fine grinding of limestone, asserting that alcohol and glycol promote ultra-fine grinding of limestone, and that the maximum specific surface area of limestone obtained as an additive is proportional to the amount of additive [18]. Zhenping Su et al conducted an experiment to use glycerol as a grinding aid, and the results showed that GL-C has good compatibility with PCE when the dosage of GL does not exceed 0.02 % [19]. In addition, many researchers have conducted studies on glycerin-based grinding aids and published experimental results for rational addition amounts and grinding properties [20–28]. However, the above-mentioned grinding aids have good grinding effects, but are expensive, so they have limitations in industrial applications.

The aim of the study is to prepare a glycerol-waste antifreeze-based cement grinding aid (GAP) and examine its effect on the grinding properties of the cement powder as compared to the case where a grinding aid is not added to verify its effectiveness.

Objectives:

- Examine the effect of GAP on the angle of repose of the powder and verify the effectiveness of the grinding aid on the flowability of the powder;
- Investigate the effect on the specific surface area and grain size distribution of cement powder;
- Investigate the effect on the surface tension of the powder, the activity index, and the strength of the cement mortar;
- Verifies the effectiveness in contrast to the commonly used TEA grinding aid.

2. Materials and Methods

2.1. Materials

Table 1 shows the chemical composition of clinker and gypsum used in the experiment.

Table 1. Chemical composition of clinker (by mass)(%).

Constituent	Content: mass %
Calcium oxide (CaO)	64.24
Silicon dioxide (SiO_2)	21.11
Iron oxide (Fe_2O_3)	3.97
Aluminium oxide (Al_2O_3)	4.88
Magnesium oxide (MgO)	1.15
Sulfur trioxide (SO_3)	1.61
R2O (K2O + Na_2O)	1.11
Tricalcium silicate (C_3S)	50.6
Dicalcium silicate (C_2S)	24.6
Tricalcium aluminate (C_3A)	6.8
Tetracalcium aluminoferrite (C_4AF)	9.4

2.2. Experiment Method

2.2.1 Preparation Method of grinding aid GAP

At room temperature, 100 g of waste antifreeze (45 % of antifreeze + 55 % of water), 65 g of glycerin, 5 g of urea, and 55 g of phosphoric acid are added in a mixing container equipped with a stirrer. This solution is stirred evenly for 1 h to make a grinding aid GAP.

2.2.2 Test Methods

A mixture of clinker and gypsum (clinker: gypsum = 95: 5) is grinded in the ball mill so that the particle size is < 5 mm. 0.02 % (mass ratio) of grinding aid is added to this mixture and fed to the ball mill (φ600 × φ600). Samples are collected and analyzed at various grinding times. In the experiment, each experimental groups are measured 5 times, and the average value is used as the actual measurement value.

1. The angle of repose is tested according to GB/T11986-1989. After the powder is poured into the funnel, the sample from the funnel is coated the disk under the funnel. At this time, the height h of the powder layer and the radius R of the disk are measured and obtained according to the formula of the powder ($\tan\theta = h / R$).

2. Zeta potential of cement is measured by the zeta potential instrument by the electrophoresis method, and the suspension liquid is prepared by stirring cement and water for 1-3 min.

3. Cement fineness is measured in accordance with GB1345-91.
4. Cement surface area is measured using automatic analyzer of the FBT-5 surface of cement.
5. Cement particle size distribution is tested the JL-1166 laser particle size analyzer determination.
6. SEM images is tested by German Zeiss LEO-1450 scanning electron microscope shot.
7. Strength of cement mortar is measured in accordance with GB/T17671-1999 strength.
8. The activity index of powder in blended cement is measured according to the GB/T 18046-2008.

Then the activity index of cement powder is determined from:

$$A_7 = \left(R_7 / R_{07}\right) \times 100, \quad A_{28} = \left(R_{28} / R_{028}\right) \times 100,$$

where A_7 and A_{28} are the activity index of powder at 7 days, and 28 days, respectively, (%); R_7 and R_{28} are the 7d and 28d compressive strength of cement mortar, respectively, (MPa); and R_{07} and R_{028} are the 7d and 28d compressive strength of the pure cement mortar, respectively, (MPa).

3. Results and Discussion

3.1. Effect of Grinding Aids on the Fluidity of Cement Powder

The angle of repose is a factor that reflects the friction characteristics between the powder particles and characterizes the flow properties of the cement powder [4, 6]. In other words, a large angle of repose means that the fluidity of the powder is deteriorated.

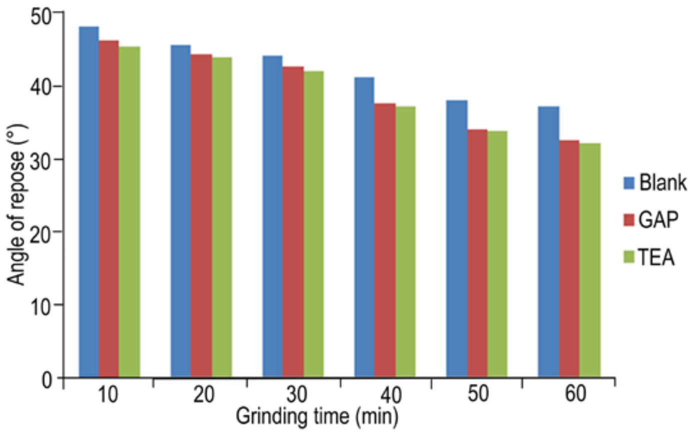

Figure 1. Effect of GAP on the repose angle of ground powder.

As shown in Fig. 1, as the grinding time increases, the repose angle of GAP and TEA tend to decrease compared to Blank. In particular, when the grinding time was 60 min, the repose angle of GAP and TEA decreased by 3.8° and 4.0°, respectively, compared to Blank. This is because the polishing aid adsorbed on the surface of the cement particles forms a single-molecule adsorption layer to reduce the contact area and surface agglomeration between the particles, thereby facilitating sliding between cement powders. Therefore, the flowability of the cement is increased and the grinding efficiency is increased.

3.2. Effect of Grinding Aids on the Fineness of Cement

In general, as the pulverization time increases, agglomeration between the cement powders occurs violently, which greatly reduces the specific surface area of the powder [5, 8, 10].

As shown in Fig. 2, as the grinding time increases, the Blaine specific surface area of GAP and TEA significantly increase compared to the blank. This is because the grinding aid prevented agglomeration between the cement particles and increased the fluidity.

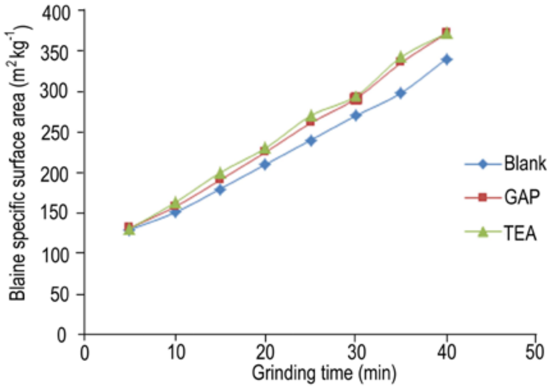

Figure 2. Effect of grinding aid on Blaine specific surface area.

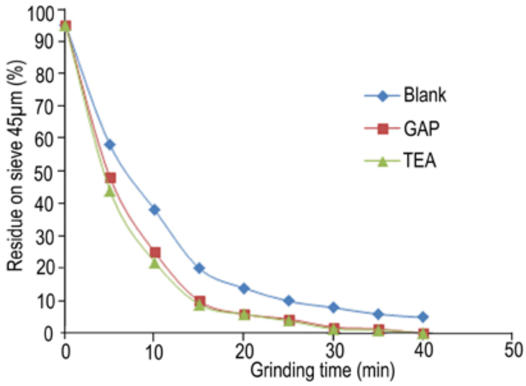

Figure 3. The effect of grinding aids on 45 µm sieve.

Fig. 3 shows the effect of grinding aid on a 45 µm sieve. As can be seen from the figure, as the grinding time increases, the residual amounts of GAP and TEA tend to be significantly less than that of Blank. This shows that the grinding aid has improved the grinding properties of the cement powder.

3.3. Effect of grinding aid on the particle size distribution of cement powder

Generally, 3–32 µm particles which play a major role in increasing the strength of cement are the optimum particle size distribution of cement [17–19].

As shown in Fig. 4, the volume of 3 to 32 µm particulates in the GAP and TEA samples is greater than that of the blank sample. This shows that the grinding aid narrows the particle size distribution by reducing the content of excessive fine particles and large particles. Therefore, it is shown that the grinding aid plays a role in rational control of the particle size distribution.

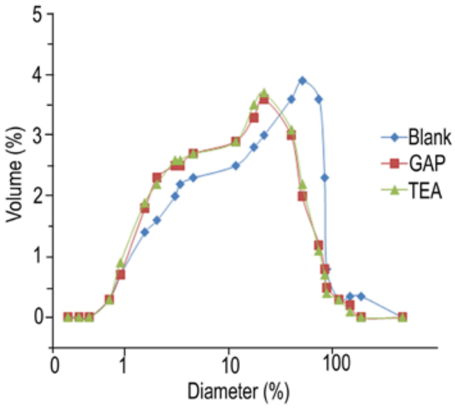

Figure 4. Particle size distribution of cement powder.

As can be seen in Fig. 5, there are many coarse grains (more than 20 µm in diameter) in the blank. With the addition of grinding aids, the particle size is relatively uniform and almost less than 10 µm.

Therefore, it was confirmed that the GAP and TEA grinding aid has a good effect on suppressing the agglomeration of the cement powder after grinding and making the grain size distribution even.

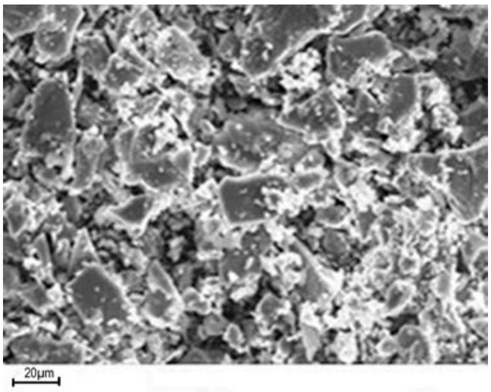

a) Blank

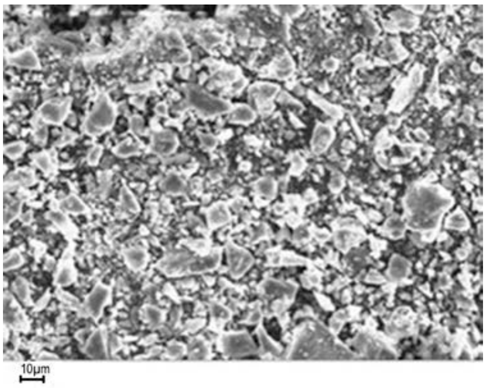

b) With GAP

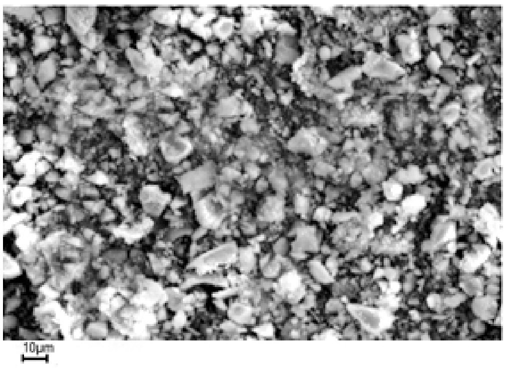

c) With TEA

Figure 5. SEM images of the particles distribution of ground cement.

3.4. Effect of grinding aid on the activity index of cement powder

The activity index is a characteristic index that defines the hydration activity of cement [12–15].

As shown Fig. 6, the activity index of the powder is improved by GAP compared to the Blank sample during the same grinding time. With the increasing of grinding time, the improvement of GAP on the 7d activity index of cement powder gradually becomes weak, while for 28d, the improvement gradually intensifies. This is because the initial activity of the powder is low, so when the particle size decreases to some extent, the initial active growth of the powder is in equilibrium. As the curing time increases, the activity increases thereafter, and as the powder particle size decreases, the increase in the activity index becomes more pronounced. During 50 minutes of grinding time, the 7d and 28d activity index of the powder is improved by 5 % and 6 %, respectively. It can be seen that the GAP grinding aid has a good effect on improving the hydration activity of the cement powder.

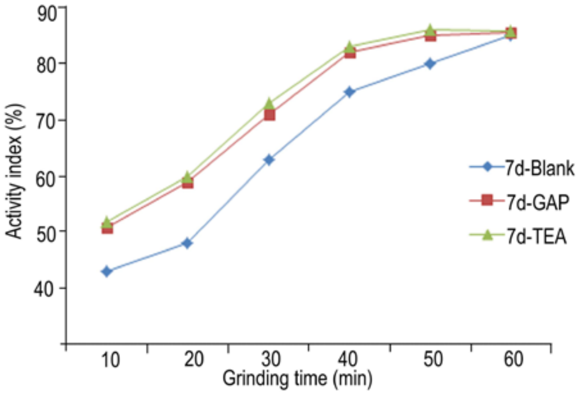

(a)

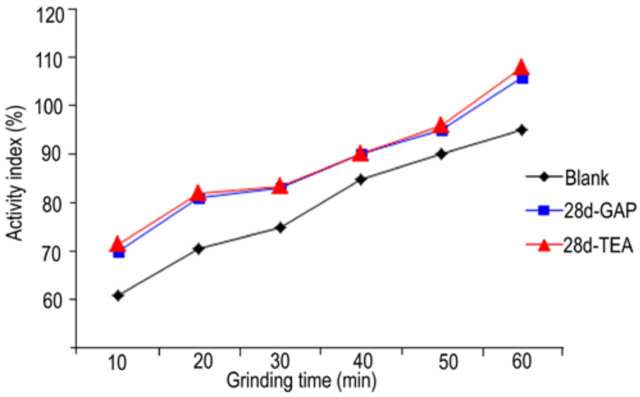

(b)

Figure 6. Effect of GAP on the activity index of cement powder.

3.5. Analysis of zeta potential of cement

Zeta potential is commonly used to characterize the adsorption properties of chemical mixtures.

When the grinding aid is adsorbed on the cement particles, the electric charge distribution on the surface of the particles is changed [20–28]. Therefore, the change in zeta potential can reflect the adsorption characteristics of the grinding aid on the surface of the cement particles. The effect of grinding aids on the zeta potential of cement is shown in Table 2. As can be seen in Table 2, the absolute value of the zeta potential for cement with GAP and TEA is significantly reduced compared to blank cements. In other words, it shows that the negative charge on the surface of the cement particles containing the polishing aid is reduced. This may be because GAP is easily adsorbed to the particle surface by functional groups (hydroxyl groups) and positively charged hydrophobic alkyl chains neutralize the charged portion of the cement particles.

Table 2. Surface tension and Zeta potential of cement powder.

Sample	Dosages of grinding aids / %	Zeta potential / mV
Blank		–10.68
With GAP	0.02	–6.07
With TEA	0.02	–6.01

3.6. Effect of grinding aid on the compressive strength of cement

According to the literature [6–10], the hydration reaction of cement is highly dependent on the size of the cement powder. Fig.7 shows the effect of grinding aid on the compressive strength of cement mortar samples. As shown in the figure, the 7d intensity and 28d intensity of GAP and TEA tended to be significantly higher than that of Blank. This can be attributed to the fact that the grain size was reduced to some extent by the grinding aid, and as a result, the cement hydration reaction was promoted.

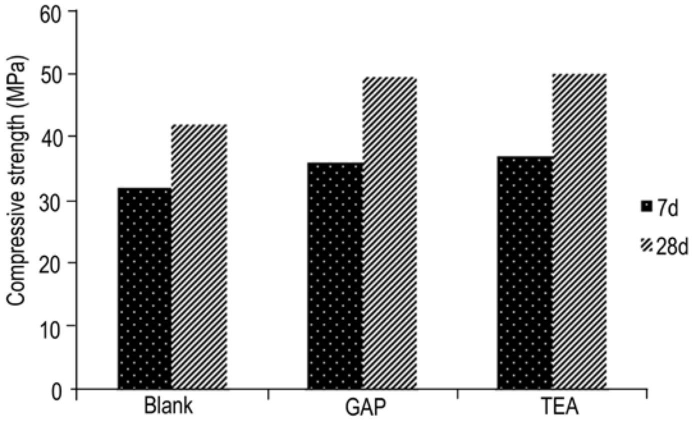

Figure 7. The impact of grinding aids on compressive strength of cement mortar.

3.7. Performance comparison of GAP and TEA

The most commonly used cement grinding aid is TEA (triethanolamine), and its effectiveness is very good, but it is expensive, so it is limited in industrial introduction [1–3] Table 3 shows the effect of the prepared GAP grinding aid and the most commonly used TEA grinding aid on the grinding performance and hydration properties of the cement powder. Compared to the blank, when GAP and TEA were added, the sieve residue of the pulverized powder decreased by 4.6 % and 5.2 %, and the specific surface areas increased by 30.5 m^2/kg and 33.7 m^2/kg, respectively. In addition, the particle content in the range of less than 32 μm was improved by 7.94 % and 9.03 %, respectively, by Blank. The results show that the grinding aid effects of GAP and TEA are almost similar. After all, compared to TEA, GAP shows that the grinding aid effect is not bad. On the other hand, GAP costs only 15/1 compared to TEA. Therefore, the use of GAP as a grinding aid provides a number of economic benefits.

Table 3. Particle characteristics and hydration activity of cement powder with different grinding aids.

Type of grinding aids	Sieve residue (%)	Specific surface area (m^2/g)	Particle size distribution (%)			Activity index (%)	
			$\leq$ 32 μm	32-65 μm	$\geq$ 65 μm	7d	28d
Blank	12.7	340.5	75.18	16.24	8.58	76	85
GAP	8.1	371.0	83.12	11.82	5.06	81	91
TEA	7.5	374.2	84.21	10.62	5.17	82	91

4. Conclusions

By studying the influence of expanded perlite cement grinding aid (GAP) prepared from Glycerol, Waste Antifreeze on the grinding performance and physical properties of cement, we can get the following conclusions:

1. Angle of repose for cement was reduced for the same grinding time for the specimens with the addition of the GAP grinding aid, compared to Blank. Therefore, the fluidity of the cement powder is greatly improved.

2. The sieve residue of the pulverized powder decreased by 4.6 % and the specific surface area increased by 30.5 m^2/kg. This shows that the manufactured GAP increases the grinding efficiency of the cement powder.

3. The particle size distribution of the cement powder was more uniform than that of the Blank, and the use of the grinding aid GAP increased the content of fine particles in the range of 3 ~ 32 μm compared to the Blank.

4. GAP grinding aid has a good effect on improving the hydration activity of cement powder and increases the compressive strength of cement mortar.

5. The effectiveness of the grinding aid of GAP is similar to that of TEA and is very economical in terms of cost.

References

1. Prziwara, P. Comparative study of the grinding aid effects for dry fine grinding of different materials. Minerals Engineering. 2019. 144. Pp. 106030. DOI: 10.1016/j.mineng.2019.106030
2. Katsioti, M., Tsakiridis, P.E., Giannatos, P., Tsibouki, Z., Marinos, J. Characterization of various cement grinding aids and their impact on grindability and cement performance. Construction and Building Materials. 2009. 23. Pp. 1954–1959. DOI: 10.1016/j.conbuildmat.2008.09.003
3. Prziwara, P. Grinding aids for dry fine grinding processes – Part I: Mechanism of action and lab-scale grinding. Powder Technology. 2020. 375. Pp. 146–160. DOI: 10.1016/j.powtec.2020.07.038
4. Prziwara, P. Breitung-Faes S. Impact of the powder flow behavior on continuous fine grinding in dry operated stirred media mills. Minerals Engineering. 2018. 128. Pp. 215–223. DOI: 10.1016/j.mineng.2018.08.032
5. Li, W. The mechanochemical process and properties of Portland cement with the addition of new alkanolamines. Powder Technology. 2015. 286. Pp. 750–756. DOI: 10.1016/j.powtec.2015.09.024
6. Toprak, N.A. The influences and selection of grinding chemicals in cement grinding circuits. Construction and Building Materials. 2014. 68. Pp. 199–205. DOI: 10.1016/j.conbuildmat.2014.06.079
7. Sverak, T.S. Efficiency of grinding stabilizers in cement clinker processing. Minerals Engineering. 2013. 43. Pp. 52–57. DOI: 10.1016/j.mineng.2012.08.012
8. Zhao, J.H. Particle characteristics and hydration activity of ground granulated blast furnace slag powder containing industrial crude glycerol-based grinding aids. Construction and Building Materials. 2016. 104. Pp. 134–141. DOI: 10.1016/j.conbuildmat.2015.12.043
9. Moothedath, S.K. Mechanism of action of grinding aids in comminution. Powder Technology. 1992. 71. Pp. 229–237. DOI: 10.1016/0032-5910(92)88029-h
10. Burmeister, C.F. Experimental and computational investigation of knoevenagel condensation in planetary ball mills. Chemical Engineering & Technology. 2014. 37. Pp. 857–864. DOI: 10.1002/ceat.201300738
11. Toraman, O.Y. Effect of chemical additive on stirred bead milling of calcite powder, Powder Technology. 2012. 221. Pp. 189–191. DOI: 10.1016/j.powtec.2011.12.067
12. Sun, Z. A grindability model for grinding aids and their impact on cement properties. Advances in Cement Research. 2016. 28. Pp. 475–484. DOI: 10.1680/jadcr.16.00001
13. Assaad, J.J. Quantifying the effect of clinker grinding aids under laboratory conditions. Minerals Engineering. 2015. 81. Pp. 40–51. DOI: 10.1016/j.mineng.2015.07.008
14. Prziwara, P. Impact of grinding aids and process parameters on dry stirred media milling. Powder Technology. 2018. 335. Pp. 114–123. DOI: 10.1016/j.powtec.2018.05.021
15. Gao, X., Yang, Y., Deng, H. Utilization of beet molasses as a grinding aid in blended cements. Construction and Building Materials. 2011. 25. Pp. 3782–3789. DOI: 10.1016/j.conbuildmat.2011.04.041
16. Benzer, H., Ergun, L., Lynch, A.J., Oner, M., Gunlu, A., Celik, I.B., Aydogan, N. Modelling cement grinding circuits, Minerals Engineering. 2001. 11(14). Pp. 1469–1482. DOI: 10.1016/s0892-6875(01)00160-1
17. Jeknavorian, A.A. Determination of Grinding Aids in Portland Cement by Pyrolysis Gas Chromatography-Mass Spectrometry. Cement and Concrete Research. 1998. 28. Pp. 1335–1345. DOI: 10.1016/s0008-8846(98)00109-4
18. Hasegawa, M. Effect and Behavior of Liquid Additive Molecules in Dry Ultrafine Grinding of Limestone. Journal of the Society of Powder Technology Japan. 2005. 42. Pp. 178–184. DOI: 10.4164/sptj.42.178
19. Sohoni, S. The Effect of Grinding Aids on the Fine Grinding of Limestone Quartz and Portland Cement Clinker. Powder Technology. 1991. 67. Pp. 277–286. DOI: 10.1016/0032-5910(91)80109-v
20. Yang, F., Hanna, M.A., Sun, R. Value-added uses for crude glycerol-a byproduct of biodiesel production. Biotechnology for Biofuels. 2012. 5. Pp. 1–10. DOI: 10.1186/1754-6834-5-13
21. Zhao, J., Wang, D., Yan, P., Zhao, S., Zhang, D. Particle characteristics and hydration activity of ground granulated blast furnace slag powder containing industrial crude glycerol-based grinding aids. Construction and Building Materials. 2016. 104. Pp. 134–141. DOI: 10.1016/j.conbuildmat.2015.12.043
22. Alper Toprak, N. The influences and selection of grinding chemicals in cement grinding circuits. Construction and Building Materials. 2014. 68. Pp. 199–205. DOI: 10.1016/j.conbuildmat.2014.06.079
23. Assaad, J.J., Issa, C.A. Effect of clinker grinding aids on flow of cement-based materials. Cement and Concrete Research 2014. 63. Pp. 1–11. DOI: 10.1016/j.cemconres.2014.04.006
24. Ma, S., Li, W., Zhang, S. Study on the hydration and microstructure of Portland cement containing diethanolisopropanola-mine. Cement and Concrete Research. 2015. 67. Pp. 122–130. DOI: 10.1016/j.cemconres.2014.09.002
25. Heinz, D., Göbel, M., Hilbig, H. Effect of TEA on fly ash solubility and early age strength of mortar. Cement and Concrete Research. 2010. 40(3). Pp. 392–397. DOI: 10.1016/j.cemconres.2009.09.030
26. Deiner, L.J., Rottmayer, M.A., Eigenbrodt, B.C. The effect of milling additives on powder properties and sintered body microstructure of NiO. Journal of Advanced Ceramics. 2015. 4. Pp. 142–151. DOI: 10.1007/s40145-015-0147-z
27. Chen, Y., Lian, X., Zheng, S. Research on superfine grinding process and kinetics of Calcined black talc in planetary mill. Procedia Engineering. 2015. 102. Pp. 379–387. DOI: 10.1016/j.proeng.2015.01.167
28. Gokcen, H.S. The effect of grinding aids on dry micro fine grinding of feldspar. International Journal of Mineral Processing. 2015. 136. Pp. 42–44. DOI: 10.1016/j.minpro.2014.10.001

Information about authors

Ri Jin Hyok
ORCID: https://orcid.org/0000-0001-5227-7544
E-mail: rijinge@163.com

Kim Yong Ho
ORCID: https://orcid.org/0000-0002-1340-0324
E-mail: lijinge@163.com

Hwang Yong Su
ORCID: https://orcid.org/0000-0001-6224-9643
E-mail: rijinge@126.com

Kang SongGun
ORCID: https://orcid.org/0000-0003-1237-3712
E-mail: lijinge@126.com

Yu Ju Hyon
ORCID: https://orcid.org/0000-0003-1712-3907
E-mail: lijingefsatr@163.com

Received 26.03.2021. Approved after reviewing 02.09.2021. Accepted 03.09.2021.

Magazine of Civil Engineering

ISSN
2712-8172

journal homepage: http://engstroy.spbstu.ru/

Research article
UDC 624.014
DOI: 10.34910/MCE.112.15

Numerical modeling of basalt roll fire-protection for light steel thin-walled structures

M.V. Gravit[1], I.I. Dmitriev[2]

[1] Peter the Great St. Petersburg Polytechnic University, St. Petersburg, Russia
[2] Graz University of Technology, Graz, Austria,

i.i.dmitriev@yandex.ru

Keywords: steel construction, thin walled structures, cold-formed steel, structural design, fire, fire safety, fire protection, fire design

Abstract. The authors investigate the fire-protective efficiency of a basalt roll material, which is used for light steel thin-walled structures. The values of fire-protective efficiency for the steel C-shaped profiles without fire protection made of basalt wool material MBOR-F were obtained in the experimental and numerical studies. This article presents the estimated dependence of the thickness of the fire-protective material MBOR F on the resistance to fire with regard to light steel thin-walled structures. The approximating functions are formed on the basis of the experimental data and presented as nomograms for heating of the steel structure. There was an absence of the samples' deformation and destruction of the fire-protective material during the fire tests. This allows us to conclude that the fire-protective efficiency of the light steel thin-walled structures increases by 2–4 times. Implementation of the study results will expand the scope of fire-protective materials for the light steel thin-walled structures, improve the quality of fire protection projects for buildings and constructions, and help ensure the fire safety of structural elements.

Acknowledgments: The authors are to the management of TIZOL JSC grateful for providing the results of the fire experiments, and also thank the specialists of Andromet LLC for providing technical and informational support in carrying out this work.

Citation: Gravit, M.V., Dmitriev, I.I. Numerical modeling of basalt roll fire-protection for light steel thin-walled structures. Magazine of Civil Engineering. 2022. 112(4). Article No. 11215. DOI: 10.34910/MCE.112.15

1. Introduction

Light gauge steel framing (LGSF) is widely used in low-rise constructions because of the wide architectural capabilities and excellent technical and economic qualities that allow for operation under dynamic conditions in a changeable market with maximum accuracy, flexibility, and efficiency. The advantages of light steel framing have already been appreciated in developed countries for several years, and buildings made from LGSF occupy a significant share of the construction market: in the UK – 20%, Sweden and Japan – 15%, Canada – 10% of total residential constructions. The share of LGSF in Russian low-rise construction is 0.5% – that is 30 times less than in developed countries [1,2].

The LGSF constructions have great perspectives in the design area [3, 4], however, low levels of fire resistance of unprotected thin-walled constructions inhibit the process of incorporating designs into construction. The fire resistance of thin-walled rods is actively discussed throughout the world, but, despite numerous investigations of these structures, this issue has not been fully studied and remains relevant. For the widespread introduction of light steel thin-walled structures into the civil engineering practice of public and residential constructions, it is necessary to conduct tests to determine the fire resistance of structures and to allow for the subsequent improvement of existing regulatory documents.

The fire protection of the building structures is an integral part of the general system to ensure fire safety and fire resistance of buildings and constructions [5,6]. The light steel framing has a short resistance period under fire loads, and because of that, it is not required by Russian fire safety standards. In some cases, these systems do not reach the minimum requirement of the safety conditions, and therefore the fire protection plays an important role in obtaining the required fire resistance of various configurations of LGSF constructions.

There are a small number of works concerning the fire resistance of LGSF, which include consideration of the regulatory framework in our country compared with the other ones. The conducted studies include those by Vatin and Garifullin [7–11], Gravit [12–15], Naser [16–18], Chen and Ye [19–23], Dias [24,25], Craveiro [26]. Researchers have also determined that cold-formed steel perforated beams can have higher fire resistance than the limit of 350 °C, according to Eurocode 3 [26 – 35]. Many studies on the behavior of thin-walled steel constructions were conducted not only for the standard fire mode, but also as numerical simulations of real fire scenarios.

Naser and Degtyareva reported the results of the fire tests on the steel beams made of galvanized C-shaped thermal profiles [16]. In these experiments the authors investigated the stress limits of the perforated beams as well as their temperature deformations. The result of this work was a nonlinear numerical model, developed by using the finite element analysis software ANSYS.

The fire test results of cold-formed steel columns of both the single and built-up section of 2xC-shaped profiles are presented in [26]. The temperature increment depended on the cross-sectional shape. Therefore, a C-shaped column with a section factor 400 m-1 and a column with built-up 2xC-shaped profile have reached the limit state for stability only after 8 minutes and 10 minutes respectively. Structures were under the temperature load in according to the standard fire curve. The critical temperature of profiles exceeded 500 °C. Numerical simulations using the Abacus software has also been conducted.

The fire resistances of the steel columns were evaluated by numerical simulations in [27], taking into account the various thicknesses of the fire protective coating made of the vermiculite plates. Three column options were considered: columns without fire protection, with protection of 20 mm thickness, and with 40 mm thicknesses. The temperature contour graphs and heating curves of the columns were obtained by taking into account the presence and absence of fire protection made of the vermiculite plates. Studies have shown that the steel columns covered by a fire-protective layer with 20 and 40 mm thickness and the unprotected steel column sustained a critical temperature of 500 °C after 82, 180 and 12 minutes, respectively.

The constructive method of the steel structures' protection with PYRO-SAFE AESTUVER T plates and the fire resistance limit of steel rod elements were considered in [28] to ensure the regulatory fire resistance requirements. This paper presents the calculated thermophysical characteristics of materials, based on which the fire resistance nomograms of the fire protected steel structures are calculated. For instance, both the steel construction with 2 mm profile thickness and the steel plate with 20 mm profile thickness sustained a critical temperature of 600 °C after 70 minutes (and 80 minutes for the steel with 3.4 mm profile thickness); the steel plate with 40 mm profile thickness sustained a critical temperature of 600 °C after 100 minutes.

Therefore, despite the fact that there are some researches into unprotected light steel structures and structures with different types of fire-protective materials (both structural and paintwork), this number of studies is insufficient, because the problem with underestimation of light steel framing is actual and the industry still has a need for new technologies and materials for fire protection.

The aim of this study was to evaluate the fire-protective efficiency of MBOR roll material based on basalt wool manufactured by TIZOL JSC (Russia) for LGSC structures. To achieve this goal, the following tasks were carried out:

1. The conduction of experimental studies of C-shaped profiles, including fire protection with MBOR rolled basalt material;

2. The modeling of the thermal effect on building structures (LGSC) in the ELCUT PC, including MBOR fire protection;

3. The creation of recommendations on the use of flame protective materials for structures (LGSC).

The results of fire tests allow us to evaluate the accuracy of both analytic and numerical (computer) modeling methods. The authors used the results of fire impact on light gauge steel structures, and carried out experiments in the testing laboratory of TIZOL JSC, for a comparative analysis.

The results of the numerical studies on the cold-formed steel galvanized profiles with fire protection by heat-insulating plates made of MBOR-F basalt wool are presented. Fire-protective efficiency and behavior of LGSC profiles are determined according to experimental studies and using linear FE models developed in the ELCUT PC and verified according to fire tests.

2. Methods

2.1. Fire test method

The tests of LGSC profiles with fire protection made of heat-insulating basalt wool plates MBOR-F and PLAZAS adhesive composition are carried out in accordance to Russian Standard No. 53295-2009 [36] with four-sided heat exposure according to the standard temperature curve according to ISO 834 [37]. The method allows for the determination of the actual efficiency of the fire protection, which is equal to the time from the onset of the thermal effects on the prototype until the limit state of this sample. The critical state corresponds to the critical temperature of heating the section of the structure.

The equipment includes:

- a test furnace with a fuel supply and combustion system;

- devices for installing the sample in the furnace;

- systems for measuring and recording parameters according to [37].

There was a standard temperature mode characterized by the equation:

$$T - T_0 = 345\lg(8t + 1) \quad (1)$$

where t is the time calculated from the start of the test, minutes;

T is the furnace temperature corresponding to time t, °C;

T_0 is the temperature in the furnace before the start of the heat exposure (ambient temperature), °C;

The structural elements based on cold-formed steel galvanized profiles without taking into account the static load were investigated to determine the behavior of light steel thin-walled structures and to increase their fire resistance. As the test object, rod structures of a composite section made by Andrometa LLC from two C-shaped profiles connected by bolt fastening are adopted (technical specification: TC 1122-002-82866678-2013 "Cold-formed profiles from galvanized steel for construction):

- sample No. 1 - 2AC 150 × 75 × 16.8 × 1.6 mm;

- sample No. 2 - 2AC 380 × 125 × 29.9 × 3.5 mm.

The coating is designed as a single-layer sheathing basalt roll material. The MBOR material is a staple canvas of basalt super thin fibers, stitched with a knitting and stitching method and lined with aluminum foil on one side. The schemes of the test structures and the basic geometric characteristics of the profile are presented in Figure 1 and Figure 2.

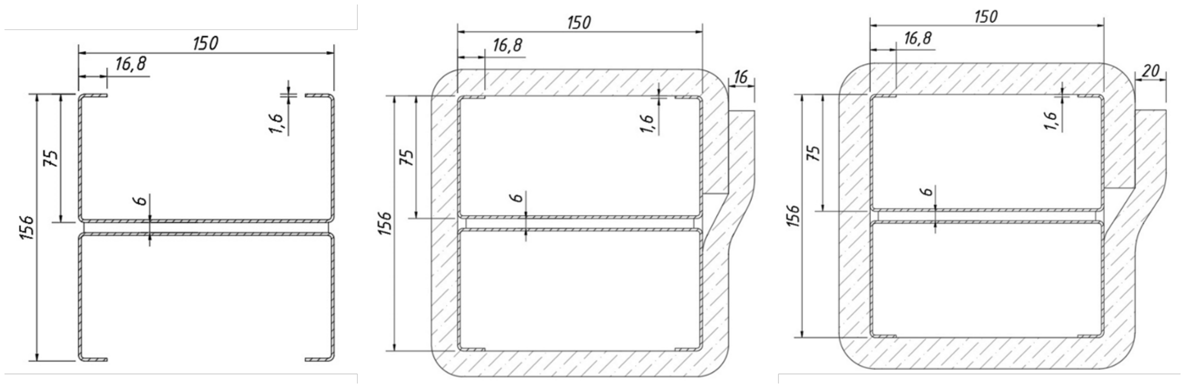

Figure 1. Test sample No. 1.

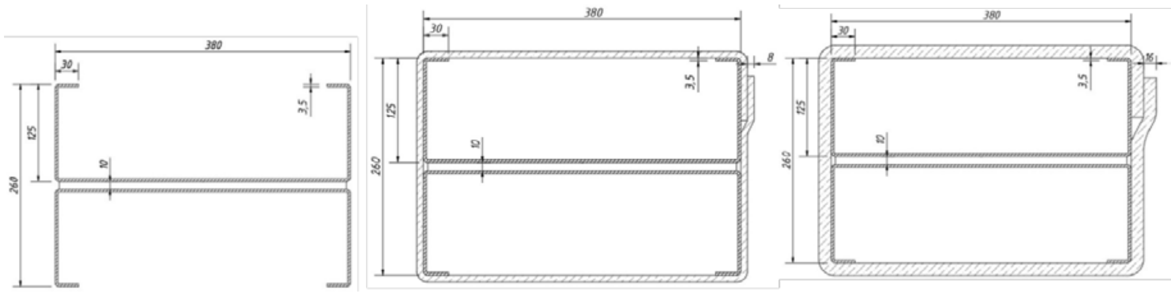

Figure 2. Test sample No. 2.

There were six test samples with a length of 1700 ± 10 mm. The concept of the reduced metal thickness, t_{red} , was used to compare metal structures. It is defined as the ratio of the cross-sectional area to its heated perimeter for each test sample by the formula (2):

$$t_{red} = \frac{S}{P} \tag{2}$$

where S is the cross-sectional area of the metal structure, mm^2,

P is the heated part of the structure perimeter, mm.

The reduced thicknesses of the steel of construction No. 1 and No. 2 according to the formula (2) are:

Sample 1, 150×150×1700 t_{red1} = 1.01 mm (section factor 990,1 m^{-1})

Sample 2, 250×380×1700 t_{red2} = 2.35 mm (section factor 423.7 m^{-1}).

The design of the furnace is shown in Figure 3. Temperature measurements of samples are controlled by thermocouples in the middle section on the inner surface. The method of attaching the thermocouples is shown in Figure 4.

Figure 3. Fire Test Furnace

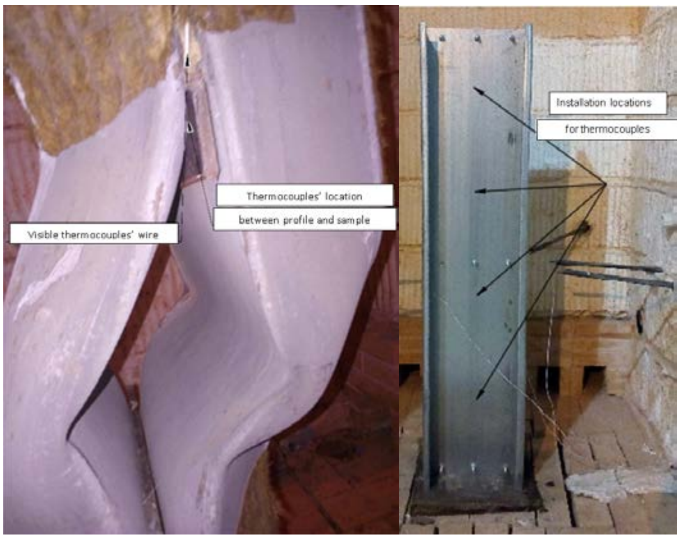

Figure 4. Installation locations for thermocouples

The test samples (Fig. 5, 6) were exposed to a high-temperature environment in a test furnace during the experimental study until the time of reaching the set temperature (t = 700°C). The higher critical temperature was chosen in order to investigate the behavior of the fire protective material also under conditions exceeding the standard ones (when tested in accordance with GOST R 53295 [36] without load, the critical temperature is 500°C). A characteristic feature of all experiments is that when the object of study reaches its limit state, the fire exposure ceases.

Figure 5. Unprotected prototype No. 1 during and after the test.

Figure 6. Prototype No. 2 protected by material MBOR-F during and after the test.

2.2. Modelling in ELCUT PC

Models of steel structures with and without fire protection developed in the ELCUT PC [38–41] were validated according to the fire tests. The two-dimensional model is calculated in the transient thermal conductivity module. Materials have isotropic properties. The heat source is distributed along the cross-sectional contour. The boundary conditions of the considered models correspond to the boundary conditions of the experimental method and belong to the first kind of model classification (the change in the temperature of the external environment is specified). The rise in ambient temperature follows the standard fire curve. The initial temperature is 20 °C. The sampling step of the model is equal to 1 mm. Iteration over temperature is equal to 60 s.

For all tested cross-sections the adopted convective heat transfer coefficient 25 W/m^{2}K used for ISO 834 fire curve for the fire test curves. The radiative heat flux was calculated using a steel (cold-formed steel with zinc coating) emissivity of 0.24 and 0.7 for the furnace electrical resistances (ε = 0.168). The Stefan-Boltzmann constant was 5.67×10-8 W/m^{2}K. The temperature distribution obtained from these numerical simulations will be used as input in the finite element structural models, considering a uniform temperature along the length of the column.

All structural calculations are performed by the finite element method based on the spatial finite element model shown in Figure 7. The properties of the elements are set in accordance with the real properties of steel and the geometric dimensions of the structures. The thermotechnical characteristics of the materials of the finite element model are presented in Figure 8 and Figure 9.

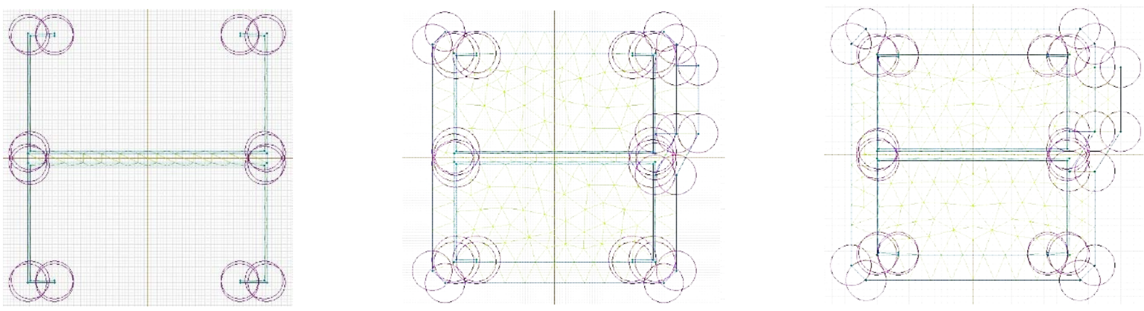

(a) Test 1 **(b) Test 2** **(c) Test 3**

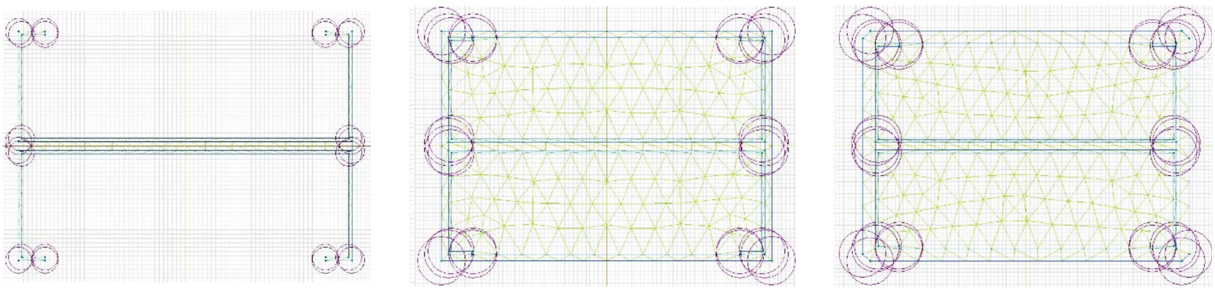

(d) Test 4 **(e) Test 5** **(f) Test 6**

Figure 7. Finite-element models of the design sections: a, b, c – sample No. 1; d, e, f – sample No. 2.

Strength characteristics of steel:

R_0 is an initial standard metal resistance, kg/cm²; and it is equal for steel C350 to $R_0 = 3500 \text{kg/cm}^2$.

E_0 is the initial modulus of elasticity of the metal at normal temperature, kg/cm², $E_0 = 2{,}100{,}000 \text{kg/cm}^2$.

The thermotechnical characteristics of materials are accepted on the basis of the document "Design of fire protection of load-bearing steel structures of multi-apartment residential buildings" [42]:

Steel density: $\gamma_{st} = 7850 \text{kg/m}^3$.

The coefficient of thermal conductivity λ_t (W/m · K) varies according to the formula (3):

$$\lambda_t = A + Bt, \tag{3}$$

where A is the initial coefficient of thermal conductivity, (W m · K);

B is the coefficient of change in thermal conductivity during heating, (W/m · K);

t is the material heating temperature, K.

The heat capacity coefficient C_t (J/kg · K) varies according to the formula (4):

$$C_t = C + Dt, \tag{4}$$

where C is the initial heat capacity coefficient, (J/kg · K);

D is the coefficient of change in heat capacity during heating, (J / kg · K);

t is the material heating temperature, K.

The values of these coefficients for calculations in software systems are presented in Table 1.

Table 1. The coefficients of the thermal characteristics of materials.

№	Steel	Fire protective material MBOR F
A	78	0.032
B	-0.048	0.00029
C	310	850
D	0.48	0.45

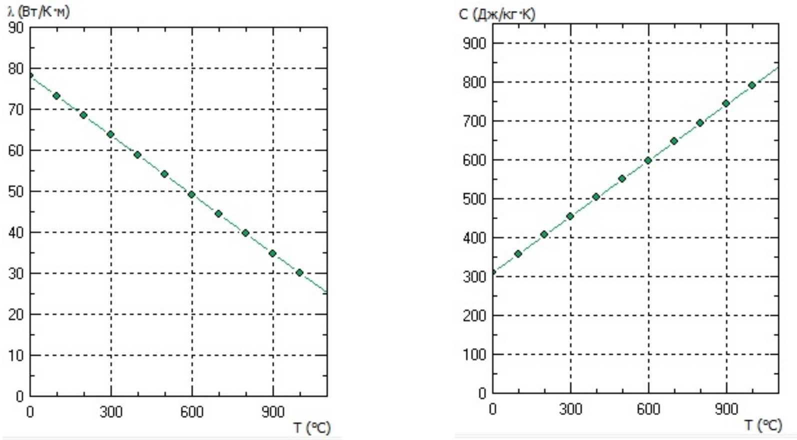

Figure 8. Changes of thermal conductivity and heat capacity of steel with heating temperature.

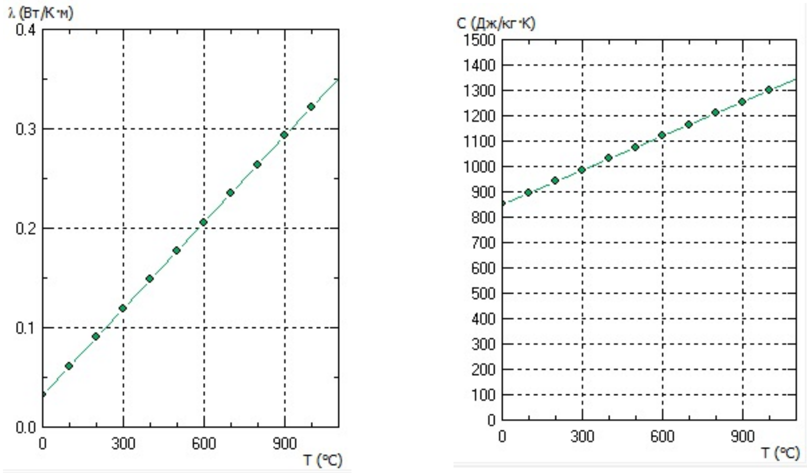

Figure 9. Changes of thermal conductivity and heat capacity of MBOR-F flame retardant material with heating temperature.

The system is uniformly heated by the external heat flow; the whole energy spends on the raising of temperature and the heating stops when the temperature at the external boundaries is equalized with the temperature of the external irradiating medium, which corresponds to a given temperature in the furnace.

3. *Results and Discussion*

3.1. Experiment Results

The experimental result of the sample is the time of onset of its ultimate state. The results of fire tests to achieve steel structures of critical temperature are shown in Table 2 (average value of thermocouples, Fig 10, 11).

Table 2. Fire Test Results.

t_{red}, mm	The time to reach the critical temperature of 700 ˚C (Temperature in the furnace, ˚C)			
	Unprotected	Thickness of the fire protective coating, mm		
		8	16	20
1.01	15:35 (743.1)	-	48:35 (899.3)	50:43 (912.2)
2.35	17:27 (759.0)	50:08 (904.4)	69:02 (969.3)	-
t_{red}, mm	The time to reach the critical temperature of 500 ˚C			
	Unprotected	Thickness of the fire protective coating, mm		
		8	16	20
1.01	4:57	-	33:35	37:43
2.35	9:15	37:08	48:02	-

3.1.1. Evaluation of the flame protective efficiency of basalt roll material

The time to reach of limit state for unprotected prototypes based on the temperature-time curves of the fire tests was 15 (sample No. 1) and 17 minutes (sample No. 2). However, if these samples are sheathed with MBOR-F basalt material, the time of fire exposure increases several times.

The fire resistance of the structure increased by three times for steel sample No. 1 with the MBOR-16F and MBOR-20F materials. There are similar results for sample No. 2. Figure 10 and Figure 11 show the data of experiments conducted at different thicknesses of the MBOR-F material for structures with reduced metal thicknesses of t_{red1} = 1.01 mm and t_{red2} = 2.35 mm.

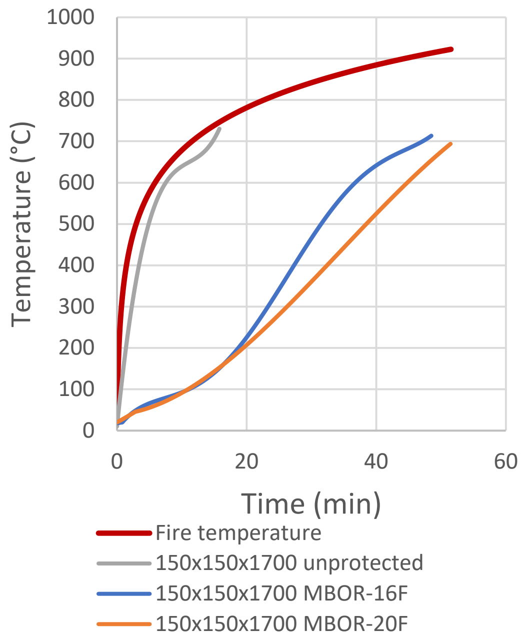

Figure 10. Experimental results for Sample No.1

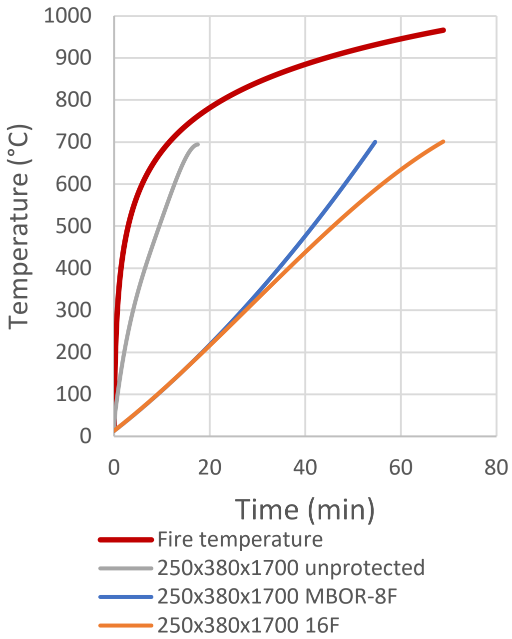

Figure 11. Experimental results for Sample No.2

Based on the results of the fire tests, an approximation of the experimental data is obtained in the form of a mathematical temperature-on-time dependence. In describing the temperature curves, polynomials were chosen as the regression functions. The value of the reliability of the approximation of test results is more than R^2 = 0.99.

Steel sample 1, 150×150×1700 with the reduced metal thickness t_{red1} = 1.01 mm (section factor 990.1 m^{-1}):

$$y = 0.399377 \cdot x^3 - 13.14785 \cdot x^2 + 154.99586 \cdot x + 10.42116$$

Steel sample 2 with the reduced metal thickness t_{red2} = 2.35 mm (section factor 423.7 m^{-1}):

$$y = -0.0155 \cdot x^4 + 0.6078 \cdot x^3 - 9.1114 \cdot x^2 + 94.023 \cdot x + 35.43$$

Based on the obtained approximating functions, a nomogram of heating temperature development of the unprotected steel elements according to the standard fire mode is shown in Fig. 12. Using this figure, the actual fire resistance limit of unprotected steel structures is determined from the loss of bearing capacity in a fire.

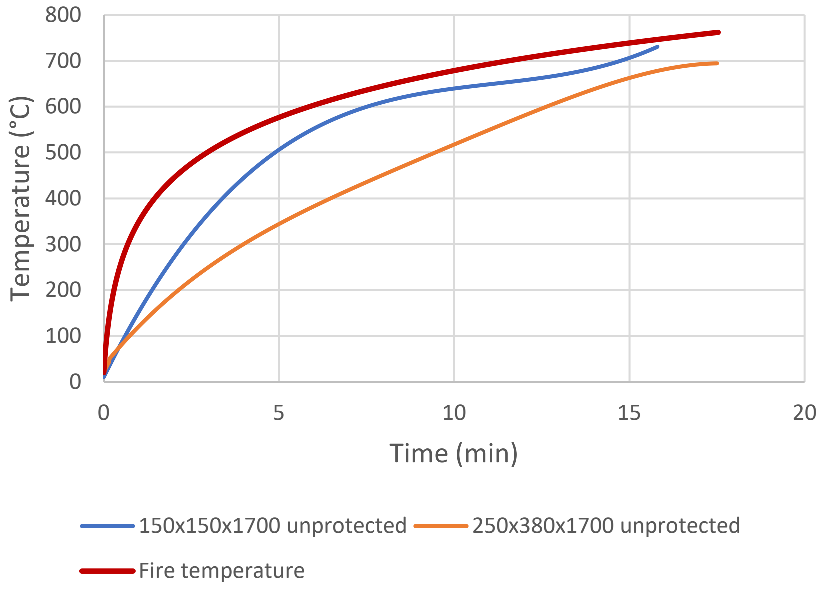

Figure 12. Temperature-time curves of the unprotected elements of steel structures obtained during two full-scale experimental tests according to the standard fire mode (ISO curve).

3.2. Simulation results

Modeling of the temperature distributions of the corresponding sections are based on the data of the fire tests (Figure 13).

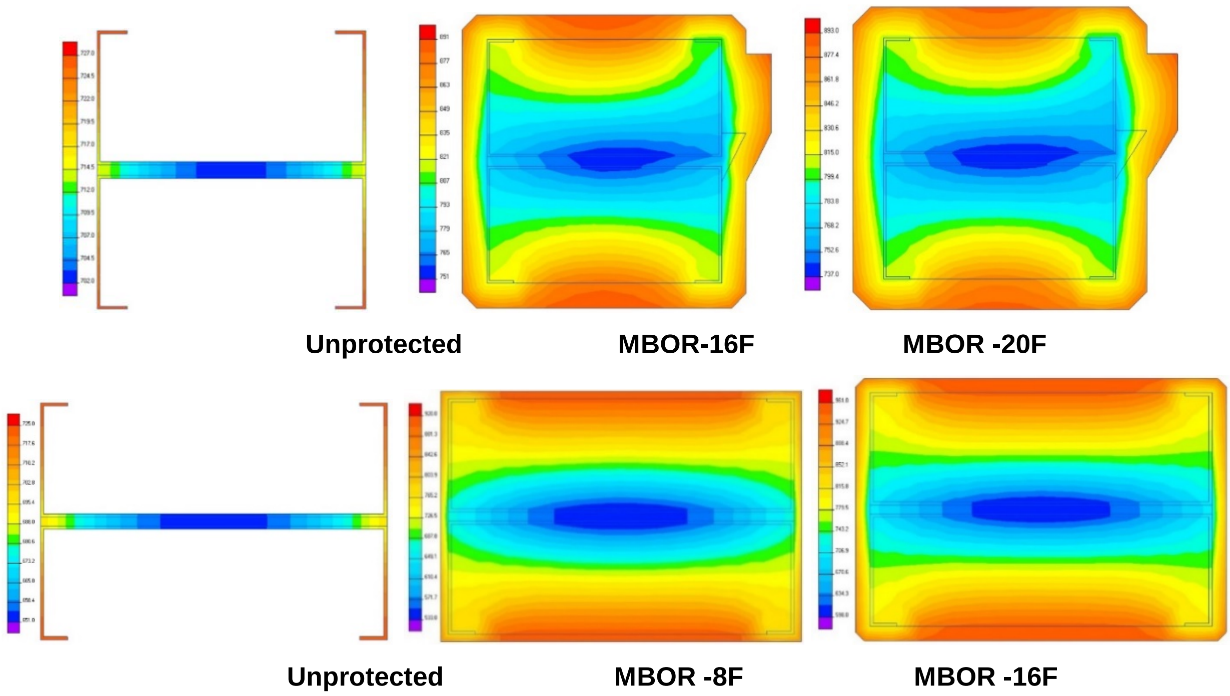

Figure 13. Temperature increase of design samples No. 1 and No. 2.

The simulated temperatures in the middle section of the built-up profile obtained by the fire test method differ from the calculation method in the software package. Moreover, the temperature of the smaller section (sample No. 1) calculated by the theoretical method is greater than the temperature obtained as a result of the experiment. An analysis of the measurement results and error sources for sample No. 2, on the contrary, sets the temperature of the real experiment larger than that calculated in the ELCUT software package. Figure 13 shows the visualization of the section heating in the corresponding measurement scale in the ELCUT software package. The convergences of the FEM to the experimental data for different test conditions are presented in Fig. 14–19.

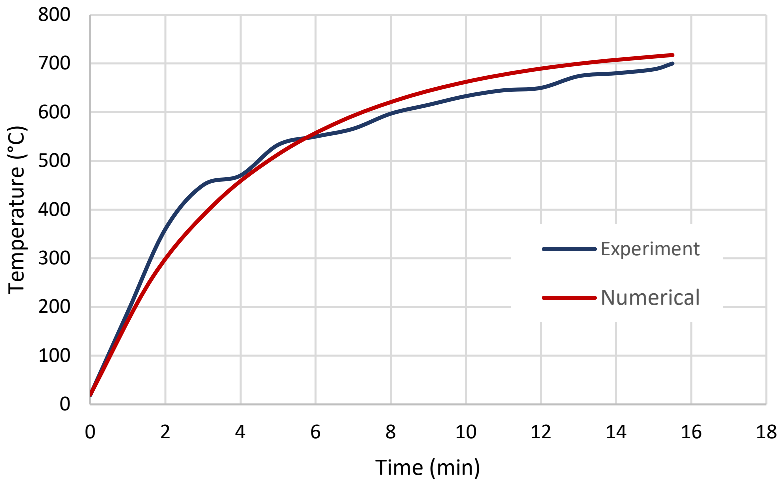

Figure 14. Test 1. First prototype without fire protection.

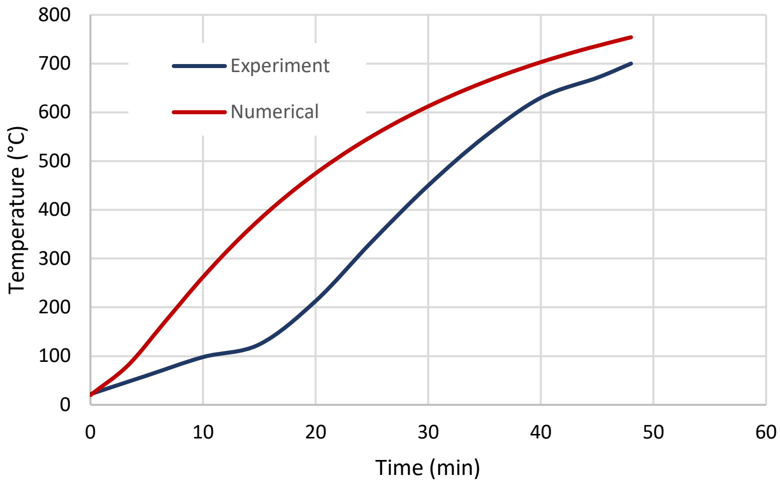

Figure 15. Test 2. First prototype MBOR-16F.

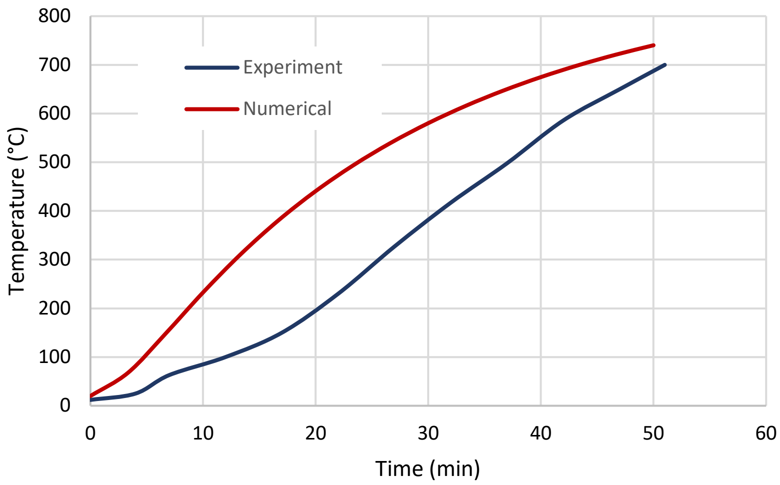

Figure 16. Test 3. First prototype MBOR-20F.

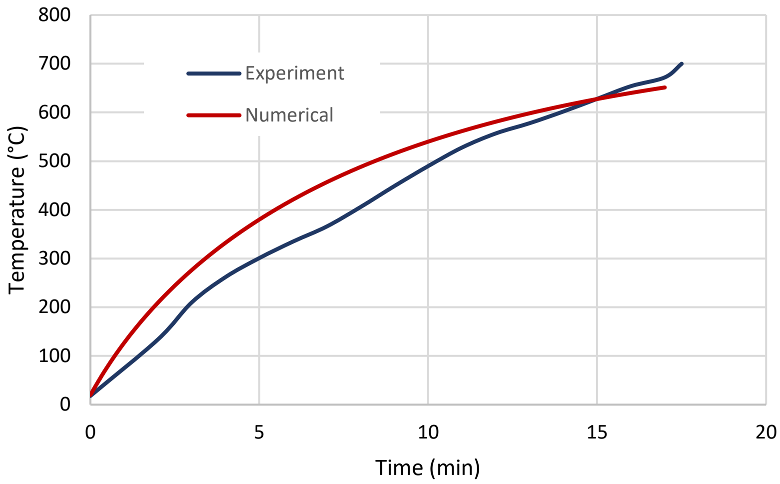

Figure 17. Test 4. Second prototype without fire protection.

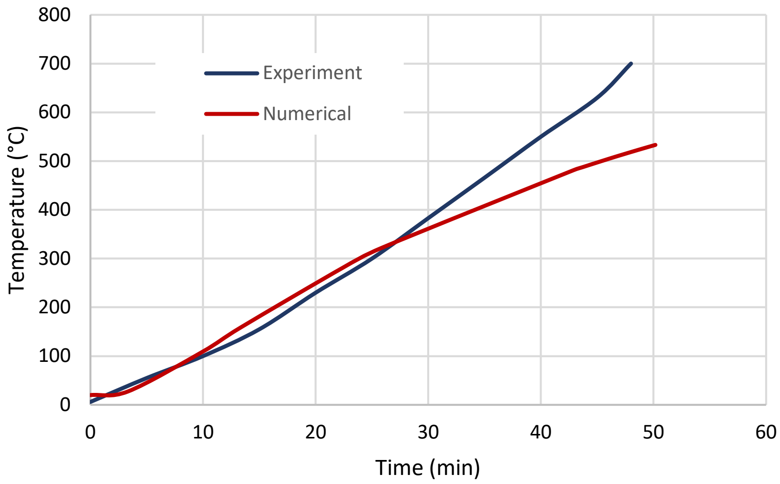

Figure 18. Test 5. Second prototype MBOR-8F.

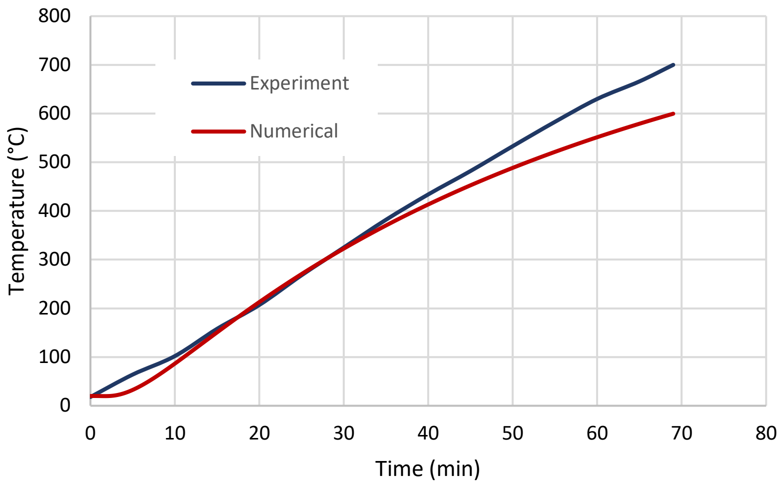

Figure 19. Test 6. Second prototype MBOR-16F.

Fig. 14–19 show the time from the start of a fire test to the achievement of a prototype with a reduced metal thickness of 1.01 mm and that fire protection with MBOR-16F basalt material of the 500 °C critical temperature was 32.5 minutes according to Russian standard No. 53295-2009. A similar sample with MBOR-20F reached its limit state after 37 minutes.

Samples with a reduced metal thickness of 2.35 mm with the coating MBOR-8F reached a critical temperature after 37 minutes, which corresponds to the 6th group of fire-protective efficiency with MBOR-16F fireproof plates in according to Russian standard No. 53295-2009, which reached a critical temperature after 48 minutes.

The simulated temperatures in the middle section of the samples obtained after reaching a given period of time are presented in Table 5. The fire resistance of the structure is evaluated by comparing the results of fire tests based on determining the time to reach the critical temperature of the steel structure with the numerical simulation tests in ELCUT PC. The calculated temperature is obtained in the course of theoretical studies and compared with the results of the standard fire tests.

The Q value taken as the deviation of the obtained temperature T_{pr} in the ELCUT PC from the critical temperature T_{cr} , calculated by formula (5), is determined in percentage by the formula:

$$Q=\left(\left(T_{pr}-T_{cr}\right)/T_{cr}\right)\cdot 100\%, \tag{5}$$

where T_{cr} is a critical temperature, °C;

T_{pr} is a simulation temperature, °C;

Q is a deviation of simulation results from experiment, %.

A table of temperatures obtained and their correlations with the fire tests are presented in Table 3.

Table 3. Temperature correlations with the fire tests.

t_{red} , mm	MBOR -F	T_{pr} , °C	T_{cr} ,°C	Time (min)	Q, %
	–	717.34		15	2.5
1.01	16	752.0	700	48	7.4
	20	737.8		50	5.4
	–	651.31		17	-7.0
2.35	8	522.7	700	50	-25.3
	16	599.7		69	-14.3

The data presented in Table 3 shows that the best convergence of the simulated temperature with the actual results of fire tests with the difference up to 7.4 % was shown in the calculations of sample No. 1. The design temperature of an unprotected structure for sample No. 2 differs by less than 10 % with fire tests and by 25.3 % and 14.3 % with using MBOR-8F and MBOR-16F fire protection means respectively.

4. Conclusions

1. The numerical simulations in the ELCUT PC of light steel thin-walled C-profile structures without fire protection and with fire protection of MBOR-F basalt roll material and PLAZAS adhesive composition manufactured by TIZOL JSC showed good agreements with the experimental data (less than 10 %) obtained in the testing laboratory JSC "TIZOL". Some deviations of the simulation results are possibly associated with insufficient data on the thermophysical characteristics of the materials under study.

2. Experimental studies of the fire resistance limits of LGSC structures were analyzed in accordance with the fire-protective efficiency. The values of fire-protective efficiency for the steel rods of a C-shaped profile without fire protection and with the use of MBOR-F basalt wool 8, 16 and 20 mm thickness were obtained.

3. The approximating functions on the basis of the fire test program were formed. The nomogram for heating the steel structure was constructed based on this data. There was no deformation of the samples and destruction of the fire-protective material in the heated surface during the fire tests. The fire-protective efficiency of the LGSC was increased by 2 to 4 times. The numerical simulation results correlated well with the experimental studies, which allows for the predicting of the necessary characteristics of materials and the optimization of the costs of their development and fire tests.

References

1. Zhmarin, E.N. International association of light-gauge steel construction. Construction of Unique Buildings and Structures. 2012. 2(2). Pp. 27–30. (Russian)

2. Construction.RU. All-Russian industry online magazine [Electronic resource]. URL: https://rcmm.ru/tehnika-i-tehnologii.html (date of application: 12.05.2015).
3. Musorina, T.A., Gamayunova, O.S., Petrichenko, M.R., Soloveva, E. Boundary layer of the wall temperature field. Advances in Intelligent Systems and Computing. 2020. Vol. 1116. pp. 429-437. DOI: 10.1007/978-3-030-37919-3_42
4. Musorina, T., Gamayunova, O., Petrichenko, M. Thermal regime of enclosing structures in high-rise buildings. Vestnik MGSU. 2018. Vol. 13. Pp. 935–943.
5. Terekh, M., Tretyakova, D. Primary energy consumption for insulating. E3S Web of Conferences. 2020. Vol. 157. Pp. 1–8 [Electronic resource]. DOI: 10.1051/e3sconf/202015706008
6. Zemitis, J., Terekh, M. Optimization of the level of thermal insulation of enclosing structures of civil buildings. MATEC Web of Conferences. 2018. Vol. 245(68): 06002. DOI: 10.1051/matecconf/201824506002
7. Vatin, N. et al. Simulation of cold-formed steel beams in global and distortional buckling. Applied Mechanics and Materials. 2014. Vol. 633–634. Pp. 1037–1041. DOI: 10.4028/www.scientific.net/AMM.633-634.1037
8. Garifullin, M., Nackenhorst, U. Computational analysis of cold-formed steel columns with initial imperfections. Procedia Engineering. 2015. Vol. 117. No. 1. P. 1073–1079.
9. Garifullin, M. et al. Buckling analysis of cold-formed c-shaped columns with new type of perforation. Advances and Trends in Engineering Sciences and Technologies - Proceedings of the International Conference on Engineering Sciences and Technologies, ESaT 2015. 2016. Pp. 63–68. DOI: 10.1016/j.proeng.2015.08.239
10. Garifullin, M.R., Vatin, N.I. Buckling analysis of thin-walled cold-formed beams — short review. Construction of Unique Buildings and Structures. 2014. No. 6(21). 2014. Pp. 32–57. (rus)
11. Vatin, N.I., Popova, Ye.N. Termoprofil v legkikh stalnykh stroitelnykh konstruktsiyakh [Thermoprofile in light steel building structures] SPb.: Izd-vo SPbGPU, 2006. 63 p. (rus)
12. Gravit, M.V. et al. Software packages for calculation of fire resistance of building construction, including fire protection. IOP Conference Series: Materials Science and Engineering. 2018. Vol. 456. No. 1. DOI: 10.1088/1757-899X/456/1/012016
13. Gravit, M., Dmitriev, I., Lazarev, Y. Validation of the Temperature Gradient Simulation in Steel Structures in SOFiSTiK. Advances in Intelligent Systems and Computing. 2019. Vol. 983. Pp. 929–938. DOI: 10.1007/978-3-030-19868-8_92
14. Gravit, M.V., Nedryshkin, O.V. Full-scale tests for the simulation of fire hazards in the building with an atrium. Advances and Trends in Engineering Sciences and Technologies III- Proceedings of the 3rd International Conference on Engineering Sciences and Technologies, ESaT 2018. 2019. P. 375–380.
15. Gravit, M.V., Golub, E.V., Antonov, S.P. Fire protective dry plaster composition for structures in hydrocarbon fire. Magazine of Civil Engineering. 2018. 79(3). Pp. 86–94. DOI: 10.18720/MCE.79.9
16. Naser, M.Z., Degtyareva, N.V. Temperature-induced instability in cold-formed steel beams with slotted webs subject to shear. Thin-Walled Struct. 2019. Vol. 136. Pp. 333–352. DOI: 10.1016/j.tws.2018.12.030
17. Naser, M.Z., Uppala, V.A. Properties and material models for construction materials post exposure to elevated temperatures. Mech. Mater. 2020. Vol. 142. DOI: 10.1016/j.mechmat.2019.10329318
18. Zhou, H. et al. Behavior of prestressed stayed steel columns under fire conditions. Int. J. Steel Struct. 2017. Vol. 17. No. 1. Pp. 195–204. DOI: 10.1007/s13296-015-0074-4
19. Chen, W. et al. Full-scale experiments of gypsum-sheathed cavity-insulated cold-formed steel walls under different fire conditions. J. Constr. Steel Res. 2020. Vol. 164. P. 105809. DOI: 10.1016/J.JCSR.2019.105809
20. Chen, W., Ye, J., Zhao, Q. Thermal performance of non-load-bearing cold-formed steel walls under different design fire conditions. Thin-Walled Struct. 2019. Vol. 143. P. 106242. DOI: 10.1016/J.TWS.2019.106242
21. Chen, W., Ye, J., Li, X. Fire experiments of cold-formed steel non-load-bearing composite assemblies lined with different boards. J. Constr. Steel Res. 2019. Vol. 158. Pp. 290–305. DOI: 10.1016/j.jcsr.2019.04.003
22. Chen, W., Ye, J., Li, X. Thermal behavior of gypsum-sheathed cold-formed steel composite assemblies under fire conditions. J. Constr. Steel Res. 2018. Vol. 149. Pp. 165–179. DOI: 10.1016/j.jcsr.2018.07.023
23. Chen, W. et al. Improved fire resistant performance of load bearing cold-formed steel interior and exterior wall systems. Thin-Walled Struct. 2013. Vol. 73. Pp. 145–157. DOI: 10.1016/J.TWS.2013.07.017
24. Dias, Y., Keerthan, P., Mahendran, M. Fire performance of steel and plasterboard sheathed non-load bearing LSF walls. Fire Saf. J. 2019. Vol. 103. Pp. 1–18. DOI: 10.1016/J.FIRESAF.2018.11.005
25. Dias, Y., Mahendran, M., Poologanathan, K. Full-scale fire resistance tests of steel and plasterboard sheathed web-stiffened stud walls. Thin-Walled Struct. 2019. Vol. 137. P. 81–93. DOI: 10.1016/j.tws.2018.12.027
26. Craveiro, H. Fire resistance of cold-formed steel columns. Universidade de Coimbra. 2015. P. 366.
27. Agafonova, V.V. Computational modeling during assessment of fire resistance of steel constructions with the use vermiculite fire protection. Izvestiya SFedU. Engineering Sciences. 2013. Pp. 173–177.
28. Golovanov, V.I., Pavlov, V.V., Pekhotikov, A.V. Fire protection of steel structures with slab material PYRO-SAFE AESTUVER T. Fire and explosion safety. 2016. Vol. 125. Pp. 8–15. DOI: 10.18322/PVB.2016.25.11.8-16
29. Gernay, T. Book Review: Fire Performance of Thin-Walled Steel Structures by Yong Wang, Mahen Mahendran, and Ashkan Shahbazian. Fire Technol. 2021. 57. Pp. 973–975 . https://doi.org/10.1007/s10694-020-01082-x
30. Seo, J.K., Lee, S.E., Park, J.S. A method for determining fire accidental loads and its application to thermal response analysis for optimal design of offshore thin-walled structures. Fire Safety Journal. 2017. Vol. 92. Pp. 107–121. https://doi.org/10.1016/j.firesaf.2017.05.022
31. Shahbazian, A., Wang, Y.-C. A fire resistance design method for thin-walled steel studs in wall panel constructions exposed to parametric fires. Thin-Walled Structures. 2014. Vol. 77. Pp. 67–76 https://doi.org/10.1016/j.tws.2013.12.001
32. Feng, M., Wang, Y.C., Davies, J.M. Thermal performance of cold-formed thin-walled steel panel systems in fire. Fire Safety Journal. 2003. Vol. 38. No. 4. Pp. 365–394. https://doi.org/10.1016/S0379-7112(02)00090-5
33. Feng, M., Wang, Y.C., Davies, J.M. Structural behaviour of cold-formed thin-walled short steel channel columns at elevated temperatures. Part 1: experiments. Thin-Walled Structures. 2003. Vol. 41. No. 6. Pp. 543–570. https://doi.org/10.1016/S0263-8231(03)00002-8

34. Wang, W., Qin, S. Experimental investigation of residual stresses in thin-walled welded H-sections after fire exposure. Thin-Walled Structures. 2016. 101. Pp. 109–119. https://doi.org/10.1016/j.tws.2016.01.005
35. Pyl, L., Schueremans, L., Dierckx, W., Georgieva, I. Fire safety analysis of a 3D frame structure based on a full-scale fire test. Thin-Walled Structures. 2012. Vol. 61. Pp. 204–212. https://doi.org/10.1016/j.tws.2012.03.023
36. Russian standard GOST 53295-2009 «Fire retardant compositions for steel constructions. General requirement. Method for determining fire retardant efficiency»
37. ISO 834-1:1999 Fire-resistance tests — Elements of building construction — Part 1: General requirements
38. Zinevich, L.V. Primenenie chislennogo modelirovaniya pri proektirovanii tekhnologii obogreva i vyderzhivaniya betona monolitnykh konstruktsiy. [The use of numerical modeling in the design of heating technology and concrete curing of monolithic structures]. Magazine of Civil Engineering. 2011. No. 2(20). Pp. 24–28. DOI: 10.18720/MCE.20.5.
39. Pukhkal, V.A., Mottaeva, A.B. FEM modeling of external walls made of autoclaved aerated concrete blocks. Magazine of Civil Engineering. 2018. Vol. 81. No. 5. Pp. 202–211. DOI: 10.18720/MCE.81.20.
40. Nazmeeva, T.V., Vatin, N.I. Numerical investigations of notched C-profile compressed members with initial imperfections. Magazine of Civil Engineering. 2016. Vol. 62. No. 2. Pp. 92–101. DOI: 10.5862/MCE.62.9.
41. Dudin, M.O., Vatin, N.I., Barabanshchikov, Y.G. Modeling a set of concrete strength in the program ELCUT at warming of monolithic structures by wire. Magazine of Civil Engineering. 2015. Vol. 54. No. 2. Pp. 33–45. DOI: 10.5862/MCE.54.4.
42. Organization Standard ADSC 11251254.001-018-03 Design of Fire Protection of Load-Bearing Steel Structures Using Various Types of Linings; Association for the Development of Steel Construction; Axiom Graphics Union: Moscow, Russia, 2018; ISBN 9785604087855.

Information about authors:

Marina Gravit
PhD in Technical Science
ORCID: https://orcid.org/0000-0003-1071-427X
E-mail: marina.gravit@mail.ru

Ivan Dmitriev
ORCID: https://orcid.org/0000-0002-9822-3637
E-mail: i.i.dmitriev@yandex.ru

Received 01.08.2020. Approved after reviewing 07.09.2021. Accepted 02.02.2022.